Design and Feasibility Testing for a Ground-based, Three-dimensional, Ultra-high-resolution, Synthetic Aperture Radar to Image Snowpacks

Stephen J. Preston

A thesis submitted to the faculty of
Brigham Young University
in partial fulfillment of the requirements for the degree of

Master of Science

David G. Long, Chair
Neal K. Bangerter
Brian A. Mazzeo

Department of Electrical and Computer Engineering

Brigham Young University

August 2010

ABSTRACT

Design and Feasibility Testing for a Ground-based, Three-dimensional,

Ultra-high-resolution, Synthetic Aperture Radar

to Image Snowpacks

Stephen J. Preston

Department of Electrical and Computer Engineering

Master of Science

This thesis works through the design of a radar-based system for imaging snowpacks remotely and over large areas to assist in avalanche prediction. The key to such a system is the ability to image volumes of snow at shallow, spatially-varying angles of incidence. To achieve this prerequisite, the design calls for a ground-based Synthetic Aperture Radar (SAR) capable of generating three-dimensional, ultra-high-resolution images of a snowpack. To arrive at design parameters for this SAR, the thesis works through relevant principles in avalanche mechanics, alpine-snowpack geophysics, and electromagnetic scattering theory. The thesis also works through principles of radar, SAR, antenna, and image processing theory to this end. A preliminary system is implemented to test the feasibility of the overall design. The preliminary system demonstrates ultra-high-resolution, three-dimensional imaging capabilities and the ability to image the volume of multiple alpine snowpacks. Images of these snowpacks display the structural patterns indicative of different layers in the snowpacks. Possible attributions of the patterns to physical properties in the snowpack are explored, but conclusions are not arrived at. Finally, lessons from the implementation of this preliminary system are discussed in terms of opportunities to be capitalized upon and problems to be overcome in future systems that more faithfully realize the complete design set forth in the thesis.

Keywords: ground-based SAR, utlra-high resolution, three-dimensional imaging, volume imaging, snowpack, avalanche

ACKNOWLEDGMENTS

For her uncommon support and sustaining love, I offer my deepest gratitude to my wife Desiree, whom I have come to love more than all the world. I also offer my appreciation to Dr. Long whose willingness to venture into the unknown, passion for cultivating students, and enthusiasm for the discipline of electrical engineering made possible my opportunity to have a new world opened to me and to pursue an idea. I offer my appreciation to the members of the Microwave Earth Remote Sensing lab who have become my friends, of whom Justin Penner, Craig Stringham, and Joe Winkler deserve special mention. I also would like to thank all those who worked on the scanning platform, particularly Don Dawson.

Table of Contents

List of Tables

List of Figures

Chapter 1

Introduction

Improved avalanche prediction requires the ability to assess shear stresses and strengths between multiple layers, or strata, in a snowpack across large areas, often in remote locations or hazardous terrain. Shear forces and shear strengths are derivative of properties of the snowpack, such as density, porosity, grain/crystal size, grain/crystal shape, cluster size, cluster distribution, and water content. Presently, these physical properties are measured locally, by means of a snow pit. This procedure is time consuming, labor intensive, and potentially dangerous. Furthermore, physical properties within a snowpack are notorious for varying widely over small areas due to rapidly varying micro-climates in mountainous terrain [1]. Presently, educated guesses as to physical properties over the large areas covered by slopes on which avalanches occur must be based on experience, weather, topology, snowpack history, and a wide array of additional factors. More objective methods for remotely quantifying physical properties over these large areas are needed.

The ability of radar to penetrate a snowpack over a large area and to detect varying electromagnetic and geometric properties within a snowpack makes radar a likely candidate to meet this need. Physical properties important to assessing avalanche risk have characteristic dielectric, conductive, geometric and magnetic properties. Insofar as the response of certain wavelengths transmitted by a radar system can be correlated to these physical properties, the radar system may provide a means to remotely collect data over large areas to quantify snowpack properties. Data analysis can then be used to predict avalanches and to create images of snowpack structures important to avalanche prediction. Toward this end, this thesis proposes a radar system capable of ultra-high-resolution (measured in inches), three-dimensional, volume imaging and demonstrates a preliminary system testing aspects of the feasibility of the overall design.

1.1 Previous Studies

Several studies demonstrate the ability of radar systems to probe a snowpack to reveal properties such as thickness, density, snow-water equivalency, and particular aspects of snowpack stratigraphy by distinguishing between certain layers in the snowpack. However, these previous studies rely primarily upon boundary reflections from within the snowpack [1], [2], [3], [4], [5], [6], [7], [8], [9], [10].

Different layers within a snowpack have changing electromagnetic and geometric properties. The layer boundaries produce specular reflections that are similar to light bouncing off a shiny surface. These specular reflections can return electromagnetic energy, with information about the snowpack, back to a radar system. Depending on the angle of incidence, specular reflections can also re-direct electromagnetic energy away from the radar system. To capture information from boundary reflections, radar systems must launch waves into a snowpack at nadir so that the direction of wave propagation is normal to snowpack layers.

Additionally, previous studies rely on range distances to locate the source of reflections within the snowpack. For range distances to accurately convey location information, the orientation of the range axis must be known or assumed. An assumption that the radar system is oriented with the range axis normal to the snowpack allows range to be used to directly map reflections to locations within the strata of a snowpack.

In practice, therefore, the radar system must accommodate the snowpack in its orientation. For this reason, previous studies positioned radar systems directly on top of the snowpack, for example, on a sled [5], [8], or beneath a low-hovering helicopter [8]. Only with great difficulty, large amounts of time, and even some danger, can such systems cover the large areas necessary to make their data provide something not offered by a simple snow pit. The slopes and the continuously varying, rugged, mountainous terrain on which snowpacks repose, conspire against the endeavor.

Additionally, previous studies primarily peer into snowpacks to acquire information unrelated to avalanche prediction. Such studies seek to determine the thickness of a snowpack, its snow-water equivalence [5], or to better understand the data from space-born synthetic aperture radars, as that data pertains to snow and ice sheets covering the earth's surface [9]. As a result, such studies talk about reflections based on snow properties, such as

density, that can only be correlated more indirectly with properties that are more important to avalanche formation. Even those rarer studies, interested in snow stratigraphy, focus on these secondary properties [10]. Furthermore, in these studies, backscatter is primarily a function of specular reflection, not the actual volumes of snow. A new system is needed that does not rely on boundary reflections and assumptions about the orientation of the range axis with respect to the snowpack, but on reflection from snow volumes. Such a system would open the possibility of capitalizing upon the abilities of radar to quickly gather data over large areas remotely.

In sum, the literature indicates research is needed to determine what kind of signals can be expected, not from electromagnetic boundaries, but from volumes of snow bearing different properties. This research would not only be helpful for the secondary properties discussed in previous studies, but much more so for properties like the shape and size of snow grains, snowpack porosity, and the distribution of water content that are more closely related to avalanche formation. Research also needs to take place to determine the wavelengths most suited to provide characteristic returns for the primary properties of interest for avalanche prediction.

1.2 Contribution

This thesis contributes to the body of published work on the remote sensing applications of radar by advancing, and in certain aspects initiating, discussions necessary to determine the feasibility of a radar-based system to remotely collect data over large areas that can be used to assist in avalanche prediction. It brings together relevant knowledge of avalanche formation and geophysical knowledge of alpine snowpacks as a basis for the design of such a system. The thesis explores known scattering mechanisms to discuss how avalanche-relevant properties of alpine snowpacks might be recognized, which wavelengths are best suited to provide this information, and to establish preliminary system requirements.

The design of a remote, radar-based system for snowpack imaging is outlined. In the process, the theory behind a synthetic aperture radar capable of imaging volumes, in three-dimensions, at large distances, and with ultra-high resolution is presented. Several design considerations for such a synthetic aperture radar are also highlighted and worked through.

Although the full system design is not implemented, a preliminary system capable of testing some of its assumptions is designed and implemented as a first step toward a more comprehensive system. Results include the demonstration of a ground-based Synthetic Aperture Radar (SAR) capable of three-dimensional, ultra-high resolution images. Three-dimensional, volume images of snowpacks are demonstrated. The images suggest patterns consistent with layered snowpack structures. Physical explanations for these patterns consistent with properties measured in the snowpack are possible, but remain inconclusive. These demonstrations raise and address other issues, like concerns about ground signals and scan times that require experience with volume images of snow to encounter.

1.3 Outline

The organization of this thesis comprises 7 chapters. The first is this introduction. Chapter 2 provides background to understand design considerations for radar-based avalanche prediction systems. The chapter discusses the mechanics behind avalanche formation. The reoccurring strata, or layers, within an alpine snowpack that cause avalanches are identified. The properties of these layers and the geophysics responsible for their formation are explained with an eye toward understanding how the layers may be detected and assessed by a radar-based system in ways that account for the whole mechanical system of a snowpack. Chapter 2 also provides fundamentals necessary to access additional avalanche research relevant to radar-based prediction systems.

Chapter 3 explains backscatter mechanisms that play a role in reflections from an alpine snowpack. The chapter presents backscatter models for snow and explains their deficiencies for avalanche prediction. The chapter uses these explanations and presentations to make design determinations, such as transmission wavelengths, and to propose further studies into the backscatter responses from different avalanche-relevant properties in a snowpack.

Chapter 4 outlines the design of a remote, radar-based system capable of collecting data about avalanche-relevant properties over large areas. Chapter 4 sets forth the prerequisites and requirements for common radar parameters for the design. The design calls for a SAR capable of imaging volumes, in three-dimensions, and with ultra-high resolution. Chapter 4 sets forth principles in the theory of radar, synthetic apertures, antennas, and

image processing algorithms and uses those principles to work out the theory behind the three-dimensional SAR system proposed. Several design considerations for the system are examined.

Chapter 5 explains why direct implementation of the system designed in Chapter 4 is impractical in current circumstances, proposing, instead, a set of goals for a preliminary system to assess the feasibility of the more comprehensive system proposed in the previous chapters. The chapter recounts the creation of a platform capable of scanning a frequency-modulated radar over a grid of dimensions 180 cm x 180 cm, the selection of a C-band radar to mount on that platform, additional infrastructure and accommodations necessary to combine these components, and how the preliminary system meets the design goals.

Chapter 6 provides the results from some of the many experiments performed with the preliminary system. The results include a demonstration of the ability to create three-dimensional, ultra-high-resolution images. A discussion follows about what the resolution offers in terms of snowpack imaging and the problems that might arise from bleeding exhibited in the images from the corner reflectors used in the demonstration.

Chapter 6 also discusses the demonstration of three-dimensional, volume images of snowpacks from two different field deployments—something previously un-demonstrated, to the authors knowledge, and an assumption upon which the design set forth in the preceding chapters relies. Analysis of the images from the two deployments suggests layered structures that extend over large areas in the snowpack. Attempts are made to attribute measurements of physical properties in the snowpack, such as water content and snow density, to these proposed layers. Consistent accounts for the attributions can be made, but the attributions remain inconclusive. The chapter also provides additional discussion of several lessons learned from the images produced from the demonstrations, lessons about bleeding, antenna beam patterns, the concern of ground signals, heating of the snowpack, and other subjects.

Chapter 7 concludes the thesis by reviewing the lessons learned from the design process and the results from the preliminary system. These lessons are used to inform adjustments that are proposed to the preliminary system for future experiments to better assess the feasibility of the system proposed in Chapter 4. In the wake of these lessons,

opinions are expressed as to the likelihood of a radar-based system to assist in avalanche prediction with the collection of data about alpine snowpack properties remotely and over large areas.

Chapter 2

Relevant Snow and Avalanche Basics

2.1 Avalanche Mechanics

Gravity continually acts upon a snowpack. The resultant force F_G at a particular location within a snowpack is the product of the mass M of the overburdening snow and the acceleration provided by gravity G,

$$F_G = MG. \tag{2.1}$$

The slope of the snowpack bifurcates the gravitational force into a compressive force and a shear force. The shear force acts parallel to the angle of the snowpack slope Θ. The compressive force acts perpendicular to the slope and to the snowpack, as shown in Fig. 2.1. Both the shear force F_S and the compressive force F_C are derived from the gravitational force F_G,

$$F_S = F_G \sin\theta, \tag{2.2}$$

$$F_C = F_G \cos\theta. \tag{2.3}$$

Compressive and shear forces deform a snowpack as ice grains in the porous material slide past one another. The resultant compressive deformation increases the density of the snowpack, increasing the number and the strength of the bonds between crystals over time. Compressive deformation makes the snowpack more stable. However, as the snowpack becomes more dense, compressive deformation slows. The steeper a snowpack-bearing slope, the less influential the compressive force becomes. Therefore, at slopes greater than about 25°, most of the deformation occurs down slope as shear deformation.

Shear deformation decreases stability. During shear deformation, ice grains slide past one another, breaking bonds between the grains. The rate of shear deformation varies with

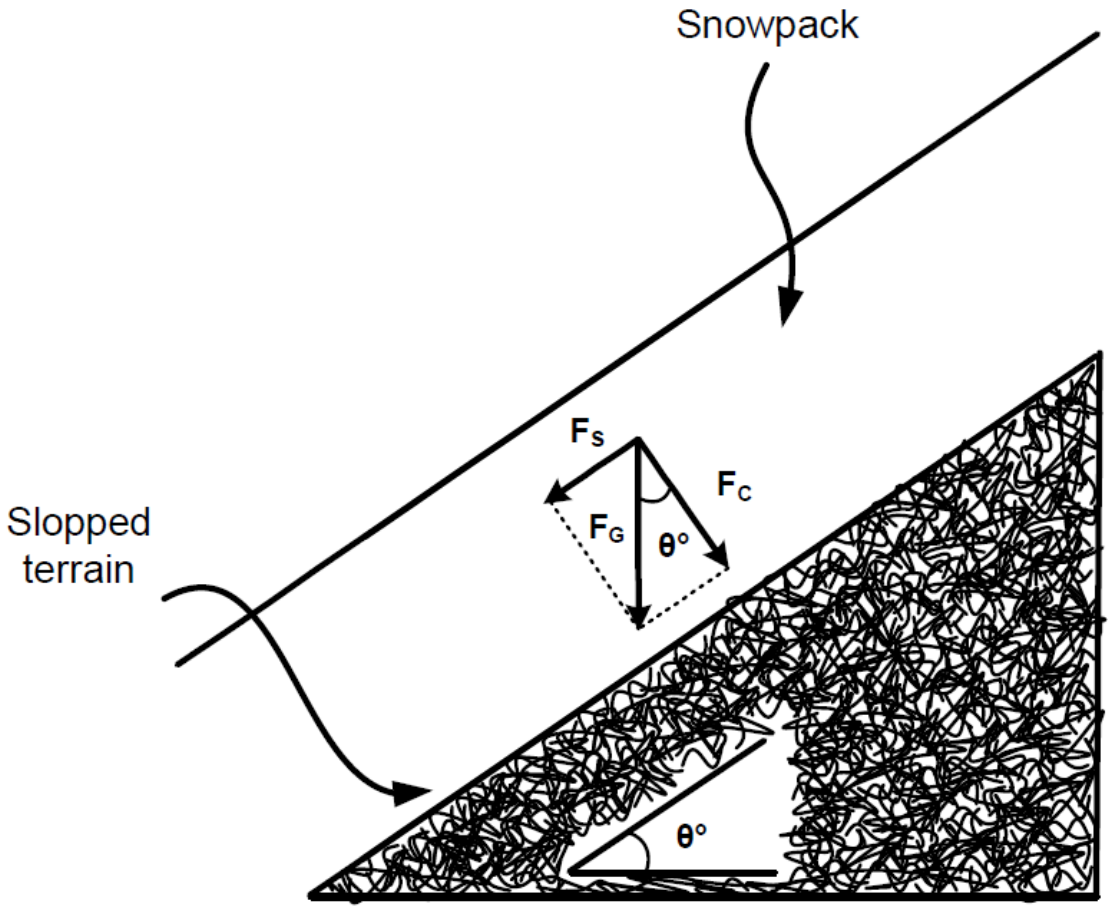

Figure 2.1: Shear F_S and compressive F_C components of the gravitational force F_G on a snowpack disposed on sloped terrain, with slope $\theta°$.

depth in the snowpack according to two factors: the depth-dependent shear force and the depth-dependent snow strength properties, which act to counter shear force.

Cohesion and friction comprise the strength properties in question. Cohesion describes the ability of bonds between individual ice grains to resist shear deformation due to the stress exerted by shear force. When the bonding strength between a large group of adjacent ice grains is strong enough, a slab forms, usually in a layer. Once a slab forms, deformation occurs primarily between the slab and adjacent layers. At this point, friction plays a dominant role.

Friction is the strength property that describes the ability of grains within a slab not to slide by adjacent grains above and below the slab. Friction also resists shear deformation.

Friction depends on factors such as the texture of ice grains in a slab and in surrounding layers, the weight at the boundary between layers, and water content at the boundary. Importantly, the strength of bonds between similar grains comprising a slab is usually greater than the strength of bonds between dissimilar grains at the upper and lower boundaries of the slab. Therefore, the rate of shear deformation is greatest at the boundary between a slab and an adjacent layer, when sufficient cohesion exists to produce a slab.

When shear deformation takes place, a certain portion of the resultant displacement is elastic and recoverable. The remaining portion is plastic and unrecoverable. When the rate of deformation is slow, the vast majority of the deformation is plastic. When the rate of deformation increases, the elastic portion greatly increases, storing more and more potential energy. If the elasticity of the snow is exceeded by too great a rate of increase, a catastrophic, brittle fracture occurs, resulting in an avalanche.

The rate of shear deformation is increased by loading events. These loading events may be, in the order in which they are likely to increase the rate of deformation, snow accumulations from a snow storm, snow accumulation from wind deposition, loading caused by the weight of a skier, or the explosive force of avalanche-control work. When no external force is present to increase the rate of deformation, the rate of deformation may be increased within the snowpack by imperfections in the snowpack, or by shear strain in its constitutive ice grains.

Ordinarily, the rate of shear deformation must exceed about 100 times an idealized rate of deformation in a typical snowpack at a representative incline to exceed the elasticity of the snowpack and for catastrophic failure to occur. The concussive impact of explosives, or the weight of a skier, however, are known for their ability to increase the rate of deformation by more than this amount. For this reason, 95% of all slab avalanche victims trigger the avalanches that overtake them [11].

Avalanches can be differentiated into two categories based on the two strength properties (cohesion and friction) discussed above. Sloughs, or loose avalanches, arise with a breakdown in cohesion. Slab avalanches arise with a breakdown in friction.

Sloughs commonly occur in new snow that does not bond well with itself. Since these avalanches often occur in the upper regions of the snowpack in relatively light, new fallen

snow, they tend to pose less threat to safety and property. Sloughs are often referred to as point avalanches because they begin at a single point, fanning out and entraining surrounding snow as they progress down slope.

Slab avalanches, however, commonly break free in deeper, denser snow upon a breakdown in the friction that prevents uncontrolled shear deformation at a boundary between layers. Such avalanches often include several layers that have consolidated over time. Unlike point avalanches, slab avalanches have a large fracture crown, which adds to their destructive power. Often the breakdown in friction in such avalanches occurs upon a prior breakdown in the cohesion of an underlying layer of weakness. As the weak layer crumbles, the slab overcomes reactive force due to friction. Slab avalanches can be very dangerous and destructive. Further discussion of avalanche mechanics can be found in references [11], [12], [13] and [14].

2.2 Snowpack Layers Associated with Avalanches

Cohesion and friction at various locations within a snowpack depend on the widely varying characteristics of the constitutive elements of the snowpack. These constitutive elements are ice grains, air, and water. At a given time, similar compositions of these basic elements tend to exist in the same regions of the snowpack, forming layers of varying thicknesses. Cohesive properties vary from layer to layer, as do the friction properties between different layers [15].

Several identifiable layers with well-defined characteristics, formed by commonly occurring physical processes, consistently manifest themselves in seasonal snow packs. The cohesive and friction properties associated with certain of these commonly occurring layers, and/or the shear forces they generate, make these layers important to avalanche formation. Layers of particular importance include layers comprising various categories of faceted ice grains, crusts, and wind-deposited layers.

2.2.1 Faceted Snow

Layers of faceted grains are important to avalanche formation because the weak bonding of faceted grains reduces cohesion within the layers and friction between adjacent layers. Additionally, faceted layers belong to the group of "persistent forms" of snow, character-

ized by their ability to contribute to avalanche formation over long periods of time. Once a faceted layer forms, the layer, with all of its destabilizing influences, persists [13]. These layers are also a concern because of the stealth of their formation during calm weather and clear skies, often occurring imperceptively within the snowpack [11].

The weak bonding of faceted grains arises both from the manner of their growth and from the ultimate shape they take. Faceted gains grow from a substrate of ice grains that are usually less than a millimeter in size. These substrate grains, which make up a snow pack, are the broken-down remnants of snow flakes. The grains fit loosely together in the snowpack, resulting in large porous regions between ice grains that contain air, liquid water, and water vapor.

Discounting the reducing and rounding effects of melting, the growth and shape of ice grains surrounded by water vapor depends on whether water vapor sublimates from or freezes to different regions of the surfaces of those grains. The surface of an ice grain describes alternating concave and convex regions, with varyings degrees of concavity or convexity. Whether water vapor sublimates from or freezes to a region at the surface of an ice grain depends on whether the surface is concave or convex, the degree of the concavity or convexity, and any motion of the water vapor relative to the region in question.

Motion of the water vapor relative to the surface of ice grains depends on the presence and strength of a pressure gradient within the porous regions of the snowpack. Pressure gradients describe the forces exerted per unit area by the water vapor acting to leave an area densely populated with water vapor for an area that is less densely populated. Differences in density from one area to another within the porous regions arise because an area at a relatively high temperature holds more water vapor, making it more crowded, than an area at a relatively low temperature. Hence, temperature gradients give rise to pressure gradients. The pressure gradients push water vapor, giving it motion relative to ice grain surfaces.

The motion of water vapor relative to ice grain surfaces determines whether water vapor freezes or sublimates predominantly according to one of two different possible regimes: the equilibrium regime and the kinetic regime. Within the kinetic regime, the relative motion of the water vapor determines the speed with which freezing and sublimating take place.

Equilibrium and Kinetic Regimes

The equilibrium regime receives its name from the fact that in the absence of a significant pressure gradient, the water vapor responsible for grain growth is said to be in equilibrium. In the equilibrium regime, a small or non-existent temperature gradient does not result in a significant pressure gradient that would push water vapor into motion. Freezing and sublimation patterns characteristic of such an equilibrium describe the growth of ice grains in the equilibrium regime.

Where water vapor is in equilibrium, water vapor tends to freeze at the surfaces of concave regions and to sublimate from convex regions. In the process, concave regions fill with ice and convex regions diminish in volume. Diminishing convex regions and filling concave regions produce more symmetrical, rounded grains. Simultaneously, shear and compression deformation grind and polish ice grains over time, also acting to produce more symmetrical and rounded grains. Figure 2.2 depicts the formation of such symmetrical and rounded grains, commonly referred to as "rounds."

The kinetic regime receives its name because of the way in which a water-vapor pressure gradient sets particles in motion, giving them kinetic energy. In the kinetic regime, a temperature gradient results in a pressure gradient large enough to push water vapor into motion at rates fast enough for the characteristic freezing and sublimating patterns of the kinetic regime to dominate. Where water vapor travels under the influence of a sufficient amount of kinetic energy, water vapor tends to freeze at the surfaces of convex regions and to sublimate from the surfaces of concave regions. Freezing and sublimating in the kinetic regime, therefore, take place at regions with curvatures opposite to the regions where freezing and sublimating take place in the equilibrium regime, as summarized in Table 2.1. In the

Table 2.1: Regions of Freezing and Sublimating in Equilibrium and Kinetic Regimes.

Regime	Concave Region	Convex Region
Equilibrium	Freezing	Sublimating
Kinetic	Sublimating	Freezing

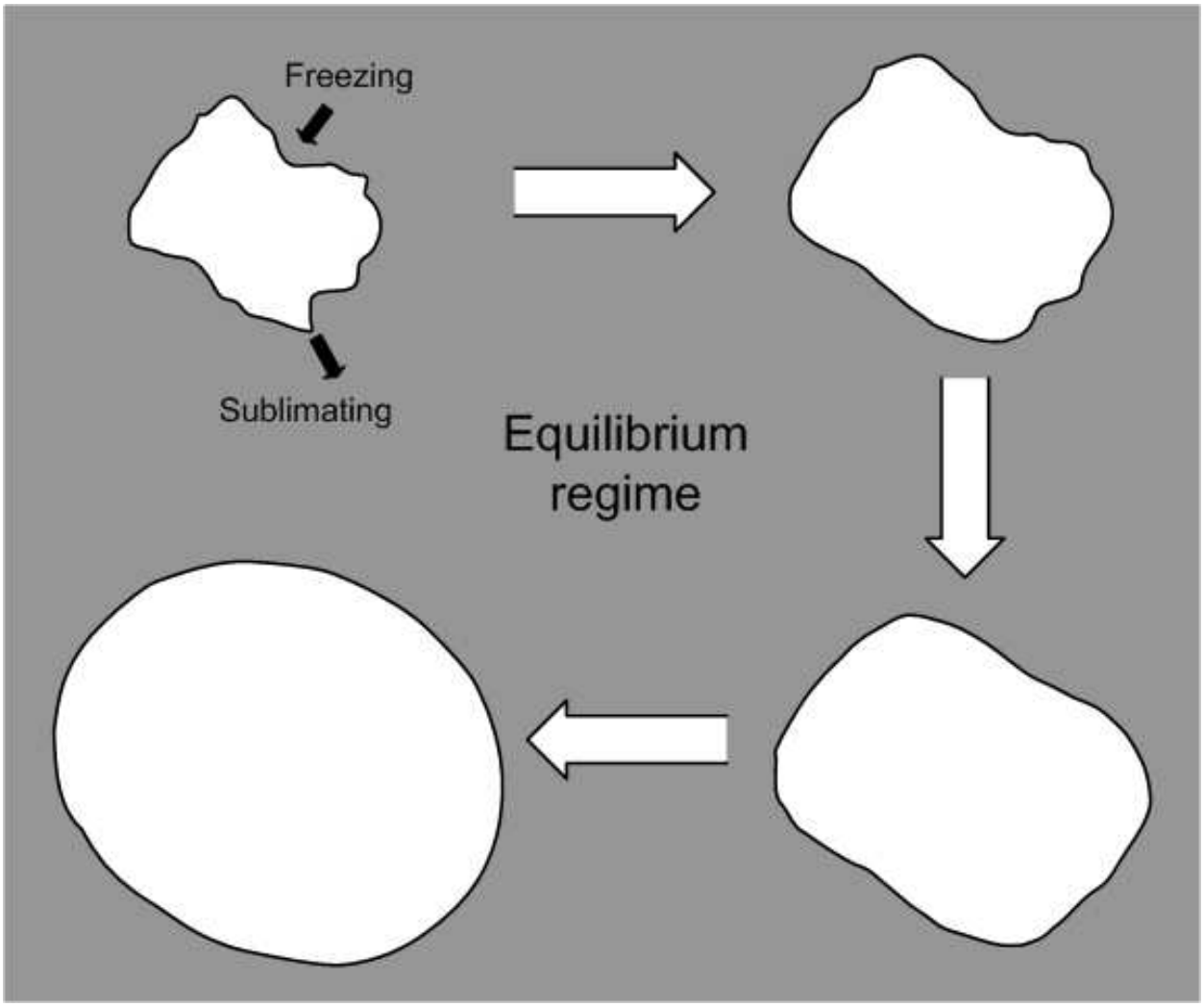

Figure 2.2: Progressive formation of a "round" ice grain, indicating patterns of freezing and sublimating in the Equilibrium regime.

process, convex regions grow and concave regions become more concave. Growing convex regions and diminishing concave regions produce angular, pointed grains. Figure 2.3 depicts the formation of such angular and pointed, i.e., faceted grains. Further discussion of the equilibrium and kinetic regimes can be found in references [16], [17], [18], [19] [20] and [21].

Implications for Cohesion in Terms of Sintering/Bonding

Cohesion measures the strength derived from bonds between ice grains within a snowpack. Bonded clusters of ice grains, the formation of which is discussed below, catch and

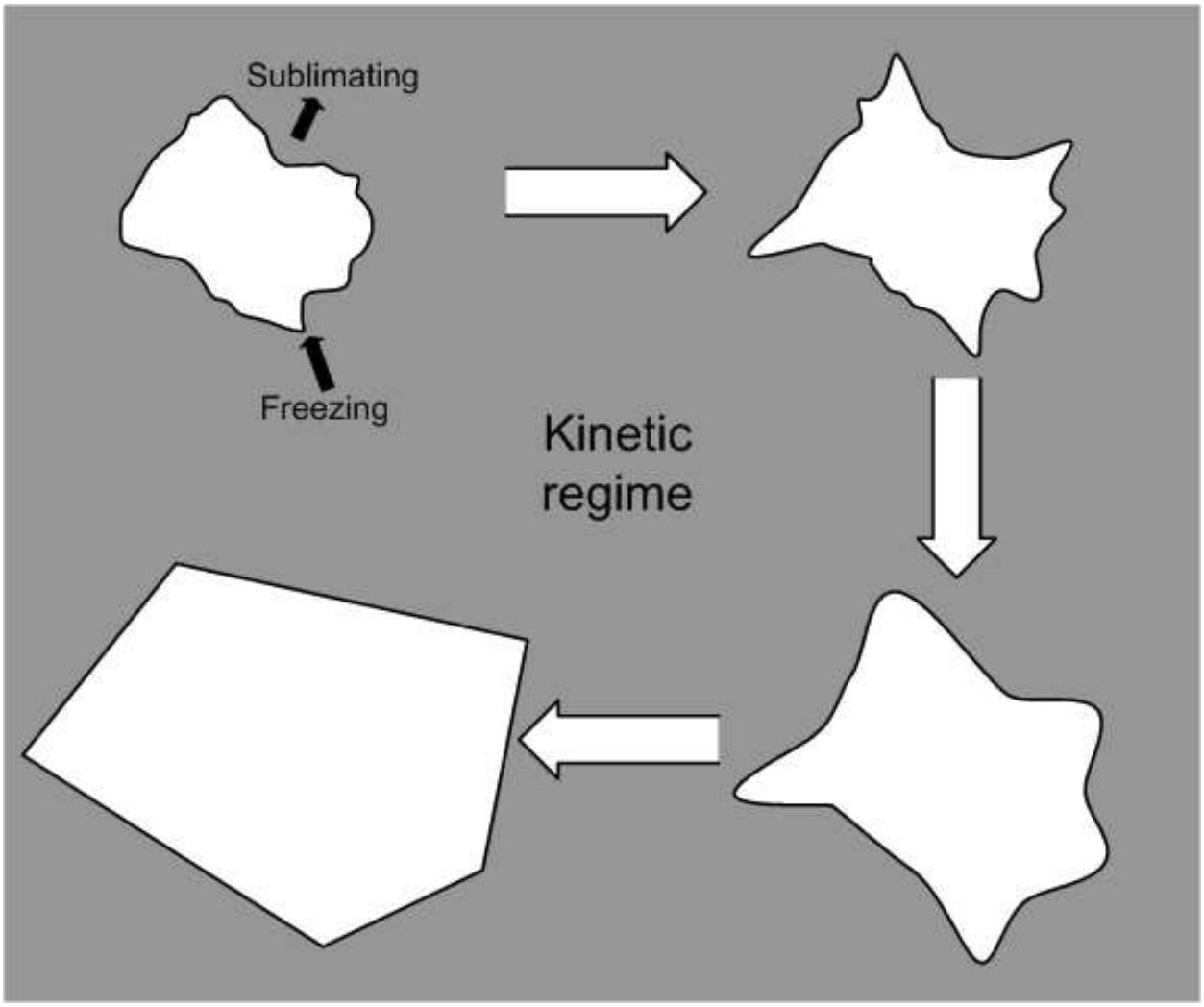

Figure 2.3: Progressive formation of a faceted ice grain, indicating patterns of freezing and sublimating in the Kinetic regime.

hold one another in place by mechanical friction. The larger the clusters and the stronger their bonds, the greater the ability of the clusters to hold ice grains in place. As stated above, faceted grains result in weak cohesion relative to that of rounded grains because of their ultimate shape and because of the manner of their growth.

The shape of faceted grains contributes in multiple ways to their weak cohesive properties. Bonds occur at the points of contact between ice grains. The greater the specific surface area, i.e., the ratio of surface area to volume, of ice grains, the more opportunities for contact and for bond forming. A spherical shape maximizes the ratio of surface area

to volume. Hence, the symmetrical, rounded grains, "rounds," produced in the equilibrium regime have many points of contact at which they may form bonds one with another [11] and [22].

Conversely, faceted grains have smaller specific surface areas, giving them less surface area along which bonds can form. Additionally, the elongated pointed regions of faceted grains tend to further separate the grains. More importantly, because these points are the regions of faceted grains that extend most outward, they are generally the regions at which contact is made with other grains and at which bonds can form. However, the elongated and sharp ends of these points make the area of contact at which grains fuse together relatively small compared to that of rounds, due to the nature of sintering, or bond formation between grains.

Where two ice grains come in contact with another, sintering takes place, and bonds form by a process known as grain-boundary diffusion. Grain-boundary diffusion can be explained in terms of a simplifying, two-dimensional image of the progression of the formation of a bond between two rounds. Such a two-dimensional image is depicted below in Fig. 2.4. As depicted in Fig. 2.4, when two rounded grains come in contact, two fluted grooves describe the space between the two grains, one opening upwards and the other downwards.

Considering either of these grooves, the stresses caused by the forces driving the two grains together are greater at the point, or interior, of the groove—the region where contact is made—than at the exterior, which opens out into the porous region, where no stresses are present. This stress gradient causes water molecules within the grain to migrate from regions of high stress to regions of low stress. As the water molecules migrate, the portions of the grains in contact with each other increases, the bond strengthens, and the grains fuse together.

The process of grain-boundary diffusion continues until the angle described by the interior, or point, of the fluted groove reaches an equilibrium value of about 145°, as shown in Fig. 2.4. Rotating the groove around an axis between the center points of the two grains describes a concave neck shape. As the angle described by the interior of the groove increases, the neck becomes fatter and the contact area between grains increases, resulting in a stronger

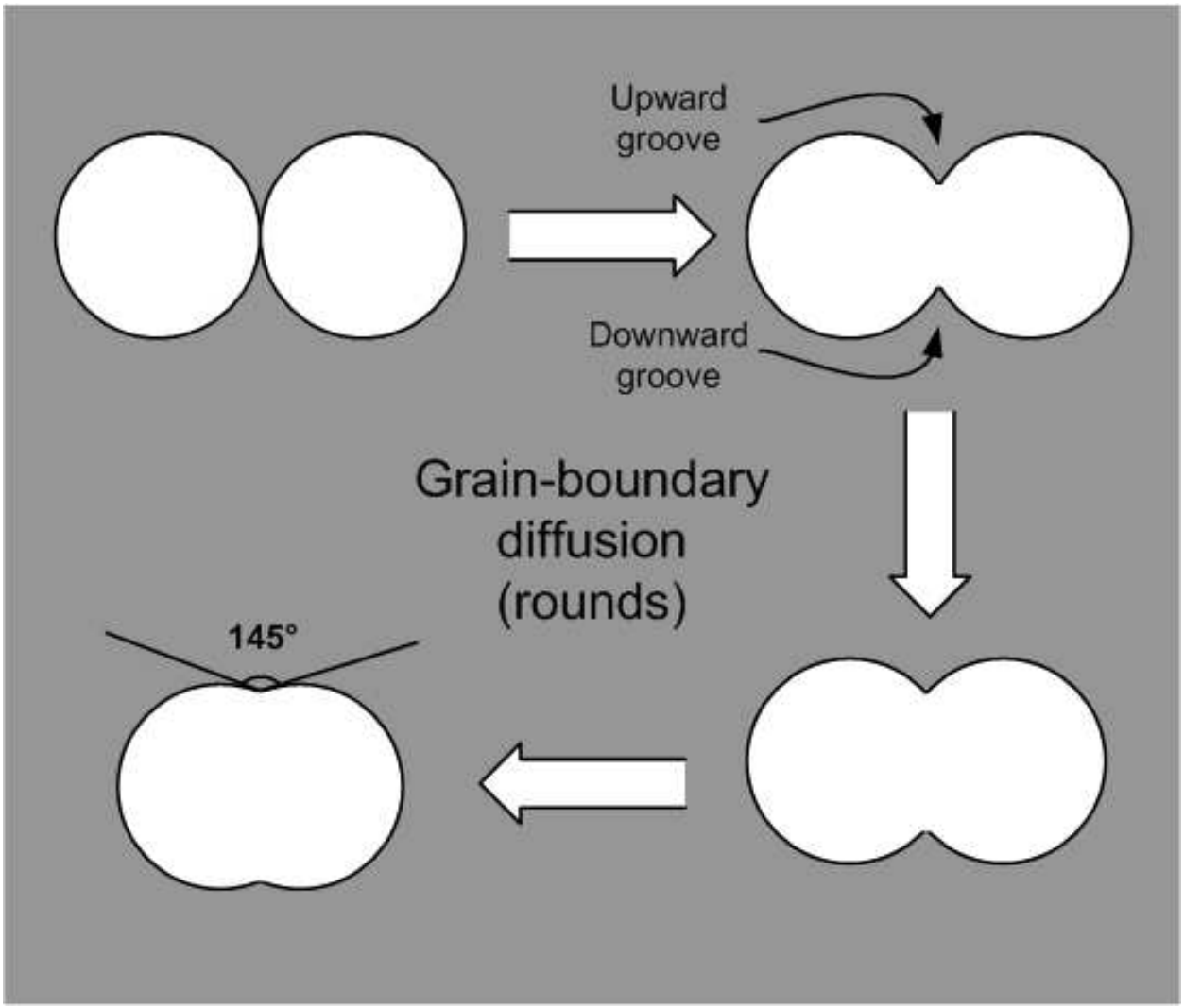

Figure 2.4: Progressive, two-dimensional depiction of grain-boundary diffusion.

bond between the fused ice grains. (Additional discussion of grain-boundary diffusion is provided in references [23] and [24].)

Grain-boundary diffusion also occurs between faceted grains. However, a little reasoning based on the demonstrated principles of grain-boundary diffusion, discussed above, suggests that grain-boundary diffusion between faceted grains leads to weaker bonds. Grain-boundary diffusion occurs most rapidly at grooves that describe highly acute angles and slows to a stop as these angles increases to an obtuse value of 145°. In faceted grains, the points at which contact is often made result in grooves that are already obtuse, approaching the equi-

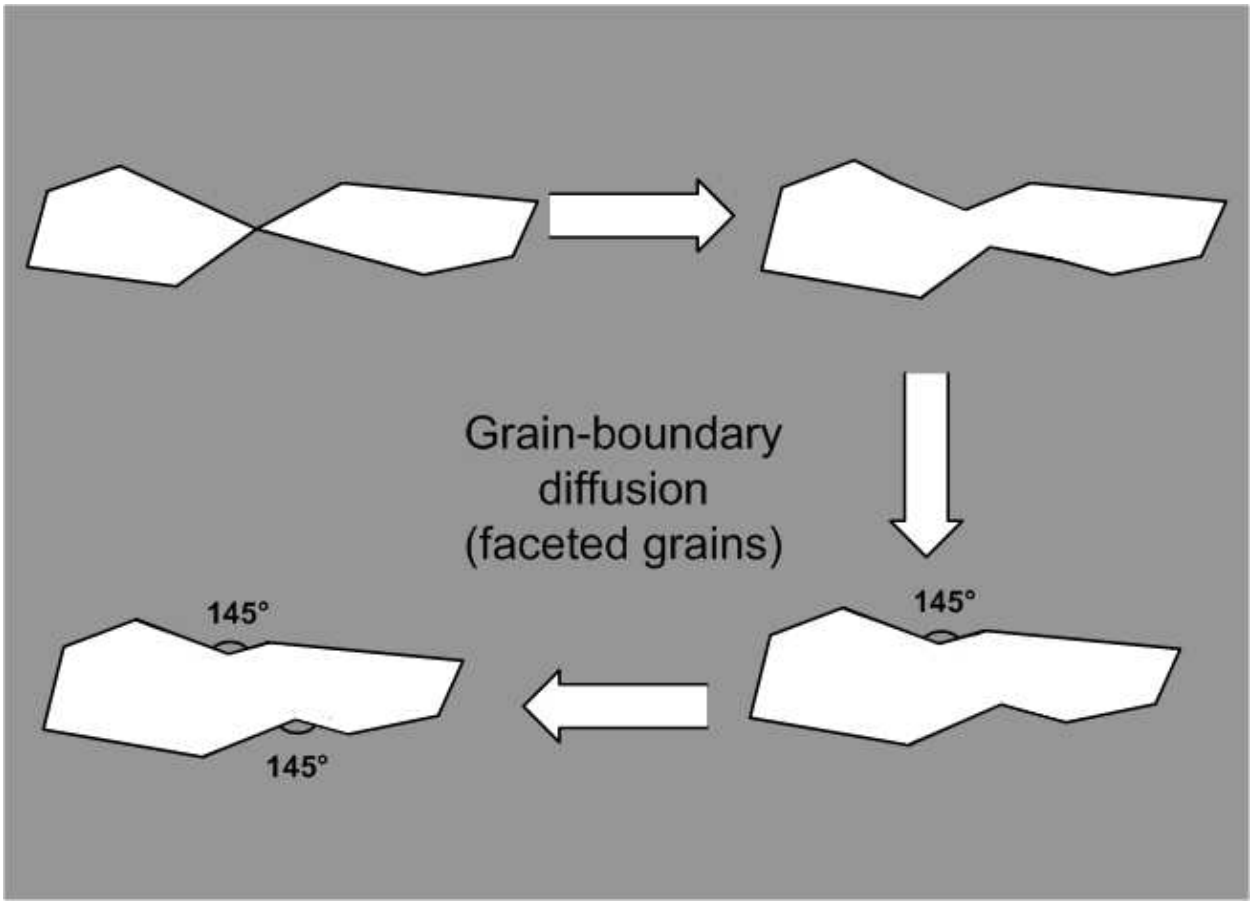

Figure 2.5: Progressive, two-dimensional depiction of grain-boundary diffusion for faceted grains.

librium value of 145° at which grain-boundary diffusion ceases. The obtuse angles described by the grooves between faceted grains are depicted in Fig. 2.5. The little grain-boundary diffusion that does take place before the equilibrium angle is reached does not much increase the size of the point at which contact is made between grains, as shown in Fig. 2.5.

Rotating the groove at the end of the elongated points, after the equilibrium angle is obtained, around an axis between the center points of the two grains, again describes a concave neck shape. However, this neck is comparatively much skinnier than the concave neck between round grains. The contact area of the skinny neck is also much less, resulting in a bond that is weaker than the typical bond between rounded grains.

The manner of growth for faceted grains also makes important contributions to their weak cohesive properties. As discussed above, in the equilibrium regime, water vapor freezes

to concave regions and sublimates from convex regions. Water vapor freezing within the concave necks that bond ice grains together increases the thickness of those necks and the strength of those bonds.

Conversely, in the kinetic regime that dominates the growth of faceted grains, water vapor sublimates from concave regions and freezes to convex regions. Water vapor sublimating from the already comparatively skinny concave necks that bond faceted grains makes those necks even skinner and further decreases the strength of the bonds. Figure 2.6 depicts a comparison between the thickening and strengthening of concave necks in the equilibrium regime and the thinning and weakening in the kinetic regime.

Factors Determining Nature of Faceted Formation

Three critical factors determine the nature of faceted growth and the ultimate characteristics of faceted grains. Those factors are, in order of importance, the nature of the temperature gradient, the degree of porosity within the snowpack, and the level of water vapor in the porous regions of the snowpack [11]. These factors are discussed below in order from the least to the most important.

The level of water vapor influences the rate at which faceted growth occurs. High levels of water vapor result in fast rates of faceted growth because the presence of greater numbers of water molecules increases the amount of material that can freeze on grain surfaces. High levels of water vapor are associated with high temperatures in the snow that cause greater amounts of evaporation from water content and greater amounts of sublimation from ice grains.

The degree of porosity within the snowpack determines how much faceted growth can occur and how large faceted grains may become. Porosity is a measure of the ratio of the volume of the porous regions of the snowpack, comprised of air, liquid water, and water vapor, to the total volume of the snowpack. When the convex regions at which faceted growth takes place run out of porous regions within which to grow, growth proceeds in ways that increase the strength of bonds between grains. For this reason, measurements of the porosity within a snowpack provide information about the potential for faceted growth and a corresponding potential for cohesion degradation.

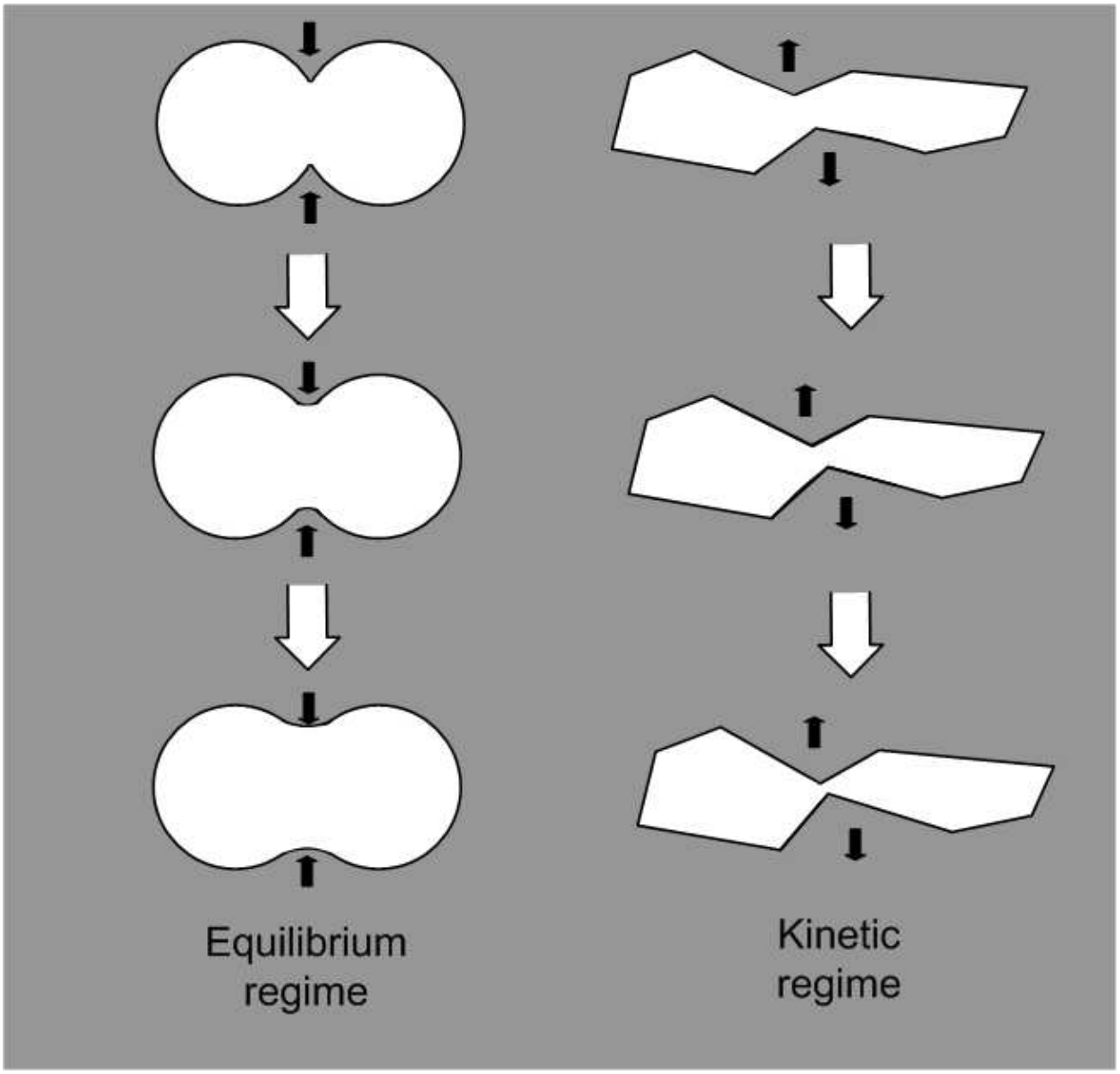

Figure 2.6: Progressive impact of freezing patterns on concave bond necks in both the Equilibrium regime (left) and the Kinetic regime (right).

The most important factor determining the nature of faceted growth is the nature of the temperature gradient. As discussed above, without a sufficient temperature gradient to cause a sufficient pressure gradient, appreciable faceted growth does not occur. Once the critical value of a temperature gradient necessary for faceted growth has been reached, further increases in the temperature gradient serve to increase the rate of faceted growth.

Not only is the level of the temperature gradient important, but so are the orientation of the temperature gradient, the history of the temperature gradient over time, and the location of the temperature gradient within the snowpack. The way in which all of these factors together consistently manifest themselves with respect to a seasonal snowpack result in three different reoccurring and identifiable categories of faceted grains, each with unique properties that are important to avalanche formation.

These three categories are, in order of the increasing likelihood with which they contribute to avalanche formation: near-surface faceted grains, buried surface hoar, and depth hoar. The formation of these different categories of faceted grains and their avalanche-relevant properties can be explained in terms of the temperature gradients that create them. An explanation of these three categories of faceted grains begins by a discussion of temperature gradients generally. The explanation then proceeds with an account, for each category of faceted grain, of the ways in which the temperature gradient factors, outlined in the previous paragraph, generate the avalanche-relevant properties of each category of faceted grain.

The critical level of temperature gradient for faceted formation is usually around 10 C°/m (1 C°/10 cm), but depends on the amount of water vapor present and decreases with higher levels of water vapor [11]. When the temperature gradient is below the critical value at a particular point in the snowpack, the equilibrium regime dominates. When the temperature gradient is at, or above this critical value, the kinetic regime dominates.

Within a snowpack, temperature gradients typically manifest themselves vertically owing to heat sources—the atmosphere and the ground—at the top and at the bottom of the snow pack. These heat sources act to increase and to decrease the temperature of the snow. However, snow is a very porous material that traps a lot of air, making snow a good insulator. As an insulator, snow resists changes in temperature imposed upon it by these

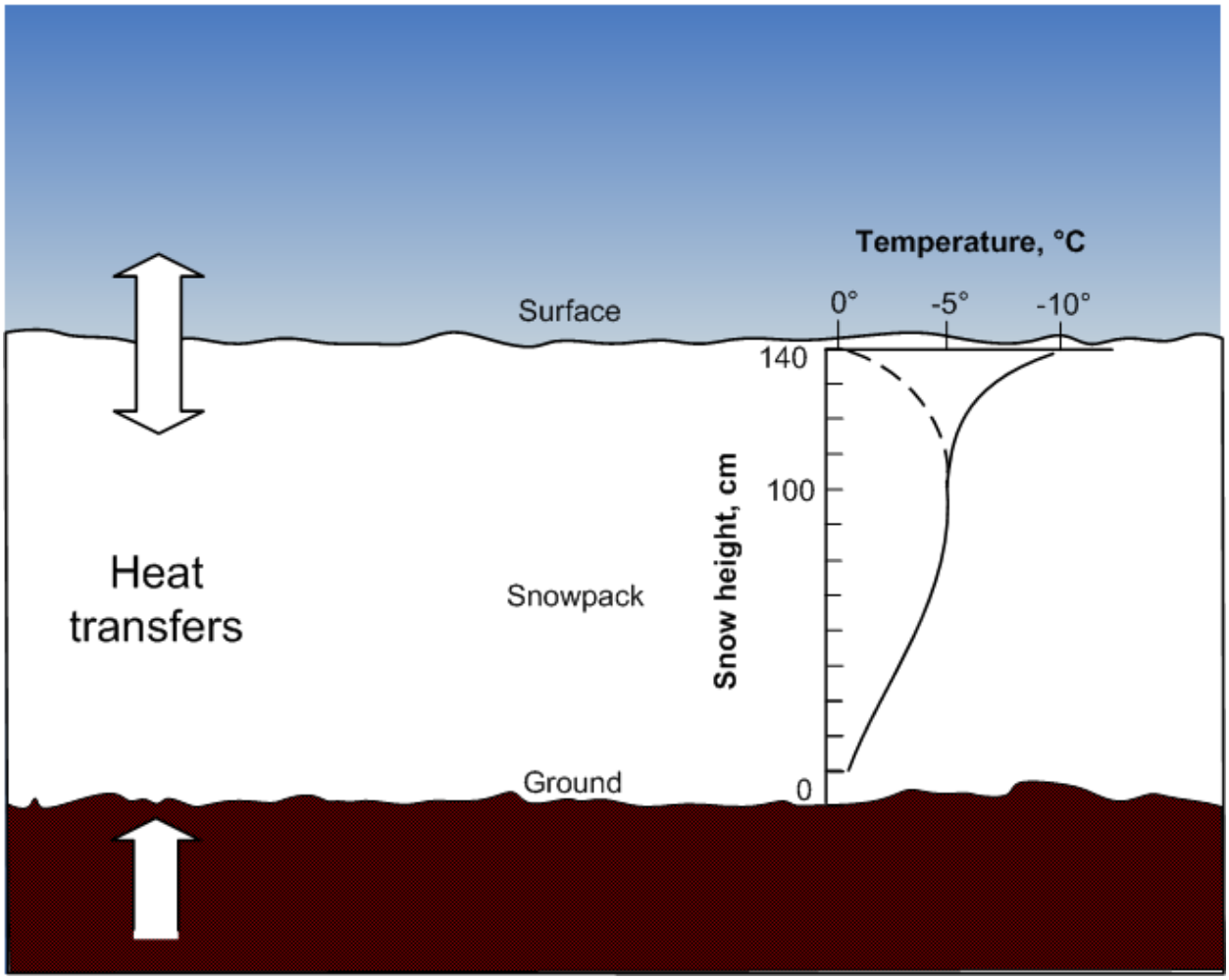

Figure 2.7: Profiles of snowpack temperature with respect to depth in response to heat transfers at sources located at the surface of the snowpack and at the ground.

heat sources. Resistance by snow to temperature change results in a graduated change, with respect to snow depth, between a relatively warm temperature and a relatively cool temperature. In this way temperature gradients, similar to those depicted in Fig. 2.7, arise.

Near-surface, Faceted Grains Near-surface, faceted grains reside within the upper reaches of a seasonal snowpack. The temperature gradients which produce near-surface, faceted grains arise as the insulating properties of a snowpack resist the diurnal fluctuations in the atmospheric temperature above the snowpack. Such diurnal fluctuations in atmo-

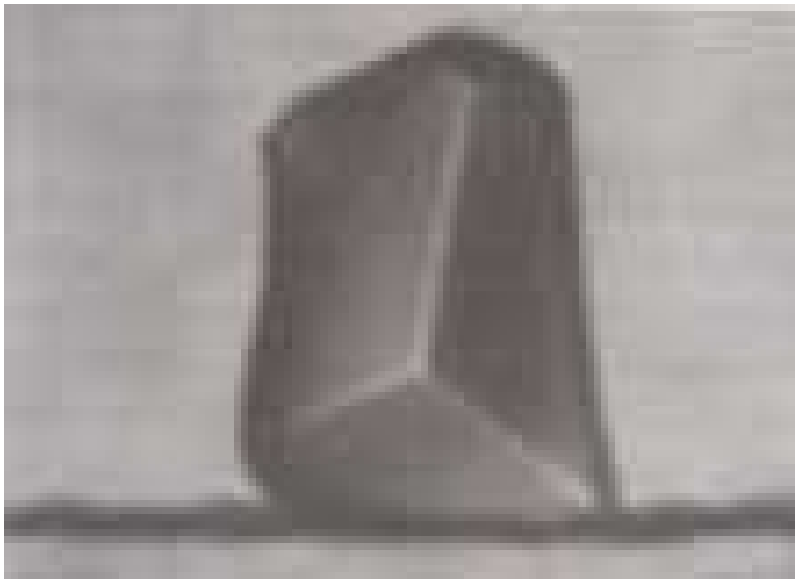

Figure 2.8: Photograph of faceted grain under magnification. Reprinted from [11].

spheric temperature are reflected in the snowpack in varying degrees, due to the insulating properties of snow, as a function of depth, as depicted in Fig. 2.7.

As temperatures swing back and forth between night and day, so do the orientations of the temperature gradients they produce. When the atmospheric temperature is hotter than the temperature of the snowpack during the day, the temperature gradient is oriented upward (higher temperatures exist higher in the snowpack), causing a pressure gradient that drives water downward. When the atmospheric temperature is colder than the temperature of the snowpack, the temperature gradient is oriented downward (higher temperatures exist lower in the snowpack), causing a pressure gradient that drives water upward.

The orientation of the temperature gradient determines whether growth takes place at the upper portion of grains or at the lower portion. Sometimes the convex regions of the upside of grains grow; sometimes the convex regions of the underside grow. The alternating cycles of growth produce elongated, angular structures with an appearance that contrasts to the pyramidal appearance of depth hoar grains (discussed below and depicted in Fig. 2.10) that grow in temperature gradients with a single orientation. The angular structures typical of near-surface faceted grains are depicted in Fig. 2.8.

These angular structures are the biggest cause of deadly avalanches [12]. Both the shape and the manner of formation of these angular structures result in the classic weak bonds, discussed above, that are typical of faceted grains. Diurnal fluctuations in atmospheric temperatures at the surface of a snowpack often produce temperature gradients strong enough to produce faceted growth, meaning that near-surface facets are commonly present in the upper layers of a snowpack. Since these layers manifest near the surface of a snowpack, there are fewer, if any, intervening layers to distribute loads experienced by a layer of near-surface facets. Additionally, once the temperature gradients that form near-surface facets dissipate, the angular structure persists for weeks, even months, making them a long term factor contributing to avalanche danger. Additional discussion of the formation and properties of near-surface facets is found in references [25] and [26].

Buried Surface Hoar Surface hoar is more correctly described as a crystalline structure than as an ice grain. Surface hoar grows when the requisite temperature gradient exists at the surface of a snowpack. The orientation of that temperature gradient is upward (higher temperatures exist above the snowpack) with the relatively high temperatures in the air above the snowpack and the relatively low temperatures at the snowpack surface. As water vapor travels downward from the more densely populated regions of relatively higher temperatures it encounters the cold surface of the snow where it freezes when the water vapor pressure of the air is greater than the equilibrium vapor pressure of the ice.

Temperature gradient levels between 100 C°/m to 300 C°/m are associated with surface hoar formation. The exact level of temperature gradient required for surface hoar formation depends on the relative humidity of the atmosphere above the surface, which usually must be greater than about 70%. The requisite temperature gradients are often generated on clear nights that allow the surface of the snow to drop in temperature through radiative, long-wave cooling [11].

Since the temperature gradients involved in surface hoar growth exist at the surface of the snowpack, faceted growth takes place in the presence of an environment of essentially 100% porosity. As long as the critical level of temperature gradient exists for a particular atmospheric humidity level, surface hoar crystals continue to grow. As a result, surface hoar

Figure 2.9: Examples of surface hoar measured at 2 cm (left) and 5 mm (right).

crystals span a wide variety of sizes, ranging from less than a single millimeter to several centimeters. Examples of 2 cm and 5 mm surface hoar crystals are depicted in Fig. 2.9. The shape of their growth depends on the temperature-dependent type of crystallization that occurs.

Once a layer of surface hoar becomes buried, the layer demonstrates weak cohesive and friction properties as a result of the location and orientation of the thermal gradients in which the layers form. The upward orientation of the temperature gradients, located at the snowpack's surface, cause surface hoar to grow upward into the air to form large, plate-like structures. These large, plate-like structures are thin and fragile. They tend to be oriented vertically with relatively large porous regions between them.

The vertical orientation of these thin, fragile structures and the large gaps between them produce a layer with cohesive properties that are much weaker in response to shear

forces than in response to compressive forces. Consequently, the deformation caused by the load from overburdening layers manifests itself as shear deformation. In terms of mechanics, shear deformation occurs much more readily as the shear loads required to rotate and topple, or fracture, the vertically-oriented, widely spaced crystals is much lower than the compressive loads required to crush the vertically-oriented crystals along their principal axis.

Toppling and fracturing surface hoar crystals can transfer gravitational potential energy into the toppling and fracturing of more surface hoar crystals. If the resultant deformation rate exceeds the elasticity within the surface hoar layer, the layer experiences a shear fracture. The shear fracture results in a vertical collapse that often produces a loud "whumph" sound that signals the beginning of an avalanche.

Surface hoar also has weak friction properties with adjacent layers. The large gaps between the vertically oriented plates that make up a layer of surface hoar correspond to large gaps between points of contact with adjacent layers. The fewer points of contact, the less friction.

The larger surface hoar crystals become, the more fragile they become. The gaps between crystals become larger, and the crystals have less buttressing support. The torque acting to rotate the crystals also increases as the distance between the layers that they span increases.

Compressive deformation typically packs ice grains in place within a snowpack, increasing cohesion over time. The dearth of compressive deformation with surface hoar crystals means that they undergo very little of the settling that would otherwise make them more stable. Lack of settling and the large shapes of surface hoar crystals ensure that the destabilizing effects of surface hoar persist for long periods. Reference [27] provides additional information about surface hoar formation and characteristics.

Depth Hoar Depth hoar grains grow in temperature gradients that are conversely related to the temperature gradients that produce surface hoar. As a result, the depth-hoar grains produced by these conversely related temperature gradients have a vastly different appearance. Nevertheless, layers comprised of depth-hoar grains, like layers comprised of surface hoar, are much weaker in response to shear forces than in response to compressive forces.

The temperature gradients involved in depth hoar formation are oriented downward (higher temperatures exist lower in the snowpack) and exist at the base of the snowpack (near the ground). The temperature gradients arise due to the heat source provided by the ground, which traps heat, primarily stored up during warmer months and augmented by a little geothermal energy, under an insulating blanket of snow. The ground warms the snow immediately above to a temperature of 0 C°/m. The insulating properties of snow resist the warming of the ground to maintain colder and colder temperatures as distance increases from the ground. The resulting temperature gradient is depicted along the lower part of the temperature curve depicted in Fig. 2.7.

The downward-oriented temperature gradient causes water vapor to rise. As water vapor rises, it comes in contact with the underside of ice grains, where it freezes at convex regions. As the water vapor continually freezes at the base of the grains, a pyramidal structure results. The base of this pyramidal structure takes on a hexagonal shape, consistent with the hexagonal shape of ice crystals at the relevant temperatures. Since ice grain growth is dominated by the kinetic regime, water vapor freezes at the outermost edges of the underside of the ice grains, resulting in an ever increasing perimeter and a hollow center.

The hollow, hexagonal pyramids take on a stepped, or striated, outer surface. These steps are also the result of the freezing and sublimating patterns characteristic of the kinetic regime. Figure 2.10 depicts examples of the stepped, hexagonal, pyramidal shape of depth hoar grains. Since these structures are hollow, they are often referred to as having a cup shape.

The dimensions of depth hoar grains, whether from peak to base, or from one end of the base to the other, commonly reach 5 mm and are known to achieve even greater values. Depth hoar grains have the potential to achieve such large sizes because of the potential of the temperature gradients that produce them to last for long periods of time and to return after intervening hiatuses. Since warmth from the ground maintains the basal layer of a seasonal snowpack at 0 C°/m throughout the winter, as long as temperatures in the snowpack above the basal layer are consistently low enough to produce a temperature gradient large enough for the kinetic regime to dominate, depth hoar continues to grow. Cold temperatures occur

Figure 2.10: Examples of faceted ice grains of the depth hoar category. Reprinted from [12].

more easily in layers above the warm ground layer when the atmosphere is closer to the ground layer early in the season when the snowpack is not as thick [12].

The ultimate size achieved by depth hoar grains is often a function of the porosity of the snowpack. To prevent the growth of depth hoar, early in the season, ski resorts, and other entities exercised to avoid avalanches, often bootpack the lower layers of a seasonal snowpack in sensitive areas. In this way, the porosity of the snowpack in the region where depth hoar forms is reduced to a level that makes faceted growth difficult. Without sufficiently large porous regions into which the convex regions of ice grains may grow, growth often occurs in ways that increase the strength of bonds between grains, even in the presence of temperature gradients where the kinetic regime dominates [11].

Like surface hoar, depth hoar produces an anisotropic response to loading. The pyramidal shape of these grains makes them strong against compressive loads. Consequently, little settling takes place to increase stability within the snowpack. However, in response to shear force, depth hoar manifests the characteristic weakness of faceted grains. As with surface hoar, most deformation in depth hoar is transferred to shear deformation. Mechan-

ically, depth hoar grains can be thought of as stacks of upside-down cups disposed with a downward tilt and with weak and relatively few intervening bonds to hold them together. In response to sufficient shear loads, the cups start to slide.

Of the three forms of faceted grains, depth hoar is the least likely to produce an avalanche because of the location at which it forms within a snowpack. New, potentially destabilizing loads, at the surface of the snowpack are distributed throughout the upper layers of the snowpack. These new loads seldom reach down to the lower layers in ways that threaten the stability of the depth hoar layers. However, a failure in a layer of depth hoar at the base of a snowpack always produces a large and dangerous slide. Additional discussion of the formation and properties of depth hoar is found in references [28] and [29].

2.2.2 Wind-deposited Snow

Wind-deposited snow acquires importance primarily because of the loading events it produces. As wind transports snow across the snowpack, the force of the wind and collisions with the snowpack break new fallen snow down to ice grains of as little as one-tenth their former size. Older ice gains also lose volume. In the tumbling process, ice grains become symmetrical. Wind and gravity tightly pack these small, rounded grains into place, resulting in a layer of dense snow.

The density of wind-deposited snow, ranging from 300 Kg/m^3 to 400 Kg/m^3, can easily exceed the density of newly fallen snow, ranging from 30 Kg/m^3 to 100 Kg/m^3, by fourfold. The density of wind-deposited snow is also usually much greater than that of the previous surface layer. A strong wind can rapidly deposit these dense snows onto a previous surface layer, producing a potentially catastrophic loading event.

Wind-deposited snow can increase the load on a snowpack by a rate up to 10 times that achievable by a snow storm. Such sudden load increases test the strength properties of the snowpack. Wind deposits have been known to alter the status of a snowpack from safe to avalanching in a matter of minutes [12].

In addition to the loading events, the cohesive nature of wind-deposited snows, with their implications for friction properties within the snowpack, are important to avalanche formation. The homogeneity, characteristics, and circumstances of deposition of wind de-

posited snow layers result in cohesive slabs. The small, rounded ice grains that make up wind deposits have lots of surface area at which bonds may be formed. Additionally, these grains are packed tightly together by the wind that drives them into place. The cohesion within wind slabs transfers much of the shear deformation that takes place because of shear forces within the snowpack to the boundaries between wind slabs and inhomogeneous layers. Owing to common bonding incompatibilities between wind slabs and various types of layers, relatively weak friction properties occur along these resulting boundaries. Additional information on wind deposited snow is found in [11] and [12].

2.2.3 Crusts

Crusts that form on the surface of a snowpack are important to avalanche formation because of the way they influence friction properties within the snowpack and because of the way they contribute to the formation of faceted layers of snow. A crust is a thin layer, from less than a centimeter to a few centimeters in thickness, of densely conglomerated ice that forms on the surface of a snowpack due to the refreezing of wet snow. An example of a snow crust is depicted in Fig. 2.11.

The wet snow that freezes to form a crust may become wet due to rain, or solar radiation and/or atmospheric temperatures. All crusts are persistent, relatively dense, smooth, and are good thermal conductors. These properties have implications for the friction between crusts and adjacent layers and the tendency of crusts to facilitate the formation of faceted grains in adjacent layers. However, the cause of the wet snow substrate from which a particular crust forms determines the degree to which a crust persists, is dense, and has smooth surfaces.

Wet snow substrates caused by rain result in crusts that are more persistent, denser, smoother, and are better thermal conductors than crusts that result from solar radiation and/or atmospheric wet snow substrates. The wetter the substrate, the stronger these properties manifest themselves after freezing occurs. The greater the manifestation of these crust properties within a particular crust, the less friction between the crust and adjacent layers [12].

Figure 2.11: Example of a snow crust harvested from the top of a snowpack.

Smooth crusts decrease friction because they prevent the mechanical friction occurring when the ice grains of adjacent layers co-mingle with and embed themselves within the crust. Apart from an absence of mechanical friction, smooth surfaces present fewer locations at which bonds can form. The otherwise weak bonding that occurs between crusts and adjacent layers, however, can be strengthened by a skim of water at the surface in which new snow can freeze.

Importantly, the high internal cohesion of dense crusts makes them a mechanical discontinuity within the snowpack. This mechanical discontinuity concentrates shear deformation within the snowpack to the layers immediately above and below the crust, increasing the potential for avalanche formation. Additionally, dense crusts can act as a barrier along

which water percolating down through the snowpack may collect, lubricate snow grains, and reduce friction and cohesion [11].

Dense crusts facilitate the formation of faceted grains. The density of crusts gives them a low permeability to water vapor, making them a barrier. The density of water vapor builds up at the barrier, providing a rich environment for faceted grain growth along with the requisite pressure gradients, [15] [30].

The high thermal conductivity of crusts also facilitates the formation of faceted grains. When cold snow falls on top of wet snow, a temperature gradient sufficient to induce growth in the kinetic regime can result as the latent heat in the wet show is transferred to the new snow. Once the formerly wet snow freezes into a crust, the high thermal conductivity of the crust maintains the temperature gradient by conducting heat from the relatively warm snow pack up to the boundary with the newer, colder snow [31].

2.3 Water Content by Percentage Volume

When a sample of snow exists at a temperature completely below freezing throughout, all water must be frozen. The sample is devoid of water content and, the snow is said to be "dry." Conversely, the longer a sample of snow exists at 0°, or above, where melting occurs, the higher the water content within the sample. However, determining the water content of a snow sample is much more complicated than measuring the temperature of the ambient environment.

Snow's properties as an insulator influence the water content of seasonal snow profoundly. The porosity of the snow, or the amount of air it traps, determines how insulated a sample of snow is from the thermal sources at its surface and at its base, acting to either increase or decrease the temperature of the snow. These insulating properties resist temperature differentials and heat transfer between the ambient environment and the snowpack and the warm ground and the snowpack.

Due to these insulating properties, daily changes in temperature take time to propagate through the snowpack. Warmer ambient temperatures take time to propagate down and melt ice grains to produce water content. Similarly, heat from the ground takes time to propagate up and melt grains.

As stated above, when the temperature of a snow sample, and not just the ambient temperature, is below freezing throughout, the sample is dry and has no water content. Dry snow can be identified in the field by its lack of cohesion. Dry snow will not form balls or clumps when compacted together. However, when the temperature of the snow is at 0 C°, an amount of water content that depends on the duration of time that the temperature of the snow has been at 0 C° is present in the snow.

Commonly, the percentage of that water content is classified as: (1) "moist," (2) "wet," (3) "very wet," and (4) "sludge." A sample with 3% water content by volume or less is referred to as moist. Moist snow can be recognized in the field because it is cohesive and forms balls and clumps when compacted. However, the water content of wet snow is not visible, even when the sample is magnified ten fold. A wet sample holds between 3% to 8% water content by volume. When magnified ten fold, the water content of a wet sample becomes visible around the crystals that comprise the sample.

A very wet sample holds between 8% to 15% water content by volume. A very wet sample can be recognized in the field because such a sample, when lightly squeezed, will render water. Samples with more than 15% water content are considered sludge [11].

The four classifications of water content can be subsumed in two categories that define the way in which the water content is distributed in a sample of snow. The distribution of water content in the moist (less than 3%) and wet (3% to 8%) classifications is distributed according to what is termed the pendular regime. Higher water contents in the very wet (8% to 15%) and in the sludge (greater than 15%) classifications are distributed according to the funicular regime. The four categories of water content and the two categories of water distribution are summarized in Table 2.2.

Table 2.2: Water Content Categories in Relation to Water Distribution Regimes.

Category	Water Content	Distribution Regime
Moist	0% to 3%	Pendular
Wet	3% to 8%	
Very wet	8% to 15%	Funicular
Sludge	more than 15%	

2.3.1 Distribution of Water Content in the Pendular and Funicular Regimes

The manner in which water is distributed in a sample of snow depends on the amount of water content as a percentage of the total volume of the snow. At different water content percentages, different forces control the distribution of water resulting in different distributions. When the water content percentage is below a critical value of about 4%, capillary and surface tension forces completely control water content distribution. For higher water content percentages, gravitational forces begin to play a role in determining water content distributions.

Although gravitational forces begin to play a role after water content percentages rise above 4%, for water contents less than 8% by volume, capillary and surface tension forces still dominate and water distribution is characterized by the pendular regime. In the pendular regime, the volume of gas (air and water vapor) in the pores between grains of ice is greater than the volume of water. Water content is distributed within the porous regions of the snow as inclusions within the gaseous volume.

Capillary and surface tension forces cause water inclusions to congregate along the bond necks and at the points of contact between ice grains where they form as menisci. Since these menisci surround the bond necks and the points of contact, they form ring shapes, known as pendular rings. Figure 2.12 depicts ring-shaped menisci inclusions, or pendular rings, distributed along the bond necks or points of contact of several ice grains. The cross-sectional area of pendular rings provides an indication of the thickness of bond necks and, indirectly, of bond strength.

When the water content reaches levels between 4% and 8% within the pendular regime, gravity begins to play a role. Although the majority of water content is still contained in pendular rings, gravitational forces begin to pull away a portion of the water content. The portion that is drawn off is distributed as spheroidal inclusions.

For water contents greater than 8%, gravity plays the dominant role and water distribution is characterized by the funicular regime. In the funicular regime, gravity begins to pull water inclusions together into large confluent water bodies. The inclusion structures characteristic of the pendular regime break down and flow into one another as water content percentages hover between about 8% and 15%. For water contents greater than 15%, gravity

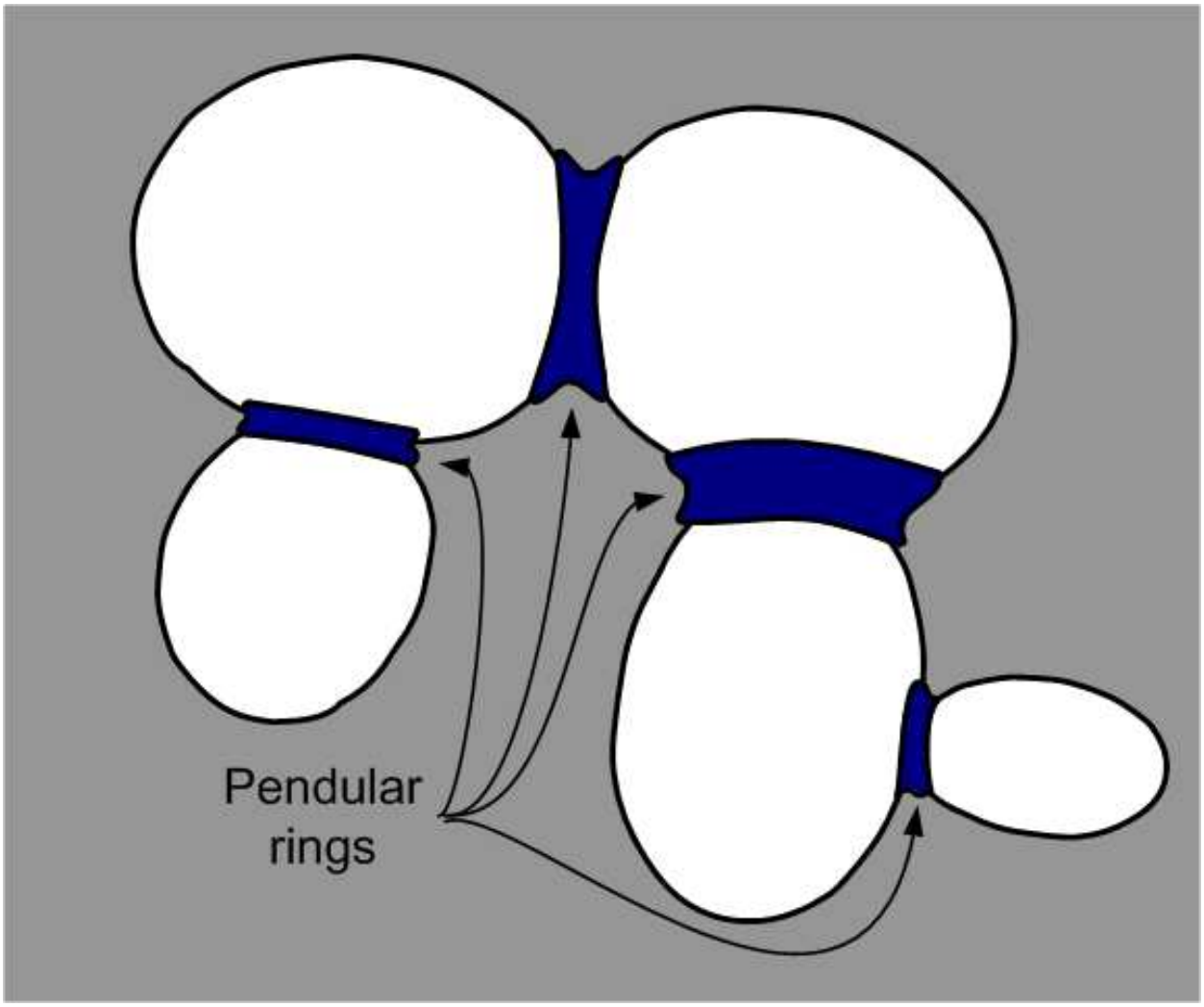

Figure 2.12: Depiction of a cluster of ice grains in the pendular regime with pendular rings at the bonds between ice grains.

acts to pull the water content in a single confluent mass. At this point, gasses like air and water vapor become the inclusions.

2.3.2 Formation of Clusters in the Pendular Regime

Clusters of ice grains form in the pendular regime. Capillary and surface tension forces in the pendular regime act to bring ice grains together. Water content affixes to ice grains in response to capillary forces; water affixed to different ice grains is brought together by surface tensions forces. As menisci at the points of contact form, water between the

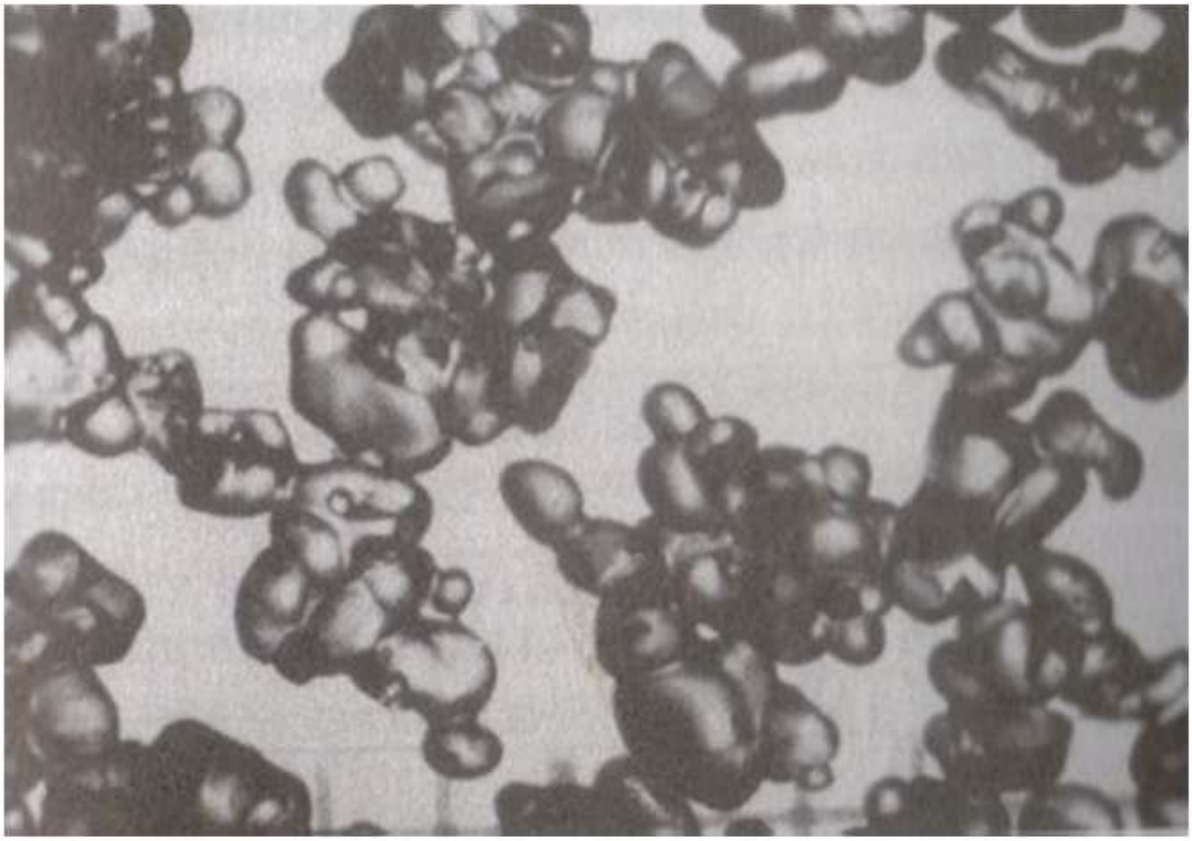

Figure 2.13: Photograph of multiple grain clusters under magnification. Reprinted from [11].

ice grains is squeezed out and ice-to-ice sintering, as discussed above, occurs. A group of different clusters of ice grains is depicted in Fig. 2.13.

Over time, the sintering process fuses the clusters together until the individual grains can become indistinguishable. In addition to the sintering process, diurnal freeze-thaw cycles can play a role. During the thaw portion of the daily cycle, ice grains melt, water content is introduced, clusters can grow, and pendular rings form. During the freeze portion of the cycle, the pendular rings freeze, increasing the strength of bonds between individual grains and making bond strength temperature dependant. A particular form of freeze-thaw metamorphosis is at work in the formation of the crusts discussed above.

Clusters increase cohesion. The large, irregular, clusters resist deformation by the mechanical friction they produce. Mechanical friction arises as the large, irregular clusters catch each other, tangling together in a manner that resists deformation.

2.3.3 Lubrication of Ice Grains in the Funicular Regime

Water content above 15% reduces cohesion. Although many clusters are empirically already present in a snowpack before water contents reach 15%, water insulates ice grains and clusters of ice grains from one another, preventing the formation of new clusters and the accompanying increase in mechanical friction. Furthermore, viscous water between grains and clusters lubricates the deformation process, breaking down cohesion. A sufficient breakdown in cohesion manifests itself as the comparatively rare, but very dangerous, wet avalanche.

2.4 Conclusion

A snowpack is comprised of different layers. Commonly occurring layers of faceted snow, crusts, and wind-deposits are responsible for a majority of avalanche activity because of their cohesive and friction properties and/or their tendency to generate large shear forces. Associated with these commonly occurring layers are characteristic densities, porosities, grain/crystal sizes, grain/crystal shapes, cluster sizes, cluster shapes, water contents, and water distributions. These characteristics identify avalanche-prone layers. The characteristics also provide an indication of a layer's cohesive properties, friction properties, and/or the shear force that it can generate. Insofar as signature electromagnetic interactions with these characteristics translate into radar cross-sections, avalanche-prone layers and their avalanche-relevant properties can be detected by radar.

Chapter 3

Potential Mechanisms for Backscatter

Characteristic densities, porosities, grain/crystal sizes, grain/crystal shapes, cluster sizes, cluster shapes, water contents, and water distributions associated with commonly occurring layers in a snowpack have the potential to cause different backscatter characteristics at different wavelengths. By identifying properties in the snowpack with these different backscatter characteristics, avalanche prediction may be aided. Several different electromagnetic phenomena that may give rise to these differing backscatter patterns are explored in this chapter to guide the design of a radar system capable of remote, large-area, data collection for avalanche prediction. In the process of the discussion, areas in need of additional research are highlighted.

3.1 Reflection at Impedance Boundaries

Previous studies rely on backscatter caused by specular reflections at impedance boundaries that occur between layers in the snowpack [1]– [10]. The shallow grazing angles involved in a remote, large-area, radar system often preclude backscatter generated in this way. However, as discussed below, surfaces that are sufficiently rough, as a function of wavelength, can produce backscatter at reflection boundaries for a large span of incidence and grazing angles. Additionally, dielectric boundaries can still play an important role at shallow grazing angles because of the electromagnetic energy that they conduct away from a radar system.

Layers within a snowpack have different dielectric-, geometric-, conductive- and permeability-related properties, indicative of different densities, ice grain and cluster sizes and shapes, water concentrations and distributions, and levels of porosity. The electromagnetic properties of a medium determine the wave impedance η of that medium. Wave impedance η, like

resistance, is a measure of the opposition electromagnetic energy encounters to continuing along its path.

Where a wave propagating in a first medium with a first intrinsic wave impedance η_1 encounters the boundary with a medium with a second intrinsic wave impedance η_2, the wave experiences different degrees of opposition. The result is that some of the wave is transmitted into the second medium and some of the wave is reflected back to the first medium. Where η_2 is greater than η_1, the wave experiences more opposition to continuing along its path and a fraction of the wave is reflected back into the first medium with a positive amplitude. Conversely, where η_2 is less than η_1, the wave experiences less opposition, resulting in a 90° phase shift and a negative fraction of the incident wave amplitude is reflected back into the first medium.

Assuming that the wave propagates at an angle of incidence normal to the boundary, all of the reflected energy returns to the source of that energy—in the case of a radar system, all of the energy becomes backscatter. The ratio of the amplitude of the electric field of the wave reflected E_r at the boundary to the amplitude of the electric field of the incident wave E_i is known as the reflection coefficient Γ,

$$\Gamma = \frac{E_r}{E_i}. \tag{3.1}$$

Therefore, the amplitude of the reflected electric field E_r, which is directly proportional to backscatter, equals:

$$E_r = \Gamma E_i. \tag{3.2}$$

3.1.1 Wave Impedance

Since the reflection coefficient Γ measures the reflection caused by the change in opposition to propagation arising from the change in wave impedances between two media, the reflection coefficient Γ can be expressed as a ratio of the difference and the sum of the two wave impedances:

$$\Gamma = \frac{\eta_2 - \eta_1}{\eta_2 + \eta_1}, \tag{3.3}$$

where wave impedance is defined as:

$$\eta = \sqrt{\frac{j\omega\mu}{\sigma + j\omega\mu\epsilon}}. \tag{3.4}$$

In Eq. 3.4, σ represents the conductivity, μ represents the permeability, and ϵ represents the complex permittivity of a medium. Permeability and permittivity are both complex, with the real part corresponding to a slow down in propagation speed and the imaginary part corresponding to polarity losses. The real part of these two terms is the product of both permeability and permittivity in a vacuum, and the relative permeability and permittivity of the medium in question. Relative permittivity and permeability can be functions of frequency and temperature. In the case of snow, the values of these terms are determined by the three constitutive elements of snow, i.e., ice, water, and air.

Where snow is dry, only ice and air need to be considered. Neither ice nor air are conductive and the relative permeability of air and ice are both unity. The permittivity of air approximates the permittivity of a vacuum. For ice, only the real part of the permittivity need be considered, as the imaginary permittivity of ice is negligible across all relevant frequencies [32] [33]. Therefore, for dry snow,

$$\eta = \sqrt{\frac{\mu}{\epsilon}}. \tag{3.5}$$

Additionally, the real part of the permittivity of ice does not vary greatly with respect to frequency and temperature. Since a cubic centimeter of water weighs 1 gram and the volume of a gram of ice is similar (albeit a little larger) than that of water, the density of snow is about equal to the ratio of ice to air. Therefore, the permittivity of dry snow is proportional to snow density.

The situation is complicated for wet snow because water has a conductivity and an imaginary component in its permittivity. These terms make wet snow lossy. Also, for water contents up to 8%, water contents in the pendular regime and the transition regime from the pendular regime to the funicular regime, permeability becomes a function of water content. The pendular rings, discussed in Section 2.3.1, provide loops through which current can

circulate. These currents produce magnetic fields that result in magnetic loss measured by the imaginary part of the permeability of the snow. For this reason, the water content of snow can be correlated with magnetic loss up to water contents of 8% [34], [35].

3.1.2 Examples of Boundary Reflections in Snow

Since the differing physical properties that make up the different strata in a snowpack have different ratios and distributions of snow, water, and air, the different strata have different real and imaginary permittivities, conductivities, and permeabilities, resulting in different wave impedances for the different layers. The different wave impedances result in reflections at boundaries that have been capitalized on in previous studies to image aspects of the physical stratigraphy of snowpacks [1]– [10]. Figure 3.1 provides an example.

In Fig. 3.1, the magnitude of backscatter is plotted as a function of range from several positions deployed along a line 3.5 meters in length. The radar system responsible for the image is positioned directly over the snowpack with the antenna mount oriented so that the direction of propagation is substantially normal to the snowpack, i.e., a nadir transmit angle. Several bands of bright return correspond to different electromagnetic boundaries within the snowpack. An interesting feature is the bright red bar at a depth of 100 cm and a distance of 3000 cm, which corresponds with the buried tracks of a snowmobile that were discovered with the aid of a snowpit dug in the area of the scan [10].

Backscatter from specular reflections have been used to produce impressive maps of property-specific stratigraphy within a snowpack. One of the more impressive examples is found below in Fig. 3.2, which provides comparison plots from the study reported in [1], in which a radar system approaching 1 cm range resolution is employed. The plot on the left-hand-side provides the probability density function for backscatter as function of snowpack depth. The plot on the right-hand-side provides the force required by a SnowMicroPen (SMP) to penetrate the snowpack as a function of depth.

A SMP is capable of providing highly accurate measurements of penetration force at extremely high resolutions measured in micrometers. The force required to penetrate snow measures the hardness of snow, a property relevant to avalanche prediction. A review of the

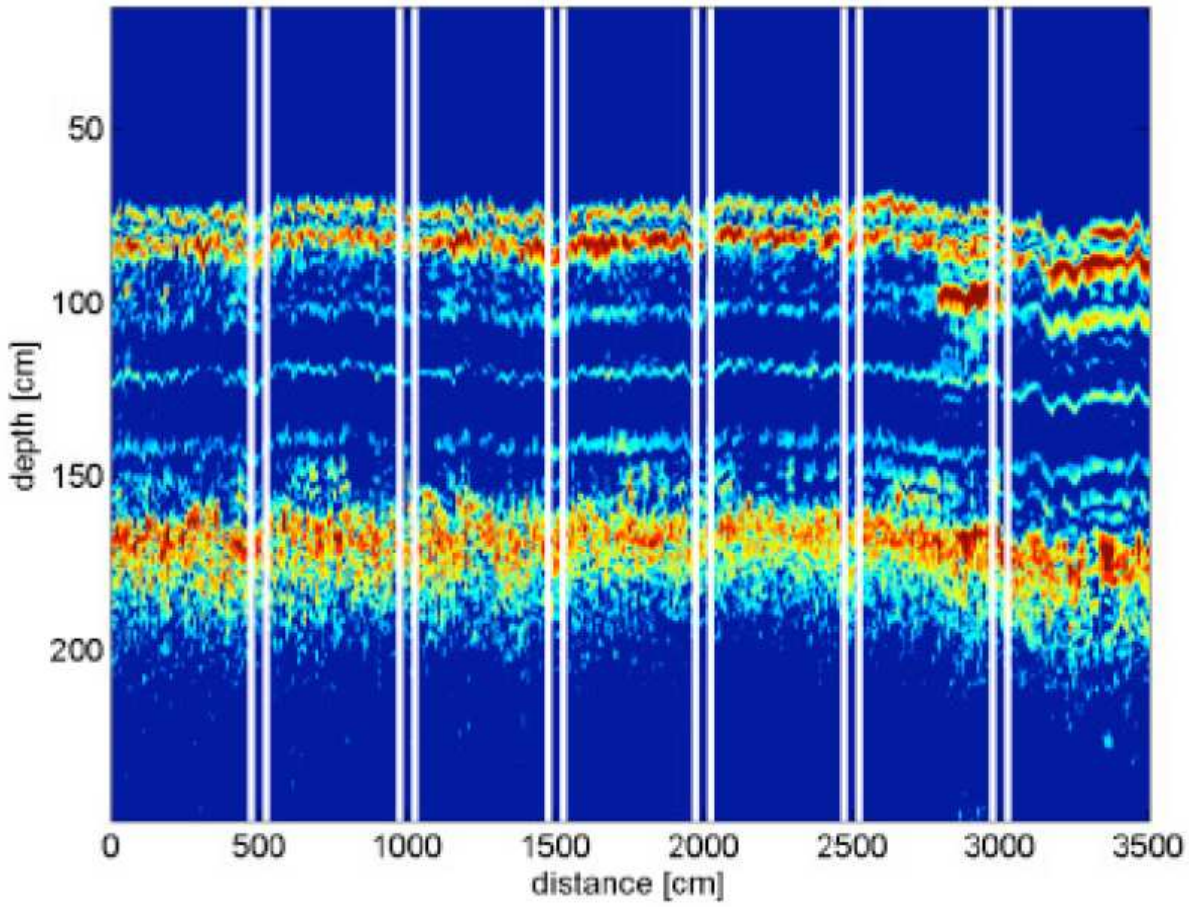

Figure 3.1: Magnitude of backscatter as a function of depth across a distance of 3.5 m, as reported by [10].

two plots in [1] shows that a majority of the hardness transitions detected by the SMP are reflected in the probability density function for the backscatter.

3.1.3 Reflections at Shallow Grazing Angles

Where a radar scans large distance of a snowpack remotely, the grazing angle is often not normal and is often very shallow. According to Snell's law of reflection, the angle of incidence and the angle of refraction are equal:

$$\Theta_i = \Theta_r. \tag{3.6}$$

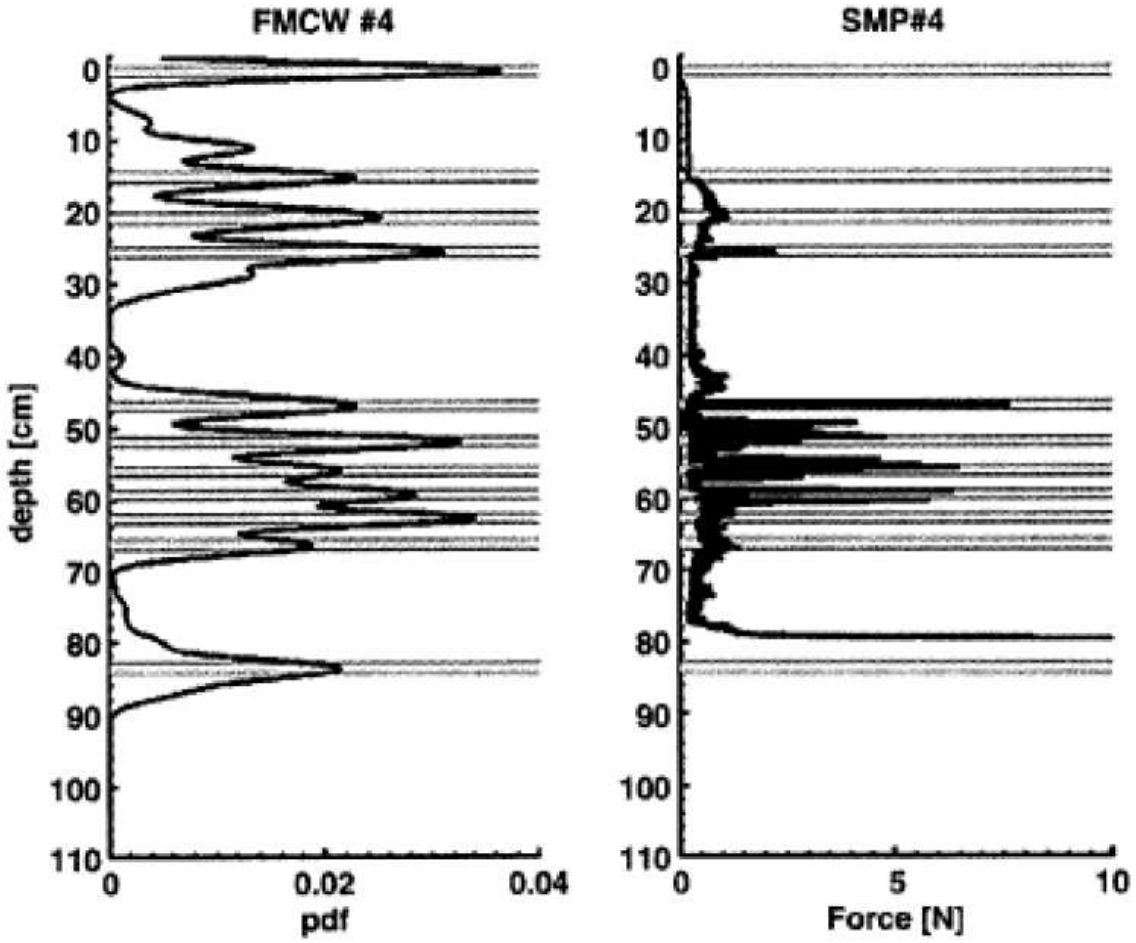

Figure 3.2: Comparison between the probability density function for backscatter from a snowpack and the force required of an SMP to penetrate the same snowpack as functions of snowpack depth. The plots are reported in [1]. On the left-hand side, a series of peaks occur in the probability density function at certain depths in the snowpack. On the right-hand side, it is learned that these peaks correspond to changes in snow hardness, or layer boundaries, as determined by changes in force required of the SMP to penetrate the snowpack at given depths. Lines are added to aid in the comparison.

This law is depicted in Fig. 3.3 in terms of an incident wave and a reflected wave at the boundary of two media with different wave impedances. The transmitted wave is also shown. The magnitude and sign of all three waves depicted, together with the angle of transmission can be determined in conjunction with Snell's law of refraction. A more through discussion of these matters can be found in [36].

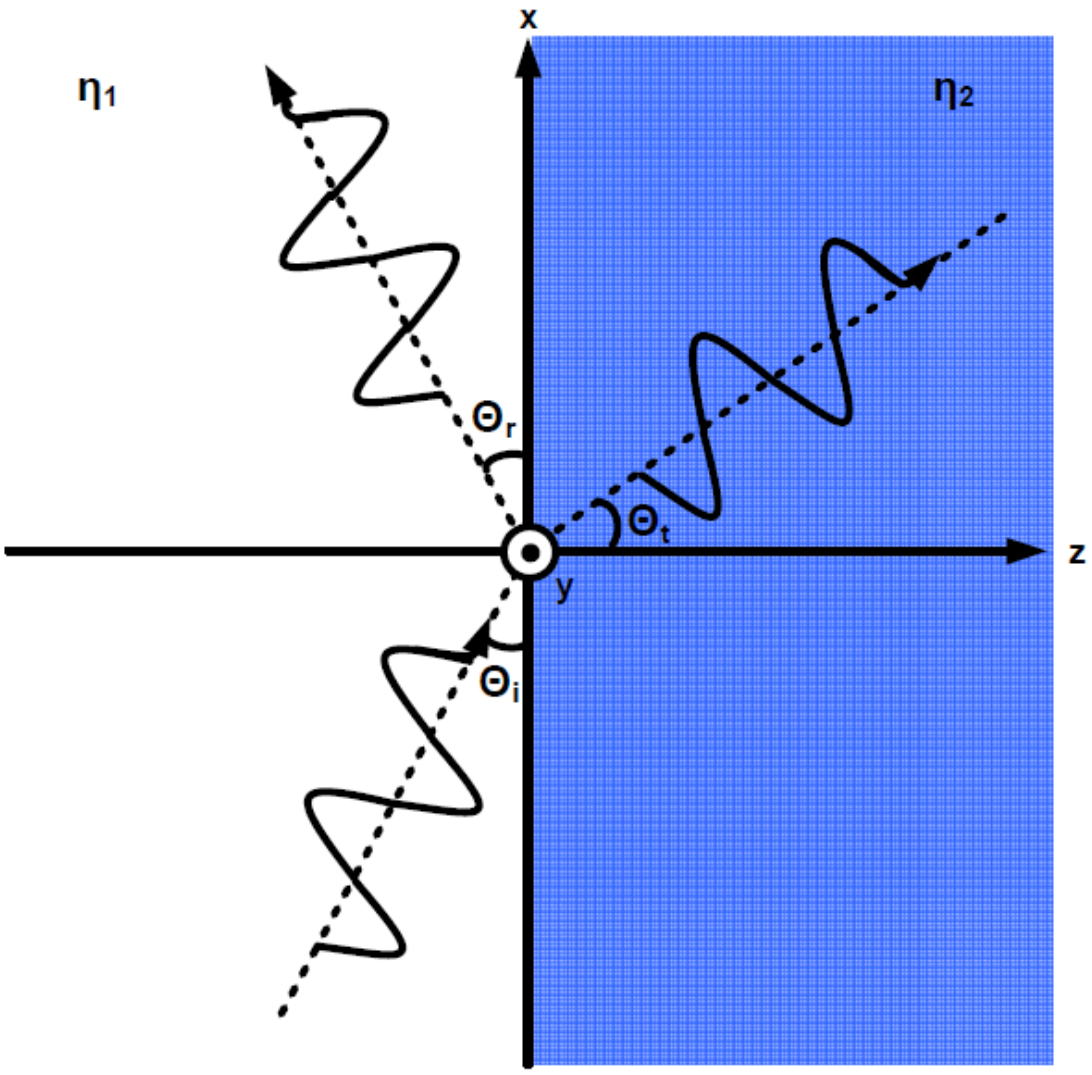

Figure 3.3: A representative depiction of Snell's law of reflection, with an incident wave, a reflected wave, and a transmitted wave depicted on a three-dimensional Cartesian coordinate system at the boundary between a first and a second medium with a first η_1 and a second η_2 wave impedance, respectively. The grazing angles for the incoming wavesΘ_i, reflecting waves Θ_r, and the transmission angle Θ_t are also depicted.

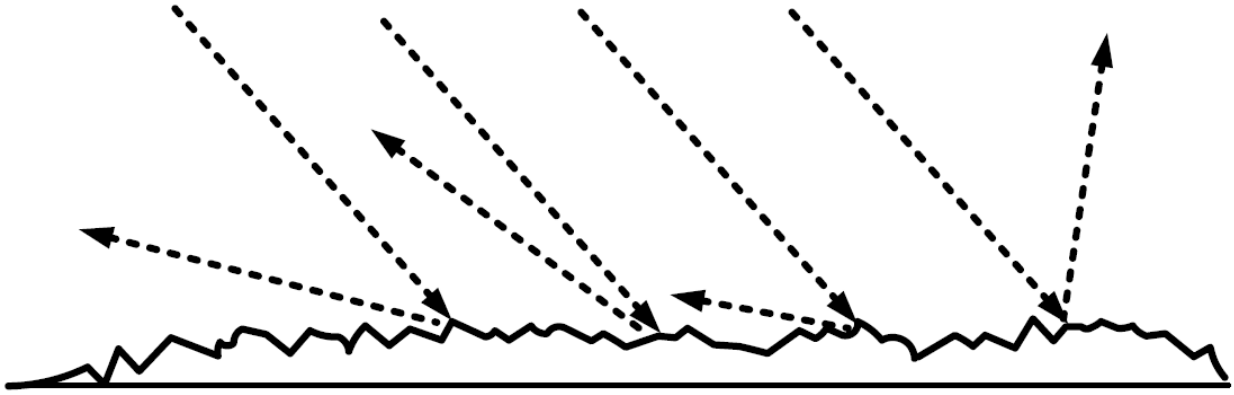

Figure 3.4: Depiction of backscatter from a rough surface. Features at the surface of a boundary determine the direction of reflection where the size of the incident wavelengths are commensurate with the size of the surface features.

For purposes of the present discussion, it is sufficient to note that a radar system transmitting the incident wave is not positioned to receive the reflected wave from a smooth surface. The energy is conducted away from the radar system for shallow grazing angles in accordance with Snell's law of reflection.

3.1.4 Surface Roughness

Not all energy, however, is conducted away from a radar system at boundaries between media with differing wave impedances. As wavelengths decrease in size, the boundary between two layers of snow appears less and less like a smooth surface to the wave. Large gaps can exist between individual ice grains and clusters of grains. Similarly, the boundary may be defined by a layer of surface-hoar plates measuring in sizes similar to the 2 cm surface hoar depicted in Fig. 2.9.

As the size of the wavelength becomes commensurate to the size of surface features at the boundary, the surface features control the directions of reflections. The ability of surface roughness to reflect waves at all angles generates backscatter even at shallow grazing angles, as depicted in Fig. 3.4. The size of wavelengths corresponding to different frequency bands of interest is provided in Table 3.1.

3.2 Volume Scattering

Although boundary reflections play important roles, as discussed above, at the shallow, non-nadir grazing angles involved in remote, large-area radar scans, the majority of the scatter for these scans comes from volume scattering—scattering from within the volume of a layer of snow as opposed to at the boundary between two layers. As electromagnetic waves propagate through a volume of snow, waves interact with grains of ice, clusters of grains, and water inclusions. Insofar as these ice particles and water inclusions have dielectric properties, the electromagnetic waves act to polarize the material they encounter. The waves are scattered and absorbed in the process. Additionally, currents generated in ring-shaped water inclusions absorb energy out of the wave and the magnetic fields generated from the pendular rings have their effect.

Unfortunately, modeling the scattering that takes place within a volume of snow is not as easy as the modeling boundary reflections at homogeneous boundaries. To precisely model the scattering and absorption that takes place in a volume of snow, Maxwell's equations need to be solved in terms of the size, shape, and location, of every grain of ice, cluster of grains, and water inclusion. Solving for such a result is not feasible. Simplifying assumptions must be made.

3.2.1 Mie Calculations

A drastic simplifying assumption, which is to be pared down later, is to work with a single ice grain, cluster of grains, or water inclusion, and to assume that the subject is a perfect sphere. This assumption is a poor assumption, especially for higher frequencies and shorter wavelengths, for many layers in a snowpack, but serves to begin discussion. Solutions to Maxwell's Equations in terms of scattering and absorption for a homogeneous, dielectric sphere in a homogeneous background media are first worked out by Mie [37]. The solutions can be expressed in terms of the absorption efficiency ξ_a, scattering efficiency ξ_s, and backscatter efficiency ξ_b of the sphere (as reported in [38]). These efficiencies express a ratio of the cross-sectional area of the sphere to which perfect absorption, scattering, and backscatter correspond. Therefore, the backscatter from the sphere can be calculated, in

terms of the radius r and the backscatter efficiency ξ_b as:

$$\sigma_b = \pi r^2 \xi_b. \tag{3.7}$$

The result for backscatter efficiency ξ_b from Mie's solution leads to an expression that takes the form of a converging series:

$$\xi_b = \frac{1}{\chi^2} |\sum_{l=1}^{\infty} (-1)^l (2l+1)(a_l - b_l)|^2, \tag{3.8}$$

where χ is the ratio of the diameter of the sphere to the wavelength λ_b in the background medium:

$$\chi = \frac{2\pi r}{\lambda_b}. \tag{3.9}$$

The terms a_l and b_l are known as the Mie coefficients and can be found with respect to the ratio of the index of refraction for the material of the sphere n_s to the index of refraction for the material of the background n_b:

$$n = \frac{n_s}{n_b}. \tag{3.10}$$

The Mie coefficients a_l and b_l can be solved for with Bessel functions with Complex arguments or with the index of refraction n and the recursion formulas provided below [39] (as reported in [38]):

$$a_l = \frac{(\frac{A_l}{n} + \frac{l}{\chi}) Re\{W_l\} - Re\{W_{l-1}\}}{(\frac{A_l}{n} + \frac{l}{\chi}) W_l - W_{l-1}}, \tag{3.11}$$

$$b_l = \frac{(nA_l + \frac{l}{\chi}) Re\{W_l\} - Re\{W_{l-1}\}}{(nA_l + \frac{l}{\chi}) W_l - W_{l-1}}, \tag{3.12}$$

where:

$$W_l = (\frac{2l-1}{\chi}) W_{l-1} - W_{l-2}, \tag{3.13}$$

$$W_0 = \sin\chi + j\cos\chi, \tag{3.14}$$

$$W_{-1} = \cos\chi - j\sin\chi, \tag{3.15}$$

and

$$A_l = -\frac{l}{n\chi} + [\frac{l}{n\chi} - A_{l-1}]^{-1}, \tag{3.16}$$

$$A_0 = \frac{\sin n'\chi \cos n'\chi + j \sinh n''\chi \cosh n''\chi}{\sin^2 n'\chi + \sinh^2 n''\chi}, \tag{3.17}$$

and n is complex.

3.2.2 Volume Backscatter Coefficient

Once the backscatter efficiency ξ_b has been computed for a spherical ice grain, the backscatter for a volume of snow σ_v comprising such ice grains can be computed. The volume scattering coefficient σ_v can be thought of as a three-dimensional radar cross-section, a measure of the cross-sectional area of a perfectly-reflecting sphere that would produce a reflection equal to that of the volume in question. The computation of σ_v requires an estimate of the number of spheres in that volume N_v. Once the estimate is made, the product of the backscatter efficiency ξ_b and the cross-sectional area of the ice grain need only be summed a number of times equal to the number of grains assumed to be in the volume:

$$\sigma_v = \sum_{i=1}^{N_v} \pi r^2 \xi_b. \tag{3.18}$$

At this point, an aside is appropriate to reconsider wind-deposited snow as explained in Section 2.2.2. Due to the abrasive processes of and the strong forces involved in wind deposition, wind-deposited ice grains are packed tightly together. Wind-deposited snow is characterized by its high density and the high number of ice grains that occupy its volume. These high numbers of particles result in strong backscatter, pursuant to Eq. 3.18, from wind deposited snow.

Wind-deposited snow plays an important role in avalanche formation by providing the shear forces that cause many avalanches. Also, wind-deposited snow accumulates over large areas, unevenly, and in very small amounts of time. These characteristics and the indication that wind deposited snow may stand out in backscatter returns suggest that a radar system's ability to scan large areas quickly to assess accumulations of such snow may prove to be one of the ways that a radar system can aid in avalanche prediction.

3.2.3 The Rayleigh and Mie Regions in χ Space

As appreciated, computation of a volume scattering coefficient by means of the Mie scattering solution is difficult and involved. Where $|n\chi| < 0.5$, certain simplifying assumptions can be made. The region of χ space over which these assumptions can be made is known as the Rayleigh region. Where these simplifying assumptions are made, Eq. 3.8 can be reduced [40] to:

$$\xi_b = 4\chi^4|K|^2, \tag{3.19}$$

where K is a complex coefficient defined in terms of the complex index of refraction of Eq. 3.10 as:

$$K = \frac{n^2 - 1}{n^2 + 2}. \tag{3.20}$$

The assumptions that can be applied in the Rayleigh region greatly simplify computation of volume scattering coefficients, as a comparison of Eq. 3.19 and Eq. 3.20 to Eq. 3.8 through Eq. 3.17 makes apparent. The Rayleigh region is characterized by more than ease of computation. Additionally, the Rayleigh region is characterized by an exponential increase in backscatter efficiency as a function of χ, the ratio of the sphere radius to wavelength.

Where χ approaches 1 and larger values, the assumptions of the Rayleigh region no longer apply. The region of χ space over which these larger values obtain is known as the Mie region. The computationally intense, but more general, Mie equations must be used to determine backscatter efficiency in this region. As with the Rayleigh region, the Mie region is characterized by its computational requirements and by the trend in backscatter efficiency as a function of χ.

In the Mie region, the trend changes from an exponential increase to damping oscillatory behavior. Figure 3.5 depicts the behavior of two spheres in the Rayleigh and the Mie regions. The first sphere is a perfectly conducting metal sphere, where $|n| = \infty$. The second is a sphere with only a finite, real index of refraction, $n = 1.29$.

The oscillations depicted in Fig. 3.5 arise due to resonances predicted by the Mie equations. Such resonant behavior is not only predicted but has been observed in spherical ice particles with resonant peaks occurring at eigenfrequencies for the spherical particles [41]. Spheres are not the only shape that exhibit resonant behavior. Ice particles of different

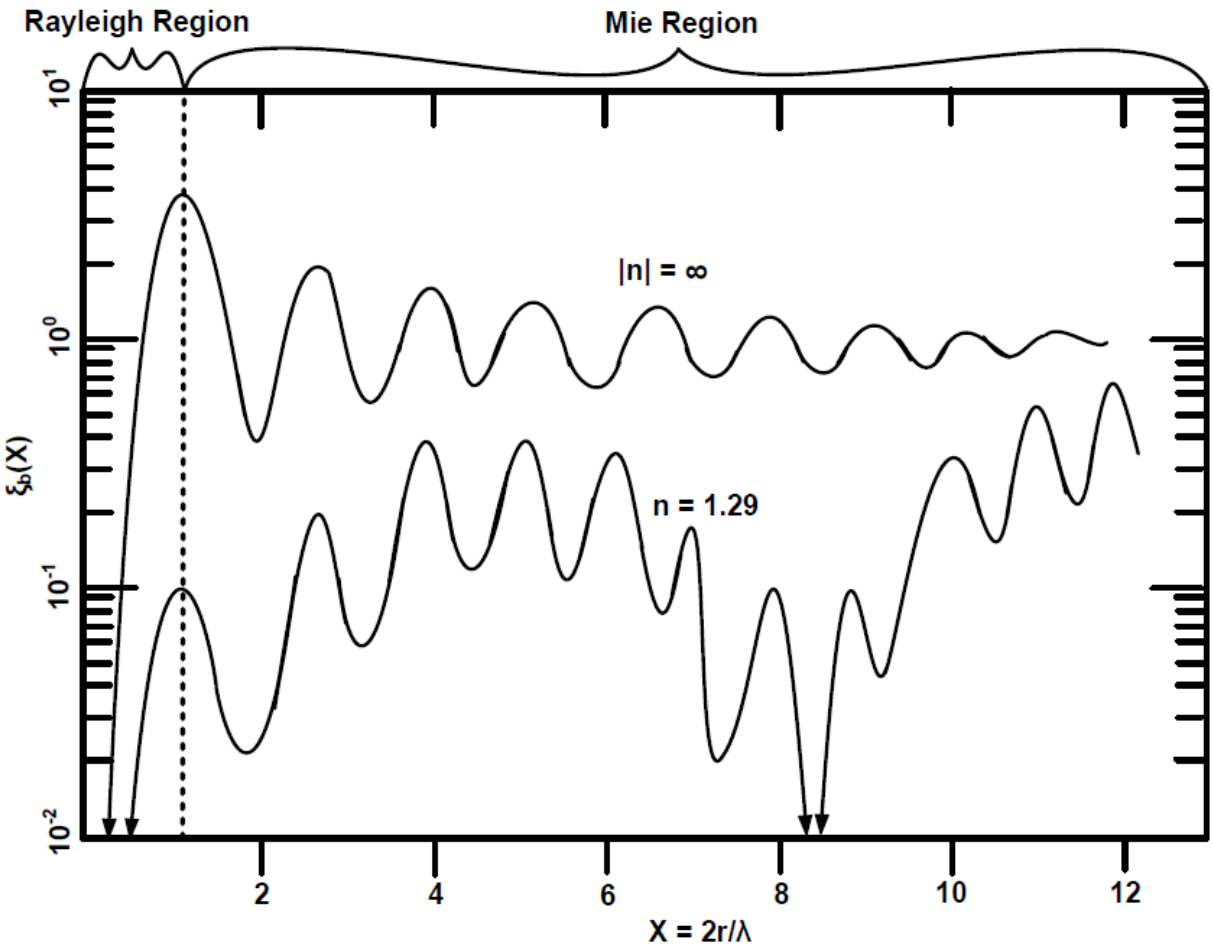

Figure 3.5: Backscatter efficiency ξ_b as a function of χ for a sphere of infinite conductivity ($|n| = \infty$) and a sphere with only a finite, real index of refraction ($n = 1.29$). The response in both the Rayleigh and the Mie regions is depicted. (Adapted from [39].)

shapes demonstrate resonant behavior defined, in part, by the shapes. Resonance occurs at eigenfrequencies determined by both the size and the shape of ice particles [41].

3.2.4 Lessons Learned from the Rayleigh and Mie Regions

The assumption of spherical particles and the ensuing discussion has some important implications for the selection of transmit frequencies/wavelengths for an avalanche-prediction radar system. First, in the Rayleigh regime, the smaller the wavelength, the better. Decreasing wavelength size increases the value of χ. As demonstrated by Fig. 3.5, even small increases, e.g., one-tenth, in χ result in increases of orders of magnitude in backscatter

Table 3.1: Frequencies and Wavelengths Corresponding to Five Contiguous, Microwave Frequencies Bands.

X-Band	Ku-Band	K-Band	Ka-Band	Q-Band
8 to 12 GHz	12 to 18 GHz	18 to 26.5 GHz	26.5 to 40 GHz	30 to 50 GHz
3.75 to 2.5 cm	2.5 to 1.7 cm	1.7 to 1.13 cm	1.13 to 7.5 mm	10 to 6 mm

efficiency. For wavelengths resulting in values of χ in the Rayleigh region for a range of sizes of ice grains/clusters, backscatter magnitude may provide a means for determining grain/cluster size.

Second, very small wavelengths are necessary to acquire information that may be available from Mie scattering. Mie scattering has the potential to provide information about size and shape because specific resonances occur at specific eigenfrequencies that are determined by size and shape. The possibility of detecting a particular size and/or shape is greatly improved by checking for resonances at multiple frequencies to look for as many points of agreement between backscatter data and expected resonance profiles. Distinguishing the resonant profiles from different ice grains for the prediction of avalanche purposes does not require exact shape recognition. Rather, for example, the ability to distinguish between the resonance behavior of rounded shapes and and the sharp angular shapes of faceted grains is all that is required.

To get a better feel for the transmission frequencies that might best take advantage of the opportunities provided by Rayleigh and Mie scattering, tables are prepared with information about different frequency bands. In Table 3.1, the wavelengths at the top and bottom of five contiguous frequency bands are provided. In Table 3.2, the values of χ corresponding to these frequency bands are provided for commonly occurring grain sizes. The effect of clustering on Rayleigh and Mie scattering is not entirely clear and has the potential to greatly complicate the preceding analysis.

The values in Table 3.2 suggest that to take advantage of information about size and shape that may be embedded in Mie-scattering resonance profiles, high frequency bands are desired. A common size associated with faceted snow in weak layers is 2 mm. This would

Table 3.2: Values of χ at Various Frequency Bands for Various Grain Sizes.

Size	X-Band	Ku-Band	K-Band	Ka-Band	Q-Band
0.5 mm	0.08 to 0.13	0.13 to 0.18	0.18 to 0.28	0.28 to 0.42	0.31 to 52
1.0 mm	0.17 to 0.25	0.25 to 0.37	0.37 to 0.56	0.56 to 0.84	0.63 to 1.00
1.5 mm	0.25 to 0.38	0.38 to 0.55	0.55 to 0.83	0.83 to 1.25	0.94 to 1.57
2.0 mm	0.34 to 0.50	0.50 to 0.74	0.74 to 1.11	1.11 to 1.68	1.26 to 2.09
3.0 mm	0.50 to 0.75	0.75 to 1.11	1.11 to 1.67	1.67 to 2.51	1.88 to 3.14
4.0 mm	0.67 to 1.01	1.01 to 1.48	1.48 to 2.22	2.22 to 3.35	2.51 to 4.19
5.0 mm	0.84 to 1.26	1.26 to 1.85	1.85 to 2.78	2.78 to 4.19	3.14 to 5.24

suggest, according to Table 3.2, a radar system transmitting at Ka-band or higher to acquire data on Mie scattering.

Radar systems transmitting at lower frequency K-bands would be able to receive Mie scattering from larger grain sizes. Although these larger grain sizes can and do play important roles in faceted weak layers, especially in layers of depth hoar, grain sizes larger than 3 mm become less and less common. Information about grain size from Rayleigh scattering could profitably be obtained from a number of frequency bands, with the X-band remaining in the Rayleigh region over all grain sizes recorded in Table 3.2. Again, the effect that clustering has on the Rayleigh and Mie regimes is unclear and adds a complicating consideration.

3.2.5 Shape-accommodating Formulas

The use of the equations for either Mie or Rayleigh scattering requires the assumptions of a perfect spherical particle. To accommodate the presence of water and variations in ice grain size, volume scattering coefficients can be calculated with Eq. 3.18 for varying sizes of spheres of ice and water with varying backscatter efficiencies. However, the ice grains, clusters, and water inclusions are not confined to spherical shapes.

The faceted grains of interest are not spherical in shape and clusters take on shapes that are much more complicated. As discussed in Section 2.3.1, water assumes narrow ring and disk shapes within a snowpack—shapes that share little in common with a perfect sphere. Importantly, the water inclusions, although small in size, have relative permittivities—many times greater than the relative permittivity of ice. Therefore, as pointed out in [42], inaccu-

rate shapes for water will have an important effect on calculations of the effective permittivity of a volume of snow and of the backscatter that volume is expected to generate. This includes the assumption that water coats ice grains with a spherical shell, a physical impossibility for reasons set forth in Section 2.3.1.

A call to better accommodate shapes, especially for water inclusions, is made by [42]. In the reference, the mixing formula of Polder and Van Santen [43] is employed to model ice grains as spheroids with various aspect ratios and surface hoar as disks. With the use of these shape-accommodating formulas, a better fit is achieved for various data sets measuring the permittivity of dry snow. The improved fits to permittivity are more impressive for wet snow. For the wet snow, the mixing formula is used to model water inclusions as needle-like shapes, more consistent with the pendular rings present in the pendular regime.

The shape-accommodating work of [42] is picked up and advanced in [44]. In [44], the mixing formula of Polder and Van Santen [43] and a Debye-like method are used to accommodate shape. The methods are fit with some empirical fine tuning to previous data sets and a large number of new measurements spanning 3 GHz to 37 GHz. As water content increases, the accommodating shapes employed by the Polder-Van Santen models are changed from needles to discs, in keeping with the distinction between the pendular and funicular regimes. Interestingly, [44] provides a rare comparison of extinction between faceted and non-faceted grains, demonstrating significantly more extinction for the faceted grains.

3.2.6 Future Areas of Research

Although the use of mixing formulas, like the Polder-Van Santen formula, demonstrates the need to account for grain and water inclusion shapes to obtain accurate dielectric permittivities, these dielectric permittivities need to be related to backscatter efficiencies and backscatter coefficients. More importantly, the shapes and sizes of various grains and water inclusions of interest need to be capitalized upon in an effort to find backscatter efficiencies and volume scattering coefficients for these grains and water inclusions of interest.

Faceted grains have very small specific surface areas because of their angular geometry, which are not taken into account by Polder-Van Santen formula that model them as elongated spheroids. Additionally, faceted grains elongate in the direction of the temperature gradient

in which they form. Perhaps this elongation would be detectable in a comparison between the backscatter from different polarizations.

Additionally, as demonstrated in Fig. 2.12, the pendular rings in clusters of faceted snow are smaller and tighter than the pendular rings in rounds. A possible way of detecting faceted snow may come from the difference in the size of the pendular rings for faceted snow as opposed to rounds. Many other possibilities exist that need to be pursued with an eye toward determining the signature for properties of interest to avalanche formation.

3.3 Penetration

Generally, as has been suggested from the discussions in this chapter, as wavelengths approach the size of the ice grains and water inclusions of interest, the likelihood of learning about those subjects of interest increases. However, as frequencies become higher and higher and wavelengths become smaller and smaller, the wavelengths become more susceptible to surface and volume scattering. At some point, the wavelengths become unable to satisfactorily penetrate the snowpack.

Previous studies relying on specular reflection demonstrate the ability of frequency bands up to Ku-band to penetrate an alpine snowpack without problem [8]. Question remain, however, about higher frequency bands. A study seeking to better understand scatterometer data of Greenland's ice sheets provides an indication [45]. In the study, three 33 cm cubes of firn snow are harvested and measured for dielectric permittivity at frequencies in Ka-band (26.5 to 40 GHz). In the process, several extinction losses are measured ranging from of 5 dB/m to 10 dB/m.

The high density of the firn samples should be taken into account. At a standard depth of 2m, a maximum 20 dB loss does not foreclose the possibility of using frequencies in Ka-band. Indeed the measurements at 37 GHz in [44] support the feasibility of using this band. However, the losses do suggest that the frequencies in Ka-band may constitute the upper limit for frequencies that can be employed to probe an alpine snowpack's properties. However, if the opportunity presents itself, higher frequencies should be tried.

3.4 Summary

The strata of a snowpack produce backscatter to a radar system with information about the dielectric, geometric, conductive, and permeability properties of the snowpack. This backscatter can come from surface reflections at boundaries or it can come from the volume of the snow itself. At the shallow grazing angles involved in remote, large-area radar scans, most boundary reflections conduct electromagnetic energy away from a radar system. Surface roughness can provide an exception where wavelengths are relatively small compared to the geometric features of a boundary, such as when a boundary is marked by the presence of surface hoar.

The majority of the backscatter involved in remote, large-area radar scans comes from volume scattering. The Mie and Rayleigh models assume a spherical scatterer can be used for a very rough approximation of volume scattering. The dependence of volume scattering on the number and density of particles, as suggested by these models, indicate that the backscatter from wind-deposited snow may stand out, allowing radar systems to capitalize on their ability to scan large areas quickly to provide information about this dangerous and difficult-to-assess snow form. Additionally, these models suggest the importance of small wavelengths and possibly the use of multiple frequencies to learn about the size and shape of ice grains.

In the Rayleigh region, small increases in frequency or small increases in scatterer size result in large differences in backscatter efficiency. In the Mie region, different sizes, shapes, and electrical properties result in different resonant frequencies. Points of agreement between an expected resonance profile and the received backscatter data may provide the means to decipher the properties upon which that profile depends. As stated, the properties can be very general, such as faceted versus rounded shapes.

The problems with assuming spherical ice grains and water inclusions becomes apparent where the results of the assumptions are confronted with data, especial with respect to water content, because of its high relative permittivity. The use of mixing formula to produce shape-accommodating models like the Polder-Van Santen model produce results that fit data much better. These models account, albeit roughly, for the thin shape of pendular rings and the elongated nature of ice grains.

Nevertheless, the models need to be translated from models of dielectric permittivity to volume backscatter coefficients. What is more, properties of shape and distribution need to be focused on in an effort to make the volume backscatter coefficients correspond to snow forms of interest, like faceted grains. Specific surface area, elongation along the axis of facet-forming temperature gradients, and size and distribution of pendular rings provide a few examples of characteristics that need modeling.

3.5 Design Parameters

Phenomena such as Rayleigh scattering, Mie resonance, and backscatter from surface roughness suggest that the highest transmit frequencies possible can provide the most backscatter and the most information about snow properties. In the Rayleigh regime, higher frequencies and their shorter wavelengths, lead to exponential increases in backscatter. At sufficiently high frequencies, resonance profiles from Mie scattering provide information about ice grain, ice cluster, and water inclusion shape and size. However, the ability of a frequency band to penetrate a snowpack places an upper limit to frequencies. Although higher frequency bands ought to be tried, indirect measurements suggest that the Ka-band defines this upper limit.

The Ka-band has frequencies sufficiently high to provide Mie scattering for ice grains 1.5 mm in size and larger–encompassing most grains of interest. Size and shape information is encoded in resonance profiles from Mie Scattering that are a function of frequency. Therefore, the more frequences within Ka-band in the transmit signal, the more information collectable about sizes and shapes. The ability to distinguish between faceted and rounded grounds would prove enormously helpful for avalanche prediction. Additionally, the smaller wavelengths associated with frequencies in this band are likely to result in backscatter at surfaces covered with the large plate-like structures of surface hoar, even when angles are shallow, possibly providing a means for detecting these dangerous structures.

Ka-band places several ice grain sizes out of the Rayleigh regime. To acquire information about size from the Rayleigh regime, a second band of transmit frequencies is beneficial. For the common sizes of ice grains found in alpine snowpacks, the frequencies of the X-band keep scattering in the Rayleigh regime. The larger wavelengths associated

with X-band are more likely to experience specular reflections away from the radar at strong boundaries, such as crusts, for shallow grazing angles, possibly providing a means for detecting these structures. Therefore, an ideal radar system transmits many frequencies in the X- and Ka-bands.

Chapter 4

Design of a Synthetic Aperture Radar System Capable of Remotely Reconstructing Snowpack Stratigraphy Over Large Areas

The stratigraphy of a snowpack can be considered in terms of the cohesive properties of the snowpack's strata, or layers, the friction properties between differing layers, and/or the shear forces that these layers generate. Snowpack stratigraphy considered in these terms comprises a mechanical system that determines whether or not an avalanche forms. Properties of layer cohesion, friction, and shear forces generated by snowpack layers are derivative properties that depend on more fundamental properties within a snowpack, such as density, porosity, grain/crystal size, grain/crystal shape, cluster size, cluster shape, water content, and water distribution.

Radar systems can remotely collect data about the backscatter from a snowpack over a large area relatively quickly. Since backscatter data may reflect the fundamental properties that are characteristic of the cohesive properties of layers, the friction properties between differing layers, and/or the shear forces that these layers generate, radar systems may overcome deficiencies in current avalanche prediction methods by assessing at least some avalanche risks at a safe distance, over large areas, relatively quickly. However, this backscatter data must be in a form that can be reconstructed to provide information about the overall stratigraphy and the corresponding mechanical system, which determines whether or not a particular snowpack slides.

4.1 Radar System Requirements

A radar-based reconstruction of stratigraphy is, however, a complicated proposition with several prerequisites. First, relevant properties of the snowpack must be detectable from backscatter data. Second, measurement of the degree to which those properties manifest

themselves must be possible from the backscatter data. Third, the relative location of the properties must also be determinable. Finally, the radar-based reconstruction must be achievable by a radar system that is practical in terms of its construction, cost, and deployment in the mountainous terrain where avalanches occur.

4.1.1 Ultra-high-resolution Requirement

In order to satisfy the first two prerequisites of detecting and assessing a property, or collection of properties, associated with poor cohesion, poor friction, and/or high shear forces, a radar system must be able to differentiate backscatter. The radar system must differentiate backscatter originating from the region of the property or properties in question from backscatter originating from elsewhere in the snowpack and from the ground. The resolution of a radar system quantifies the ability to differentiate backscatter from different regions. Since the layers in which avalanche-relevant properties reside can be relatively thin, the regions from which backscatter must be differentiated are small. A radar-based reconstruction of stratigraphy capable of satisfying prerequisites one and two, therefore, requires ultra-high resolution.

4.1.2 Requirement to Account for the Orientation of a Radar System Relative to the Layers in a Snowpack

As discussed above, at shallow grazing angles, layer boundaries produce specular reflections that conduct electromagnetic energy away from a radar system. To receive backscatter from specular reflections at boundary layers, the radar system must be oriented so that its range direction, or line-of-sight, is normal to the snowpack and its layers. There are additional reasons why the orientation of the radar's line-of-sight can be important.

As discussed below in the section on radar basics, the principal axis along which resolution is measured for all radar systems is defined by the line-of-sight of the radar system. Resolution along a radar system's line-of-sight is known as range resolution. However, ultra-high range resolution alone is not sufficient to differentiate the backscatter from different regions in a snowpack. The orientation of a radar system's line-of-sight relative to the orientation of the planes described by the layers within a snowpack plays important roles.

Figure 4.1 depicts a stationary radar system deployed in a setting of mountainous terrain where avalanches occur. Slopes are the dominant feature of mountainous terrain. The sloping nature of mountainous terrain greatly changes the relative orientation of a radar's line-of-sight to layers in a snowpack from one location to another. Additionally, mountainous terrain is rugged, and the surface of the bed on which a snowpack reposes undulates and varies widely from location to location. As the stationary radar system scans across a snowpack, the slope and the undulations greatly change the relative orientation of the radar system's line-of-sight. Usually, the resultant lines of sight correspond with shallow grazing angles at which specular reflections conduct electromagnetic energy away from a radar system. As a result, the line-of-sight will vary from less common orientations normal, or near normal, to the layers in the snowpack (as in the expanded view of angle 1 in Fig. 4.1) to more common orientations that are widely oblique and even parallel to the planes described by the layers in the snowpack (as in the expanded view of angle 2 in Fig. 4.1). These oblique angles for the line-of-sight correspond with shallow grazing angles at which specular reflections conduct electromagnetic energy away from a radar system.

In the expanded depictions of the relative orientations of the radar system to the snowpack layers in Fig. 4.1, the hash marks disposed along the two-sided arrows, which depict different lines-of-sight, indicate regions that are distinctly resolvable for a radar system with ultra-high-range resolution. However, even with ultra-high-range resolution, at least four distinct problems prevent the satisfaction of the first three prerequisites outlined above.

First, prerequisites one and two, that properties or collections of properties relevant to possible avalanche formation be detectible and quantifiable are not satisfied because specular reflections at non-nadir, shallow grazing angles do not produce backscatter with information about the snowpack. Second, prerequisites one and two are not satisfied because the backscatter from the regions where these properties may occur is often confused with backscatter for regions with different properties.

Figure 4.1 is helpful in demonstrating why this occurs. Where the orientation of the line-of-sight is normal, or near normal (as in the expanded depiction for angle 1) relative to the planes described by the snowpack layers, individual, distinct layers, depicted by pattern and color variations, occupy distinctly resolvable regions along the line-of-sight. For example,

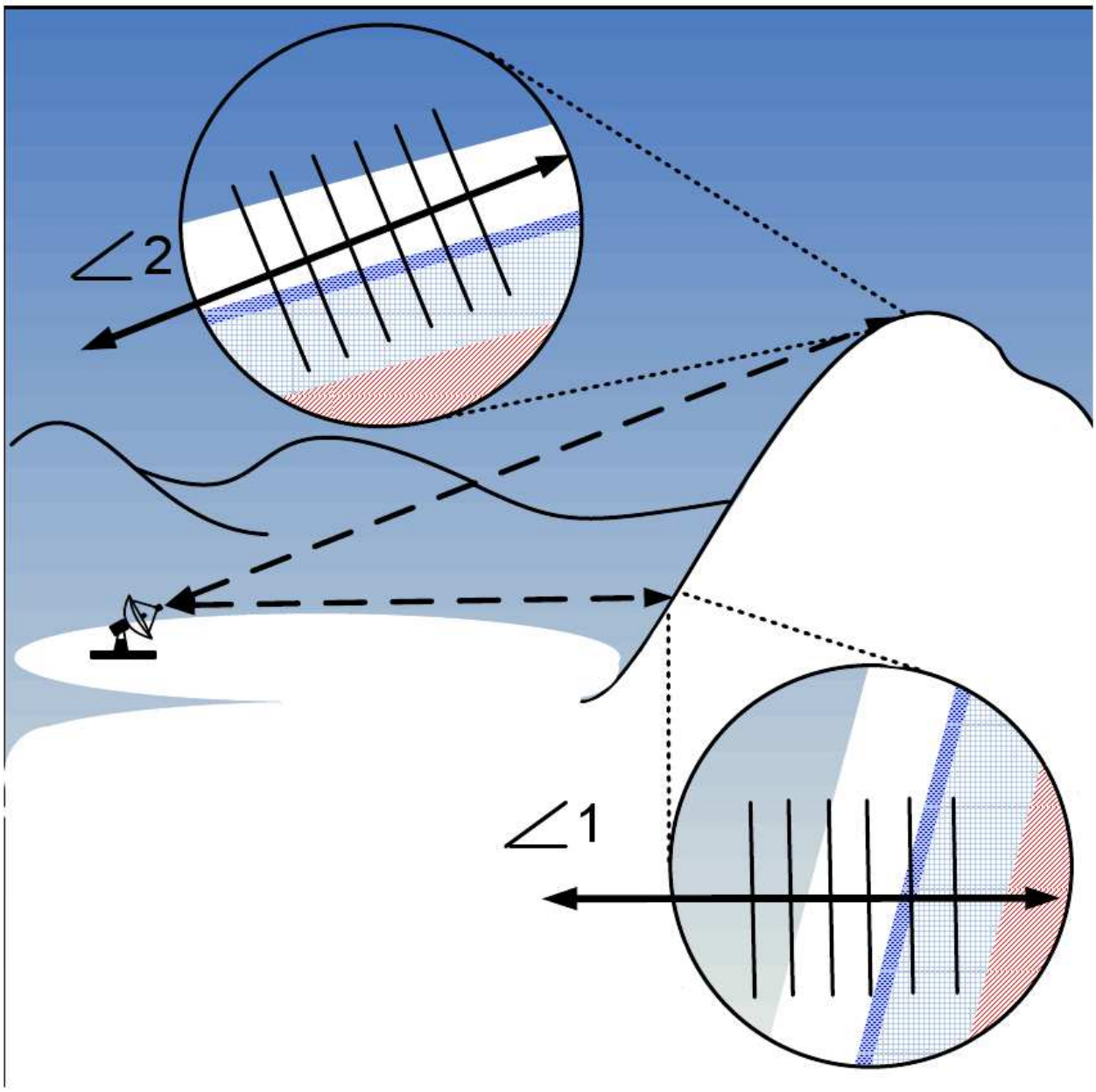

Figure 4.1: Deployment of a stationary radar system in mountainous terrain with expanded views of the orientation of the radar system's line-of-sight relative to the snowpack layers.

in the expanded depiction for angle 1, the white layer entirely occupies the third resolvable region; and, the dark blue layer (possibly representing a frozen crust) occupies a large enough portion of the fourth and fifth resolvable region to be detected and assessed despite competing backscatter from white and light blue layers. The light blue layer and the red layer (possibly comprising dangerous faceted crystals) will entirely occupy additional resolvable regions, thereby becoming detectable and quantifiable.

However, where the orientation of the line-of-sight becomes more acute, as it approaches a parallel orientation (as in the expanded depiction for angle 2) relative to the snowpack layers, the backscatter from individual, distinct layer can become confused. For example, in the expanded depiction for angle 2, the distinctly resolvable regions indicated by the hash marks cut across all four layers depicted. Backscatter from adjacent layers becomes combined. As a result, detection of distinct properties within distinct layers becomes highly problematic and measurement of those properties becomes even more difficult still.

Third, prerequisites one and two are not satisfied because the range resolution relative to layer thickness also changes as the orientation of the radar system relative to the snowpack layers changes. As the relative orientation goes from normal to parallel, becoming more acute, the range resolution more finely cuts across snowpack layers, as observable in the comparison between angle 1 and angle 2 in Fig. 4.1. The changing resolution relative to layer thickness further complicates interpretation of the backscatter.

Fourth, the prerequisite of being able to determine the relative location of properties within a snowpack is not satisfied. A radar beam at an acute grazing angle to the layers in a snowpack travels a greater distance through each layer than a radar beam normal to the layers of the snowpack (as appreciated from a comparison of the expanded depictions for angle 1 and angle 2). The different distances traveled by a radar beam have implications for a radar system's ability to determine the relative location of different regions within a snowpack. Therefore, to satisfy the first three prerequisites for a radar-based reconstruction of snowpack stratigraphy, a radar system must not only have ultra-high-range resolution, but must also account for variations between the orientation of the radar beam relative to snowpack layers.

4.1.3 Discounting the Effect of Varying Orientations of a Radar System Relative to the Layers in a Snowpack by Three-dimensional, Ultra-high-resolution, Volume Imaging

The effect of variations in the relative orientation of a radar system's line-of-sight to snowpack layers can be discounted for a radar system capable of imaging a snowpack in three dimensions. Such a radar system must offer ultra-high resolution, not just along the system's line-of-sight, but also along two additional axes orthogonal to the line-of-sight. The images rendered from such a radar system are sometimes referred to as tomographic images.

In a tomographic image, the three orthogonal dimensions along which resolution is defined combine to create voxels, the three-dimensional analog to the pixel. The resolution along each of the three axes defines the size of the three dimensional region of the snowpack about which each voxel provides backscatter information. These voxels are arrayed to produce a series of cross-sectional images that combine to account for the volume being imaged. The term tomography comes from the Greek terms "tomos," meaning a slice or a section, and "graphein," meaning to write [46]. Figure 4.2 depicts a collection of empty voxels defining the structure of a tomographic image.

A three dimensional image of volume, with a structure as depicted in Fig. 4.2, presents backscatter as stacks of resolution cells, or voxels, each voxel corresponding to the backscatter from a particular region in the snowpack. Volume scattering, as opposed to specular reflections, becomes the primary source for the backscatter imaged in the voxels. Since volume scattering is much less affected by the grazing angle, the angle no longer needs to be maintained normal to the snowpack at nadir.

Also, when the resolution is the same along all three axes, the most that the snow-layer, relative resolution may vary is by a factor of $\sqrt{3}$, consistent with a 45° tilt on two dimensions. The orientation of the line-of-sight of the radar system may vary with respect to the layers in a snowpack, but if the resolution along all three axes, depicted by the two-sided arrows in Fig. 4.2, is commensurate with the thickness of the thinnest relevant layer, the backscatter from that layer will be primarily confided to a band of voxels. Therefore, a radar capable of three-dimensional, ultra-high-resolution, volume images greatly discounts

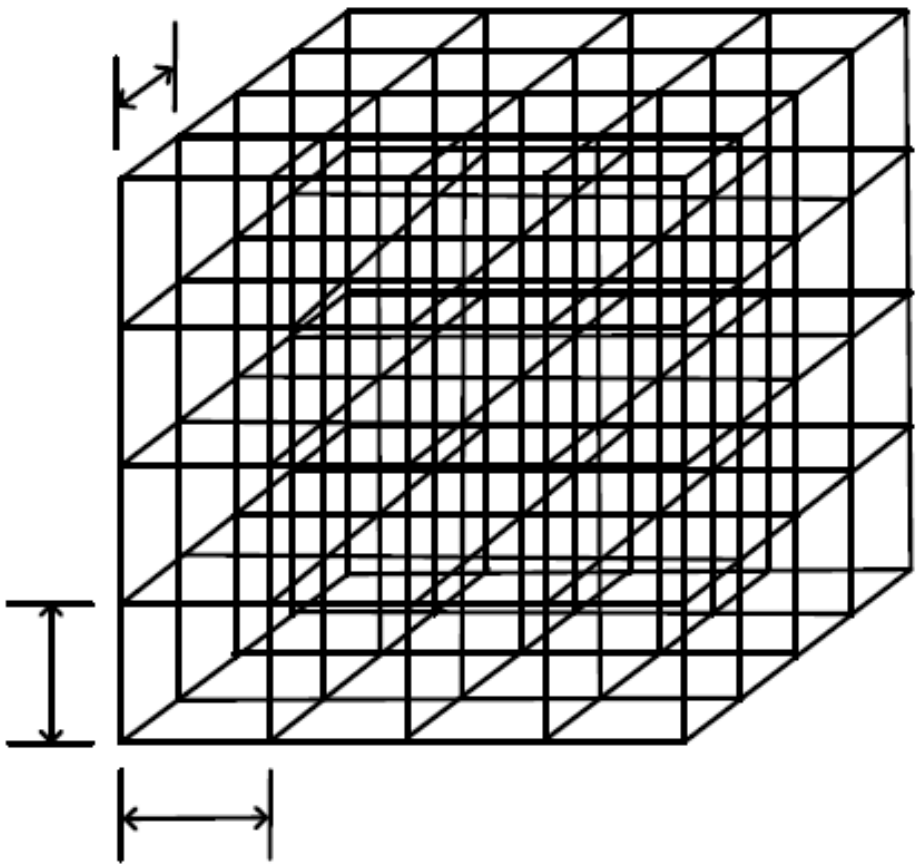

Figure 4.2: A collection of empty voxels depicting the structure of a three-dimensional, volume, or tomographic image.

the importance of the relative orientation of the radar system to snowpack layers for the reconstruction of snowpack stratigraphy.

Consequently, the radar system is better able to detect and to assess the properties of the layers, regardless of the orientation of the line-of-sight, satisfying the first two prerequisites for reconstructing the stratigraphy of a snowpack. Additionally, the third prerequisite of being able to determine the relative location of snow properties is satisfied since the relative location of each voxel is known. Prerequisite four, namely, that the radar system is practical in terms of its construction, cost, and deployment in mountainous terrain, requires

a radar system that can run on low amounts of power. As discussed in more detail below, low power permits use of smaller, cheaper, and more rugged components.

4.1.4 Summary of Radar System Requirements

Based on the four prerequisites discussed above, a radar system is required that can image volumes in three-dimensions, with ultra-high resolution, and with low power. Although radar systems exist that can image, have ultra-high resolution, run on low power, and even image in three dimensions, no radar system presently exists that satisfies all requirements concurrently. A new radar system must be developed. An understanding of the workings of this new system requires an understanding of twists on some of the most fundamental principles of radar. Therefore, an explanation of this new radar system proceeds by briefly laying a foundation with some basic radar principles.

4.2 Radar Basics

A radar (an acronym for Radio Detection and Ranging) system transmits electromagnetic energy at radio frequencies. All radars modulate the radio signal they transmit. The modulation in the transmit signal results in information in the receive signal reflected back to the radar from a scatterer (the term scatterer is used with the understanding that the scatterer may be an aggregate of several smaller scatterers). The vestiges of the modulation in the transmit signal picked up in the receive signal provide information from which knowledge may be derived about a scatterer. This section on radar basics discusses ways in which (1) the distance to and (2) the location of a scatterer can be determined. The section also discusses (3) resolution between scatterers with respect to range, and (4) resolution between scatterers with respect to axes orthogonal to the axis range.

4.2.1 Range

Range is a measure of the distance between a radar system and a scatterer responsible for backscatter detected by the radar. As mentioned, range is measured along the axis defined by a radar system's line-of-sight. Modulation of the transmit signal can be used to determine the range of a scatter by the appearance of a vestige of the modulation in the echo from that

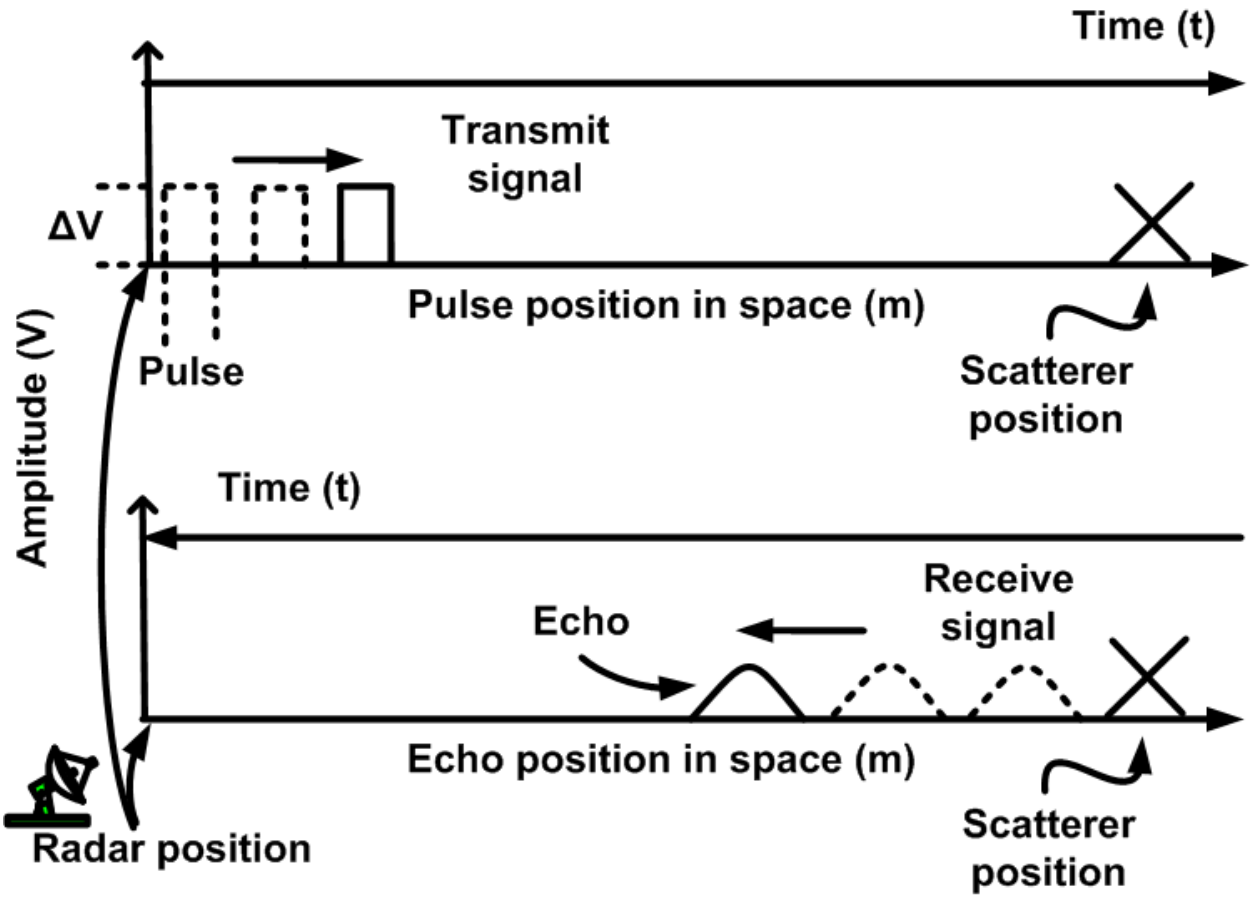

Figure 4.3: Use of amplitude modulation to determine range.

scatterer. To determine range, the transmit signal may be modified in terms of amplitude, frequency, or phase.

Amplitude Modulation Approach to Range

The most basic radar systems rely on amplitude modulation to produce pulses of electromagnetic radiation in the transmit signal. The pulse of electromagnetic radiation travels to a scatterer and returns in the form of an echo (Fig. 4.3). Range is determined by the delay time between the transmit signal and its echo, known as the "time-of-flight" τ.

The time-of-flight represents the time required for the transmit signal to reach and to return from a scatterer. As shown in the top half of Fig. 4.3, as time progresses, a pulse of electromagnetic energy, corresponding to a modulation of a radar system's voltage, travels

along the radar system's line-of-sight to a scatterer. In the bottom half of Fig. 4.3, the echo from the scatterer is depicted taking the same amount of time to return to the radar system, where the echo will cause an increase in the radar system's voltage, resulting in detection of the scatterer. Hence, the scatterer's range is simply half the time-of-flight τ multiplied by the speed of light, as expressed (for an alternative discussion see [47]):

$$R = \frac{c\tau}{2}. \tag{4.1}$$

Frequency Modulation Approach to Range

Frequency modulation radar systems (FM radars) modulate the frequency of the transmit signal through a range of frequencies. Since frequency describes the rate of change in phase with respect to time, the notion of an instantaneous frequency changing with respect to time is a construct. In actuality, phase is what changes from time to time. The construct of instantaneous frequency is arrived at by taking the derivative of the rate of change of phase with respect to time. A function that describes a linear rate of change in frequency is really derivative of a quadratic function describing changes in phase with respect to time [48].

Figure 4.4 plots the instantaneous frequency for a transmit signal (solid line) with respect to time for a Linear Frequency Modulated, Continuous Wave (LFM-CW) radar. The bandwidth B is the difference between the maximum frequency and the minimum frequency of the transmit signal. In a LFM-CW radar, when the transmit frequency reaches the maximum frequency, the radar returns the transmit frequency to the minimum frequency, below the central frequency f_c corresponding to the horizontal axis in Fig. 4.4. Figure 4.4 also depicts the time-delayed receive signal (dashed line) as an echo from a scatterer.

In such a radar system, the rate of instantaneous frequency change has a constant magnitude. As a result, the frequency value of the transmit signal changes with respect to time with the saw-wave pattern depicted in Fig. 4.4. The instantaneous frequency in the receive signal follows the same saw pattern with respect to time at the same rate of change. However, the receive signal is shifted in time with a delay τ due to its time-of-flight to and back from the scatterer.

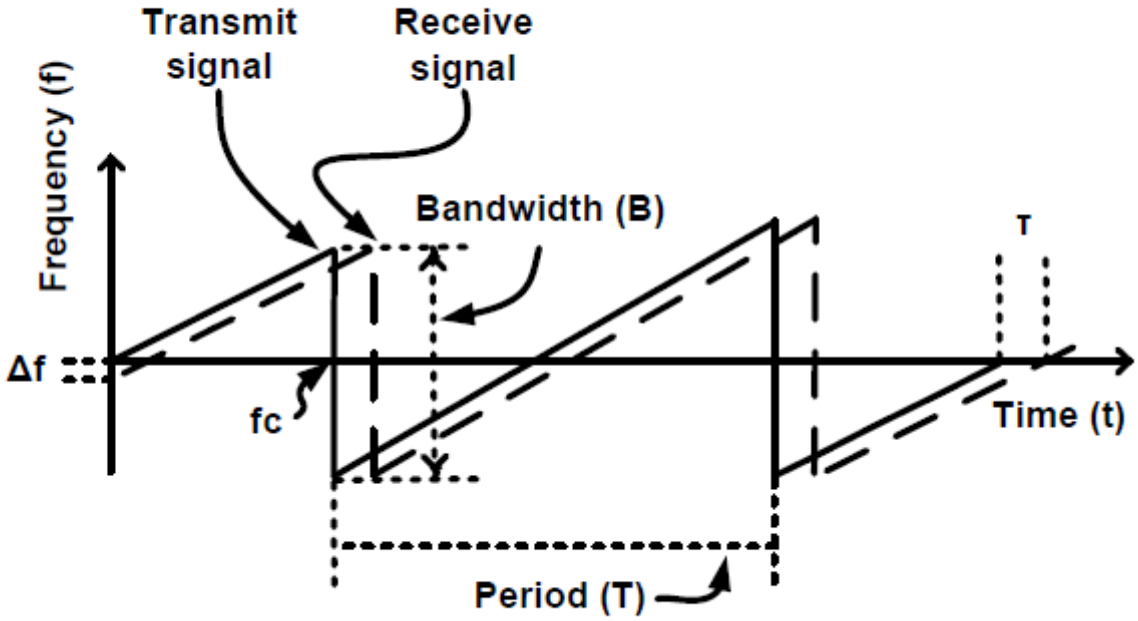

Figure 4.4: Use of frequency modulation to determine range.

The manner in which FM radars modulate transmission signals, as described above, determines the manner in which FM radars can determine scatterer range. As with other forms of radar, range may be determined by the delay time between the transmit signal and its echo. Hence, a scatterer's range is simply half the time-of-flight τ multiplied by the speed of light (Eq. 4.1).

Time-of-flight is determined from a measure of the change in instantaneous frequency Δ_f between the instantaneous frequency of the transmit signal and that of the receive signal. From the change of instantaneous frequency Δ_f, the time required for this change, i.e., the time-of-flight τ can be determined if the rate of frequency change r is known,

$$\tau = \frac{\Delta_f}{r}. \tag{4.2}$$

As depicted in Fig. 4.4, during the time period for each cycle T, the transmission signal begins at the lowest frequency and rises to the maximum frequency. In the process, the transmit signal spans the bandwidth B. The rate of frequency change, therefore, is equal to the bandwidth divided by the period T,

$$r = \frac{B}{T}. \tag{4.3}$$

LFM-CW radars determine the change in frequency Δ_f by passing the transmit and the receive signals to a mixer. The output of the mixer provides signals at frequencies equal to the sum and the difference of the two inputs. The sum frequency is filtered out, leaving the difference frequency, i.e., the change in frequency Δ_f. As discussed, dividing the change by the rate of change provides the time-of-flight, from which range is determined by Eq. 4.1. (Eor an alternative discussion see [38].)

4.2.2 Use of Range and Antenna Orientation to Locate a Scatterer in Three-dimensional Space

A radar can locate a scatterer in three-dimensional space by determining the range to the scatterer and the direction from which the scatterer causes the echo in the receive signal to re-traverse that range. The range and the direction create a vector that points to the location of the scatterer. An echo from a scatterer must come from a direction receiving sufficient radiative energy from the radar, as determined by the three-dimensional beam pattern of a radar's antenna. Since a radar antenna radiates electromagnetic energy in a predetermined, three-dimensional pattern, the direction from which the echo returns to the radar can be approximated by the orientation of the antenna, i.e., the radar system's line-of-sight. This conceptually intuitive point can be quantified by the radar equation, which describes the amount of power available from a known scatterer at a particular location in three-dimensional space for a particular antenna configuration (see [49]).

Antenna Beam Patterns

The radiation pattern of an antenna is expressed in terms of Watts per steradian. A steradian is the three-dimensional analog of the radian, describing two-dimensional angular

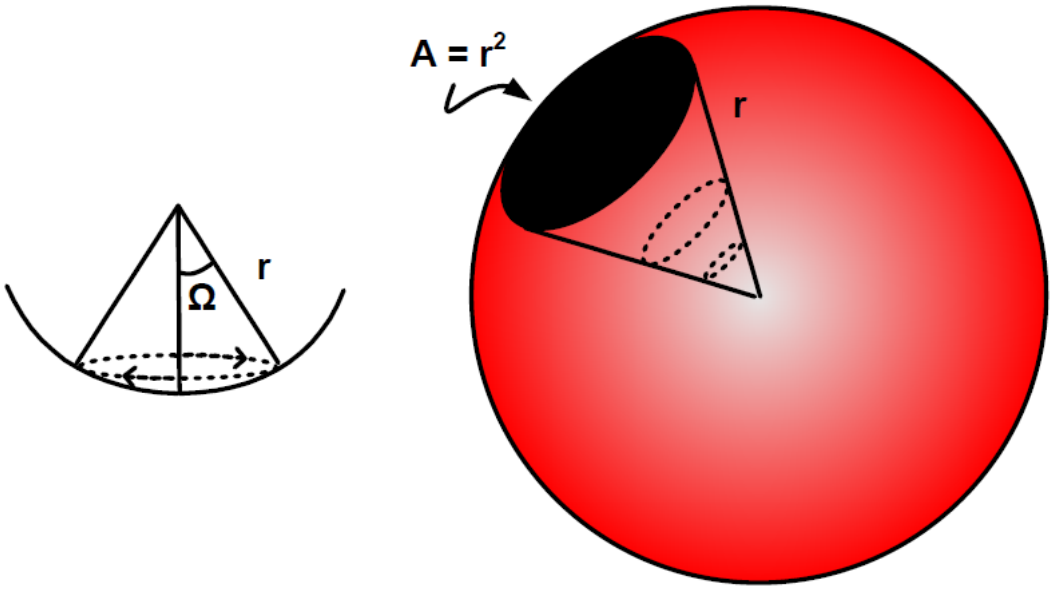

Figure 4.5: Diagram of a steradian.

spans in three-dimensional space, just as the radian describes one-dimensional angular spans in two-dimensional space. More precisely, a steradian describes the solid angle Ω (an angle rotated about a central axis resulting in a cone-like shape) subtended at the center of a sphere of radius r by a portion of the surface of the sphere having an area equal to the radius squared, as shown in Fig 4.5.

Radiation patterns are usually depicted in a normalized form known as the normalized radiation pattern. The normalized radiation pattern is normalized with respect to the maximum value of the radiation pattern. The ratio is expressed in terms of decibels (dB). The normalized radiation pattern is a function of both azimuth ϕ and elevation Θ.

Commonly, normalized radiation patterns are depicted as cross sections of the overall patterns in terms of a single axis, usually azimuth. The cross section is taken for a particular value of elevation or azimuth, for example, elevation equals zero. The depiction can be presented in terms of a polar diagram (decibels are plotted as a function of radially distributed

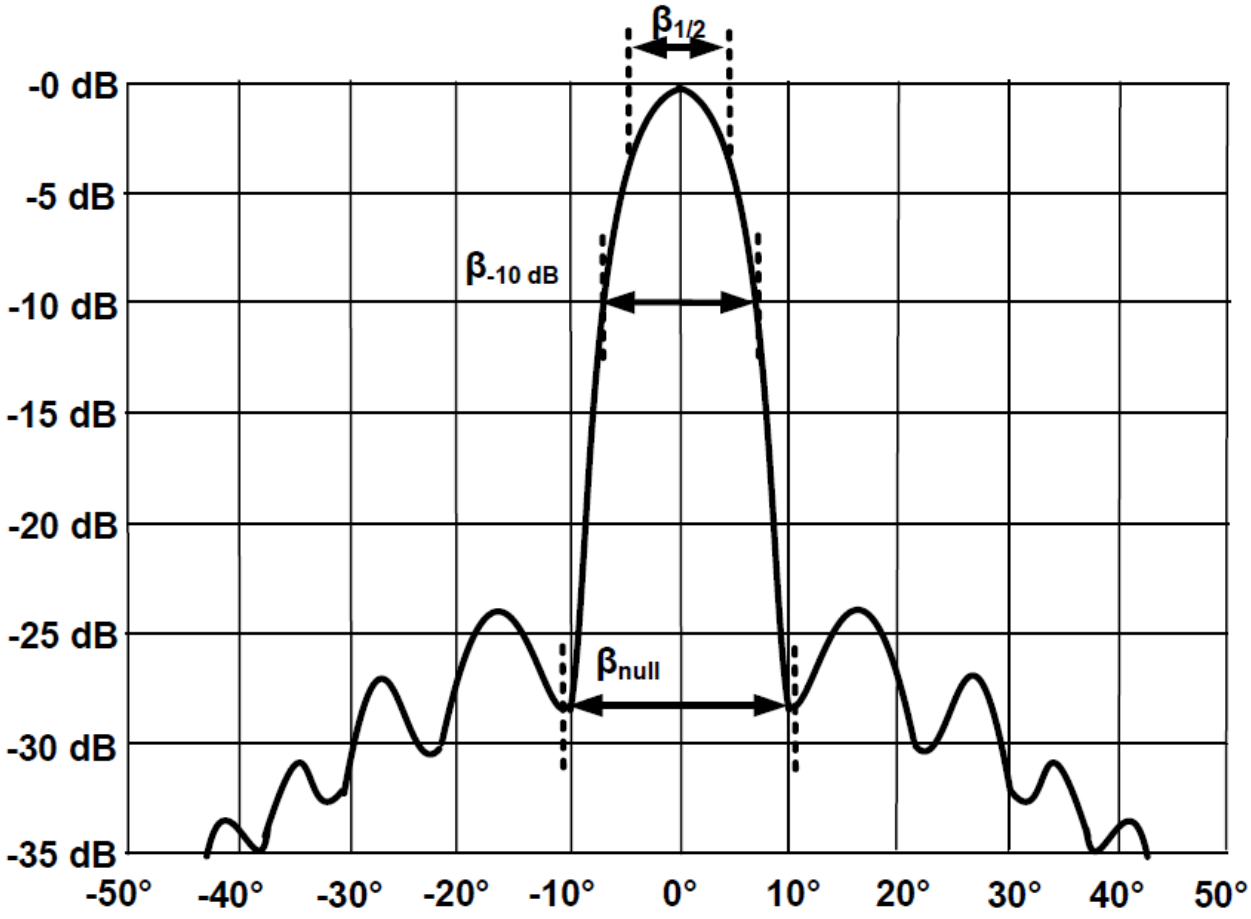

Figure 4.6: Beam pattern as a function of azimuth at elevation zero.

angles) or a rectangular diagram (decibels are plotted as a function of linearly distributed angles). An example of a rectangular diagram of a cross-section at an elevation of zero is presented in Fig. 4.6.

As illustrated in Fig. 4.6, a main beam usually occupies the central angles of a beam pattern. The width of the main beam can be described in terms of cut off points such as -3 dB (a one-half reduction in power), -10 dB, and null-to-null. Often, as in Fig. 4.6, there is a drop of 20 dB, or greater, to the nearest side lobe. Since a drop of 20 dB is equal to about one-hundredth of the original power, the vast majority of the power is radiated by the antenna in the direction of the main beam, as determined by the orientation of the

antenna. As a result, the vast majority of the backscatter reflected back from the antenna has its origin at a scatterer in the path of the main beam. (For an alternative discussion of steradian and beamwidth see [38].)

Determination of Beam Path from Antenna Orientation

By windowing out side lobes, a radar system can insure that only scatterers in the path of the main beam produce sufficient backscatter to be detected. Where the main beam is centered about zero degrees in terms of both azimuth and elevation, the normal to the antenna's aperture (an antenna's aperture is the area from which the antenna radiates) describes the direction of the main beam. As stated, combining the directional information with the range information generates a vector pointing to the location, in three dimensional space, of the scatterer detected by the radar.

4.2.3 Resolution

Resolution quantifies the ability to distinguish the backscatter originating from a first scatterer from the backscatter originating from an adjacent, second scatterer in terms of the distance between the two scatterers. Resolution is defined along an axis. The axis described by the path of the main beam is known as the range axis, and the resolution along this axis is known as the range resolution. When backscatter data is processed to form an image, as discussed below, the two- and three-dimensional cells that make up a radar image are defined by resolution along a second and a third axis respectively.

Range Resolution for Amplitude Modulated Radar

For amplitude modulated radar (AM Radar), range resolution is a function of pulse duration. The dependence of resolution on pulse duration becomes clear by assuming a first scatterer separated from a second scatterer by a distance less than half the distance covered by the speed of light during the pulse duration, as depicted in Fig. 4.7. In Fig. 4.7, three different scenarios are depicted in which the relative distances between two scatterers is increased. The top portion of Fig. 4.7 shows a transmit pulse as it approaches, encounters, and passes the two scatterers at various points of time within a series of discrete samples

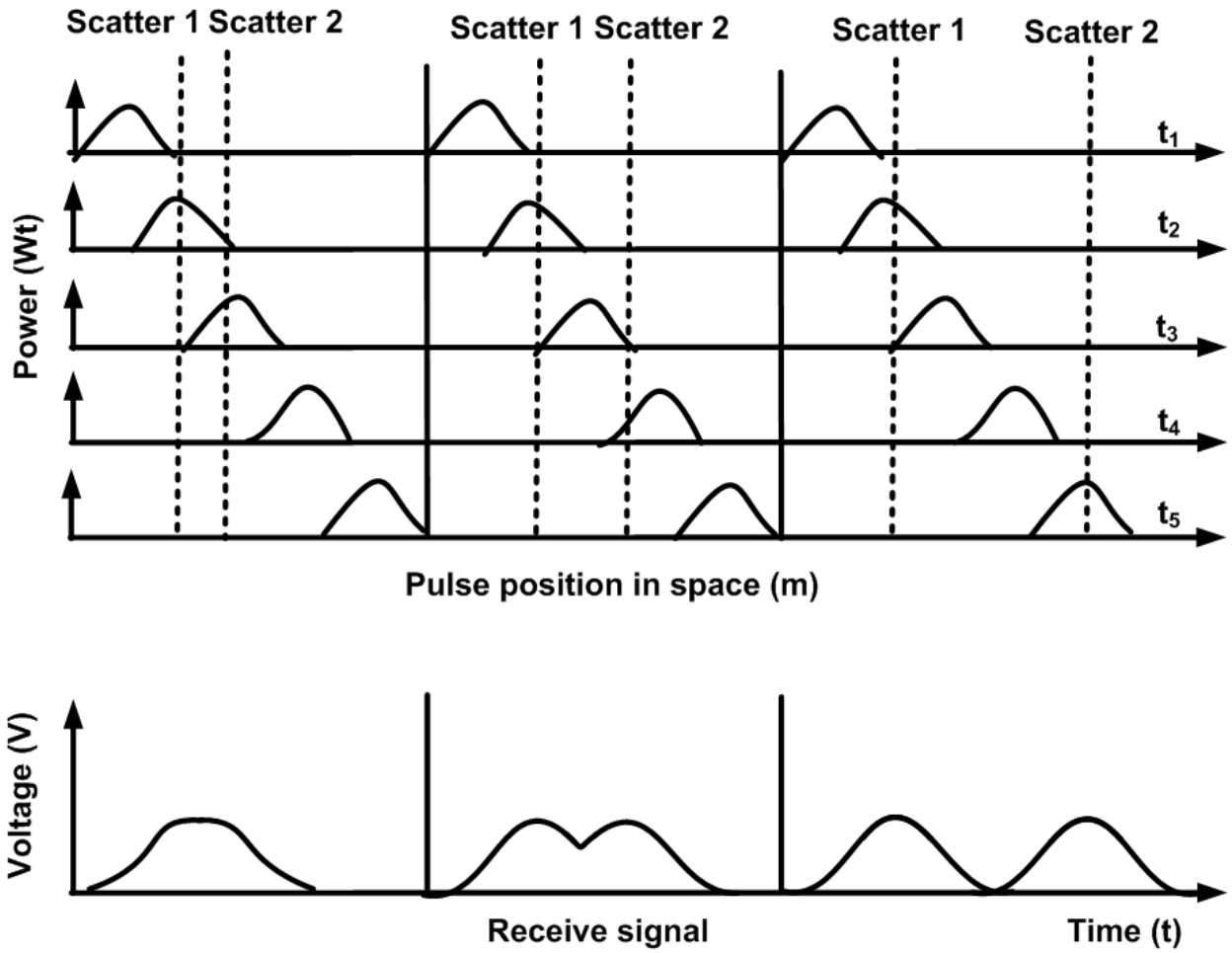

Figure 4.7: Resolution as a function of pulse duration for amplitude modulated radar. (Adapted from [38], Fig. 17.9.)

of time. The bottom portion of Fig. 4.7 shows the echo from the two scatterers in the receive signal. Unlike the top portion of Fig. 4.7, in the bottom portion of Fig. 4.7, time is continuous and is depicted across the horizontal access.

In the first scenario depicted in Fig. 4.7, the distance between the two scatterers is less than half that traveled by light during the pulse. As a result, the echo from the second scatterer overlaps the echo from the first scatterer when the two echoes are received by the radar system, as shown for the first scenario in the bottom portion of Fig. 4.7. Unless something is known about the scatterers beforehand, which is generally not the case, the

echoes from the two scatterers cannot be distinguished. In the second scenario, the scatterers are spaced further apart, but their echoes still result in some ambiguity in their return signals.

In the third scenario, the scatterers are spaced further apart than light can travel in the time of the corresponding pulse's duration. As a result, the two scatterers can be resolved in the receive signal. The resolution of an AM radar systems can, therefore, be expressed in terms of pulse duration,

$$\Delta_r = \frac{ct_p}{2}. \tag{4.4}$$

AM radars have poor resolution because light travels about 300 meters in a single microsecond. Achieving pulse durations of less than a micro-second is difficult, because of the amount of energy that must be concentrated in each pulse. As electromagnetic energy radiates from a radar system's antenna, it spreads in three-dimensional space so that only a very small fraction reaches any particulary scatterer. Similarly, electromagnetic energy reflected back to the radar also spreads in three-dimensional space so that the amount of energy from a particular scatterer is a very small fraction of the transmitted energy. To compensate, the amount of energy transmitted must be very large.

However, to achieve any kind of resolution, the energy must be crammed into short pulses, resulting in enormous amounts of power. For example, the amount of energy that must be concentrated in a microsecond, or near microsecond, pulse requires megawatts of power for a typical weather radar system. Further shortening pulse duration requires even more power, placing impractical demands on circuitry, the antenna, and the power supply of a radar system.

To meet these demands, AM radar systems tend to be large, expensive, bulky, fragile, and relatively un-portable. Even when compromised by these incumbrances, an AM radar has poor resolution, measured in tens to hundreds of meters. However, to resolve the layers in a snowpack, resolution must be measured in centimeters. As explained below, to achieve range resolutions measured in centimeters and to avoid large power requirements, frequency modulation is required.

4.2.4 Power Distribution Afforded by Frequency Modulation

FM radars have a distinct advantage with respect to power requirements. For an equal amount of transmission energy, the Signal to Noise Ratio (SNR) for pulse-modulated radars and FM radars is about the same [50]. However, pulse-modulated radars must concentrate all of their energy during a short pulse. Conversely, FM radars can distribute energy uniformly throughout the entire frequency modulation cycle of arbitrary duration. Since FM radars can distribute the energy over arbitrary durations of time, they do not require large bursts of power. The ability to distribute power throughout an entire cycle has important implications for SNR and hardware.

Since the hardware associated with FM radars does not have to handle large pulses of power, the size, weight, and expense of hardware can all be reduced. As appreciated, circuitry capable of handling Watts, or even fractions of Watts, as opposed to a mega Watt or more, is relatively small, light weight, and inexpensive. Radar systems of extreme light weight, versatility, and low expense can be constructed when power requirements are low [51].

Range Resolution for Frequency Modulated Radar

For an AM radar, range resolution is a function of pulse duration, i.e., a width defined by a span of time in the time domain. For FM radar, range resolution is inversely proportional to a span of frequencies in the frequency domain [52].

In the frequency domain, the width of the transmit signal is determined by the bandwidth of the transmit signal. Due to the inverse relationship between the frequency and the time domains, the larger the bandwidth over which an FM radar sweeps a transmit signal, the narrower the constructive pulse width in the time domain for the signal. Hence, larger bandwidths result in better resolution for a radar system.

Figure 4.8 depicts the inverse Fourier transform on two transmit signals with differing bandwidths. The first transmit signal has a larger bandwidth than the second. As the inverse Fourier transform on the two transmit signals shows, the width of a signal in the time domain is inversely proportional to the width of the signal in the frequency domain [53].

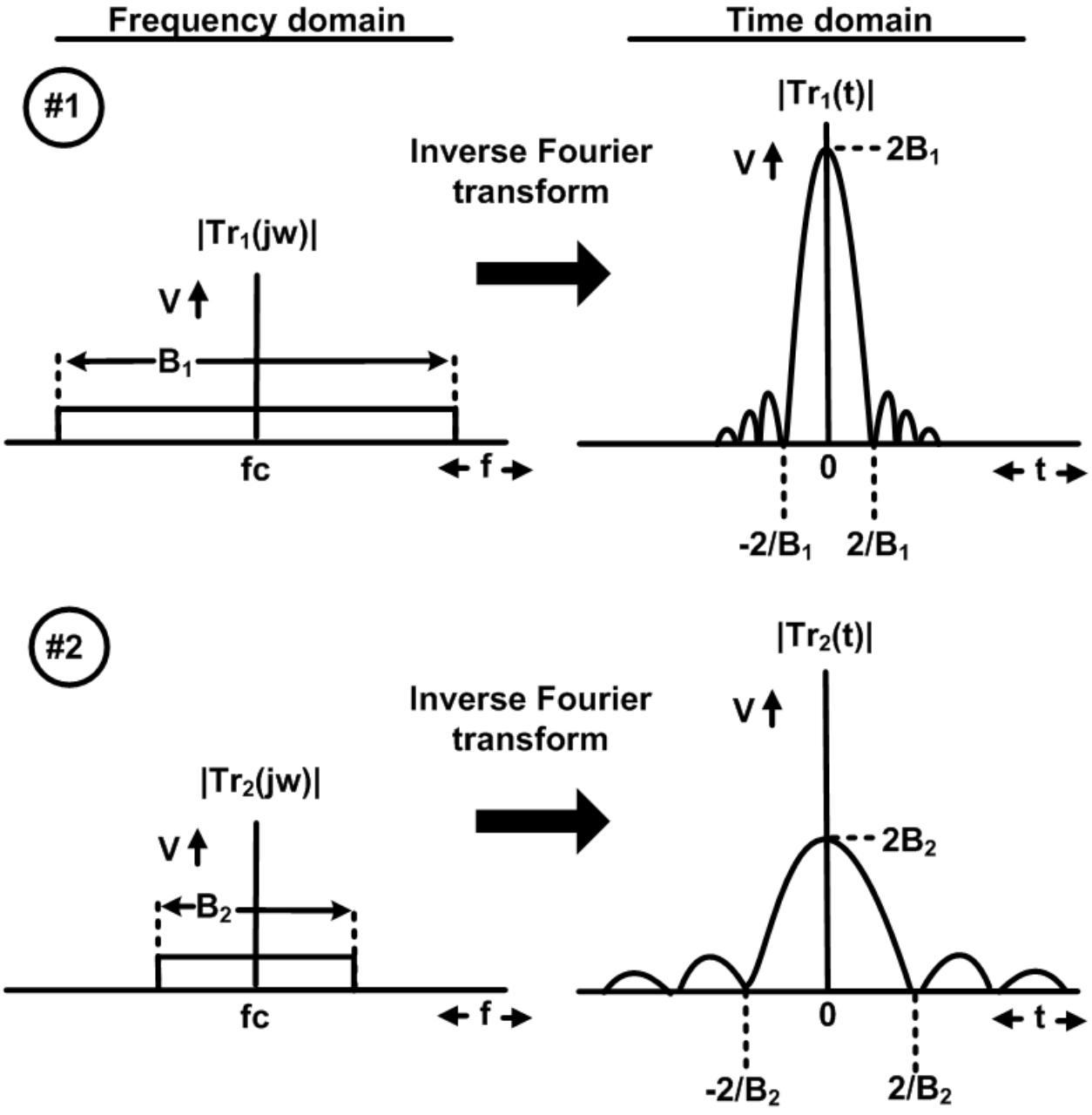

Figure 4.8: Inverse relationship between the frequency and time domains. (Adapted from [53], Fig. 4.11.)

The inverse relationship between the bandwidth B of the transmit signal and the constructive pulse width t_{cp} of that signal can be expressed as:

$$t_{cp} = \frac{1}{B}. \tag{4.5}$$

Additionally, the relationship in Eq. 4.5 suggests that an equation analogous to Eq. 4.4, which determines range resolution for AM radars, can be created for FM radars, namely:

$$\Delta_r = \frac{c}{2B}. \tag{4.6}$$

Ultra-high Range-resolution Requirement

As stated, range resolution must be high in order to satisfy the first two prerequisites of the radar system, namely, the ability to detect and to measure a property, or collection of properties, associated with poor cohesion, poor friction, and/or high shear forces. The layers that exhibit these properties of interest can vary widely in their thicknesses. Often layers of interest can be as thin as a couple of centimeters, or even a centimeter or less. In order to detect and to measure properties, the ratio of backscatter from the layer of interest to backscatter from the surrounding snow in the cell of resolution must be as large as possible.

According to Eq. 4.6, a radar system with a bandwidth of 15 GHz, would have a range resolution of 1 cm. Although such a resolution would be ideal, practical limitations make a bandwidth of 1.5 GHz more attainable. Referring back to Eq. 4.6, a bandwidth of 1.5 GHz results in a resolution of 10 cm (approximately 4 inches). A resolution of 10 cm corresponds to a layer-of-interest-to-surrounding-snow ratio of about 1 to 9 for the very thinnest layers, holding open the possibility of detecting and measuring the properties of even the thinnest layers of interest—many layers of interest are much thicker, will have better ratios, and will be much easier to detect and to assess.

As discussed above, a radar system capable of reconstructing the stratigraphy of a snowpack must be able to image in three dimensions. In fulfillment of this requirement, the resolution along each axis of the imaging voxels should be equal, i.e., 10 cm.

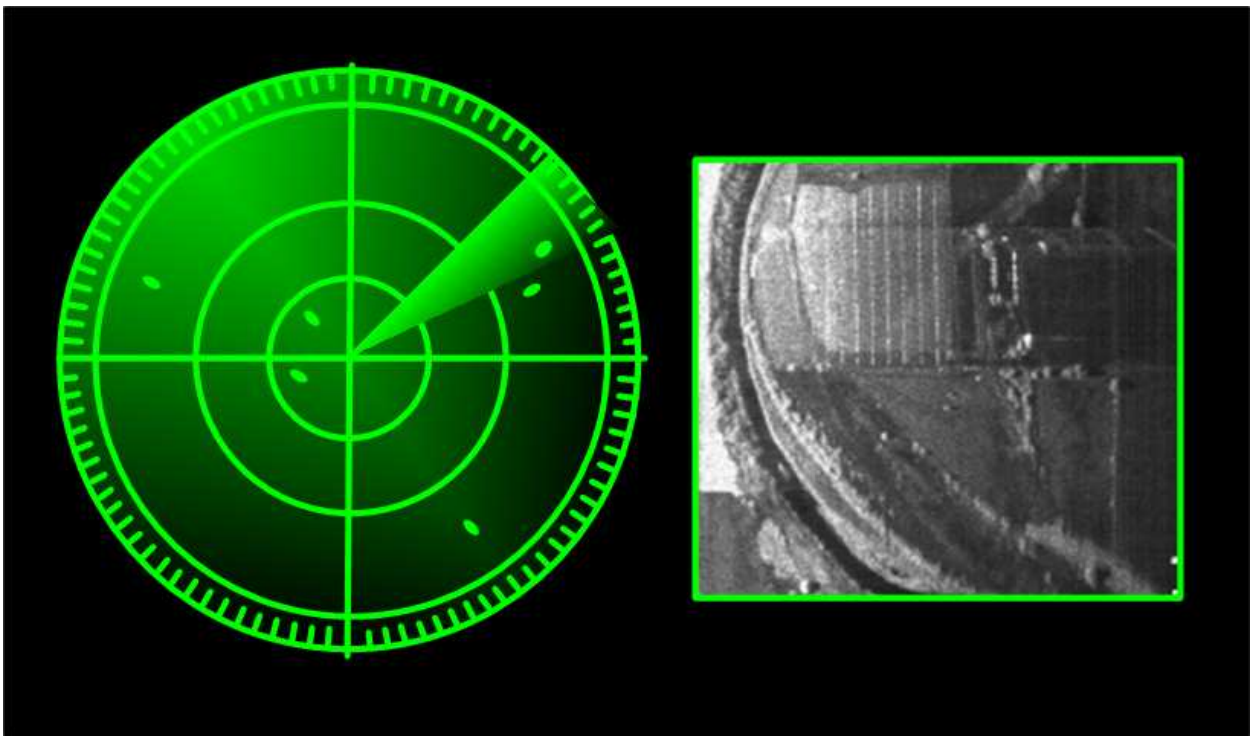

Figure 4.9: Comparison between a radar detection display and a radar image.

4.2.5 Imaging

The common conception of a radar system embodies the function of these systems during the Second World War, namely, the detection of scatterers, or targets, and the determination of the location of these targets in multi-dimensional spaces. Less widely appreciated is the ability of radar systems to make two-dimensional, and even three-dimensional maps, or images, of the backscatter characteristics of a particular region. Figure 4.9 contrasts the traditional notion of radar, embodied by a phosphorescent radar sweep display, with an example of an image produced by a radar system.

As discussed, an image of the backscatter of a snowpack may be able to reconstruct a stratigraphy of that snowpack over large areas in terms of avalanche relevant properties. As also discussed, such an image is comprised of pixels, or voxels in the three-dimensional case, that are delineated one from another along multiple, orthogonal axes. The creation of these pixels/voxels requires the ability to determine location and resolve along multiple, orthogonal axes.

Footprint Location Determination and Resolution

To image in three dimensions, location determination and resolution must be possible along three orthogonal axes. Frequency modulation of the transmit signal makes possible location determination and resolution along a first axis. However, a means for determining backscatter location and for resolving backscatter from different regions must still be provided for two additional, orthogonal axes.

The location determination and resolution necessary for imaging can be achieved in two orthogonal dimensions by means of the footprint illuminated by the antenna of a radar system. In Fig. 4.10, the depicted antenna illuminates a footprint in a plane orthogonal to the range direction. A non-coherent radar system attached to this antenna records the backscatter from all the scatterers in the illuminated footprint—the differing phase from the various scatterers adding constructively and destructively—to provide a real measurement of the intensity of the backscatter in the illuminated footprint.

Since the backscatter from the entire illuminated footprint is combined in a single measurement, the dimensions of the illuminated footprint define the resolution of a non-coherent radar system. As depicted, the height and the width of the footprint respectively define the elevation and the azimuth resolutions. Antenna footprints can also be used to determine the location from which backscatter arises.

By moving the antenna, the resultant footprint illuminates different regions of the orthogonal plane. By temporally indexing the location of the antenna with the region predicted to be illuminated by the footprint from the moving antenna, an image of the intensity of the backscatter from different regions can be produced. This non-coherent radar mapping mode is known as Real Beam Ground Mapping (RBGM) [54].

In Fig. 4.11, the antenna of a radar system is mounted on an airplane to perform RBGM. The flight path of the plane describes a trajectory such that at different times the footprint of the antenna occupies a different cell in an imaging grid. Measurements of the footprint at times when it is centered in different cells in the grid are combined to create an image of the intensity of backscatter. The resolution of the image mapping backscatter intensity is defined by the dimensions of the footprint.

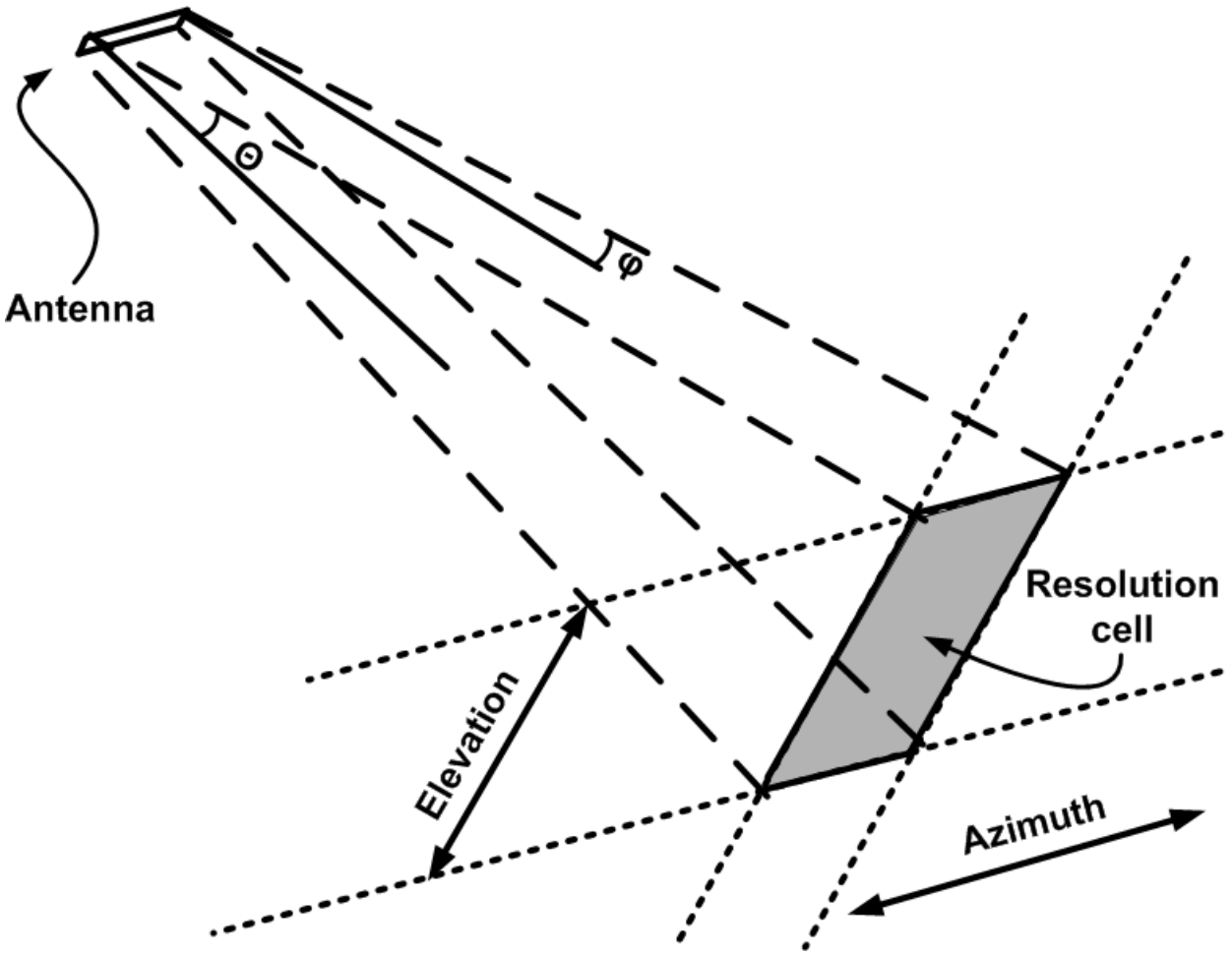

Figure 4.10: Footprint-dependent resolution for azimuth ϕ and elevation Θ.

Footprint Resolution

The dimensions of the footprint illuminated by an antenna are functions of the azimuth and elevation beam widths and the range, as depicted in Fig. 4.12 for a circular antenna with a circular footprint. Footprint dimensions increase with range as demonstrated by the four footprints in Fig. 4.12. Since the footprint is circular, the variable Θ is used for both azimuth and elevation angles. The azimuth and elevation dimensions of the footprint can be expressed as:

$$\Delta_{az} = R\Theta_{az}, \tag{4.7}$$

$$\Delta_{el} = R\Theta_{el}. \tag{4.8}$$

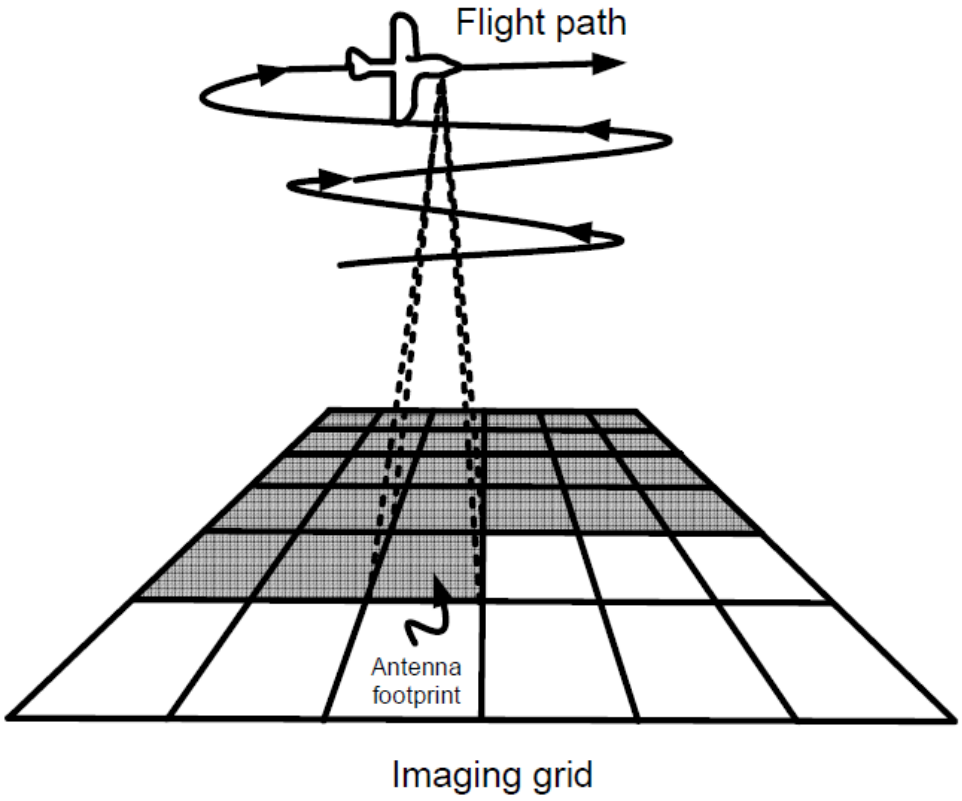

Figure 4.11: Real Beam Ground Mapping.

4.2.6 Inverse Relationship Between Antenna Size and Beam Width

Equations 4.7 and 4.8 show that the antenna of a radar system must have a small beam width to support fine footprint resolution. An antenna couples electromagnetic energy traveling in a wire or a wave guide into the air or vice versa. The orientation and distribution of electromagnetic energy, in terms of a real or impressed current, over the area at which this coupling takes place determines the way in which that electromagnetic energy propagates, including the confines of the beam width.

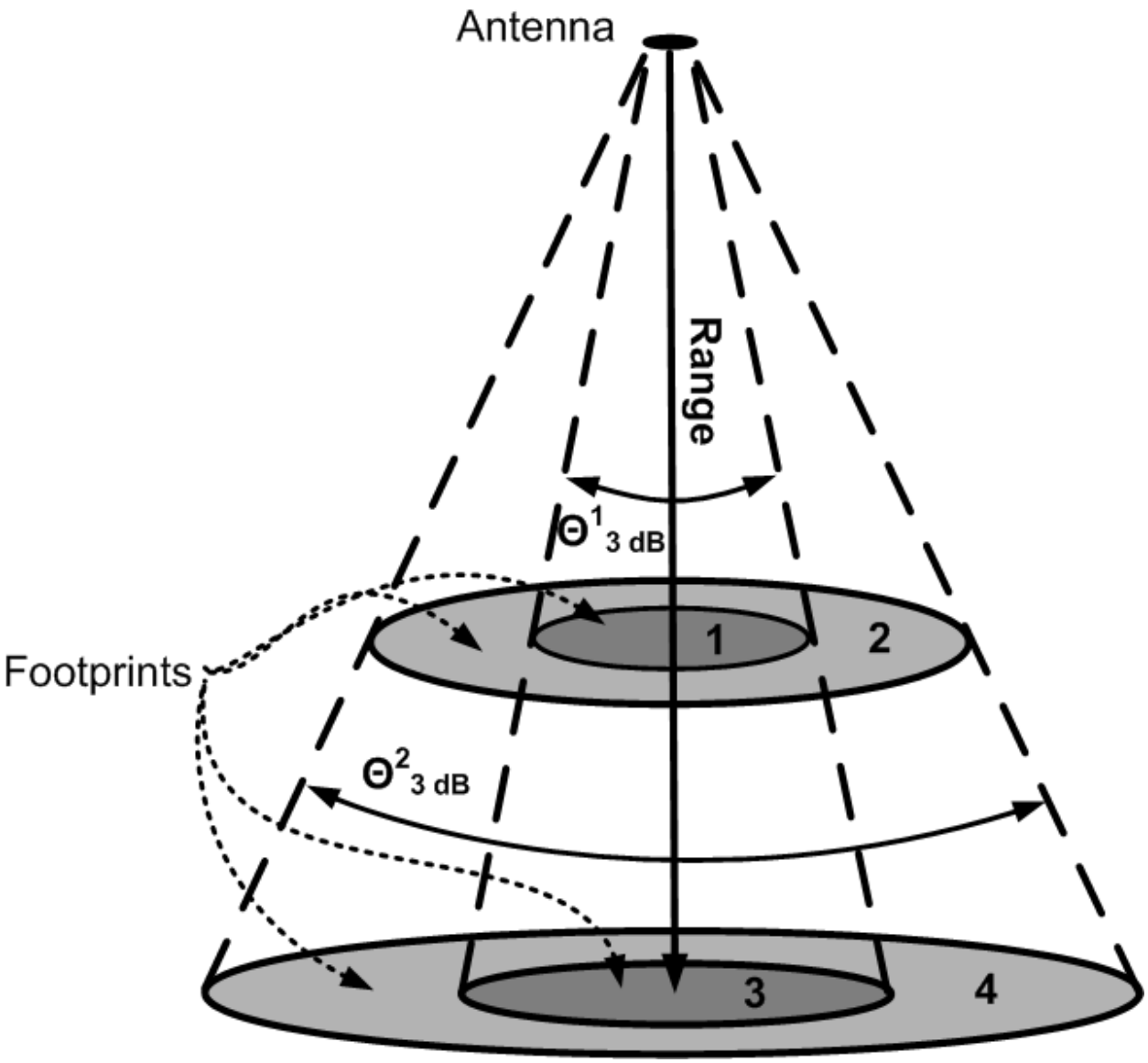

Figure 4.12: Footprint dimensions as a function of range and beam width.

Beam Width from the Perspective of Signals and Systems

From the perspective of signals and systems, the coupling of electromagnetic energy that occurs at an antenna can be viewed as a dynamic system. The current distribution across the coupling area of the antenna constitutes the input signal. The antenna beam width constitutes the output signal generated by the system. Maxwell's equations hold the

same regardless of the location of a unit of current, resulting in the same radiative properties and making the system position invariant.

The output of an invariant system to an input signal can be determined by convolving the input signal with the response of that system to a single impulse. The nature of the impulse depends on the nature of the system. For example, the output signal $y(t)$ from a system that is time invariant can be determined by convolving the input signal $x(t)$ with the response from the system to a unit of energy at time zero, with infinitesimally small duration, known as a delta function. This response is the impulse response $h(t)$ [55]. Therefore,

$$y(t) = \int x(t)h(t - t')dt'. \tag{4.9}$$

The impulse provided to the coupling system of an antenna is not a delta function, but is defined by the function that describes a unit of current on the coupling area of the antenna with respect to position, not time. Assuming a sinusoidally alternating current, which to first order approximates the transmit and receive signals of an antenna, the impulse is a sinusoid defined by a specific frequency, which in the frequency domain manifests as a pair of frequency-shifted delta functions.

The impulse response for this position-invariant system is determined by the response of the system to this sinusoid. This response can be derived directly from Maxwell's equations, but with some difficulty. The sinusoidal nature of the impulse results in electromagnetic waves that lend themselves to description by the wave equation:

$$\bigtriangledown^2 \vec{E} + k^2 \vec{E} = j\omega\mu\vec{J}, \tag{4.10}$$

where $\vec{E}$ is a vector describing the radiated electric field, k is the wave number, and $\vec{J}$ is a vector describing the current at the antenna.

Unfortunately, the wave equation provides solutions, such as longitudinal waves, that are not permitted by Maxwell's equations. To avoid this problem, the wave equation is reworked with some vector identities to be expressed in terms of a vector $\vec{A}$ known as the

magnetic vector potential, which is consistent with Maxwell's equations,

$$\bigtriangledown^2 \vec{A} + k^2 \vec{A} = -\mu \vec{J}. \tag{4.11}$$

Altering the wave equation so that it is consistent with Maxwell's equations by means of the magnetic potential vector is ubiquitously described in the literature and can be found in many textbooks, such as [56]. By solving for the magnetic potential and setting the equation for the magnetic potential equal to the convolution of the unknown impulse response $g(\vec{r}-\vec{r}')$ and the current distribution $\vec{J}$, the impulse response can be solved for,

$$\vec{A}(\vec{r}) = \frac{-\mu \vec{J}(\vec{r})}{(\bigtriangledown^2 + k^2)} = \int \vec{J}(\vec{r}) g(\vec{r} - \vec{r}') d\vec{r}'. \tag{4.12}$$

The derivation of the commonly-used solution requires many steps, including the use of spherical coordinates and the solving of a differential equation. The derivation of a Green's function will not be undertaken here, as the subject is treated in several readily-available texts, such as [57]. The result $g(\vec{r} - \vec{r}')$, however, is provided:

$$g(\vec{r} - \vec{r}') = \frac{\mu}{4\pi} \frac{e^{-jk|\vec{r}-\vec{r}'|}}{|\vec{r} - \vec{r}'|}. \tag{4.13}$$

As appreciated, the Green's function is a function of two variables: $\vec{r}'$, which corresponds to a point in space on the area of the antenna at which coupling of electromagnetic energy takes place, and $\vec{r}$, which corresponds to a point in the spatially characterized output. However, for all points in the output signal at a sufficient distance from the antenna, certain simplifying assumptions can be made. The region over which the particular set of assumptions important to this discussion can be made is known as the Far Field Region, traditionally defined as any point greater than ten wavelengths from the antenna.

In the Far Field Region, the phase term can be simplified by the mathematical approximation that:

$$\vec{r}' \simeq r - \hat{r} \cdot \vec{r}', \tag{4.14}$$

where the term $\hat{r}$ is a unit vector from the antenna to the output point in question, so that the phase term is:

$$e^{-jk|\vec{r}-\vec{r}'|} \simeq e^{-jkr}e^{-jk\hat{r}\cdot\vec{r}'}. \tag{4.15}$$

The magnitude term can be further simplified insofar as the $\hat{r}$ term can be neglected:

$$\frac{1}{|\vec{r}-\vec{r}'|} \simeq \frac{1}{r}. \tag{4.16}$$

At this point, the system output $\vec{A}_{ff}(\vec{r})$ can be determined by convolving the spatially distributed input signal $\vec{J}(\vec{r}')$ with the Green's function,

$$\vec{A}_{ff}(\vec{r}) = \frac{\mu}{4\pi}\frac{e^{-jkr}}{r}\int \vec{J}(\vec{r}')e^{-jk\hat{r}\cdot\vec{r}'}d\vec{r}'. \tag{4.17}$$

Beam width with respect to azimuth and elevation can now be determined by changing from a Cartesian coordinate system to a spherical coordinate system defined in terms of azimuth ϕ and elevation Θ angles. A Cartesian coordinate system is maintained at the antenna so that:

$$\hat{r} = \hat{x}\sin\theta\cos\phi + \hat{y}\sin\theta\sin\phi + \hat{z}\cos\theta, \tag{4.18}$$

$$\vec{r}' = x'\hat{x} + y'\hat{y}, \tag{4.19}$$

and

$$\hat{r}\cdot\vec{r}' = x'\sin\theta\cos\phi + y'\sin\theta\sin\phi. \tag{4.20}$$

Therefore, the relevant wave numbers can be expressed as:

$$k_x = k\sin\theta\cos\phi, \tag{4.21}$$

$$k_y = k\sin\theta\sin\phi, \tag{4.22}$$

and

$$k\hat{r}\cdot\vec{r}' = k_x x' + k_y y'. \tag{4.23}$$

After the following discussion on aperture antennas, the foregoing results for the wave numbers will be used to explore the relationship between antenna size and beam width.

Aperture Antennas

Having determined the spatial impulse response of the system, having made the simplifying far-field approximations, and having changed the output coordinate system to be expressed in terms of azimuth and elevation angles, this discussion has almost advanced to the point where the inverse relationship between antenna size and beam width can be easily explored. One conceptual development remains. Beam width can be effected not only by the shape and size of the antenna's coupling area, but the relative magnitudes of the current distributed across that area. To understand the relationship between antenna size and beam width, it is necessary to make the relative magnitude irrelevant by making it uniform across the coupling area.

Many antennas radiate electromagnetic energy by sending a current down a wire or across a metal strip. However, the current takes time to travel down the wire or strip. If the current is an alternating current, the current is not uniformly distributed in terms of phase, resulting in differing amplitudes. Aperture antennas, however, are capable of providing a uniform phase and amplitude distribution and can be made with a coupling area of any shape or size.

An aperture antenna, as its name implies, can be understood as a hole in a sheet of conducting material. Plane waves arrive along an orientation normal to the surface of that plate. As the plane waves encounter the sheet, the waves are either diffracted as they pass through the aperture or are converted into surface currents on the sheet.

The antenna system, as developed in the previous section, expects a current distribution as its input. Although an aperture antenna has no current distribution across the aperture that makes up the coupling area of the antenna, a constructive current distribution can be impressed within the aperture. The impressed current is the equivalent current capable of generating the uniform electromagnetic fields that appear on either side of the aperture.

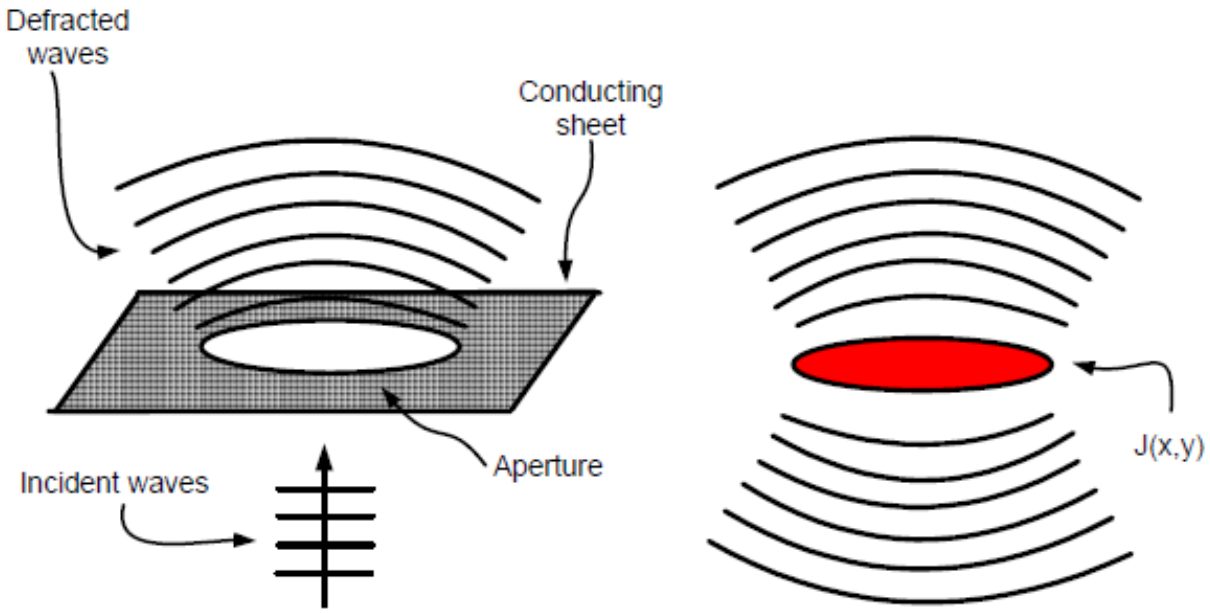

Figure 4.13: Aperture diffraction.

The current can be derived by the continuity boundary condition on the magnetic field, as required by Maxwell's equations:

$$\vec{J}(x,y) = \hat{z} \times \{\vec{H}(z=0^+) - \vec{H}(z=0^-)\}, \tag{4.24}$$

leading to:

$$\vec{J}(x,y) = -\hat{x}\{\frac{E_o(x,y)}{\eta_o} + \frac{E_o(x,y)}{\eta_o}\}, \tag{4.25}$$

leading to:

$$\vec{J}(x,y) = -\hat{x}\frac{2E_o(x,y)}{\eta_o}. \tag{4.26}$$

An illustrative example of incident waves, aperture, conducting sheet, diffracted waves, and impressed current $J(x,y)$ is provided in Fig. 4.13.

The preceding derivation ignores the influence of any surface currents on the conducting sheet. A horn antenna provides an example of an aperture antenna for which these surface

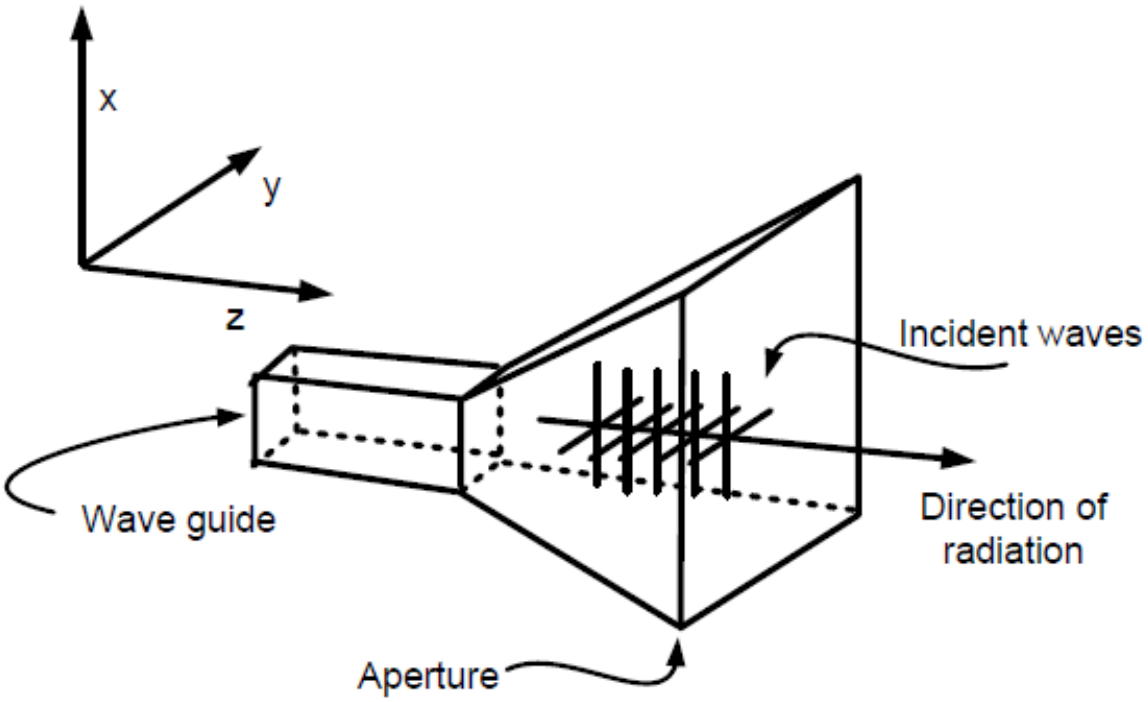

Figure 4.14: Uniform distribution across the aperture of a horn antenna.

currents can be ignored. In a horn antenna, the plane waves incident upon the aperture are provided by a waveguide that is tapered into a horn shape at its far end. The aperture is described by the perimeter of the mouth of the horn without any surrounding conducting material. Figure 4.14 depicts a horn antenna on a coordinate system providing definition of the plane of the aperture and the direction of electromagnetic radiation. As indicated in Fig. 4.14, the waveguide delivers incident waves of uniform amplitude and phase to the aperture. The uniformity of the phase distribution is important to the synthetic aperture radar systems discussed below, which cannot be created without accurate phase information.

Inverse Relationship Between Antenna Size and Beam Width

With the spatial impulse response of the system, simplifying far-field approximations, the output coordinate system expressed in terms of azimuth and elevation angles, and uniform illumination, the conceptual foundation is in place for an intuitive explanation of the inverse relationship between antenna size and beam width. To demonstrate this inverse relationship, a sinusoidal current is applied across a square area, with a uniform amplitude, producing a two dimensional rect function in terms of the amplitude. This two-dimensional rect constitutes the current distribution, which is convolved with the Green's function below.

$$\vec{A}_{ff}(\vec{r}) = -\hat{x}\frac{\mu}{4\pi}\frac{e^{-jkr}}{r}\int\int \frac{2E_o(x',y')}{\eta_o}e^{-j(k_x x'+k_y y')}\,dx'dy'. \tag{4.27}$$

From the way in which the magnetic vector potential is derived, the electric field in the far field can be found from the magnetic vector by,

$$\vec{E}_{ff} = j\omega\hat{r}\times(\hat{r}\times\vec{A}_{ff}) = \Upsilon(r,\vec{\theta},\phi)F(\theta,\phi), \tag{4.28}$$

where $\Upsilon(r,\vec{\theta},\phi)$ is a term that takes care of terms unrelated to the beam pattern and $F(\theta,\phi)$ describes the pattern of the electric field. The cross products of Eq. 4.28 and the scaling factor in Eq. 4.27 can be peeled off:

$$\Upsilon(r,\vec{\theta},\phi) = -\hat{r}\times\hat{r}\times\hat{x}\frac{\mu}{4\pi}\frac{e^{-jkr}}{r}, \tag{4.29}$$

so that

$$F(\theta,\phi) = \int_{a/2}^{a/2}\int_{b/2}^{b/2}\frac{2E_o(x',y')}{\eta_o}e^{-j(k_x x'+k_y y')}\,dx'\,dy', \tag{4.30}$$

where a is the length of the aperture with respect to the x axis, b is the length of the aperture with respect to the y axis, and the function $F(\theta,\phi)$ is known as the beam pattern and determines the beam widths with respect to azimuth and elevation.

Since the incident electric field $E_o(x', y')$ takes a value of one at all locations on the aperture, the terms in the beam pattern equation can be rearranged to take the form:

$$F(\theta, \phi) = \int_{a/2}^{a/2} \frac{2E_o(y')}{\eta_o} e^{-jk_x x'} \, dy' \int_{b/2}^{b/2} \frac{2E_o(x')}{\eta_o} e^{-jk_y y'} \, dx'. \tag{4.31}$$

Equation 4.31 is recognizable as having the same form as a Fourier Transform for each dimension of the two-dimensional surface of the coupling area of the antenna. As discussed above in Section 4.2.4, the Fourier transform of a rect function is a sinc function. Whereas, in Section 4.2.4, the rect function describes the input in the frequency domain, the rect function for the antenna system describes the input current distribution in the spatial domain of the antenna's coupling area. Similarly, whereas, in Section 4.2.4, the sinc function describes the output in the time domain, the sinc function for the antenna system describes the output in the beam width domain of the antenna's azimuth and elevation beam patterns.

As in Section 4.2.4, the larger the rect function, the higher and the more narrow the sinc function. Therefore, the greater the length of the antenna in one dimension, the more narrow the beam width corresponding to that dimension. This inverse relationship is depicted below in Fig. 4.15 for a square antenna coupling area of two different sizes, each with uniform current distributions.

Returning to the equation for beam pattern and performing the transforms provides the result:

$$F(\theta, \phi) = \frac{2}{\eta_o} [\frac{\sin \frac{\pi a}{\lambda} \sin\theta \cos\phi}{\frac{\pi a}{\lambda} \sin\theta \cos\phi}][\frac{\sin \frac{\pi b}{\lambda} \sin\theta \sin\phi}{\frac{\pi b}{\lambda} \sin\theta \sin\phi}], \tag{4.32}$$

where the $sin\theta \cos\phi$ and $sin\theta \sin\phi$ terms fall out from Eqs. 4.21 and 4.22. Focusing on elevation angle and setting azimuth to zero, an equation for the beam width can be derived. Noting that a sinc function has a magnitude of zero when its argument is an integer,

$$\frac{\sin \frac{\pi a}{\lambda} \sin\theta}{\frac{\pi a}{\lambda} \sin\theta} = 0, \tag{4.33}$$

when

$$\frac{\pi a}{\lambda} \sin\theta = 1. \tag{4.34}$$

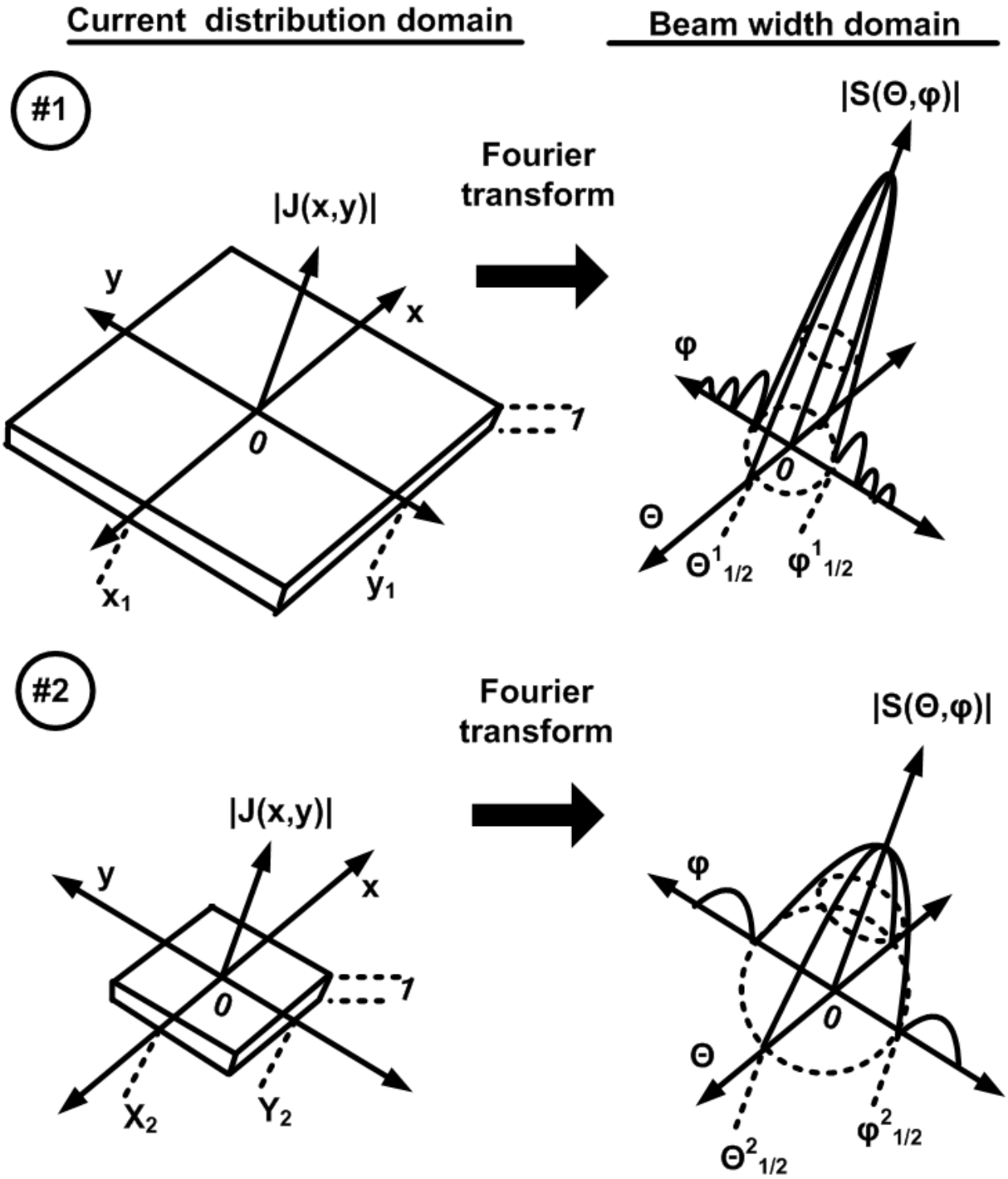

Figure 4.15: Inverse relationship between aperture dimensions and beam widths.

Therefore, discounting the factor of π with the factor of 2 necessary to provide the entire beam width Θ_{null}:

$$\Theta_{null} = \arcsin \frac{\lambda}{a} \tag{4.35}$$

which by the small angle approximation, assuming $\lambda/a << 1$, can be approximated as:

$$\Theta_{null} \simeq \frac{\lambda}{a}. \tag{4.36}$$

4.3 Synthetic Aperture Radar

The dependence of resolution upon beam width (Eqs. 4.7 and 4.8) and the inverse relationship between beam width and antenna size (Eq. 4.36) require impractically large antenna sizes. For example, to obtain 10 cm resolution in azimuth and elevation at a frequency of 15 GHz and a range of 300 m, Eqs. 4.7, 4.8 and 4.36 require an antenna of 60 m by 60 m. Not only would the construction of such a large antenna be cost prohibitive, but the deployment and the scanning of such an antenna over avalanche terrain are impractical.

A practical solution to the problem for the required resolution entails synthesizing a large antenna aperture from a smaller antenna. A radar system relying on a synthesized antenna aperture is known as a Synthetic Aperture Radar (SAR) system. Figure 4.16 depicts a small antenna occupying several different positions over time. As explained below, information received from these different positions allows a SAR system to achieve much smaller resolutions than those predicted by Eqs. 4.7, 4.8 and 4.36 for the small antenna aperture from which a synthetic aperture is created.

A non-coherent RBGM system ignores different phases associated with backscatter traveling different paths back to the system antenna. Hence, backscatter sums constructively and destructively in a non-coherent fashion. Conversely, a coherent SAR system harnesses phases associated with echoes traveling different paths to variously located antenna positions, such as those depicted in Fig. 4.17, to synthesize a large aperture from a small antenna.

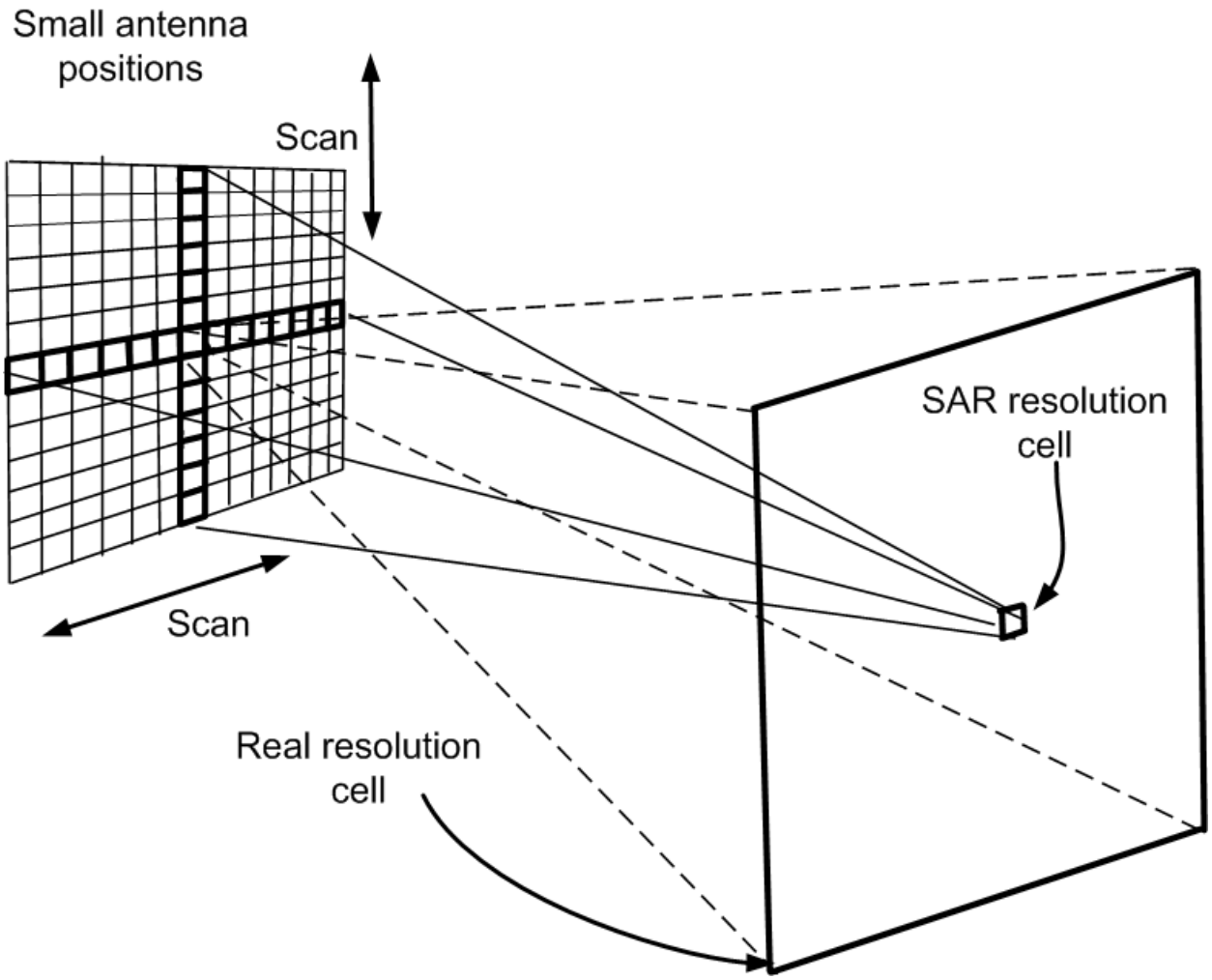

Figure 4.16: Footprints for a real and a synthetic aperture created from a single small antenna.

4.3.1 Focusing Metaphor

As discussed in [38], such a synthetically-derived aperture can be viewed as the lens of a camera. Just as the aperture of a camera focuses the light received by the camera from a subject at a particular location, the synthetic aperture of a SAR system focuses on a scatter at a particular location by accounting for the proper delay time for each constitutive antenna position so that the backscatter from that scatterer can come into phase. The scatterer comes into focus as the backscatter from the scatterer in question adds coherently. Backscatter from locations on which the system is not focused are sum destructively, causing the response from the focused location to come to the fore.

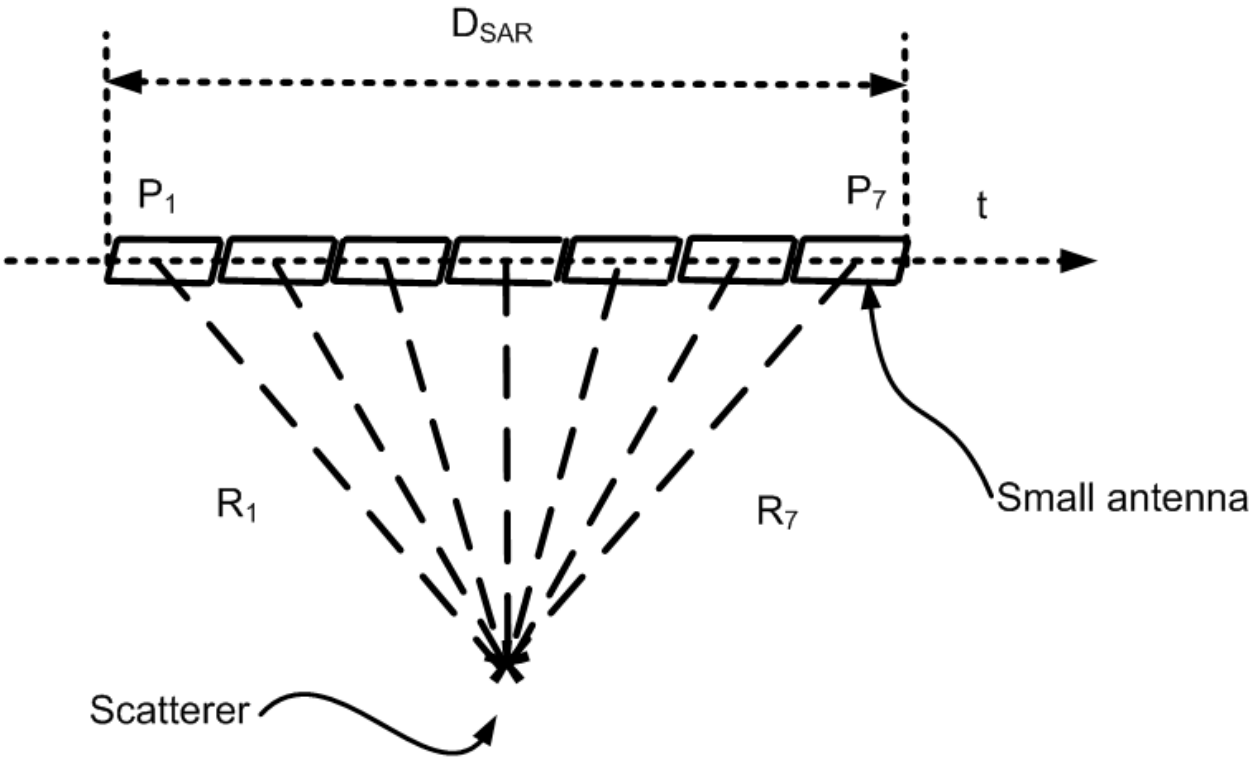

Figure 4.17: Differing ranges to a single scatterer from different antenna positions.

Intuition into the manner in which a synthetic aperture is created by coherently focusing upon particular locations in a field of view is aided by an example of a radar system that only records real data. Such a system, as depicted in Fig. 4.18, relies on an array of antennas that transmit and receive at the same time and a summer that sums the returns from the antennas. Each antenna in the array is identical to the others and is equally spaced from adjacent antennas. However, the cabling lengths between the antennas in the array and the summer differ.

The cable lengths are adjusted to re-phase the backscatter from the various antennas. Cables corresponding to antennas closer to the scatterer (those in the middle of the array) are longer to allow the phase to progress to the phase reached at antennas farther from the scatterer. For this reason, the cables depicted in Fig. 4.18 are less and less doubled back on themselves for antennas at the edges of the array.

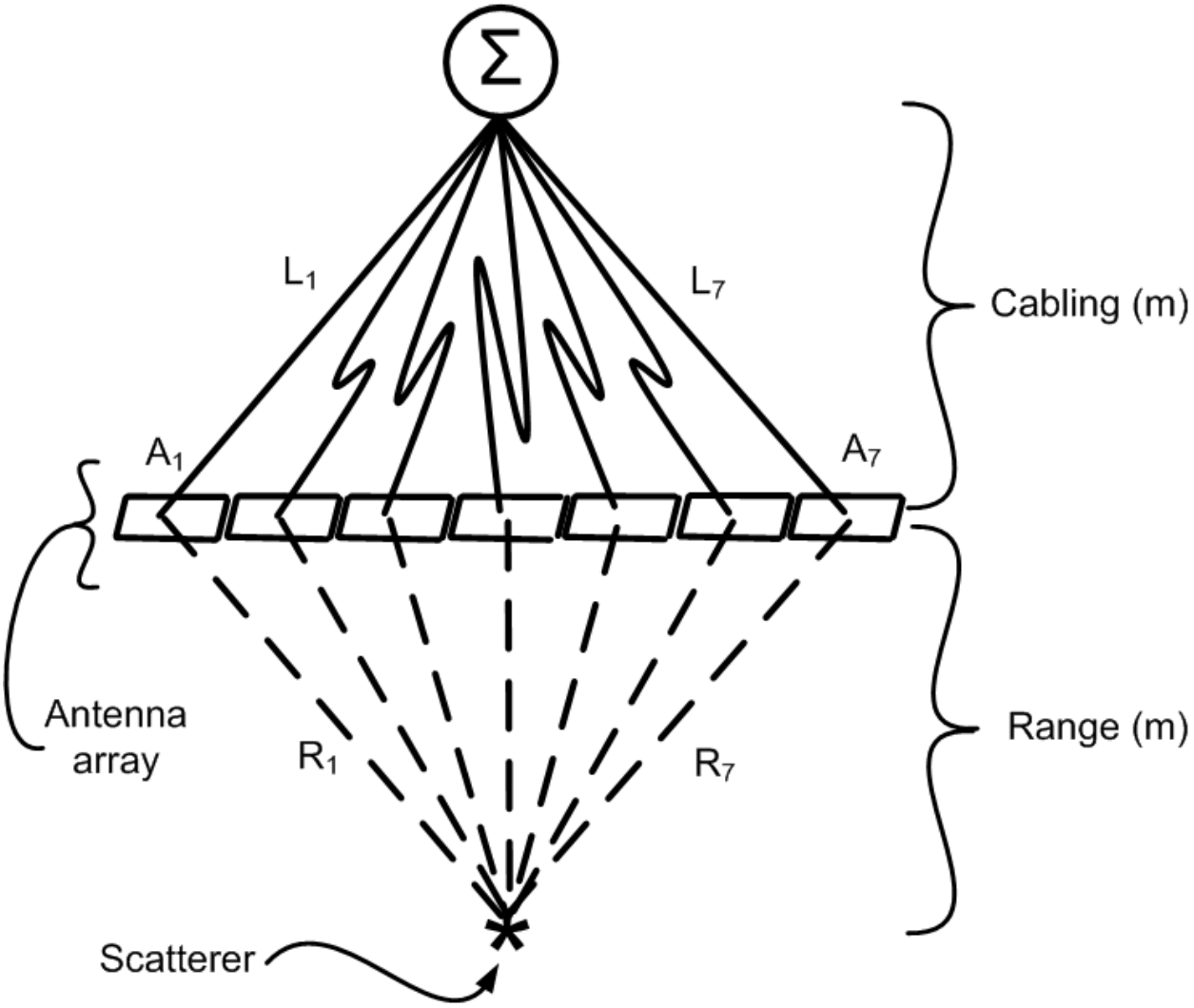

Figure 4.18: The focusing of an array on a particular scatterer location. (Adapted from [38], Fig. 9.1.)

The illustration becomes even more clear by making a false assumption, for the sake of argument, that the phase velocity in the cabling is the same as it is in free space. Under this assumption, re-phasing occurs when the sum of the distance to the scatterer and the distance of the cable associated with each antenna are equal, as expressed by the equation:

$$L_1 + R_1 = L_2 + R_2 = L_3 + R_3 = L_4 + R_4 = L_5 + R_5 = L_6 + R_6 = L_7 + R_7. \qquad (4.37)$$

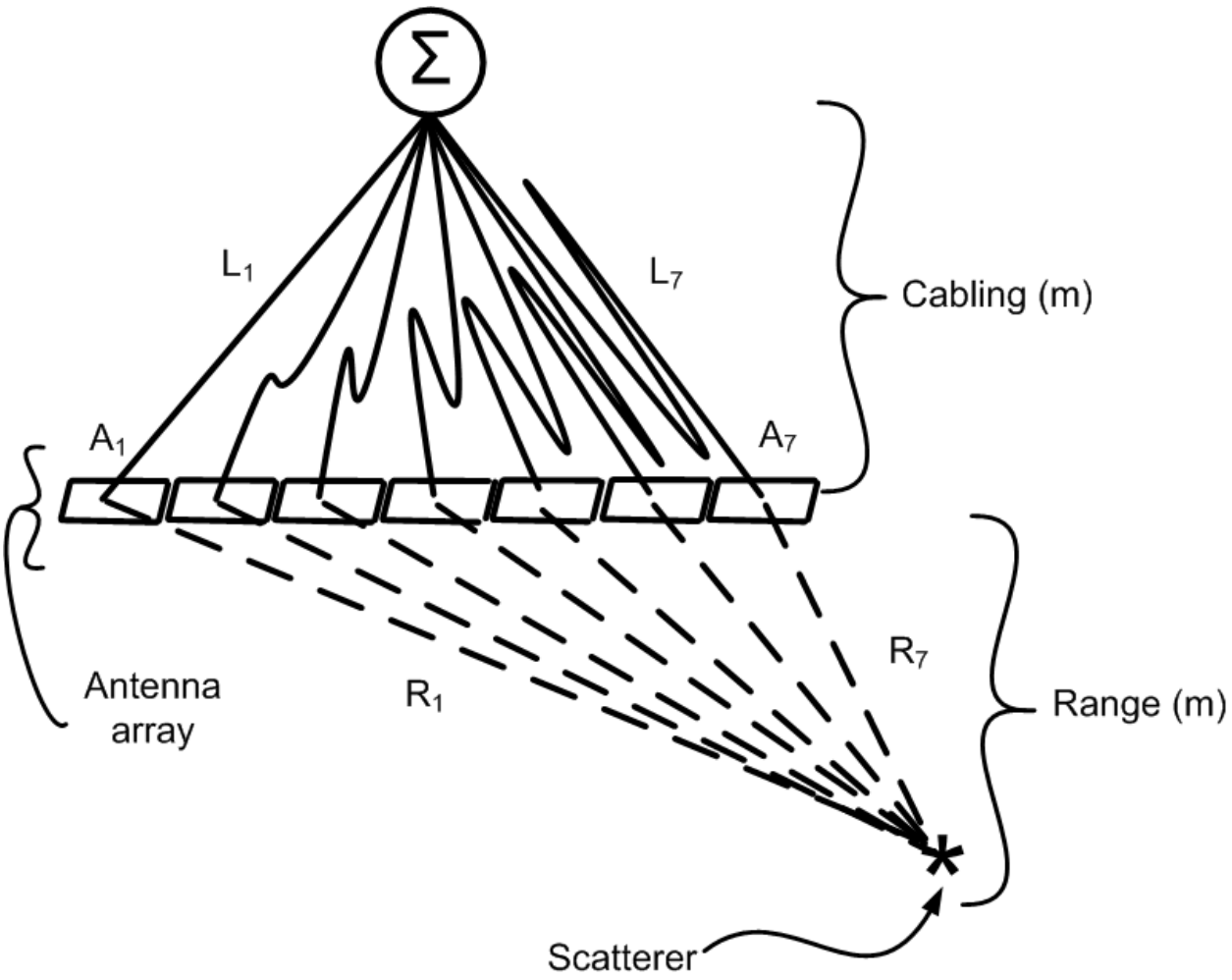

Figure 4.19: The focusing of an array on a scatterer offset to the side.

Therefore, the backscatter from the location at which the array is focused sums constructively and comes to the fore.

By changing the cable lengths, the antenna array can focus on a different location, as depicted in Fig. 4.19. In Fig. 4.19, the antennas to the right are closer to the target. Therefore, the cables attached to the antennas on the right are longer to allow the phase to progress to the point it reaches for the antennas on the left, over the long distances traveled by the backscatter to these antennas.

The same focusing ability of the real antenna array depicted in Fig. 4.18 and Fig. 4.19 can be created synthetically with a single antenna that occupies the same positions at dif-

ferent times. This synthetic approach is depicted in Fig. 4.20 in terms of a data capturing step (upper half of Fig. 4.20) and a data processing step (lower half of Fig. 4.20). The data capturing step involves positioning a single antenna at different positions at different times. At each time-specific position, the antenna captures backscatter from a common scatterer with different phase, arising from differing distances between the antenna and the scatterer. A voltage amplitude, induced by the backscatter, with an amplitude and phase, is recorded at each temporally-indexed, antenna position.

The data processing step involves shifting the phase of each of the time-indexed measurements of voltage amplitude and phase in memory. This phase shift is accomplished by multiplying each measurement by the appropriate phase. In traveling to and from the scatterer to each antenna position, a phase shift of $2kR_i$ accumulates, where k denotes the wave number and i denotes the time-indexed antenna position. Therefore, the appropriate phase by which to multiply each measurement is the conjugate of the same phase accumulated for the position corresponding to that measurement, as depicted in the lower half of Fig. 4.20.

Once multiplication by the measurement-specific phases brings the phases of each measurement in sync, the measurements are added by the summer. In this way, the backscatter from the scatterer at the location of interest adds constructively and comes to the fore. The synthetic array can be re-focused to an alternative location of interest, as in Fig. 4.19, by multiplying by the conjugate of the phases that would accrue for each antenna position over for this new location of interest.

Therefore, by accounting for the phase to each antenna position for backscatter from a location of interest, an aperture focused on the location of interest can be synthetically stitched together from time-indexed positions of a moving antenna. The resultant synthetic aperture can be steered electronically by changing the phases by which each time-indexed, antenna-position measurement is multiplied, in a manner analogous to the way in which an array of antennas can electronically steer a beam pattern. The real and synthetic arrays depicted in the previous figures are all deployed along a single axis to create an aperture of length D_{SAR}, as depicted in Fig. 4.17. However, the same principles that allow for the synthetic creation of an aperture in a first dimension allow for the creation of an aperture in two dimensions.

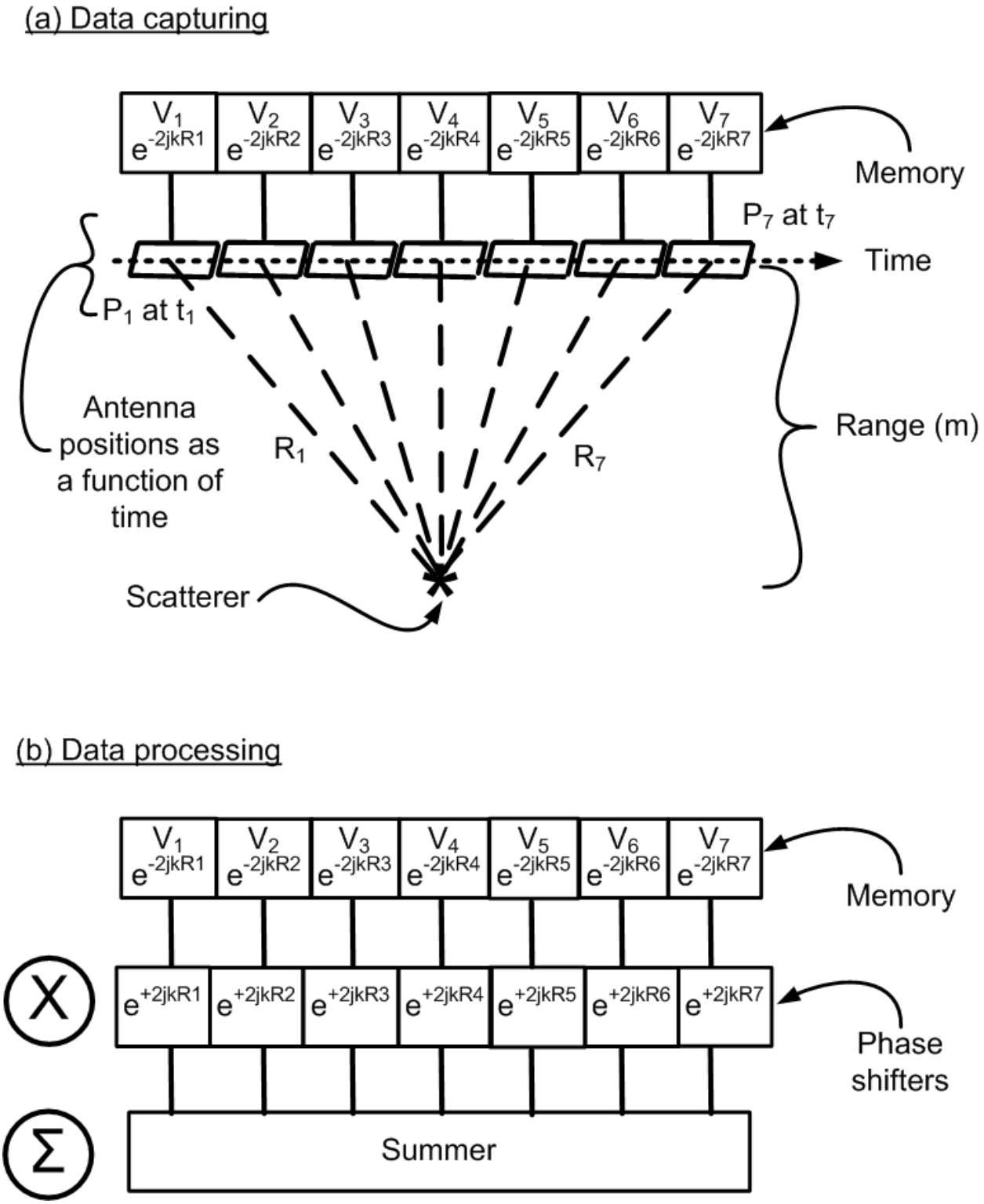

Figure 4.20: Capturing of backscatter by a synthetically created array (aperture) and processing of that backscatter to focus on a particular scatterer. (Adapted from [38], Fig. 9.1.)

4.3.2 Phase Progression as a Carrier of Information Determining Backscatter Location

A SAR system uses phase information not only to synthetically stitch together a larger aperture, allowing for improved resolution, but also uses phase information to determine the location, with respect to an axis along which the antenna is deployed, of the resolved backscatter. As the antenna progresses along the length of the synthetic aperture, the slant range R_s (the distance from an antenna position to a scatterer) varies with the position of the antenna, causing phase to change according to the formula:

$$\phi = 2kR_{si}, \tag{4.38}$$

where i indexes an antenna position.

For a predetermined range along the direction normal to the synthetic aperture, backscatter travels different slant ranges to the different antenna positions. According to Eq. 4.38, different phase shifts result that can be used to determine the location from which the backscatter originates. However, phase shifts between antenna positions can be ambiguous as they cannot be used to determine location where the different slant ranges vary by more than a quarter of a wavelength—a phase shift of π radians. To determine the location of backscatter along the axis of the aperture for larger distances, information about the progression of phase is required.

As discussed, the different slant ranges from each antenna position result in a different phase corresponding to each position. Regardless of the time taken to move the small antenna from one location to another, the antenna positions in a synthetic aperture can be indexed to times that would be required to achieve each position if the small antenna were to move at a uniform rate. By indexing antenna positions to these times, the phases corresponding to these positions can also be indexed, and a time dependent function of phase $\phi(t)$ can be created.

The phase function $\phi(t)$, as indicated by Eq. 4.38, is a function of slant range R_s. When slant range R_s, which is a function of antenna position, is also related to the same time index created by the assumption of uniform motion, the resultant time-dependent function

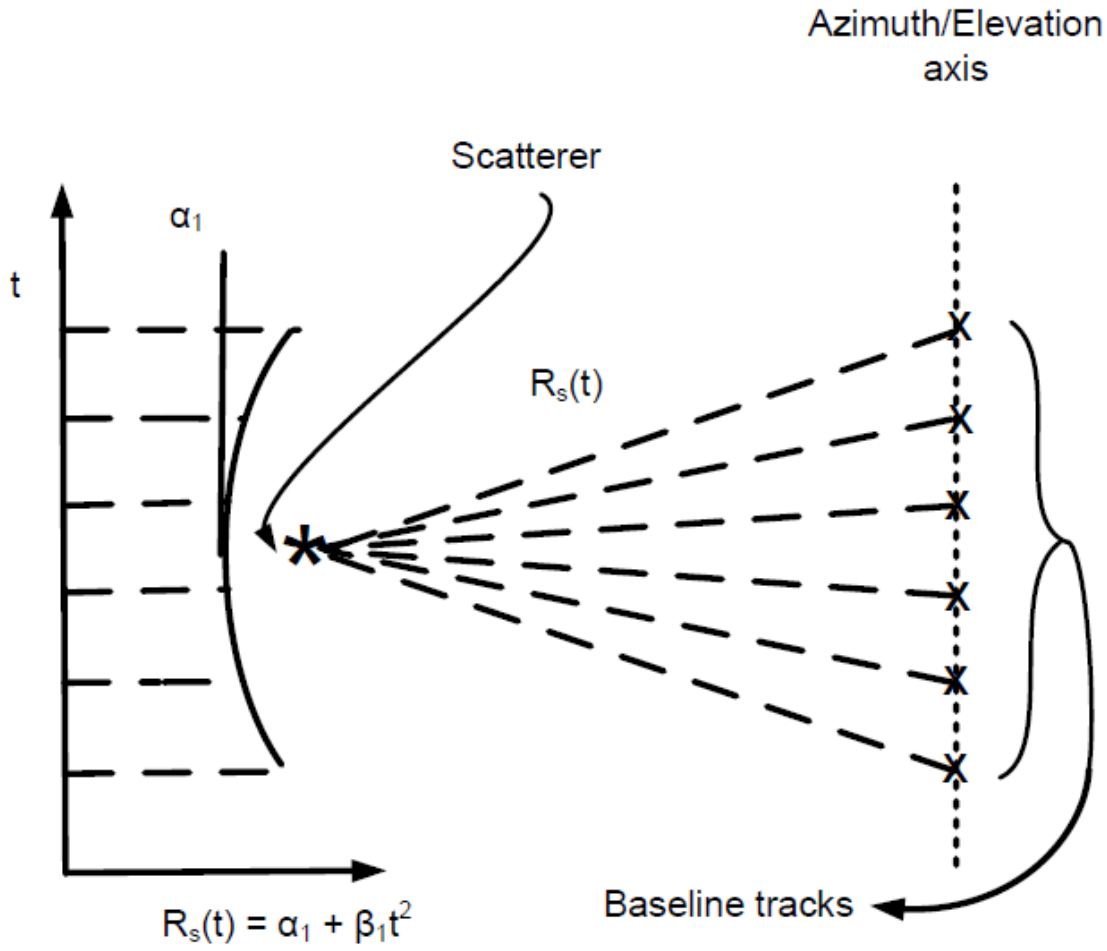

Figure 4.21: Schematic depiction of the variation of slant-range R_s with respect to an axis (azimuth or elevation) orthogonal to the range axis. These slant ranges R_s correspond to discrete time samples.

is a parabola:

$$R_s(t) = \alpha + \beta t^2, \tag{4.39}$$

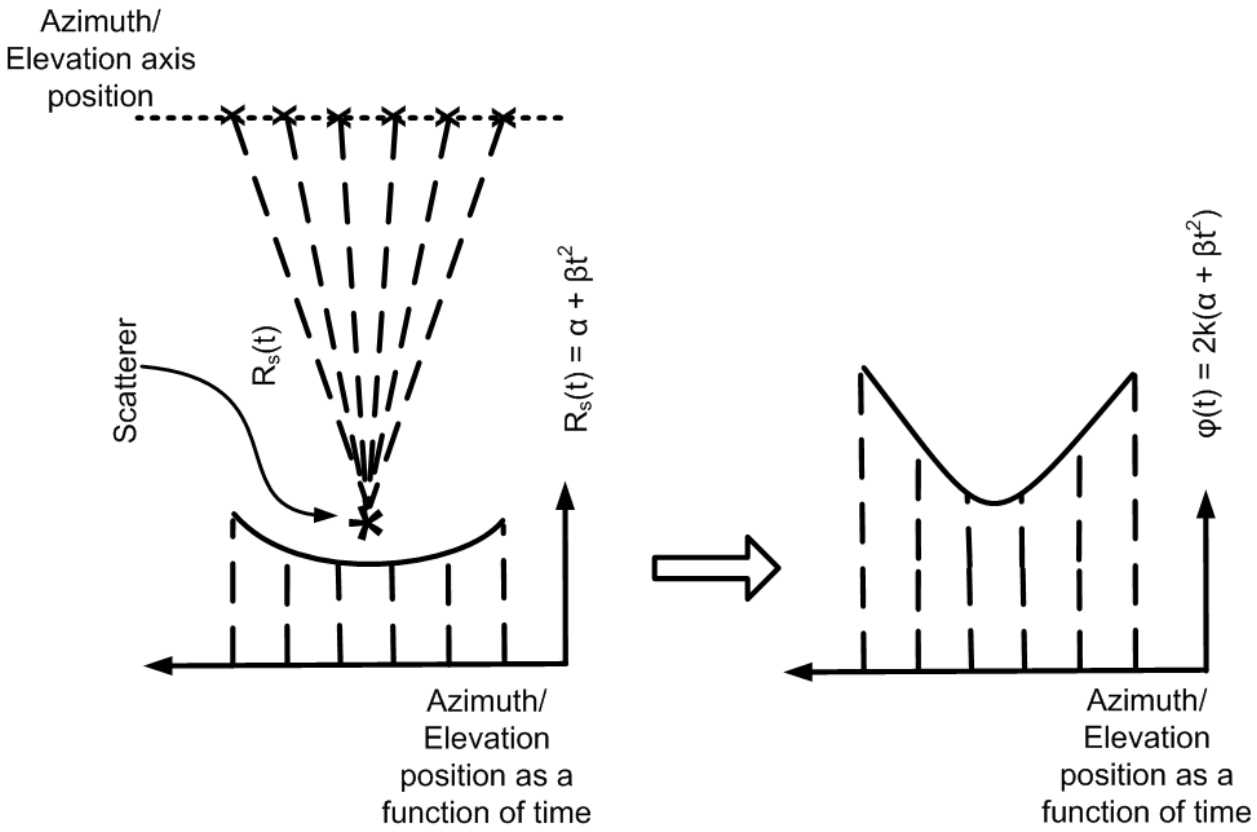

Figure 4.22: Changing slant range R_s and phase progression $\phi(t)$ as a function of position/time, resulting in parabolic and more hyperbolic shapes respectively.

where α is the range to the scatterer along the axis normal to the synthetic aperture from its center and β describes the concavity of the parabolic shape. Figure 4.21 depicts discreetly sampled slant ranges describing a parabolic shape as a function of time.

The function that describes phase progression $\phi(t)$, therefore, is:

$$\phi(t) = 2kR_s(t) = 2k(\alpha_1 + \beta t^2). \tag{4.40}$$

The additional factor of $2k$ results in more of a hyperbolic than a parabolic shape. The parabolic shape of slant range R_s and the hyperbolic shape of the phase progression $\phi(t)$, which are both functions of position-dependent time, are compared in Fig. 4.22.

The farther a scatterer is from being centered with respect to the synthetic aperture, the more the slant range changes as a function of antenna position/time and, therefore, the

more the phase changes. The increasing rate of change in slant range, which drives the rate of change in phase progression, can be seen by comparing Fig. 4.21 and Fig. 4.23. In Fig. 4.23, the scatterer is offset to one side. The more the scatterer is offset to the side of a particular antenna position, the larger the component of the slant range R_s from the antenna position that traverses the distance along the axis defined by the synthetic aperture. The greater the component of the slant range R_s traversing this axis, the greater the slant range R_s. Therefore, the position of the antenna along the axis of the synthetic aperture plays a larger role in determining the slant range R_s.

The increasing rate of change in slant range as a function of antenna-position/time can be seen in the slope of the parabolic shape of the function describing slant range. For a scatterer centered in front of the synthetic aperture, at a great distance from the synthetic aperture, the change in slant range between antenna positions is very small. Therefore, the slope of the parabola is very small between these time-dependent antenna positions. For a scatterer closer to and distinctively offset to one side of the synthetic aperture, as in Fig. 4.23, the slopes between time-dependent, antenna positions on the parabolic fit are larger, corresponding to the steeper walls on either side of the parabola, as shown in Fig. 4.23.

Since the rate of phase progression $\phi(t)$, as shown by Eq. 4.40, depends on the rate of change in slant range $R_s(t)$, the rate of phase progression increases the more offset a scatterer is from center. The rate of phase progression, for a particular range, therefore, determines the location of a scatterer along the axis defined by the synthetic aperture, whether azimuth or elevation.

The rate of phase progression is simply the slope of the function describing phase $\phi(t)$, which can be found by taking the time derivative of this function. As discussed in Section 4.2.1, the derivative with respect to time of the phase function is the instantaneous angular frequency $w(t)$,

$$w(t) = \frac{d}{dt}\phi(t) = 4k\beta t. \tag{4.41}$$

So the instantaneous frequency is $f(t)$:

$$f(t) = \frac{w(t)}{2\pi} = (\frac{4k\beta}{2\pi})t = (\frac{4\beta}{\lambda})t. \tag{4.42}$$

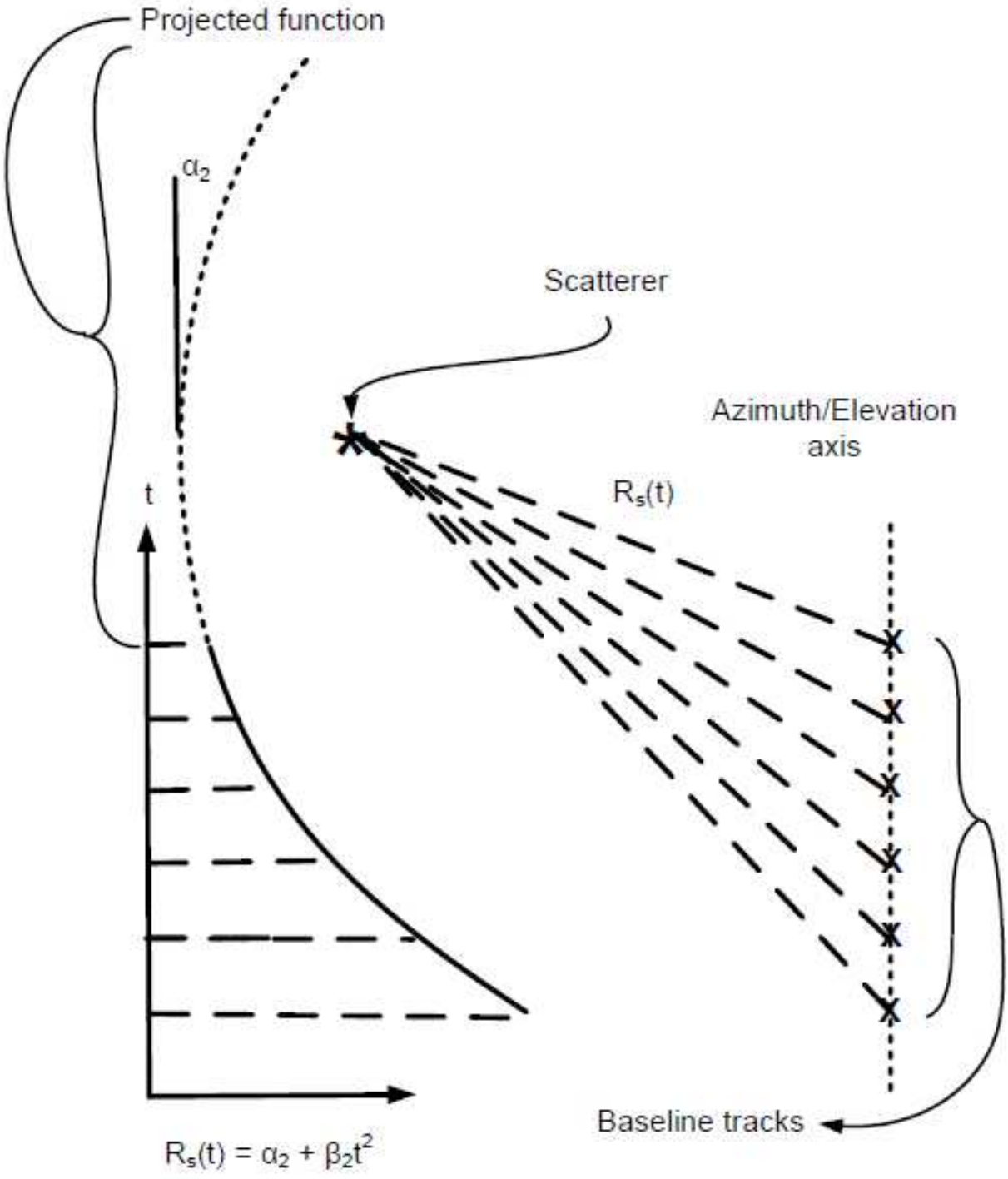

Figure 4.23: Schematic depiction of the variation of slant-range R_s length with respect to an axis orthogonal to the azimuth and cross-track axes. These slant ranges correspond to discrete time samples for a scatterer offset to one side.

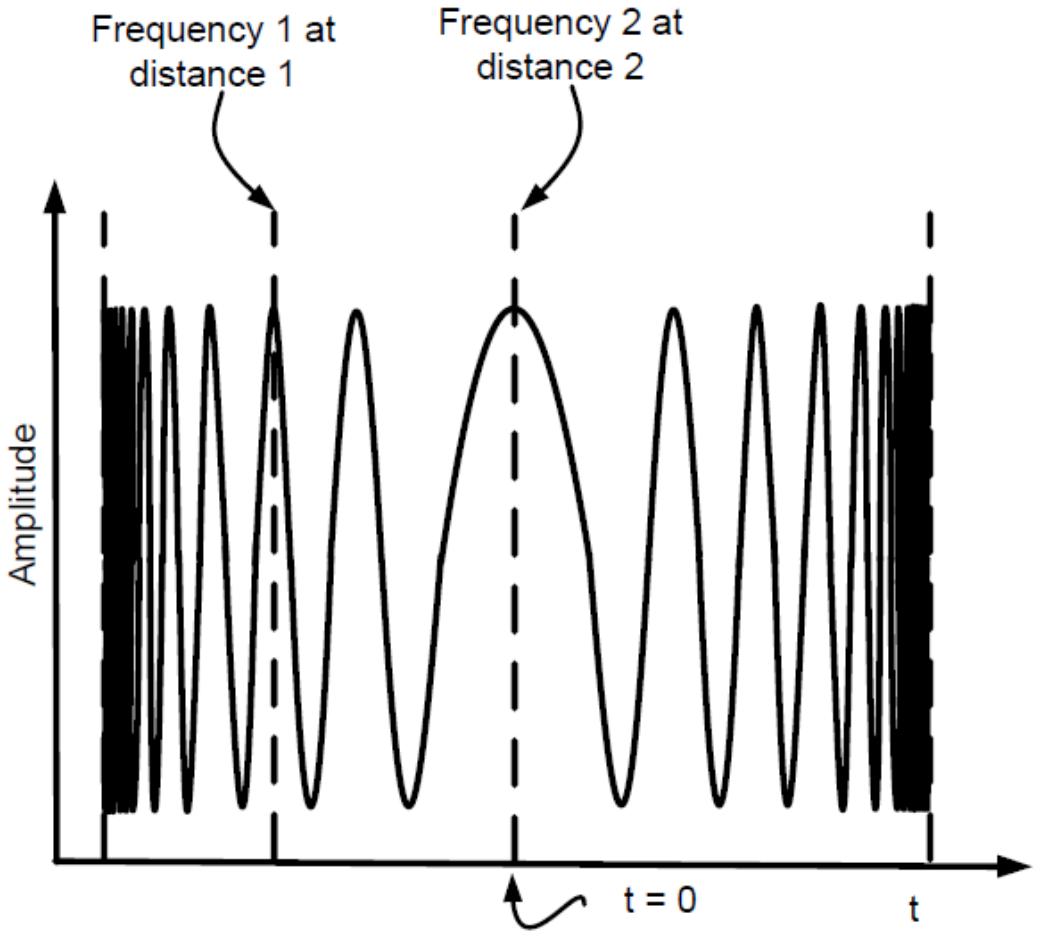

Figure 4.24: Linear chirp created by differing slant ranges.

Equations 4.41 and 4.42 describe a linear change in frequency with respect to time, or a chirp, as shown below in Fig. 4.24. As discussed in the section on range resolution, instantaneous frequencies within a chirp can also be indexed to location. Each frequency, or phase progression rate, corresponds to a different distance relative to the center of the synthetic aperture. The higher the frequency, the greater the distance.

As discussed, an FM radar embeds a frequency chirp in the transmit signal, from which range distances normal to a synthetic aperture are determined. By deploying a small antenna to create a synthetic aperture in a direction orthogonal to the range direction, a

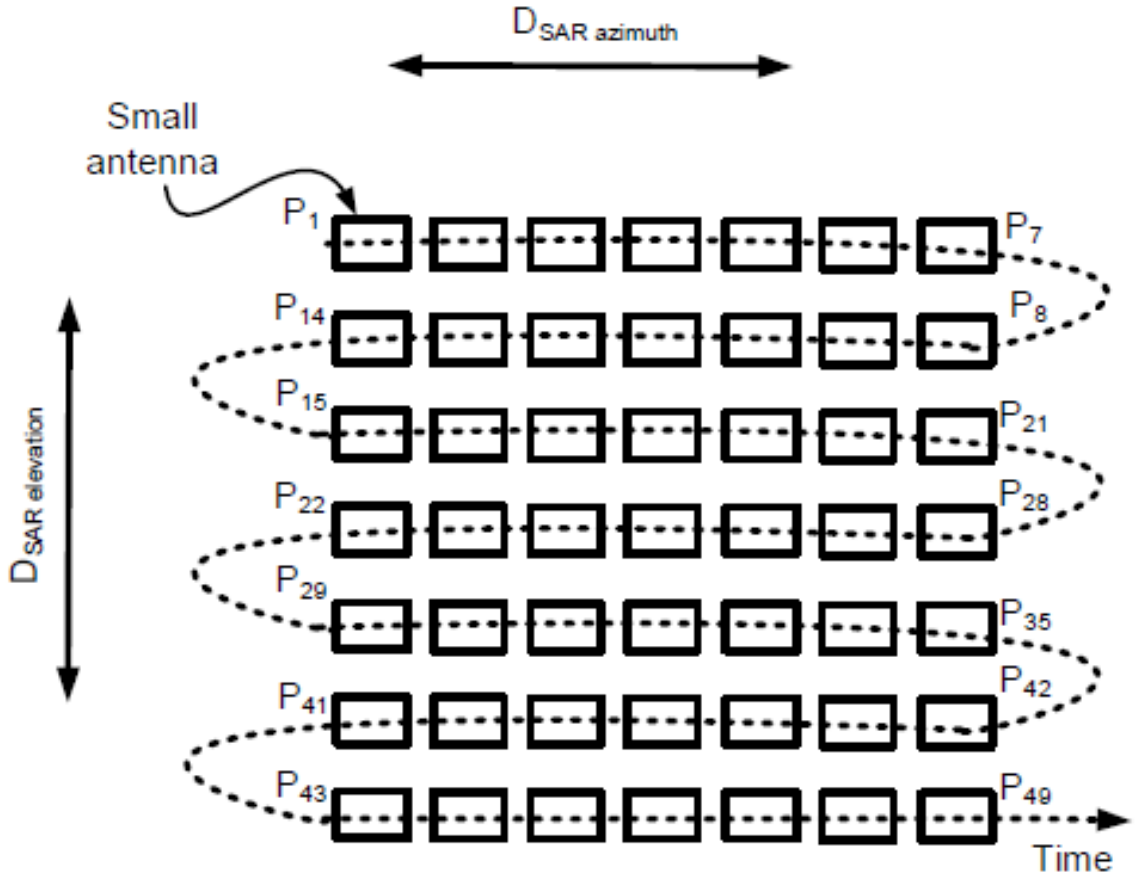

Figure 4.25: Two-dimensional synthetic aperture created by a grid of positions occupied over time by a small antenna.

second chirp is created for the azimuth direction. By deploying the same antenna in a second direction orthogonal to the first two—so that the antenna occupies the points in a two-dimensional grid similar to that depicted in Fig. 4.25—a third chirp may be created for elevation.

In other words, for each position in the azimuth direction, the antenna occupies a series of positions in the elevation direction to create a chirp in the same way as the azimuth chirp is created. These three chirps correspond to three orthogonal axes, as shown

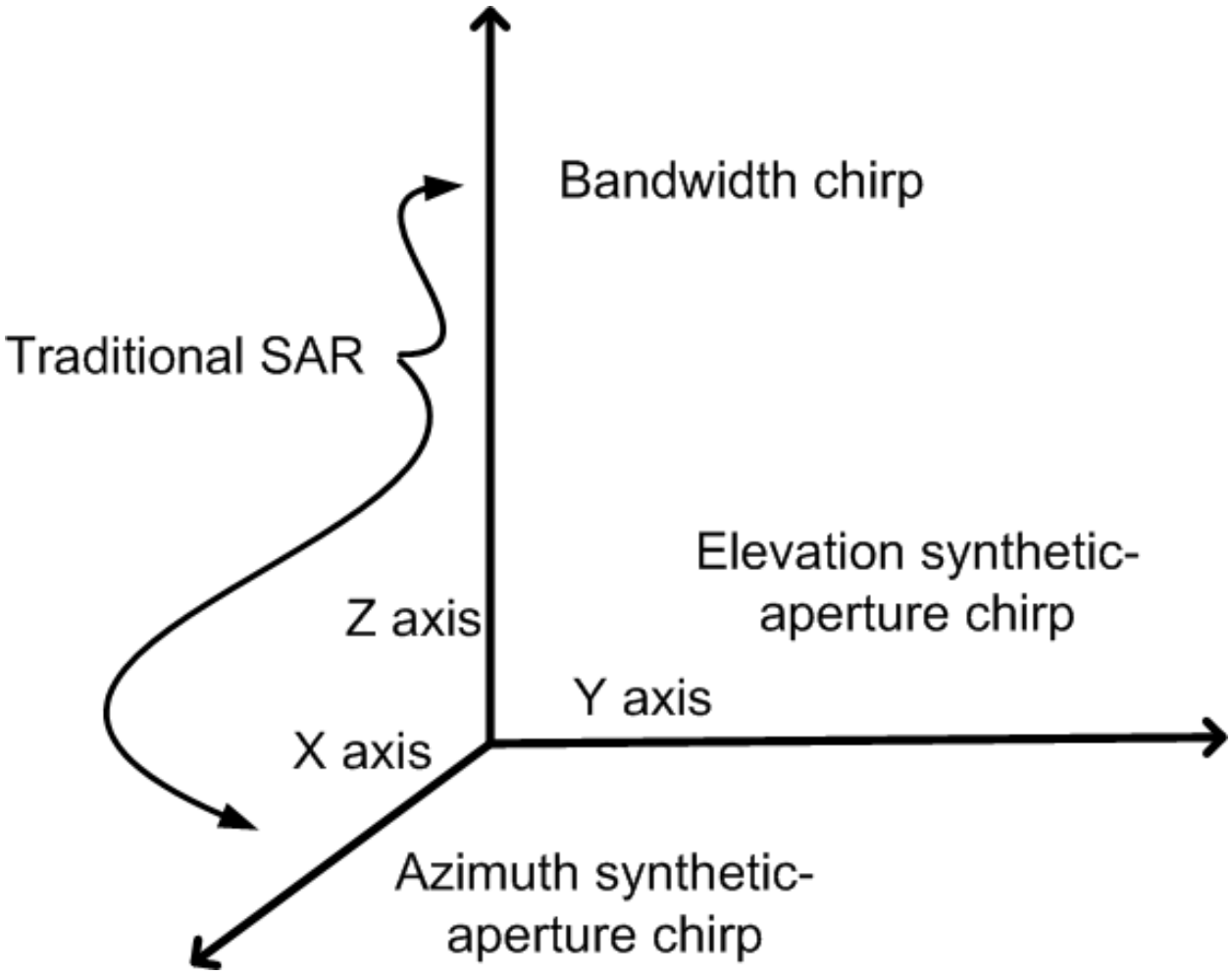

Figure 4.26: The three orthogonal chirps used to determine backscatter location in three dimensions.

in Fig. 4.26, allowing the location of backscatter to be pinpointed in three-dimensional space. In this way the backscatter from volumes can be mapped and imaged.

Need for a Ground-based Platform

Although the technology of using SAR radar systems to image volumes is not prevalent, it has been demonstrated for airplane-mounted antennas [58] [59] [60] [61]. For example, airplanes have been used as a platform to scan an antenna in grid patterns similar to the pattern in Fig. 4.25 to map the density of forest canopies [62]. However, motion problems rule out the use of airplanes as a platform for a two-dimensional, SAR system used to image a snowpack in three dimensions.

The creation of synthetic apertures requires knowledge of antenna position to within a fraction of a wavelength because SAR systems rely on phase information to stitch together the synthetic aperture and to determine the locations from which backscatter originates. The location of an antenna mounted on an airplane platform can only be determined to an accuracy measured in tens of centimeters to meters. However, the wavelengths corresponding to frequencies in X- and Ka- bands suggested in Chapter 3 range from 3.75 cm to 7.5 mm (See Table 3.1). Therefore, antenna location must be known to within about a millimeter of accuracy. A ground-based platform is much more suited to achieve this kind of accuracy.

4.3.3 Azimuth and Elevation Resolutions for a Synthetic Aperture

The small aperture of a small antenna can be stitched into an antenna that is large in two dimensions by a phase-informed focusing of time-indexed antenna positions. According to Eqs. 4.7, 4.8 and 4.36, the larger the aperture, the better the resolution in azimuth and elevation. These equations suggest that arbitrarily fine resolution can be achieved for azimuth and elevation by simply scanning a small antenna over a sufficiently-large, two-dimensional grid of positions.

Although it is correct that larger position grids increase resolution, resolution cannot be made arbitrarily fine. Additionally, these real-antenna-based equations are off by a factor of 2 in describing the resolutions achievable for a synthetic aperture, for reasons discussed below.

Small-antenna Dependent Limit on Resolution

Achievable resolution has a floor dictated by the ceiling that is set for the potential length D_{SAR} of the aperture in a given dimension. This ceiling on aperture length is inversely proportional to the beam width of the small antenna used to generate the synthetic aperture. Resolution is, in turn, as shown below, inversely proportional to the small antenna beam width.

Figure 4.27 depicts the inverse relationship between small antenna beam width and potential aperture length. In Fig. 4.27, the leading edge of the beam width of the small antenna in a first position coincides with the trailing edge of the small antenna in a second

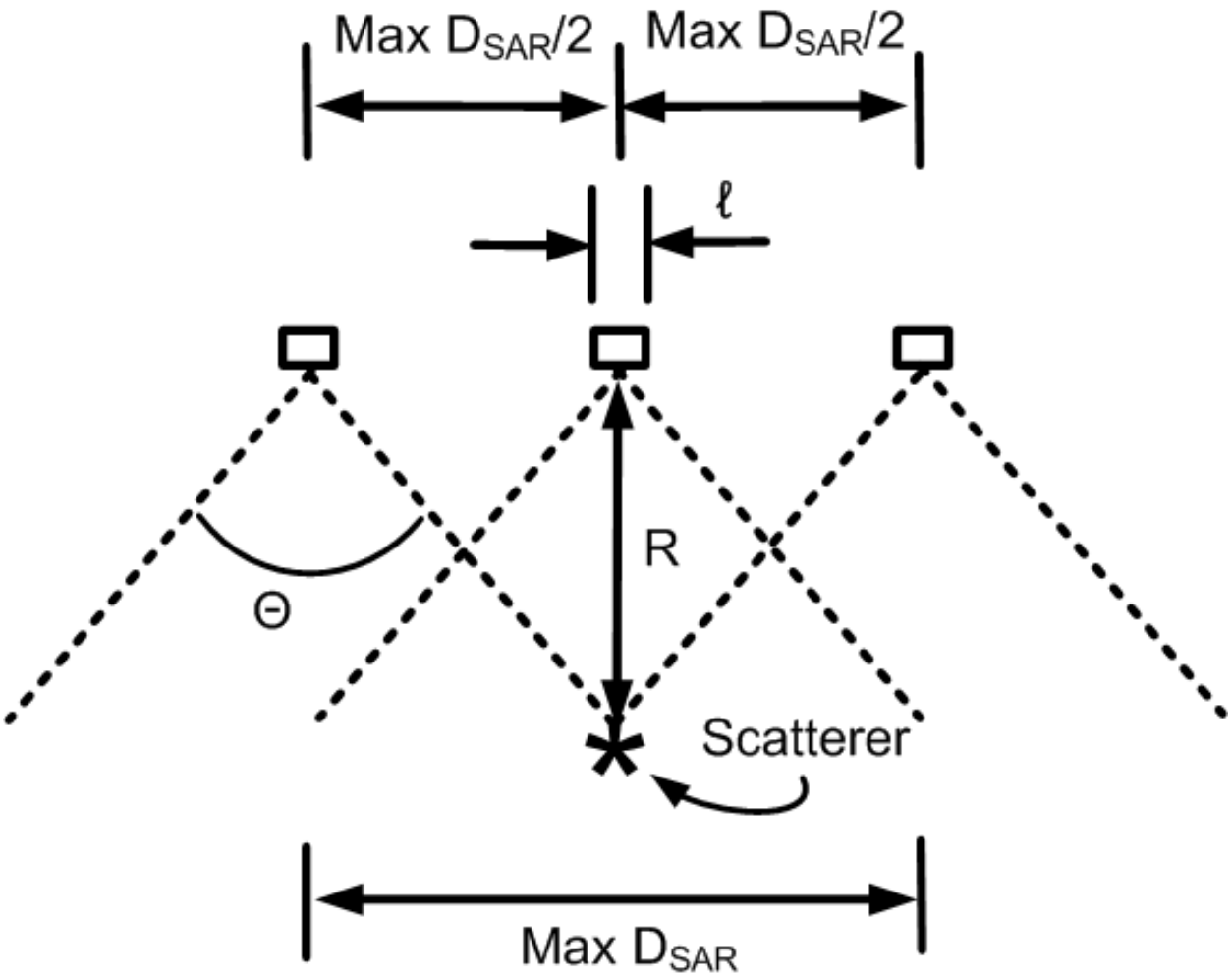

Figure 4.27: Limit on the length of a synthetic aperture imposed by the beam width of the small, constitutive antenna. (Adapted from [38], Fig. 9.7.)

position at a certain range. As appreciated, the maximum length of the synthetic aperture cannot exceed the distance between the two positions. In a scenario where the length of the synthetic aperture exceeded this limit, the beam from at least one position would not encompass the scatterer depicted in Fig. 4.27.

The maximum length of a synthetic aperture is equal to the distance between the two antennas. Otherwise, the beams from all the antenna positions would not encompass the scatterer. The beam from a third antenna position located equidistant from the first two spans the distance between the first two positions at the range in question. Therefore, the maximum dimension of the synthetic aperture depends on the span of the beam from the

small antenna at the range in question,

$$D_{SAR_{MAX}} = R\Theta. \tag{4.43}$$

Equations for Resolution as a Function of Synthetic Aperture Dimensions

For real antennas, footprint resolution is determined by the product of beam width and range (Eqs. 4.7 and 4.8). Equation 4.36 states that beam width for a given dimension is primarily the ratio of wavelength to the length of the aperture in that dimension. This relationship does not hold, however, for a synthetic aperture.

The beam width of an antenna, for a given dimension, results from differing phases associated with waves originating at different locations of an aperture. Differences in phase arise when the beam, or a portion thereof, describes an angle that is not normal to the antenna surface, resulting in different, position-dependent, travel distances for the waves, as shown for a synthetic aperture in Fig. 4.28. The contours of the beamwidth are defined when the differing phases add destructively at a certain angle, preventing the transmission and reception of power at that angle.

In Fig. 4.28, a portion of the beam describes an angle $\Theta_{1/2}$ from antenna positions 1 and 2. (These positions correspond to locations at the leading and trailing edges of an aperture.) Since the scatterer that reflects these beams is far off, the paths traveled from the two positions to the scatterer can be considered to be parallel. As the position on the right is closer to the scatterer, the distance to the scatterer from that position, i.e. R_7 is less than the distance to the scatterer from the position on the left R_1. A simple trigonometric calculation determines the difference in the distance traveled for the two positions $\Delta x sin\Theta_{1/2}$. For a real antenna, the differential phase can be determined from this differential distance:

$$\Delta\phi = k\Delta x sin\Theta_{1/2}. \tag{4.44}$$

When the differential phase equals π radians

$$k\Delta x sin\Theta_{1/2} = \pi, \tag{4.45}$$

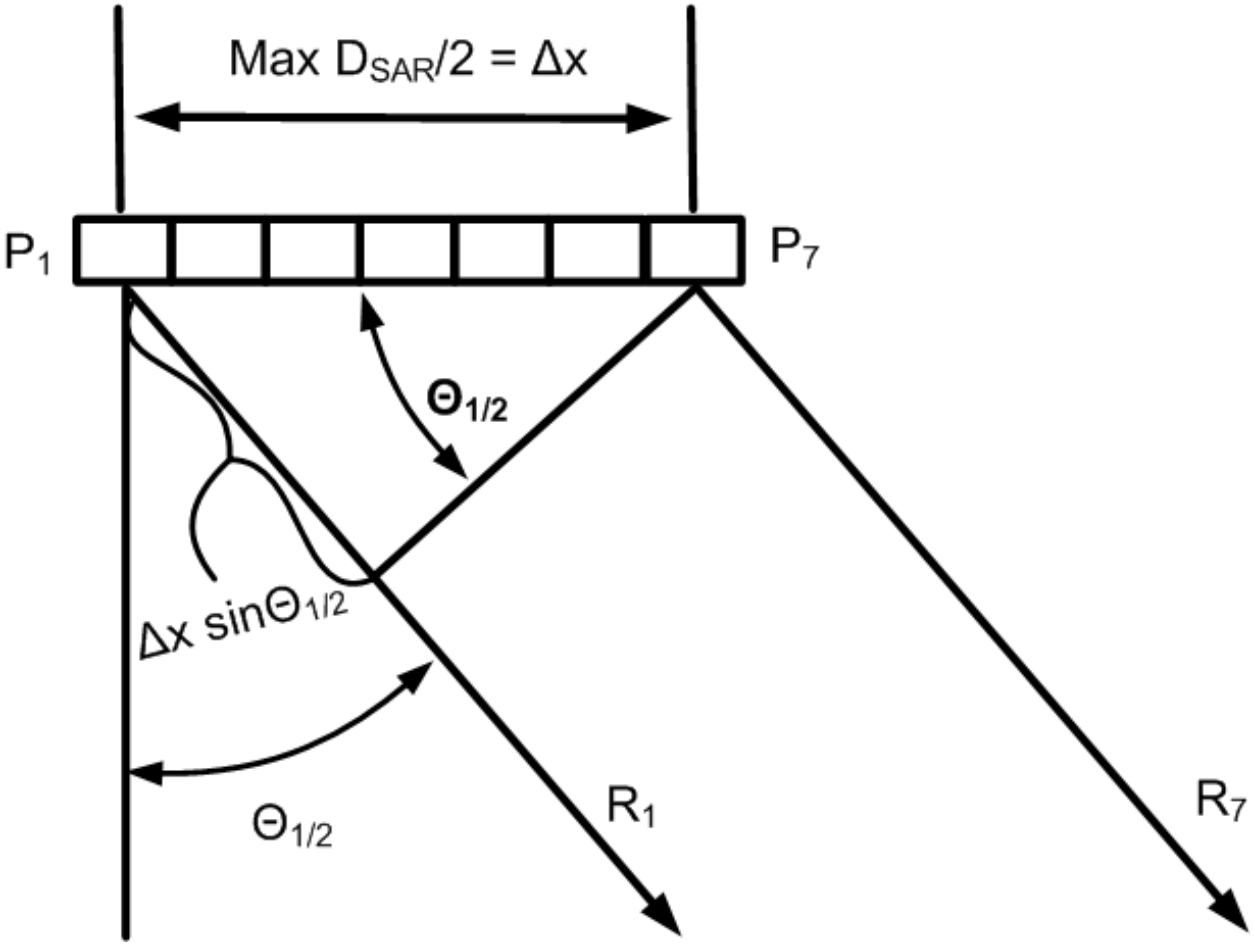

Figure 4.28: Phase shift between antenna positions. (Adapted from [38], Fig. 9.7.)

the beams from the two antenna positions cancel each other out, defining the limit of the beam width. Therefore,

$$\Theta_{1/2} = \arcsin \frac{\pi}{k\Delta x} = \arcsin \frac{\lambda}{2\Delta x}. \tag{4.46}$$

So the half beam width can be stated and approximated as:

$$\Theta_{1/2} = \arcsin \frac{\lambda}{2\Delta x} \simeq \frac{\lambda}{2\Delta x}, \tag{4.47}$$

and the full beam width can be approximated as:

$$\Theta \simeq \frac{\lambda}{\Delta x}. \tag{4.48}$$

The discrepancy between beam width equations for real and synthetic apertures arises because in a synthetic aperture, the difference in phase with respect to two locations of the aperture accrues not only in route to a scatterer, but along the return path as well. In a real antenna, only the phase accumulated during the trip to the scatterer is important because all locations across the aperture are available to receive backscatter. In a synthetic aperture, the antenna only exists at one location at a time. As a result, all backscatter must return along the same antenna-position-specific path that the original beam traveled to the scatterer. Therefore, the phase accumulation is double for a synthetic aperture, meaning the phase differential accumulates to π twice as quickly, or in half the length, with the result that at the beam-width limit:

$$2kD_{SAR}sin\Theta = \pi. \tag{4.49}$$

So the beam width becomes

$$\Theta = \arcsin\frac{\pi}{2kD_{SAR}} = \arcsin\frac{\lambda}{2D_{SAR}} \simeq \frac{\lambda}{2D_{SAR}}. \tag{4.50}$$

At this point, Eqs. 4.7 and 4.8 can be modified to provide the azimuth and elevation resolutions for a SAR radar system.

$$\Delta_{r_{az}} = \frac{R\lambda}{2D_{SAR_{az}}}, \tag{4.51}$$

$$\Delta_{r_{el}} = \frac{R\lambda}{2D_{SAR_{el}}}. \tag{4.52}$$

In the event that the synthetic aperture can be deployed to a sufficient length to achieve maximum resolution, Equation 4.43 can be substituted into Eqs. 4.49, 4.51, and 4.52, which in turn can be informed by Eq. 4.36 to provide a result for the absolute resolution achievable for a given small antenna dimension,

$$\Delta_{r_{MAX}} = \frac{\pi}{2kD_{SAR_{MAX}}} = \frac{R\lambda}{2D_{SAR_{MAX}}} = \frac{R\lambda}{2R\Theta} = \frac{\lambda}{2\Theta} = \frac{\lambda}{\frac{2\lambda}{l}} = \frac{l}{2}, \tag{4.53}$$

where l is the given small antenna dimension.

Table 4.1: Length of Each Dimension of a Synthetic Aperture as a Function of Range and Frequency.

Frequency (GHz)	Band	100 m	300 m	500 m	1000 m
15	Ku	10 m	30 m	50 m	100 m
22.25	K	6.74 m	20.2 m	33.71 m	67.43 m
33.75	Ka	4.4 m	13.3 m	22.2 m	44.4 m
40	Ka	3.75 m	11.25 m	18.75 m	37.5 m

As shown in Eq. 4.53, when the synthetic aperture can be deployed to a sufficient length, resolution is independent of range and is a function of only the dimension of the small antenna used to create the synthetic aperture along the axis being resolved. When the synthetic aperture cannot be deployed to a sufficient length to achieve maximum resolution, Eqs. 4.51 and 4.52 determine resolution.

To collect snowpack data over large areas, areas that would include the slopes on which avalanches form, data must be collected from ranges of a little under 100 m to 1000 m, on the very high end. According to Eqs. 4.51 and 4.52, these ranges play an important role in determining azimuth and elevation resolution. Frequency/wavelength also plays an important role, with higher frequencies improving resolution. Potential interactions with snow crystals, ability to penetrate snowpack, and implications for resolution suggest frequencies in the X-, Ku-, K-, and Ka- bands be employed. Table 4.1 provides the lengths of a side of a square synthetic aperture for which an antenna needs to be deployed for selected ranges between 100 m and 1000 m and selected frequencies from the K-bands.

4.3.4 Resolution, Bandwidth, and Angle of Integration

As discussed in Section 4.3.2, the location from which backscatter originates can be determined from chirps corresponding to three orthogonal axes. As discussed in Section 4.2.4, the degree to which backscatter can be resolved with respect to the range axis, the axis normal to the surface of the synthetic aperture, is a function of the bandwidth of the chirp in the transmission signal (see Eq. 4.6). Therefore, the achievable resolution with respect to the azimuth and elevation axes should also be a function of available bandwidth within the chirps corresponding to these axes. Mathematically, this expected result can be demonstrated.

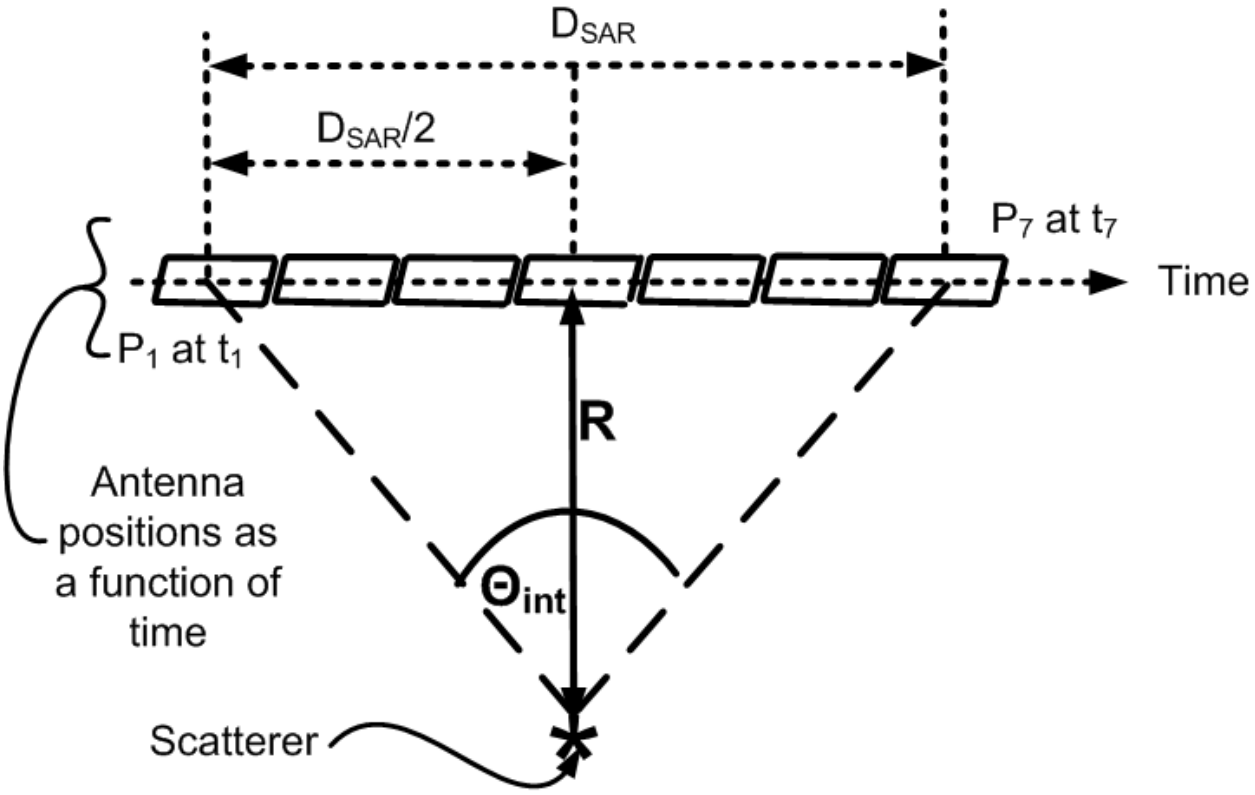

Figure 4.29: Depiction of the geometry of the angle of integration Θ_{int}

The distance between the center of the aperture and a scatterer D and the length of the aperture, D_{SAR}, determine the angles over which backscatter is received. The largest angle is known as the angle of integration, Θ_{int}, and is depicted in Fig. 4.29.

The angle of integration can be determined trigonometrically,

$$\Theta_{int_{1/2}} = \arctan \frac{\frac{D_{SAR}}{2}}{D}. \tag{4.54}$$

Rearranging either Eq. 4.51 or Eq. 4.52 in terms of Eq. 4.54 and using the small angle approximation provides a result that allows resolution to be expressed in terms of angle of integration Θ_{int} and the central frequency f_c,

$$\Delta_r = \frac{D\lambda}{2D_{SAR}} = \frac{c}{2f_c 2\tan\Theta_{int_{1/2}}} \simeq \frac{c}{2f_c\Theta_{int}}. \tag{4.55}$$

The product of the central frequency f_c and the angle of integration Θ_{int} approximates the bandwidth $B_{az/el}$ of the chirp generated by the different phases arising from the different slant ranges to the target. Therefore, resolution along the azimuth and elevation axes can be expressed as:

$$\Delta_r = \frac{c}{2B_{az/el}}. \tag{4.56}$$

As predicted, Eq. 4.56 has the same form as the equation used to determine range resolution (Eq. 4.6). Interestingly, the higher the central frequency and the shorter the wavelength, the better the resolution. This observation corresponds with intuition because at shorter wavelengths, phase changes more rapidly with differing slant ranges. Additionally, the larger the integration angle, the better the resolution. (For an alternative discussion see [54].)

4.3.5 Deployment Modes

To improve resolution, the bandwidth of the transmit signal and the size of integration angles should be maximized. Different approaches to deploying the constitutive antenna result in differing integration angles. Three common modes of deployment are referred to as the stripmap mode, the geometric mode, and the steered spotlight mode. These three modes are depicted in Fig. 4.30.

The stripmap mode deploys the constitutive antenna in a straight line. The circular mode circles the constitutive antenna around a target location, and the spotlight mode pivots the antenna around one location before moving to a next location. Although much larger angles of integration are achievable by the spotlight mode and especially by the circular mode, these methods are limited in the areas they cover. Scanning of large areas, such as those where avalanche issues are a concern, are best achieved with the stripmap mode, the mode for which resolution is explored in the preceding sections.

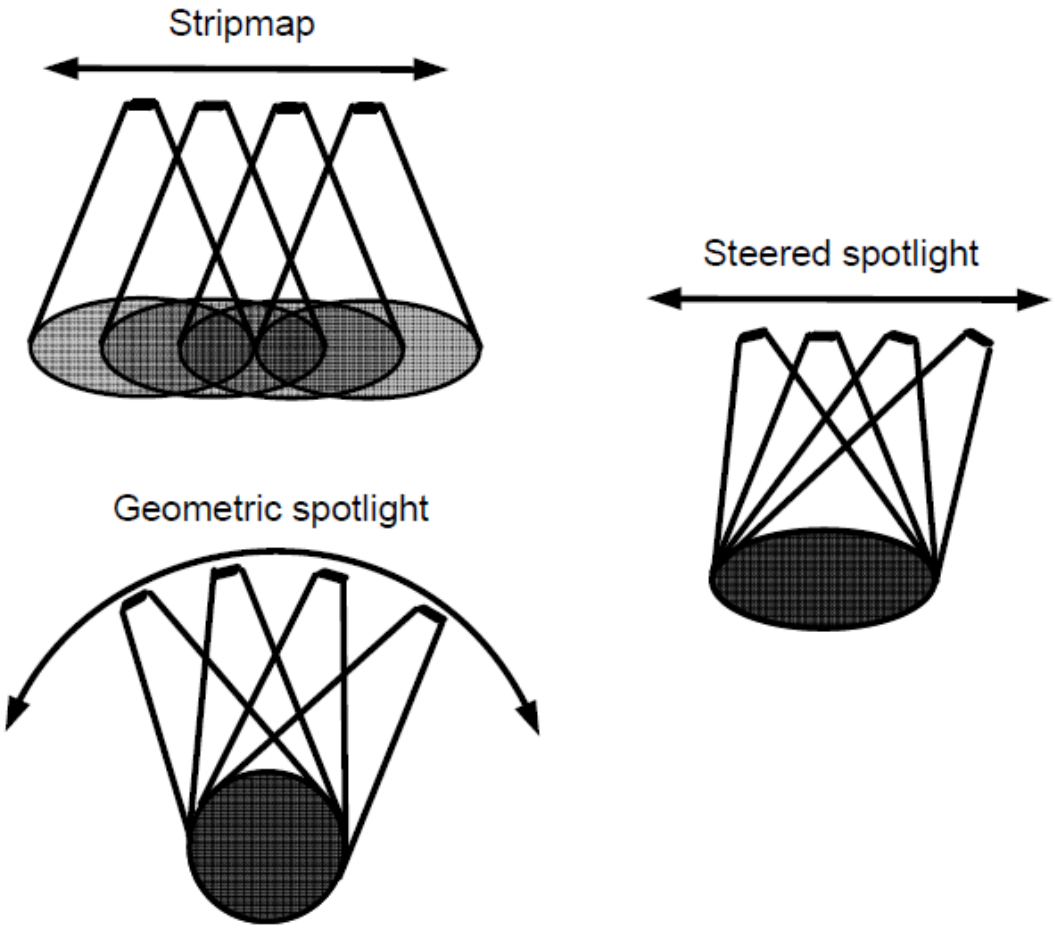

Figure 4.30: Three modes of deploying a synthetic aperture.

4.3.6 Sampling Requirements

A coherent radar system, such as a SAR system, relies on information about the progression of phase to determine the location of backscatter. To acquire information about phase progression, phase must be sampled at a sufficient rate such that phase measurements are unambiguous. In other words, sampling must occur with sufficient frequency that phase changes are less than π radians between samples.

Phase is simply the distance traveled to and from a scatterer divided by wavelength and multiplied by 2π radians. Change in phase, therefore, is simply a function of the change in slant range ΔR_s between adjacent antenna positions,

$$\Delta\phi = 2\pi\frac{2\Delta R_s}{\lambda}. \tag{4.57}$$

An equation for change in slant range can be written in terms of some consideration of a scatterer disposed at the leading edge of the beam width extending from a first antenna position. The scatterer, beam width, and antenna position are depicted on the left-hand side of Fig. 4.31. It is important to note that the scatterer is disposed at a great distance from the first antenna position, much greater than would appear from the left-hand side of Fig. 4.31, as indicated by the dotted lines.

On the right-hand side of Fig. 4.31, a second, advanced antenna position is depicted. Under the assumption that the scatterer is sufficiently far away, the lines described by the leading edges from beams from the two antennas can be considered in parallel one to another. Assuming that the two leading edges of the beam from the two antennas are parallel to each other, the change in slant range between the two positions can be determined by simple trigonometry.

As the antenna on the right-hand side of Fig. 4.31 progresses forward, it becomes closer to the scatterer, decreasing the slant range. The amount of the decrease is equal to the opposite side of the shaded, acute angle on the right-hand side of Fig. 4.31. The angle of the shaded, acute angle is half the beam width $\Theta_{1/2}$. The hypotenuse of the triangle is the distance between the two antenna positions d. Therefore, the change in slant range ΔR_s is a decrease equal to:

$$\Delta R_s = d\sin\Theta_{1/2}. \tag{4.58}$$

The need to keep phase changes to less than π, the equation for phase change (Eq. 4.57), and the equation for the change in slant range (Eq. 4.58) lead to the following intermediate result:

$$\pi = 2\pi\frac{2d\sin\Theta_{1/2}}{\lambda}. \tag{4.59}$$

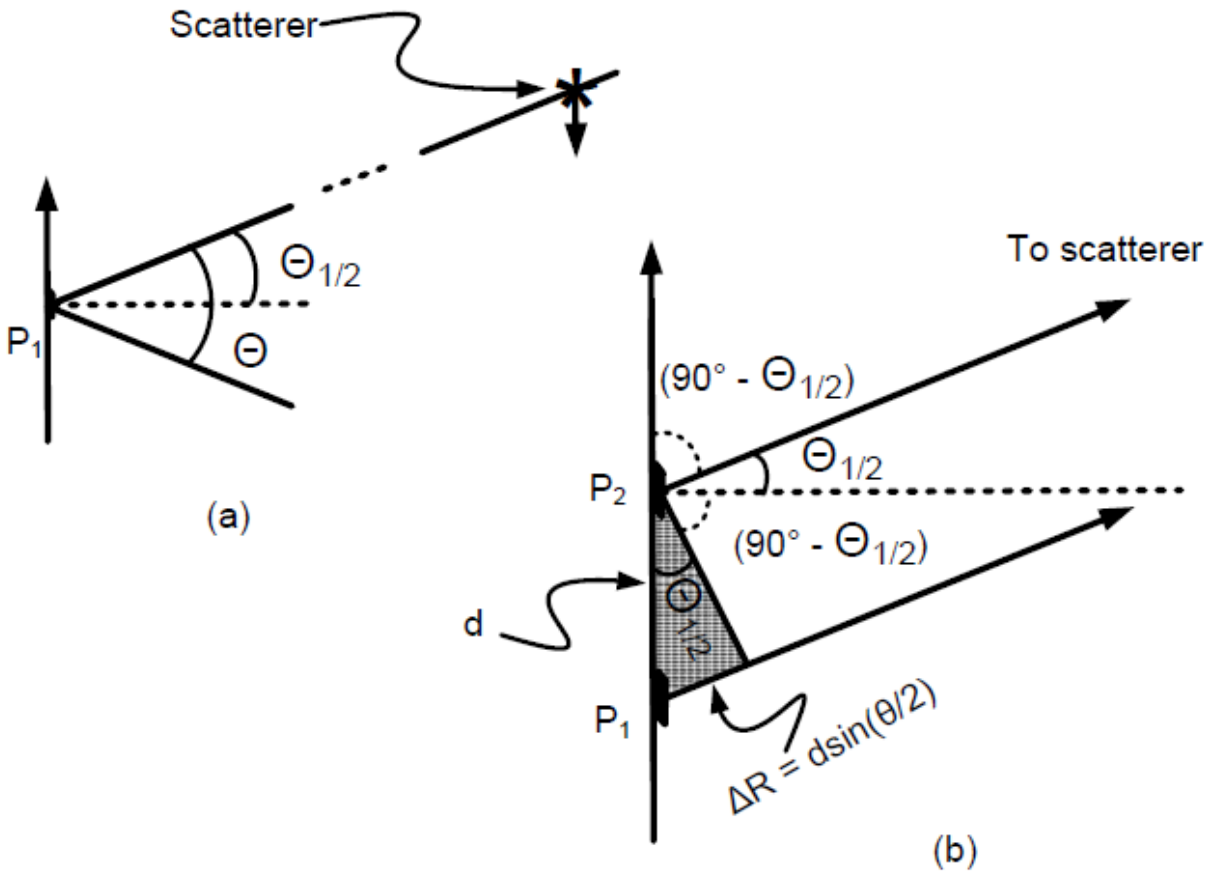

Figure 4.31: Change in slant range as illustrated for a scatterer starting at the edge of an antenna beam from a first antenna position and obtaining a new slant range after the antenna achieves a second position. (Adapted from [54], Fig. 21-10.)

The maximum distance allowable between samples to avoid ambiguous phase changes can now be solved for:

$$d = \frac{\lambda}{4 \sin \Theta_{1/2}}, \tag{4.60}$$

which by the small angle approximation becomes,

$$d = \frac{\lambda}{4\Theta_{1/2}}, \tag{4.61}$$

which, when modified by Eq 4.36, is approximated as:

$$d \simeq \frac{l}{4}. \tag{4.62}$$

Equation 4.62 can now be related back to resolution to provide an equation for the requisite sampling rate, in terms of distance between antenna positions, to achieve a certain resolution. From Eq. 4.51 or Eqs. 4.52, 4.54, and 4.36:

$$\Delta_r = \frac{R\lambda}{2D_{SAR}} = \frac{\lambda}{2\Theta_{1/2}} = \frac{l}{2}. \tag{4.63}$$

The sampling distance can then be determined by combining the result in Eq. 4.62 with the result in Eq. 4.63,

$$\Delta_r = 2d, \tag{4.64}$$

which is then solved for d.

$$d = \frac{\Delta_r}{2}, \tag{4.65}$$

which is the Nyquist requirement. Failure to sample at least as frequently as the distance prescribed in either Eq. 4.62 or Eq. 4.65 results in backscatter from one location aliasing to another location.

4.4 Processing

The previous sections discuss the collection of data over different frequencies, azimuth angles, and elevation angles. The different frequencies and angles produce different magnitudes and phases for the backscatter from the same volume of space. Without these changes in frequency and angle, only a single magnitude and phase would be present. These differing magnitudes and phases are responsible for the data that is captured by the radar. The data is indexed by antenna position and transmit frequency. Processing this data involves taking the different magnitude and phase information and reconstructing a map of the backscatter originating from different regions in the volume of space down range from the synthetic aperture.

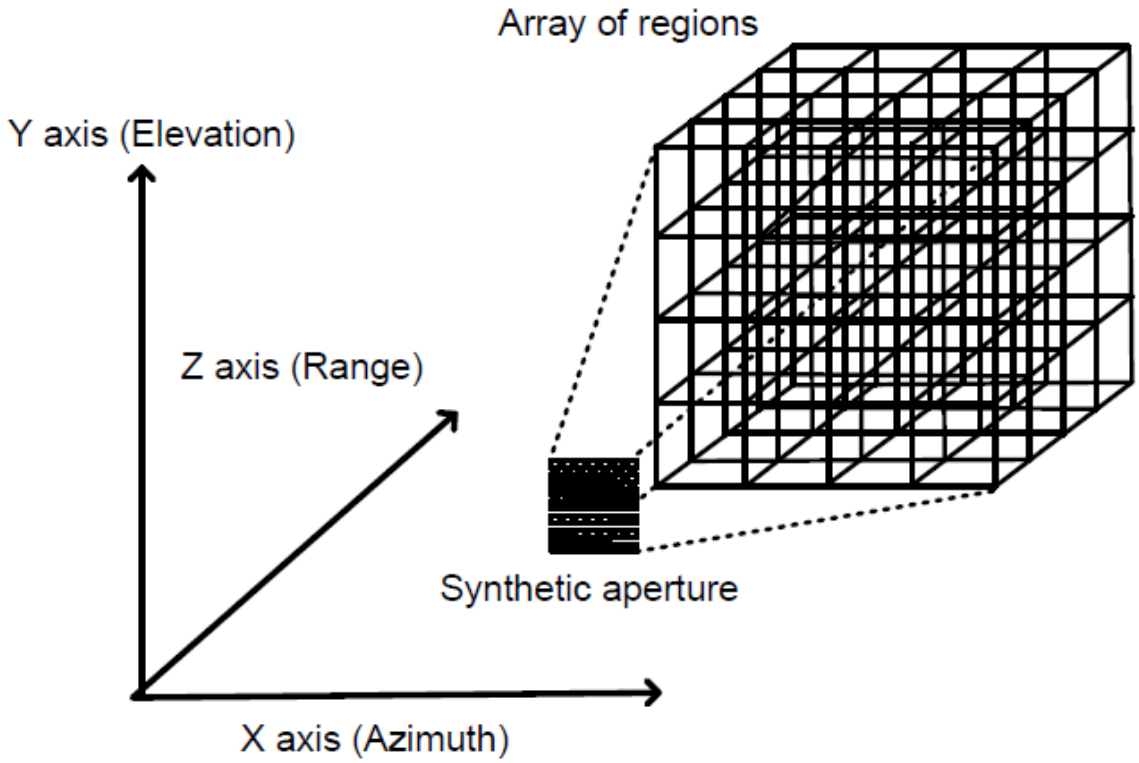

Figure 4.32: Three-dimensional coordinate system used to describe a synthetic aperture and regions from which backscatter originates.

The different regions from which backscatter can originate and the different antenna locations used to generate a three-dimensional SAR are defined by a three-dimensional coordinate system. A serviceable example of such a coordinate system is defined by assigning the azimuth and elevation directions respectively to the x and y axes of a traditional, three-dimensional Cartesian coordinate system. The z axis defines the direction described by a vector normal to the synthetic aperture.

Figure 4.32 depicts this coordinate system, with a synthetic aperture generated by an antenna deployed in azimuth and elevation. The figure also depicts an array of cubes representing various regions from which backscatter can originate. As appreciated, these

cubes closely resemble the array of imaging voxels depicted in Fig. 4.2. SAR processing uses the data collected from a set of regions from which backscatter can originate, similar to those depicted in Fig. 4.32 and assigns values to voxels similar to those depicted in Fig. 4.2. The goal of SAR data processing is to make the dimensions and locations of the array of regions and the dimensions and locations of the array of voxels to overlap on the same grid system, producing a three-dimensional map of complex reflectivity, or backscatter.

4.4.1 SAR data

SAR data provides the means to move from the physical world, the array of regions from which backscatter can originate in a volume, to the image of that volume. SAR data comprises measurements of the voltage induced by backscatter reflected from different regions. Each measurement is indexed to the position from which the underlying microwave energy is transmitted and received, making SAR data a function of position. Additionally, the measurements comprising SAR data are indexed to the time delays accompanying their reception, making SAR data a function of position and time delay. For a three-dimensional SAR, position is a function of azimuth and elevation, allowing the following function to be written to describe SAR data:

$$SAR_{data} \equiv d(x, y, t). \tag{4.66}$$

For a frequency modulated radar system, time delay coincides with frequency. For this reason, SAR data can be stored as a function of frequency. Understanding time delay as a function of frequency is particularly convenient when frequency in the transmit signal is modulated in discrete steps. These discrete steps manifest themselves in the return signal and provide a means for indexing the SAR data. As an example of how SAR data might be stored, a two-dimensional matrix might include a first dimension defined by position and a second by frequency. Additional possibilities for representing azimuth, elevation, time delay/frequency are possible.

Often it is difficult to capture phase information and store that information with the data. Instead of storing complex values with real and imaginary parts that carry magnitude and phase information, it is not uncommon for SAR data to be entirely real. The phase

information, however, remains latent in the real data and can be recovered by a Fourier-based method of transformation.

4.4.2 Point Spread Response (PSR)

The reflections from scatterers are recorded in the data for each antenna position. Moving from data to an image of those scatterers requires (1) the gathering up of energy corresponding to the various scatterers of the volume being imaged as received at various antenna locations and (2) determining the location of those scatterers from that energy. Various algorithms, tailored to different deployment modes for the antenna positions in the synthetic aperture, can achieve this goal. All of these algorithms must know where to look in the SAR data for the energy associated with each scatterer.

The Point Spread Response (PSR) for a particular antenna deployment mode provides the requisite information about where in the SAR data energy for a scatterer at a given location can be found. The PSR provides this information by assuming that isotropic point scatterers reside at any location of interest downrange from the synthetic aperture. Since the point scatterers are isotropic, as depicted in Fig. 4.33, the path from each position to any given scatterer is a straight line.

Assuming stripmap mode, the differing distances from antenna positions to a scatterer describe a parabolic shape when plotted as a function of position, as explained above in Section 4.3.2. Although SAR data is not indexed as a function of distance, it is indexed as a function of delay time, which is, in turn, a function of distance. However, when delay time, or time-of-flight, is plotted as a function of position, the parabolic shape becomes more hyperbolic (as it did with phase—see Fig. 4.22) because the differences in distance become multiplied by a factor of 2 for the round trip.

Where the antenna is deployed in two dimensions to form the synthetic aperture for a three-dimensional SAR system, the situation is nearly the same. The only difference is that, this time, the more-hyperbolic shape takes on a three-dimensional form. An example of such a shape formed by the times-of-flight to a single scatterer is provided in Fig. 4.34.

The contour of the shape provides a pictorial depiction of how far into the SAR data an algorithm must go at each position to collect the energy associated with the scatterer at

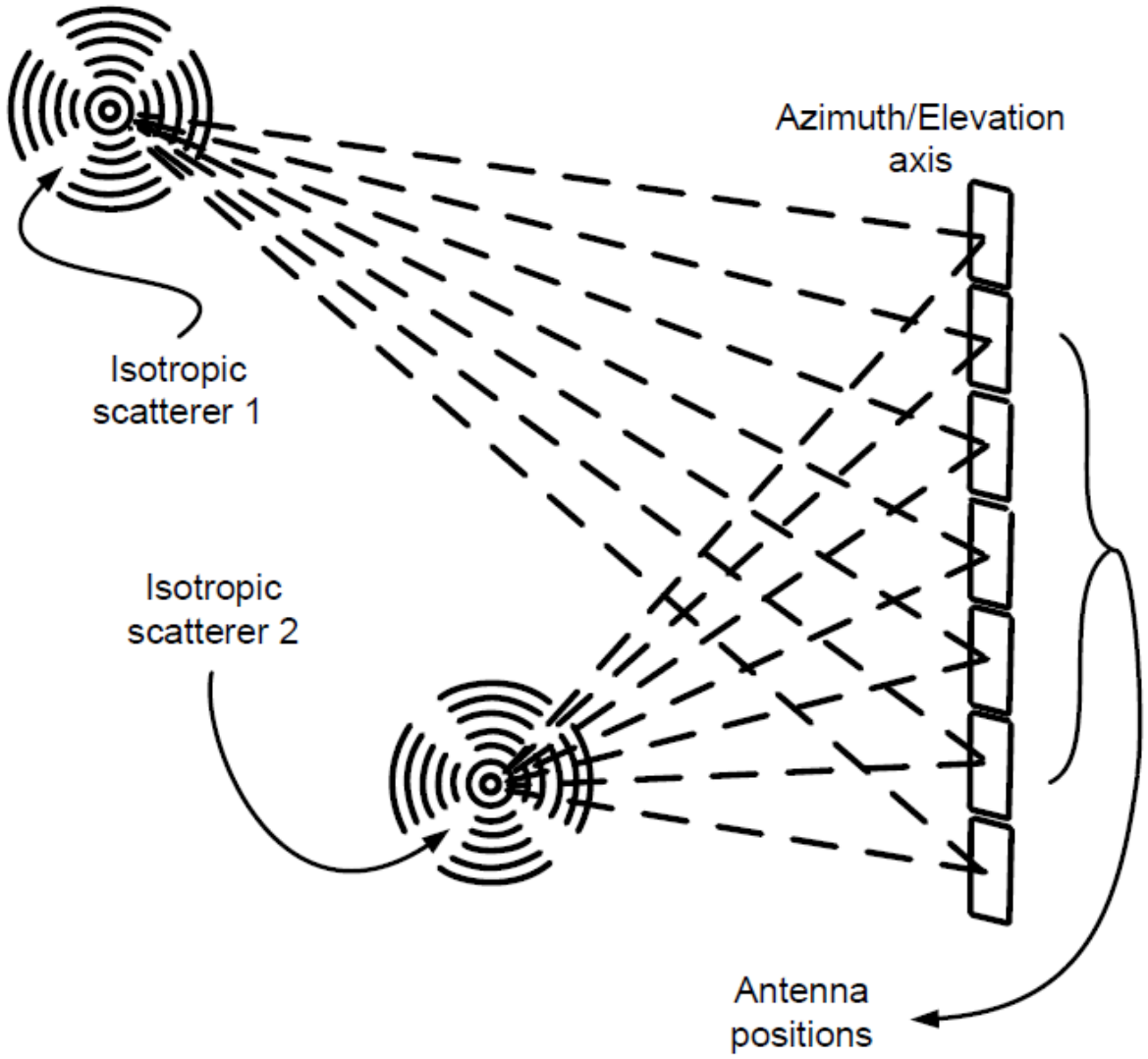

Figure 4.33: Straight lines to antenna positions from isotropic scatterers.

the particular location that would create the corresponding shape. Different locations render different contours. By following the contour for all of the locations necessary to create the desired image, an algorithm generates the image.

Even if the change in slant range is smaller than the resolution of the SAR system with respect to the z axis, causing all of the energy from each position to be stored in the SAR data in the bin corresponding to the same time-of-flight for each position, the phase

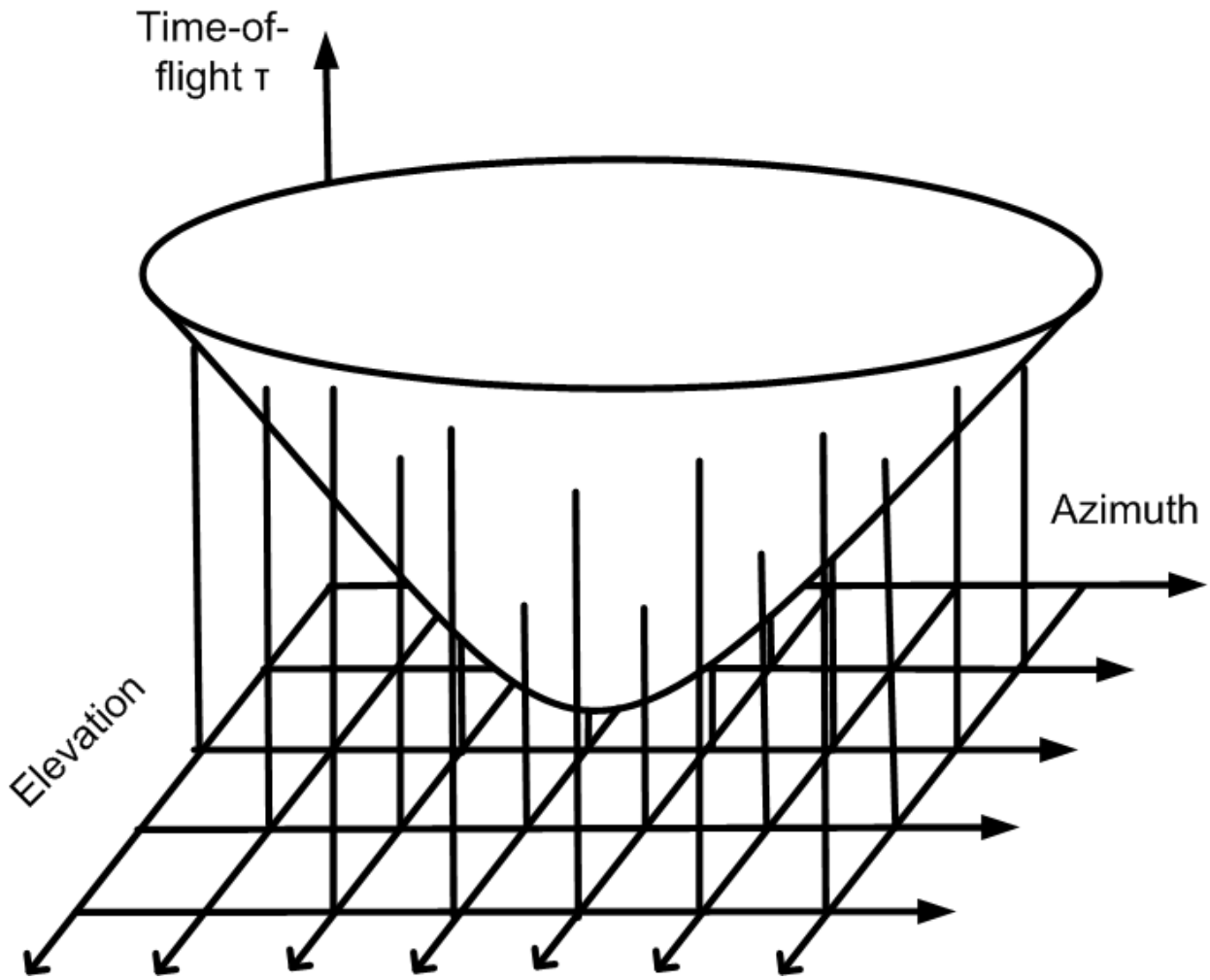

Figure 4.34: Shape generated when time-of-flight τ is plotted as a function of position for a two-dimensional synthetic aperture.

information from those bins is still present. When the data is phase shifted and summed for a particular location of interest with respect to the x and y axes, the different phases cause the elements to add destructively for locations that are not the location of interest. For the location of interest, the differing phases add constructively to increase the final value of the sum for that location. The location of interest, at which processing is computationally focused, comes to the fore.

The contour of a shape described by times-of-flight to a particular location is described by the equation:

$$h(x_a, y_a, x_s, y_s, z_s) = \frac{2}{c}\sqrt{((x_a - x_s)^2 + (y_a - y_s)^2 + z_s^2)}, \tag{4.67}$$

where the factor of 2 is included for a round trip along the path to and from the scatterer, c represents the speed of light, x_a and y_a represent the antenna location, and x_s, y_s, and z_s represent the location of the scatterer within the coordinate system.

A few simple manipulations of Eq. 4.67 indicate a constant degree of concavity for the hyperbolic shape corresponding to any particular location within a plane defined by a constant downrange distance along the z axis. To demonstrate the constant degree of concavity, a shift is introduced into the scatter position with respect to the x axis (a similar shift can be introduced with respect to the y axis),

$$h(x_a, y_a, x_s, y_s, z_s) = \frac{2}{c}\sqrt{((x_a - (x_s + \delta x_s))^2 + (y_a - y_s)^2 + z_s^2)}. \tag{4.68}$$

Mathematically, this shift can be transferred to the antenna positions,

$$h(x_a, y_a, x_s, y_s, z_s) = \frac{2}{c}\sqrt{((x_a + \delta x_a) - x_s)^2 + (y_a - y_s)^2 + z_s^2)}, \tag{4.69}$$

resulting in a shift of the position of the center of the hyperbola and nothing more.

Conversely, the antenna positions cannot be shifted with respect to the z axis. As a result, changes in the scatterer position with respect to the z axis remain in the equation to alter the degree of concavity. Scatterers closer to the synthetic aperture have a higher degree of concavity than those that are farther away.

From the perspective of signal processing, PSR can be viewed as the impulse response. As discussed above, however, the PSR is only partially position invariant. The impulse response is position invariant for constant scatterer distances with respect to the z axis, but position variant otherwise.

4.4.3 Algorithims

Conceptually, it is sufficient to say that the energy along the contour of a hyperbolic shape corresponding to a downrange location must be summed to image that location. In terms of processing, however, an algorithm is required that accesses and sums the SAR data along the hyperbolic contours corresponding to the different locations being imaged. Different algorithms can be employed that leverage knowledge provided by the PSR. Two such algorithms are discussed below. The matched filter, although computationally intensive, is discussed first because it lays the groundwork for understanding a more efficient algorithm known as backprojection.

Matched Filter

A matched filter looks for an expected signal in a received signal. The matched filter performs this search by determining the cross correlation between the two signals. The cross correlation is determined by convolving the received signal with a time-reversed conjugate of the known signal. In the presence of white Gaussian noise, the cross-correlation at the heart of a matched filter results in the highest possible SNR.

In the context of SAR processing, the received signal is embodied in the SAR data. The information needed to construct the known signal that we are looking for is provided by the PSR and an exponential term for phase accumulation. The PSR gives the expected magnitude for an isotropic scatter at every location downrange that could be the subject of the imaging process. These constructive isotropic scatterers are assumed to radiate back to the antenna with unit amplitude through lossless space. The unit amplitude of these constructive scatterers suggests that their magnitude is best modeled by a shifted delta function δ_{known} for each position.

To pick the appropriate information from the SAR data for scatterers located downrange, the delta function must be a function of everything of which the SAR data and the scatterers are functions, i.e., for SAR data, the antenna positions variables (x_a and y_a) and the time-of-flight variable (τ), and for scatterers, the position variables (x_s, y_s, and z_s). To pick out the right values from the SAR data, for a particular scatter location (x_s, y_s, and z_s) and antenna position (x_a and y_a), the delta function must be zero everywhere except at the

particular time-of-flight necessary for the backscatter in question to arrive at that antenna position. This can be accomplished by shifting the delta function by this time-of-flight.

Since the delta function has a magnitude of one for the time-of-flight necessary to reach the scatterer in question from the antenna position in question, it preserves values from the SAR data necessary to determine the backscatter from a particular location downrange of the synthetic aperture. If the position-specific, time-of-flight values for which the delta function were non-zero were plotted with respect to position, the hyperbolic shape corresponding to the scatterer in question would be described. As a function, the information embodied in the PSR takes the form:

$$\delta_{known}(x_a, y_a, \tau, x_s, y_s, z_s) = \delta(\tau - \frac{2}{c}\sqrt{(x_a - x_s)^2 + (y_a - y_s)^2 + z_s^2})). \tag{4.70}$$

The time shift in the delta function acts to time reverse the known signal as required for a matched filter. Since the delta function is real-valued, taking its conjugate does not change anything. The phase term is constructed around the time of flight:

$$\tau = \sqrt{((x_a - x_s)^2 + (y_a - y_s)^2 + z_s^2)}), \tag{4.71}$$

and is expressed as a positive exponential because it is the conjugate of the actual phase:

$$phase\ term = e^{j2\pi\tau}. \tag{4.72}$$

The matched filter is then constructed by convolving the SAR data with the product of the PSR and the phase term. An imaging function $I(x, y, z)$ results that maps the backscatter to voxels corresponding to the regions from which backscatter originates in the downrange volume,

$$I(x, y, z) = \int\int\int SAR_{data}(x_a, y_a, \tau)\delta_{known}(x_a, y_a, \tau, x_s, y_s, z_s)e^{j2\pi\tau}\ dx_a dy_a d\tau. \tag{4.73}$$

Since SAR data is recorded digitally, the integration operations are often, in practice, replaced with summations. Additionally, time-of-flight corresponds to frequency in frequency

modulated radars. Due to the fact that the transmit frequency is incremented in discrete steps, the discrete frequencies in the return signal provide a convenient discrete basis for digital storage of SAR data. As a result, the variable for time-of-flight τ is often replaced by frequency,

$$I(x,y,z) = \sum\sum\sum\ SAR_{data}(x_a, y_a, f)\delta_{known}(x_a, y_a, f, x_s, y_s, z_s)e^{j2\pi\tau}\ dx_a dy_a df. \quad (4.74)$$

The convolution/summation operations sum the values picked out of and preserved from the SAR data over the various antenna positions to determine the backscatter from the location of interest. Another way to look at Eqs. 4.73 and 4.74 is to notice that the three integration/summation operations integrate, or sum, out the variables from the data function, i.e., $dx_a,\ dy_a,\ d\tau$, the variables that give structure to the data in the data domain, leaving only the variables that give structure to the image, i.e., x_s, y_s, z_s, in the image domain. Importantly, the same variables that define the image in three-dimensional space define the volume being imaged in three-dimensional space.

As appreciated, the matched filter defined in Eqs. 4.73 and 4.74 is computationally inefficient. For each location in the image corresponding to each downrange location in the volume being imaged, each element value stored in the SAR data must be multiplied by the corresponding value of the PSR function, even though the vast majority of the values are zeros, making most of the integration/summation operations incremental accumulations of zeros. Furthermore, finding the value from the PSR function involves the computationally expensive step of taking a square root to determine time-of-flight. The backprojection algorithm, discussed below, provides a means for avoiding some of these unnecessary calculations.

Backprojection

The backprojection algorithim does not rely on a delta function to scale all non-relevant values of the data set by zero for each location of interest. Instead, the backprojection algorithim simply projects back into the SAR data with respect to the time dimension to pick out the relevant values from the data and sum them, leaving all non-relevant data

values alone, hence the name, "backprojection algorithim." The algorithm can be expressed in equation form for continuous time as:

$$I(x,y,z) = \int\int SAR_{data}(x_a, y_a, \frac{2}{c}\sqrt{((x_a - x_s)^2 + (y_a - y_s)^2 + z_s^2)})e^{j2\pi\tau}\, dx_a dy_a, \quad (4.75)$$

or for discrete time as:

$$I(x,y,z) = \sum\sum SAR_{data}(x_a, y_a, \frac{2}{c}\sqrt{((x_a - x_s)^2 + (y_a - y_s)^2 + z_s^2)})e^{j2\pi\tau}\, dx_a dy_a. \quad (4.76)$$

Equations 4.75 and 4.76 are mathematically justified because they are equivalent to Eqs. 4.73 and 4.74. The integration/summation over relevant values for a particular scatterer location offers the same result offered by an integration/summation over relevant values and non-relevant values scaled by zero. The efficiency gains resulting from backprojection are apparent in the loss of an integration/summation operation with respect to the time/frequency domain—only the relevant times associated with the time-of-flight from a particular antenna location to a particular scatter location are involved. As with the matched filter, the equation for the backprojection algorithm integrates out the variables for the antenna position, leaving only the variables needed to define the scatterers in both the image domain and the physical world. Backprojection, therefore, is a much more effective algorithm for going from the data domain to the image domain.

Range Compression

The first step to the backprojection algorithm is to range compress the SAR data. As discussed above in Section 4.2.1, the range of a scatterer is determined by detecting the modulation applied to the transmit signal in the receive signal and determining the distance traveled during the corresponding time delay. The ability to differentiate modulation in the return signal as a function of time determines range resolution.

Range compression is the process by which the modulation in the transmit signal is correlated with that modulation in the receive signal in the presence of white, Gaussian

noise on both the real and imaginary channels. Since the transmit signal is known, the cross-correlation between transmit and receive signals that is range compression is also a matched filter. The matched filter can be implemented as a simple convolution between the receive signal and the conjugate of the time-reversed transmit signal.

For AM radar, the transmit signal is a series of rectangular pulses, as is true with the receive signal. The convolution of these signals creates triangles with a base length, defined with respect to time, twice as long as the pulse. As discussed above, therefore, targets with a time-of-flight less than half the pulse length cannot be distinguished (Section 4.2.3).

As discussed above, modulation of frequency allows for much finer resolution (Section 4.2.4). A linear chirp over frequencies in the time domain describes a rectangular function in the frequency domain. An inverse Fourier transform on the this rectangular function produces a sinc function (see 4.8). When the rectangular transmit and rectangular receive signals are convolved in the frequency domain, the resultant triangular shape is very similar to a sinc function in the time domain. Such a sinc function can be distinguished from adjacent sinc functions, even where they are separated by very little time. Resolution is greatly improved.

The origin of the term range compression can be seen in the resultant sinc function. In the upper half of Fig. 4.35, the transmit and receive signals are plotted as functions of time before the two signals are range compressed. The transmit signal comprises a linear chirp within a pulse. The receive signal comprises a time-reversed, attenuated version of the chirped transmit pulse and occupies a significant amount of time. The receive signal, after range compression, is depicted in the lower half of Fig. 4.35. After range compression, the receive signal occupies a relatively short duration with a sinc function. Such a sinc function is referred to as being compressed with respect to time relative to the time-reversed pulses in the upper half of Fig. 4.35. The compression in the receive signal allows returns to be distinguished over much smaller time intervals, resulting in much finer resolution.

Although conceptually range compression can be thought of as a convolution that implements the cross-correlation of a matched filter, the form in which the data is provided by the FM radar must also be taken into account. As discussed above in Section 4.2.1, in FM radars, transmit and receive signals are mixed, resulting in sinusoidal time-domain data

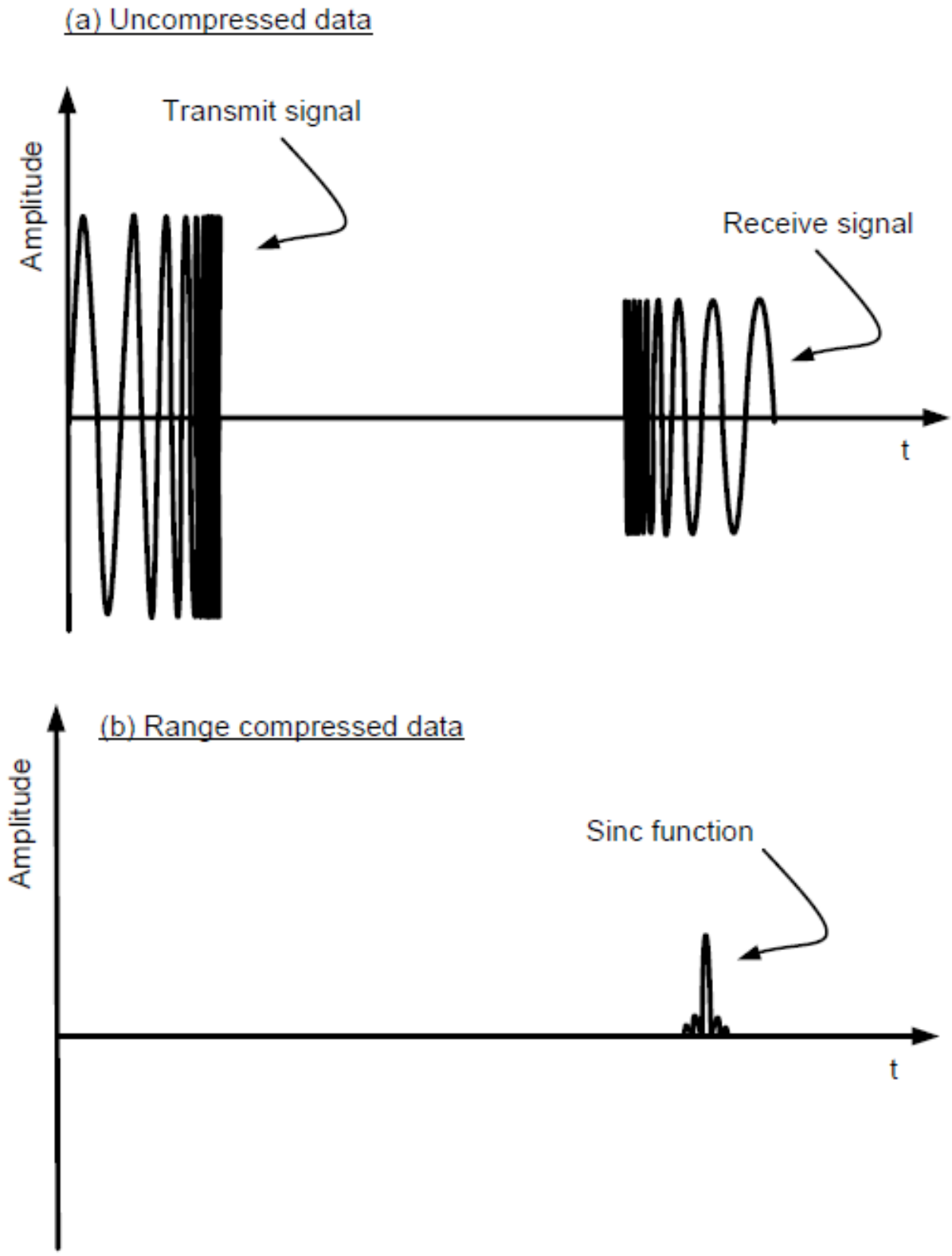

Figure 4.35: Transmit and receive signals, together with the result from range compression.

at frequencies that are the sum and the difference of the frequencies of the transmit and the receive signals. The sum data is filtered, leaving only the time-domain difference data, which is usually sampled and provided in discrete form.

However, as also discussed in Section 4.2.1, range corresponds to frequency. To acquire these range-determinative frequencies, the discrete time-domain data must be transformed to discrete frequencies. These discrete frequencies correspond to range bins, which include the return from scatterers over the range interval covered by the respective bins. In practice, the transformation on the discrete time-domain data is often performed with the computationally efficient Fast Fourier Transform (FFT). Use of the FFT is conceptually justified because an FFT can be used to perform a convolution in discrete time [63]. The series of multiplications of the transmit and receive signals that takes place in the radar mixer can be viewed as the series of multiplications that takes place under the integral or summation operations. The FFT simply takes this series and combines them as they would be combined in traditional convolution.

Once the SAR data has been range compressed, the data is enhanced for the back-projection algorithm in two ways. First, and most importantly, the range resolution has been improved drastically. Second, since matched filters deliver the highest possible SNR in the presence of white noise, the matched filter involved in range compression provides quality data in terms of SNR. For these reasons, SAR data is usually range compressed before processing by means of the backprojection algorithm.

4.5 Conclusion

A linearly chirped, high-bandwidth radar system with a two-dimensional synthetic aperture, transmitting at high frequencies over large integration-angles, and deployed in stripmap mode from a ground-based platform meets the requirements of a radar system capable of assisting in avalanche prediction. The data from such a radar system should be range compressed and processed with the backprojection algorithm for efficient, quality imaging.

For the purposes of avalanche prediction, to capitalize on a radar system's ability to gather large amounts of data about a snowpack quickly and over a large area, certain

prerequisites arise. The system must be able to (1) detect, (2) measure, and (3) determine the relative location of avalanche-relevant properties in the snowpack. Additionally, (4) the system must be practical and deployable in rugged mountainous terrain. These prerequisites translate into radar parameters in terms of the requirements that the radar system (a) has ultra-high resolution, (b) is capable of imaging three-dimensional volumes with ultra-high resolution, and (c) runs on low power.

In fulfilling these requirements, such a radar system includes a linear chirp in the transmit signal because the inverse relationship between the frequency and time domains results in superior range resolution for systems that employ frequency modulation. The higher the bandwidth of the chirp, the better the resolution. For the purposes of imaging a snowpack, resolution of about 10 cm (4 inches) is desirable. Equation 4.6 requires a bandwidth of 1.5 GHz or better.

Additionally, linear chirp modulation frees resolution from pulse-width dependency, allowing pulses to be stretched arbitrarily to accommodate power needs. As a result, power demands can be measured in Watts and fractions of a Watt, as opposed to megawatts. These low power demands allow for light-weight, portable, and inexpensive components that can be combined in a system deployable in the mountains.

To fulfill the requirement of three-dimensional imaging, a two-dimensional synthetic aperture is relied upon. Relying on expected differences in phase between antenna positions for backscatter from different downrange locations, the two-dimensional synthetic aperture is able to determine the location of backscatter with respect to azimuth and elevation. By determining location with respect to range, azimuth, and elevation, the system is capable of imaging in three dimensions.

The two-dimensional synthetic aperture makes use of a small, easily-deployable antenna to create an aperture of a size that would be impractical to deploy. The size of this aperture allows for high resolution along azimuth and elevation by increasing the angle of integration over which data is collected. Equation 4.55 states that resolution along azimuth and elevation is a function of frequency. Therefore, high frequencies are desirable for high resolution. For this reason, and for the electromagnetic interactions possible with different

snowpack properties for the corresponding wavelengths (see Chapter 3), recourse is made to frequencies in the X- and Ka- bands.

To collect data over large areas, the synthetic aperture is deployed according to stripmap mode. In stripmap mode, resolution can be determined by the dimensions of the synthetic aperture and the range, which are related to the angles of integration, by Eqs. 4.51 and 4.52. These equations indicate that for frequencies in the K- bands, at distances between 100 m and 1 km, the dimensions of the synthetic aperture can be anywhere from 3.75 m to 100 m, depending on the frequency and the distance.

Additionally, the antenna used to create the synthetic aperture must be small. A larger antenna would trigger the fundamental limit on resolution imposed by Eq. 4.53. For 10 cm resolution, the dimensions of the antenna must be 20 cm or less.

The spatial sampling within the synthetic aperture must be high to avoid aliasing. To avoid aliasing the Nyquist criterion must be satisfied and the dimensions of the constitutive antenna must be taken into account. According to Eq. 4.62 and Eq. 4.65, for 10 cm resolution, sampling needs to occur with respect to each dimension at least every 5 cm and every quarter of the antenna's length in that dimension. Therefore, although it is desirable that the antenna be small, it is also important that the antenna not be too small, as this would impose a requirement for too-frequent, time-consuming spatial sampling.

The radar system provides a data set indexed by antenna position and time-of-flight, or frequency, so as to lend itself to quality-enhancing range compression and the efficient backprojection algorithm. These algorithms assume that phase delays do not accrue relative from one location to another across the antenna's aperture. To assure the avoidance of aperture-location-specific-phase delays, the antenna should be a horn antenna.

Chapter 5

Preliminary System to Test Feasibility

To evaluate the theory of the previous chapters, a SAR radar system informed by the principles previously developed needs to be realized. Ideally, such a system would meet the parameters previously outlined. The implementation of such a system, however, requires a significant investment and the overcoming of certain obstacles. Due to resource limitations, the system must be implemented on a smaller scale from inexpensive and available components.

Such a system has parameters that approximate those outlined in a way that best utilizes resources to meet three goals. First, the system needs to provide a means with which to acquire familiarity with the issues, including problems and potentials, involved in acquiring and processing three-dimensional volume SAR data at high frequencies. Second, the system needs to provide indications suggesting where additional allocations of resources are likely to be rewarded with the best results. Third, the system needs to support new components that better accommodate the conclusions of the previous chapters and which may become available in the future.

5.1 Obstacles to Implementing the System Design of the Previous Chapter

Although the design specifications from the previous chapters have been achieved in different radar systems in isolation, they have not been brought together. Bringing together the parameters in a single realized system creates many problems that need to be worked through. For example, although SAR apertures are commonly created over large distances, creating them at the high frequencies of X- and Ka-bands imposes a requirement that the location of the positions at which samples are taken be known with a great deal of accuracy to respect phase information requirements for shrinking wave lengths.

To accurately track phase progression, the location at which the samples that make up the synthetic aperture are taken should be known to within a tenth of a wavelength [64]. At 15 GHz, the middle of Ku-band, the wavelength is 2 cm long, meaning that the position of each constitutive sample be known relative to some predefined point within the synthetic aperture to within 2 mm. At 40 GHz, the top of Ka-band, the wavelength is 7.5 mm long, meaning that position information must be accurate to within less than a millimeter. The samples do not need to be taken at exact locations as long as sampling occurs with sufficient spatial frequency, but the relative locations at which they are taken does need to be known accurately. Achieving this accuracy over grids with dimensions measured in several to tens of meters presents possibly the largest challenge to implementing the conclusions of the previous chapters. A number of possible solutions present themselves involving cables, multiples antennas, directional mirrors, or even robotic helicopters capable of determining their location with lasers and weigh stations.

Short wavelengths are not the only challenges that high frequencies bring. The precision required of the hardware necessary to generate, modulate, transmit, and receive wavelengths approaching or measured in millimeters makes the fabrication of such hardware difficult [65]. The wavelengths associated with frequencies in Ka-band approach or are measured in millimeter lengths, making the requisite hardware difficult to acquire affordably.

Large bandwidths also present problems. Many of the important results in the chapter on design, in terms of the antenna beam width, the creation of the synthetic aperture, and the processing of the resultant data, assume a single frequency. This assumption is justified where the bandwidth is a small fraction of the central transmit frequency. However, as the bandwidth is increased to 1.5 GHz and above, the assumption becomes problematic, requiring additional mathematical considerations in the design process [66]. Additionally, although low power transmissions for research purposes over large bandwidths do not present problems, transmission over large bandwidths with the power required to transmit and receive at a distance of a 1000 m is likely to present conflicts with existing allocations by the Federal Communication Commission. Happily, at high frequencies conflicts are less likely to occur and special licenses may be granted for the sparsely populated mountainous terrain where avalanches are a concern. Additionally, important research has shown that resolution may

be improved by stitching together non-continuous allocations of bandwidth from available swaths of the electromagnetic spectrum [67].

5.2 Availability of Signal-conditioning Modules

The hardware necessary to generate, modulate, transmit, receive, and record information about the wavelengths involved in the radar system make up the heart of the radar system. This hardware is referred to as the signal-conditioning module. The signal-conditioning module determines the bandwidth and the central frequency of the radar system. Several possibilities for the signal-conditioning module exist.

The microSAR developed at Brigham Young University is a precedent for student development of small, light-weight, and portable signal-conditioning modules [51]. The microSAR transmits at a central frequency of 5.4 GHz, within C-band (4-8 GHz), and transmits across a bandwidth of 90 MHz. Apart from the low frequencies, the low bandwidth affords a range resolution of 1.7 m, about the thickness of the snowpack. Additionally, there may be issues with microSAR being insufficiently rugged for the deployment demands imposed by snowpack imaging in mountainous terrain.

The microSAR precedent can be followed to develop a new, higher-frequency, higher-bandwidth system. As demonstrated by the microSAR program, however, the development process is involved. As discussed above, developing a system at higher frequencies presents additional challenges. Improving the bandwidth also presents challenges.

Commercially available network analyzers perform the essential functions of frequency generation, reception, and recording across large bandwidths. Commonly available network analyzers span frequencies from 50 MHz to 20 GHz, and network analyzers that span frequencies between 50 MHz to 40 GHz and 10 MHz to 110 GHz are also available. The ability to generate and record the returns from frequencies across such large spans makes network analyzers a good core around which to build a signal-conditioning module [68] [69].

However, the transformation of a network analyzer into a signal-conditioning module is more complicated than it would first appear. Network analyzers, as their name implies, are designed to measure reflection coefficients, not backscatter. Making the transition requires a thorough knowledge of the inner workings of a particular network analyzer and significant

development. The systems are not designed to transmit electromagnetic energy over the airwaves like radars, requiring the development of complicated amplification solutions. A synthetic aperture system needs to record measurements over a large number of locations over a large number of frequencies. To image snow with sufficient SNR, several hundred measurements may need to be taken at each frequency at each location. Network analyzers are not designed to record such large data sets parsed in the ways required. Network analyzers are typically designed to provide frequencies and record samples for a limited number of increments over a selected bandwidth. To satisfy Nyquist sampling requirements and avoid aliasing, this sampling limitation would effectively limit the bandwidth, unless additional measurements are made stitched together. Network analyzers are not designed for cold and rugged environments such as those encountered doing snow research. These are just a sampling of the problems that would be encountered during the transformation of a network analyzer into a viable signal-conditioning module for snow research.

Private industry has made available different signal-conditioning modules. These modules are designed to acquire data for two-dimensional images from airborn platforms. The resolution requirements for these images are not as fine as those needed to study snow. However, the modules are rugged, designed to collect backscatter, designed to store backscatter in a way that lends itself to the creation of a two-dimensional synthetic aperture focused on a snowpack, and have better bandwidths than the student-developed microSAR.

In keeping with its tradition of supporting student research, ARTEMIS INC., has generously made available its microASAR module for snow research during the winter months of 2010. The module is small (22.1 x 18.5 x 4.6 cm), light-weight (less than 3.3 kg), and rugged. The module transmits in C-band at a central frequency of 5.4 GHz and has an adjustable bandwidth of up to 200 MHz (80 cm range resolution). The module stores data sets conveniently indexed by frequency and position on flash-memory cards that can easily be downloaded for processing. Two separate antennas are required for use with the module, one to transmit and one to receive. Figure 5.1 pictures the module with the cover plate and circuit board removed.

As private industry continues to improve upon existing technologies, a trend is developing for modules with higher frequencies and higher bandwidths. The potential exists for

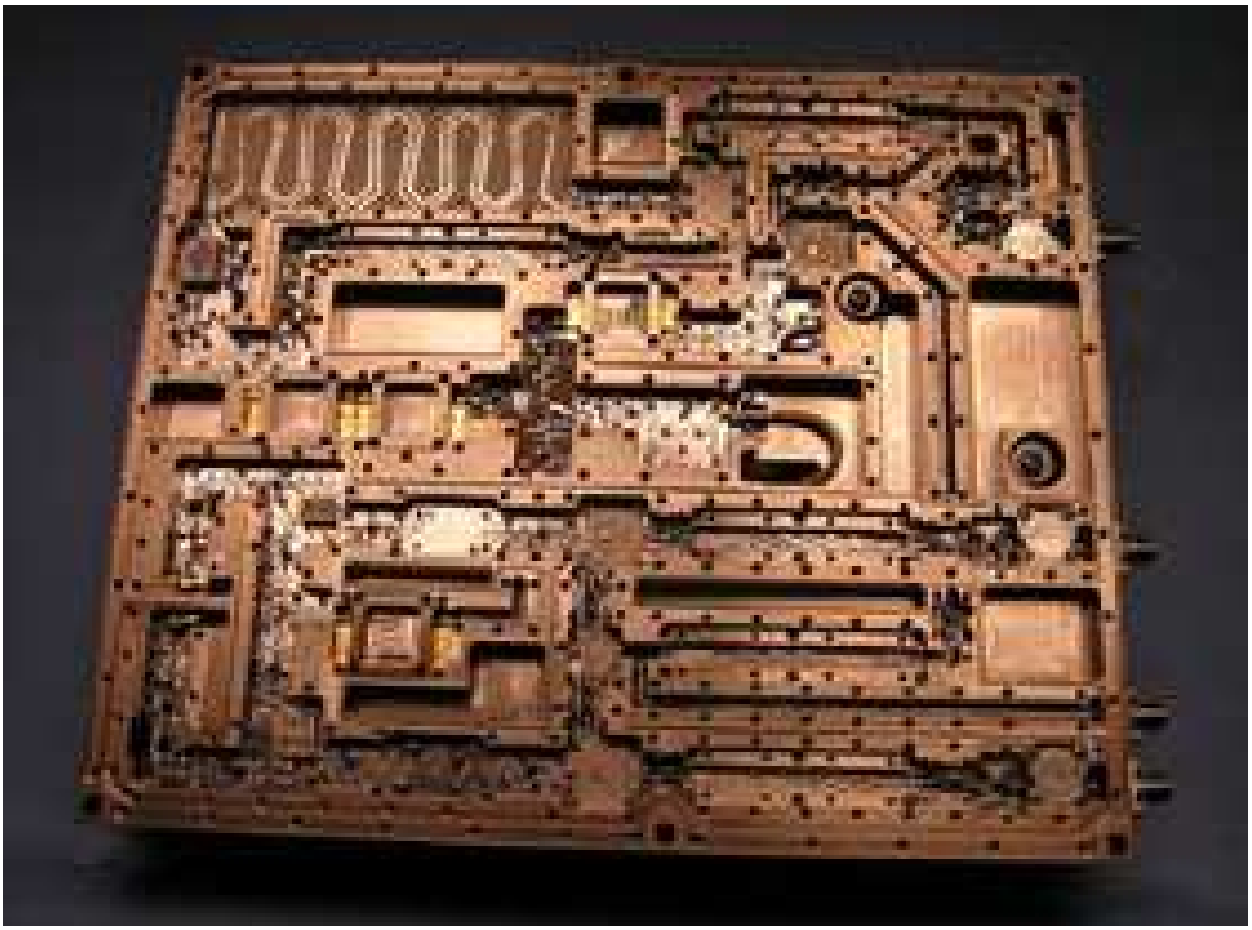

Figure 5.1: MicroASAR with cover plate and circuit board removed to show the radio frequency hardware. (Reprinted from the website of ARTEMIS INC.)

continued cooperation with private industry. Therefore, additional components to a preliminary system for snowpack research need to accommodate signal-conditioning modules with higher frequencies and higher bandwidths.

5.3 Scanning Platform

Aside from the signal-conditioning module, antenna system, and the infrastructure to support these components, a platform is required that is capable of scanning the antenna(s) attached to the signal-conditioning module from position to position within the grid that makes up the overall system's synthetic aperture. The desire to support high frequencies and small wavelengths entails the need to pinpoint the relative location of the positions at

which samples are taken with a high degree of accuracy. In order to support wavelengths at the upper frequencies of Ka-band, the platform must be able to pinpoint the location of the antenna mount to within less than a millimeter. Meeting this standard for accuracy is much easier with a ground-based platform that utilizes tracks.

To meet goal (1) of a system with which familiarity with the issues involved in ultra-high- resolution, volume imaging can be acquired, the ground-based platform should be able to scan the antenna mount to create an aperture of dimensions large enough to allow ultra-high-resolution, volume imaging (at least at close range) for a readily available signal-conditioning module. To meet goal (2) of determining where to invest in system improvements, the platform should be able to create a synthetic aperture of sufficient size to allow volume imaging at significant ranges so that the viability of larger platforms can be assessed. The platform should also be able to create a synthetic aperture large enough to determine the feasibility of volume imaging of a snowpack and how best to make improvements on images. To meet goal (3), the system needs to be able to support signal-conversion modules at higher frequencies in the future. Practical constraints also require that the platform be easy to store and to move. A scanner that multiple people can be fit through doorways fulfills this requirement.

A grid with dimensions of 180 cm x 180 cm (6 ft x 6 ft), for the C-band central frequency of 5.4 GHz, allows for azimuth and elevation resolutions of 10 cm at a range of 6.8 m. Although this places a severe range limitation that prevents the system of achieving the end of collecting data over large areas, it allows goal (1) to be achieved—acquiring familiarity and experience with the issues involved in ultra-high-resolution, volume imaging. For the Ka-band frequency of 40 GHz, dimensions of 180 cm x 180 cm, allow for 10 cm resolution at a range of 50 m. Although a range of 50 m is also not enough to accomplish the end of collecting data over large areas, the range should be enough to achieve goal (2) in terms of assessing the feasibility of achieving high-resolution at larger ranges with larger platforms. Additionally, goal (2) is met by allowing near-range, volume images of snow to be tried in a way that would suggest what changes might improve those images. By being able to support frequencies to the top of Ka-band, the platform achieves goal (3) of being able to support higher frequency signal-conditioning modules in the future. These high frequencies

are important for more than just achieving high resolutions, as discussed in Chapter 3, they are important for gathering information about avalanche-relevant properties in the snowpack.

To be able to support the short wavelengths transmitted by high-frequency modules, the location of the each antenna position from which measurements are collected must be known to within a millimeter relative to a reference location within the aperture. A near-field scanner is another instrument tasked with providing information about antenna location within a plane. The demonstrated success of near-field scanners makes their inverted T-shape design, comprising a horizontal and a vertical component, a good guiding concept for the ground-based platform. In the inverted T-shape design, a pair of horizontally disposed tracks provide the bed on which a platform with vertically-disposed tracks can slide back and forth. The vertically disposed tracks provide the guidance for the antenna mount, which can move up and down. The ability to move side to side and up and down allows the antenna mount to accesses any location within the dimensions of the horizontal and vertical runs along the two sets of tracks. A visualization generated in AUTOCAD and provided in Fig. 5.2 of the inverted T-shape design of the ground-based platform helps to visualize these principles of motion.

The design of the ground-based platform is depicted in Fig. 5.2. To provide the stability for accurate determinations of location on the vertical component, the vertical component sits on a base plate 2 ft wide x 3 ft deep. Affixed to the back corners of the base plate and extending to the top of the vertical component are aluminum angle pieces providing a strong back to counter strong winds that may be encountered in mountainous terrain.

Since the run along the tracks of the horizontal component is 180 cm, or 6 ft, and the base plate is 2 ft wide, the total length of the horizontal component is 8 ft. The horizontal component comprises a rectangular box of $9^{3/4}$ inches in height to provide room for a motor to drive the vertical component under the base plate. To provide rigidity for more accurate measurements along the horizontal component, the extruded, aluminum tubing, of dimension 2 inches x 3 inches, along the four corners of the horizontal component have a thickness of a quarter inch. Similarly, the two vertical columns that support the tracks of the vertical

Figure 5.2: Drawing of design for a ground-based platform generated in AUTOCAD, demonstrating the inverted T-shape design that allows motion along the horizontal component extending out of the picture and along the vertical component. The rendering also depicts the horn antennas on the antenna-mount plate disposed more than half way up the vertical component with the bronze-colored microASAR module, discussed below, positioned underneath.

component have a thickness of a quarter inch, but have dimensions 3 inches x 3 inches. The total height of the scanner is just over 7 ft.

To reduce weight, the scanning platform is constructed of aluminum, with the cutting and welding done by the BYU Precision Machining Workshop. As aluminum is notorious for warping when welded, the top of the rectangular, horizontal component is provided with two flat-bottomed grooves milled on a precision mill capable of holding a tolerance to 1/10,000 of an inch. The grooves provide a perfectly flat bed for the horizontal tracks to sit in. The necessity of the grooves is shown by the height of their walls, which vary by a quarter of an inch. Without these grooves, this quarter inch (6.35 mm) variance would throw the ability of the scanner to provide accurate measurements to within less than a millimeter. As welds were not made along the length of the vertical, extruded aluminum tubing, similar grooves are not made along their length.

Four teflon-coated tracks (make, model, and size: PCB LINEAR, MINI RAIL, 20 mm), are mounted along the rigid structure provided by the vertical and the horizontal components. Bolts placed every 60 mm in the tracks insure that the base plate and the antenna mount do not drift as the four teflon carriages to which they are each affixed slide along the tracks. To determine how far along the tracks the base plate and the antenna mount move relative to a horizontal and a vertical starting position, the base plate and the antenna mount are translated from side to side and up and down by two rotating acme screws (make, part number and size: THOMSON BSA, M23S12-XCT7505-72").

The acme screws are 6 ft long and have a diameter of 0.75 inches. Each rotation of the screws translate a nut a 1/5 of an inch (5.08 mm). The screws are precision milled so that position can be determined as a function of rotation to within 0.003 inches per foot (0.018 inches/0.457 mm over 6 ft.). The nuts that translate down the screw, and to which the base plate and the antenna mount are attached, have a non-slip mechanism to insure, especially for the vertical component, that a nut does not slide backwards once the screw, around which the nut is wrapped, ceases to rotate.

Two stepper motors (make, model, and size: APPLIED MOTION, STM23, NEMA 23) rotate the screws. A stepper motor uses electromagnets in an alternating fashion to attract iron teeth on a rotor, thereby rotating the rotor in increments, or steps. The stepper

motors used have 2,000 steps per rotation. Each step corresponds to 3 μ of translation down the screw. A driver coupled to each motor sends pulses of current to control how many increments the motor rotates and the rate at which the motor cycles through those increments. Stepper motors have the advantage that/ after the prescribed number of steps per rotation, the motors return to the starting position, preventing errors from cascading between rotations.

Although the number of steps that each motor advances the corresponding screw can be used to determine locations, greater accuracy is achieved by taking readings from optical encoders attached to the motor drive shafts. An optical encoder works by shining light through a disk in which slots, which allow light to pass through, encode information about the number of rotations. The optical encoders attached to the drive shafts of the motors exceed the increments per rotation of the stepper motor.

The motors are controlled from a laptop with control software written in C++ by Justin Penner, a fellow candidate for a Master's degree. The control software communicates with the serial command language of the motors via CAT 5 cable. The communications include commands that advance the motors to positions in pre-defined grids set up from user-friendly graphical-user-interfaces, which receive position information errors. The control software also packages the position information to communicate with the signal-conditioning module so that measurements of backscatter can be indexed to the positions from which they were taken.

The vertical component of the scanning platform is pictured in Fig. 5.3. In the figure, the antenna mount and the screw used to advance the mount are clearly visible. In Fig. 5.4, the scanning platform is pictured from the side.

To determine the accuracy of the scanning platform, a laser pointer is attached to the antenna mount and the scanner is run through a series of scans. A grid of centimeter cubes is printed on two 3 ft x 6 ft sheets of paper that are attached to boards straitened with aluminum beams. The grid is placed parallel to the plane of the synthetic aperture 4 feet in front of the laser pointer. A series of scans are run, and the laser beam does not vary more than 4 mm with respect to each axis during any of the scans.

Figure 5.3: Picture of the vertical component of the completed scanning platform with an antenna mount and the driving screw visible.

Figure 5.4: Side view, allowing the completed scanning platform to be viewed in its entirety. The screw used to translate the base plate horizontally is visible within the box of the horizontal component. The driving motor for the horizontal component is attached on the far end.

The 4 mm variances are somewhat more than the desired tolerance under 1 mm. Nevertheless, the variations follow certain constant patterns that could be accounted for in processing with compensation functions. Additionally, the measurements were made with several bolts removed from the tracks so that the tracks can flex to accommodate for binding occurring because of screw offset. Continual work to better align the screws in addition with compensating functions applied to position data hold open the possibility of achieving tolerances of less than 1 mm.

The scanning platform is deployed in cold weather to capture data about snowpacks. Different components respond with differing amounts of contraction in response to cold weather. Unfortunately, the rigidity of the scanner makes it very sensitive to the alignment of its components, causing the scanner to bind up and cease to function in cold temperatures.

To prevent these problems, the scanning platform is deployed inside a plastic tent that is transparent to the radar. The tent is constructed from a frame of 1 inch PVC pipe that is covered with 6 mill greenhouse plastic. The tent is heated to a temperature between 55° F to 65° F with one or two 1500 Watt space heaters depending on the how quickly the tent needs to be heated and the temperature outside the tent. The tent has the added advantage of functioning as a radome to protect the signal-conditioning module and the scanning platform. The plastic tent, of dimensions 10 ft x 10 ft x 5 ft, is pictured in Fig. 5.5.

5.4 Selection of and Modifications to the Signal-conditioning Module

For purposes of acquiring familiarity with ultra-high resolution, volume imaging and for purposes of testing the feasibility of imaging a snowpack, the microASAR module made available by ARTEMIS, INC. is mounted on the scanning platform (see bronze-colored unit in Fig. 5.2). Of the options discussed above, only the student-developed microSAR and the microASAR can be mounted on the scanning platform without investing overmuch effort in developing the modules for deployment. Of the two, the microASAR offers larger bandwidth, is more rugged, and can more easily be fine tuned to capture data suited for the scanning platform on which it is deployed at the very close ranges that need to be used.

The microASAR includes a Field Programmable Gate Array (FPGA) chip and a Direct Digital Synthesizer (DDS) chip. The DDS chip takes a fixed-frequency reference

Figure 5.5: Plastic tent used to keep the scanning platform warm and to prevent binding, with its PVC frame visible through the greenhouse plastic.

clock and creates the discrete frequencies necessary to the chirped transmission signal. The FPGA stores and implements parameters that control the performance of the module.

The parameters stored and implemented by the FPGA, include the bandwidth, the Pulse Repetition Frequency (PRF), the rate at which frequencies are cycled through, or the ramp rate, the number of frequency steps included in the chirp, and the parameters of various filters. The parameters can be changed through a programming cable attached to the chip in communication with the XILINX programming environment.

To improve range resolution, Craig Stringham, a PhD candidate having expertise with the microASAR module and the programming of FPGA's took responsibility for reprogramming the FPGA. Through the FPGA, the module's bandwidth is changed to 200 MHz.

Additionally, according to Eqs. 4.7 and 4.8, the near range needs to be decreased to as low as 5 m to achieve resolutions around 10 cm, so the module's filters are adjusted so as not to filter out the near range responses. Additionally, the ramp rate is increased to 1.249 x 10^{13} to improve near range resolution.

To avoid aliasing with respect to range, the PRF is changed to 3,826 Hz to insure that long-range backscatter from a first pulse is not confused with near-range backscatter from a second pulse. Additionally, to avoid aliasing, the number of frequency samples in each chirp is increased to 673. Also, a bank of attenuation switches is adjusted to avoid overpowering the low noise amplifier on the receive side of the module with return from near range targets. The attenuators, however, remain high enough to capture enough backscatter to achieve high SNRs from the relatively light response from a snowpack.

Although, as discussed in Chapter 3, shorter wavelengths increase the likelihood of backscatter bearing the stamp of avalanche-relevant properties, and, as discussed in Chapter 4, shorter wavelengths improve resolution, especially at long ranges, the relatively long wavelength of the microASAR is short enough to accomplish the elements of the first two goals set forth at the beginning of this chapter. First, the wavelengths are short enough to achieve ultra-high-resolution, volume imaging at short ranges so that experience can be acquired with producing such images, pursuant to goal (1). Second, the feasibility of producing a volume image of a snowpack can be determined. Additionally, a previous study supports the use of a C-band based module for preliminary studies.

During the winters of 2002 and 2003, this previous, NASA-sponsored study took measurements, at nadir and other angles, from a Frequency Modulated Continuous Wave (FMCW) radar across the C- (2 GHz to 6 GHz), X- (8 GHz to 12 GHz) and Ku- (14 GHz to 18 GHz) bands [7]. The 4 GHz of bandwidth provided for in each of these bands allows for 7.5 cm (3 inch) resolution. The antennas of the radar system are moved over a distance of 3 m with the range-response recorded as a function of distance. The sweep of the antennas is not used to create a synthetic aperture, but is used to create something of a RBGM. Ground truth is provided from snow pits from which data is extracted about snow density, temperature, crystal type, and hardness as a function of depth. Figure 5.6 depicts

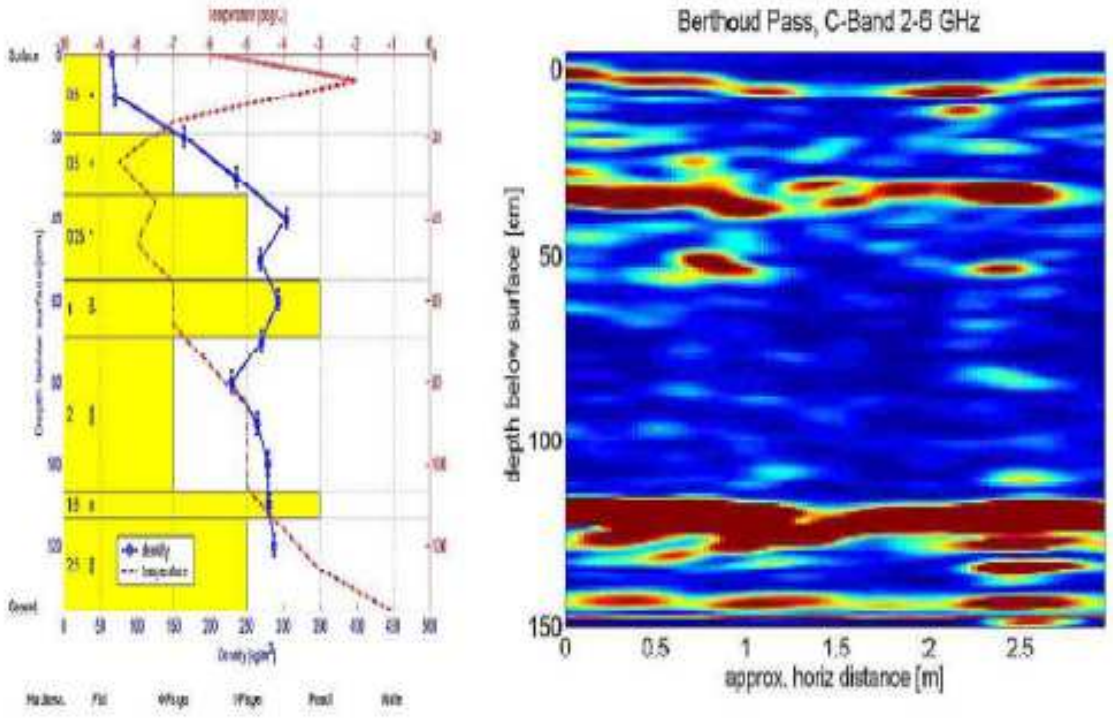

Figure 5.6: Comparison between parameters measured from a snow pit and backscatter magnitude from a C-band FMCW radar. Referring to the plot on the left of measurements from the snow pit: the vertical axis corresponds to the snow depth, from 0 to 150 cm, and is incremented in 20 cm intervals; the horizontal axis corresponds to the snow density, temperature, and hardness. The blue line corresponds to the snow density, ranging from 0 to 500 g/cm^3 and is incremented at intervals of 50 g/cm^3; the red line corresponds to the temperature, ranging from $-10°$ C to $0°$ C, and is incremented every $1°$ C; and, the yellow bars correspond to the hardness of the snow as measured by the hand-hardness scale. The plots are originally reported in [7].

the magnitude of backscatter as a function of depth across a 3 m distance for C-band (right) compared to the parameters measured from the snow pit (left).

As seen in Fig. 5.6, red bands indicative of intense backscatter return can be seen at the surface of the snowpack and at boundaries that correspond to hardness discontinuities in the profile of the snowpack. Also, the dark blue region in the lower center of the backscatter plot corresponds with the large weak layer of faceted snow that would be the origin of any avalanches in a snowpack with this profile. Although the backscatter in Fig. 5.6 arises primarily from boundary reflections, these results suggest that wavelengths from C-band

are capable of interacting with a snowpack. Therefore, a C-band system should allow the feasibility of creating a three-dimensional, non-nadir, volume image of a snowpack to be determined.

5.5 Antenna Selection

To insure uniform phase across the area of the antennas employed, horn antennas are selected. (See horn antennas in Fig. 5.2.) To allow for a resolution of 10 cm in compliance with the antenna-dependent fundamental limit on resolution provided in Eq. 4.63, antennas with dimensions of 9.78 cm x 13.18 cm are selected. The horn antennas are WAVELINE INC., model 5999 horn antennas with a frequency range of 4.90 to 7.05 GHz and with beam widths of about 30° in each plane. To accommodate the micoASAR module, two antennas, one for transmission and one for reception, are employed. The antenna mount is fabricated so that the antennas can be rotated 90° to capture data at various combinations of vertical and horizontal polarities.

5.6 Conclusion

Ideally, for the application in question, a radar system would be deployed over large synthetic apertures measured in tens of meters, transmitting at different frequencies in the X- and Ka-bands over bandwidths of 1.5 GHz or larger. Difficulties bringing these elements together, such as creating a sufficiently large synthetic aperture, the accuracy required for position measurements at high frequencies, problems incorporating large bandwidths, and difficulties in finding/developing high frequency hardware require that studies at a smaller scale be performed first with a preliminary system.

The preliminary system is designed to meet the goals of (1) providing familiarity with the problems and potentials of ultra-high-resolution, volume imaging, (2) suggesting where additional allocations of resources are likely to be rewarded with the best results, and (3) supporting new, better-suited components. The core components of the preliminary system include: a signal-conditioning module that performs the transmission, reception, and recording of electromagnetic energy, a scanning platform used to create the synthetic aperture, and the antennas used in transmission and reception.

A variety of different signal-conditioning modules with different bandwidths and transmission frequencies may become available with or without different investments in development. Therefore, in compliance with goal (3), a scanning platform is designed to achieve the millimeter accuracy that would be required of future signal-conditioning modules transmitting in Ka-band. Initially, however, the system is equipped with the microASAR module that transmits in C-band over a bandwidth of 200 MHz because of its rugged reliability, the convenient format in which it records data, and because it can be deployed with only minor adjustments. Two horn antennas of dimensions 9.78 cm x 13.18 cm are chosen to provide uniform phase distributions in the transmission signal and to allow for 10 cm resolution.

To meet goal (1), the preliminary system needs to demonstrate ultra-high resolution, volume imaging in a way that affords understanding of potentials that can be exploited and problems that need to be overcome in future snowpack imaging systems. To be considered ultra-high resolution, at least along some axes, the resolution should be measured in inches. To meet goal (2), the demonstration of volume images of a snowpack would help to determine which parameters need to be improved to better assess the feasibility of radar-based avalanche detection from snowpack-stratigraphy images. The ability to distinguish individual layers would provide even more information from which determinations can be made about how to proceed. Goal (3) is met by a scanning platform capable of supporting signal-conditioning modules at higher frequencies.

Chapter 6

Lessons Learned from Preliminary System

As discussed, researchers have demonstrated the ability of FM radar to find properties of snowpack stratigraphy from boundary reflections where the antenna line-of-sight can be maintained normal to the strata by placing the antenna mount directly above the snowpack [1]–[10]. However, to capitalize on the ability of a radar to scan large areas remotely, changes in the orientation of the radar system's line-of-sight relative to the snowpack have to be mitigated in their effect by the capability for ultra-high-resolution, volume images. These images must rely on backscatter from volume scattering within snow, not electromagnetic boundaries. Non-nadir images of snowpack volumes relying primarily on volume- scattering based backscatter are yet to be demonstrated. For reasons discussed above in Chapter 5, an ideal radar system capable of meeting all of the theoretical requirements set forth in Chapter 3 and Chapter 4 cannot be implemented. However, the preliminary system set forth in Chapter 5 is implemented to demonstrate non-nadir, ultra-high-resolution, volume imaging of snow based primarily on volume scattering, which is a prerequisite to the larger goal of remote, large-area, radar-based data collection that is useful for avalanche prediction.

The limitations of the preliminary system must be acknowledged at the outset. The limited dimensions of the scanning platform (180 cm x 180 cm/ 6 ft x 6 ft), which determine the dimensions of the synthetic aperture, and the central transmit frequency (5.4 GHz) of the microASAR module rule out the possibility of demonstrating ultra-high-resolution along the range axis—although ultra-high resolution may still be obtained along the two remaining axes, volume imaging at the large ranges required for large-area collection of data, as indicated by Eq. 4.7 and Eq. 4.8. The 200 MHz maximum bandwidth of the microASAR module places a limit on range resolution of 0.75 m pursuant to Eq. 4.6. Although 10 cm resolution along azimuth and elevation can still be obtained at very close ranges, fine

resolutions along these axes may be compromised by the coarse range resolution. Also, the large wavelength (5.53 cm) associated with the central frequency of the microASAR module is much less likely to reveal avalanche relevant properties in the snowpack for reasons provided in Chapter 3.

Nevertheless, several helpful determinations can be made by the preliminary system. In accordance with the first and second goals of the preliminary system, the ability to create ultra-high resolution, three-dimensional images in C-band allows for the discovery of advantages and obstacles that need to be overcome for future systems. Additionally, in accordance with the second goal, the yet to be demonstrated non-nadir, volume imaging of snow can be demonstrated. Actual non-nadir, volume images of snow hold the promise of remote, large-area collection of data from which images of snow can be generated. Images for C-band data may hint at the possibilities for higher frequency data to distinguish important snowpack layers. Also, in accordance with the second goal, images for C-band data can be used to determine which aspects of the signal-conditioning module need to be improved, and in which order, to better assess the possibility of stratigraphic images that can be used in avalanche prediction.

This chapter discusses the ability of the preliminary system to produce non-nadir, three-dimensional, ultra-high-resolution images. Two different deployments of the preliminary system into mountainous terrain are also discussed together with the volume images of alpine snowpacks obtained during these deployments. The data from these deployments are analyzed to learn lessons that can advance further attempts to create a radar-based avalanche prediction system.

6.1 Demonstration of Three-dimensional Imaging with Ultra-high Resolution Along Azimuth and Elevation

Several tests deployments were done on the roof of the Clyde building. After overcoming several obstacles, a test was performed from which thee-dimensional images could be rendered. For the test, three separate targets are placed on the roof. The first target is a trihedral corner reflector with dimensions of 21 cm on each side. The second and third targets are larger trihedral corner reflectors with dimensions of 48 cm on each side. The

Figure 6.1: Range set up on the roof of the engineering building with corner-reflector Targets #1 through #3 positioned from left to right. The scanning platform is in the plastic tent in the foreground.

location of the targets in three-dimensional space is measured with reference to the center of the antenna mount from its initial position in the grid from which a synthetic aperture is created.

Figure 6.1 pictures the range with the targets appearing as numbered from left to right. The first target sits atop a pile of wet snow. The second target sits atop a metal fixture on the roof of dimensions 1 ft x 2 ft with a base 1 ft above the roof. The third target sits atop a cardboard box. Within the plastic tent on the left-hand side of the picture is the scanning platform used to create the synthetic aperture, the first node of which is located at

the bottom corner of the scanning platform on the side closest to the operator. The laptop used to control the scanning platform can also be seen.

A scan is performed to create a synthetic aperture of dimensions 130 cm x 130 cm. A larger scan would have been performed, but for some mechanical difficulties with the scanning platform. The nodes in the grid that make up the synthetic aperture are spaced at intervals of 3.33 cm with respect to the azimuth axis and 2.5 cm with respect to the elevation axis. The scan takes 2 hours to complete with the motors rotating to advance the base platform and the antenna mount 0.6 inches per second and pausing for 0.4 seconds at each node.

The microASAR module stores backscatter data for hundreds of pulses at each node and indexes the data to the corresponding nodes with the aid of the control software. A rendering of the processed data is provided in Fig. 6.2. The rendering is a three-dimensional image comprised of transparent tiles that represent different regions within the imaged volume that are tinted in accordance with the backscatter magnitude originating from those regions. The rendering is made with the VOL3D shareware tool for MATLAB [70].

The three targets in the three-dimensional rendering of Fig. 6.2 correspond to the three targets pictured in Fig. 6.1. In interpreting Fig. 6.2, care must be taken since the voxels are approximately twice as long with respect to range as they are with respect to azimuth and elevation, as discussed in the caption, where the dimensions of the volume imaged are given. The three targets appear as expected with respect to range and azimuth, and, as expected, the third target, which sits atop the large box in Fig. 6.1 is higher than the other targets.

6.1.1 Target Verification

Target #1 is much fainter than the other two targets, as expected. The radar cross section σ of a trihedral corner reflector is provided by:

$$\sigma = \frac{12\pi a^4}{\lambda^2}, \tag{6.1}$$

where a is the side dimension of the corner reflector. Since the side dimension is increased by a power of 4 in Eq. 6.1 and the ratio of the large (48 mm) corner reflectors to the small

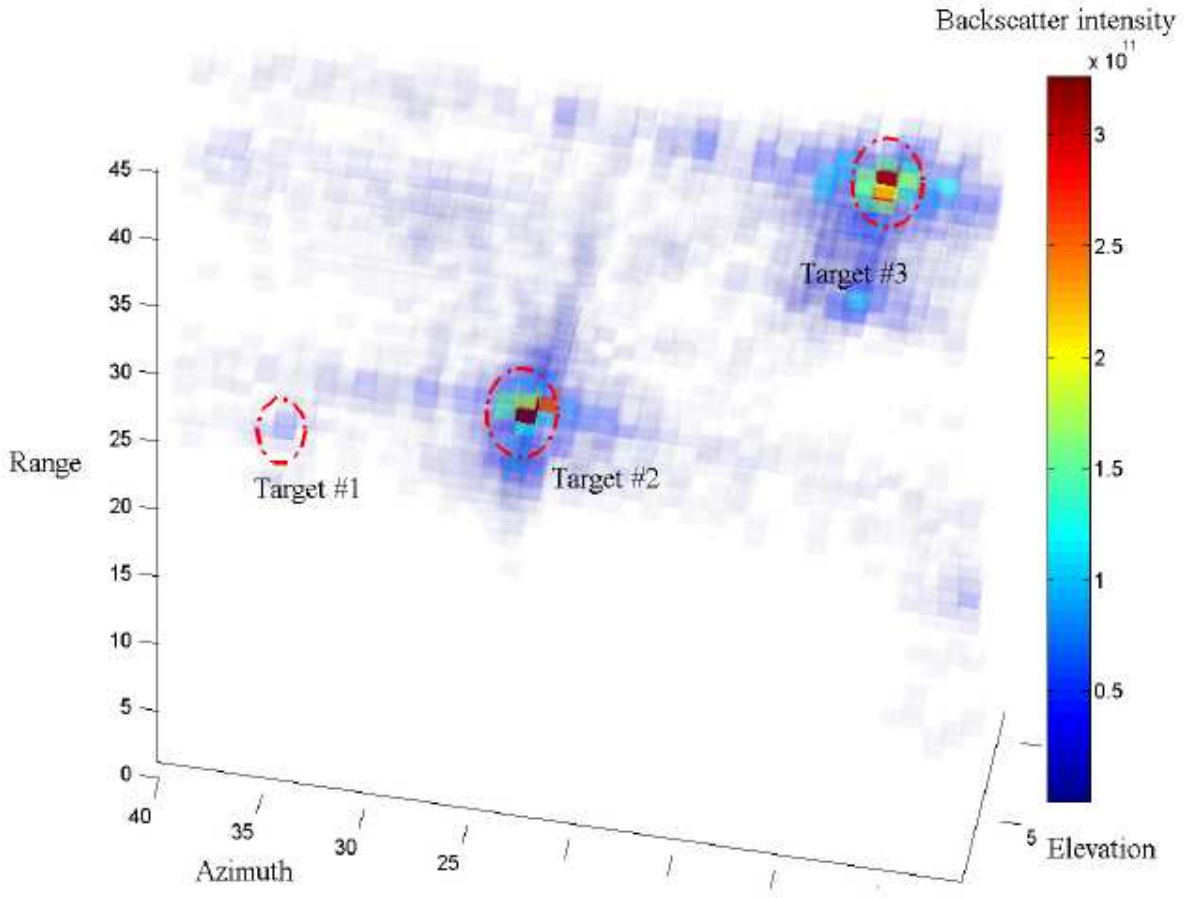

Figure 6.2: Three-dimensional rendering of processed data captured from the range depicted in Fig. 6.1. The targets are numbered, with Target #1 appearing much lighter because of its reduced size. The range, azimuth, and elevation axes are rendered according to voxel numbers. However, the dimensions of the voxels differ for the different axes. Each voxel represents 40 cm along the range axis and 21.5 cm along the azimuth and elevation axes. Voxels are counted from the bottom right corner of the grid generated from the scanning platform. The image encompasses a volume from 0 m to 18 m down range, from -5 m to 3.5 m across azimuth, and from -0.72 m to 1.5 m across elevation. These measurements are taken with respect to the origin for the image, defined as the position of the first node in the grid that makes up the synthetic aperture.

corner reflector (21.5 mm) is 2.2, the larger reflectors should be about 23 times as bright. The response for Target #1 seems to be even greater than the value predicted by Eq. 6.1 because of the pile of very wet, dense snow atop which it sits. In a similar experiment (not reported here), the response from snow of lower water content and density is found to rival the response from a 21.5 mm corner reflector. The theory that the snow pile contributes to the return of the small corner reflector is supported by the fact that the brightest return appears to come from below the height at which the small corner reflector sits. Closer inspection of Target #2 from the proper angles (not shown in Fig. 6.2) reveals it to be the brightest target, as expected because of the metal fixture atop which it sits and which elongates its reflection with respect to elevation.

To ensure that the targets appearing in Fig. 6.2 correspond to the targets pictured in Fig. 6.1, their location, as reported by the imaging voxels, is verified. The location of each target on the range is measured with respect to range, azimuth, and elevation relative to the center of the antenna mount, where the antenna mount rests at the first node position in the grid of nodes used to create the synthetic aperture. The location of each target is determined in the image by means of the voxel count along each axis.

In Fig. 6.2, Fig. 6.3, and Fig. 6.4, the voxels are created by an interpolation factor of 2 applied to a predetermined, range-specific set of resolutions, so that the dimensions of each voxel are half the allowable resolution with respect to each axis. The maximum range in these figures is less than 20 m, which according to Eq. 4.7 and Eq. 4.8 corresponds to azimuth and elevation resolutions of 43 cm. To determine the location of each target with greatest accuracy from the images produced by the data, the location around where each target should appear is imaged with an interpolation factor of 2, but with the range-specific resolution corresponding to each target calculated according to Eq. 4.7 and Eq. 4.8. The target-specific range resolutions vary from 19 cm to 37 cm.

The location of each target with respect to each axis is determined by finding the center of the voxel with the brightest return, counting the number of voxels to this brightest voxel, multiplying the distance per voxel along the respective axis, adding the location of the initial voxel, and adding an axis-specific half distance to place the return in the center of the brightest voxel. In the event that the brightest voxel is flanked by one or more equally

bright, or very bright voxels, further additions and subtractions of appropriate weight are made to find the target center.

Tables 6.4, 6.2, and 6.3 compare the physical measurements of each target, with respect to all three axes, to the voxel-dependent location for each target in the images rendered from the data. Comparison of the physical measurements to the voxel-based determinations reveals that for all but two exceptions, the two forms of measurement agree to within about half the resolution distance along the corresponding axis. The biggest exception, the 54 cm discrepancy between the elevation measurements for Target #1, has a good explanation. Although the imaged bright spot appears low relative to the physical measurement for Target #1, the bright spot can be explained by the thick mass of wet, dense snow atop which Target #1 sits.

Table 6.1: Comparison Between Physical Measurements and Voxel-based Determinations of the Location of Target #1.

	Range	**Azimuth**	**Elevation**
Physical Measurements	9.04 m	2.44 m	0.01 m
Voxel-based Determinations	9.00 m	2.35 m	-0.55 m
Resolution	0.80 m	0.19 m	0.19 m

Table 6.2: Comparison Between Physical Measurements and Voxel-based Determinations of the Location of Target #2.

	Range	**Azimuth**	**Elevation**
Physical Measurements	10.57 m	-0.48 m	0.20 m
Voxel-based Determinations	10.45 m	-0.38 m	0.20 m
Resolution	0.80 m	0.22 m	0.22 m

The results in Tables 6.4, 6.2, and 6.3 verify the three-dimensional imaging capabilities of the preliminary system. The centers of the three targets are located within half the resolution distances along all three axes, with exceptions being either slight or explainable.

Table 6.3: Comparison Between Physical Measurements and Voxel-based Determinations of the Location of Target #3.

	Range	**Azimuth**	**Elevation**
Physical Measurements	17.22 m	-4.45 m	1.00 m
Voxel-based Determinations	16.70 m	-4.45 m	1.20 m
Resolution	0.80 m	0.37 m	0.37 m

The azimuth and elevation resolutions for the three targets are 19 cm, 22 cm, and 37 cm, or 7.5 inches, 8.7 inches, and 14.6 inches. Therefore, the preliminary system has demonstrated that it can be consistent with the requirements of ultra-high-resolution (measured in inches), three-dimensional imaging. Should the synthetic aperture be extended to the full dimensions of 180 cm x 180 cm that the scanning platform can allow, the resolution for the first target could be dropped as low as 3 inches at 5 m.

6.1.2 Problem of Bleeding as Uncovered by Three-dimensional Imaging Demonstration

With the ability of the preliminary system to image volumes in three dimensions with ultra-high resolution along two of the three axes, the data generated by the system can be examined for advantages that can be capitalized on and obstacles that need to be overcome. The ability to achieve resolution in inches is certainly an advantage, with 3-inch resolution corresponding to the thickness of some of the smaller and more interesting layers within a snowpack. However, examination of Fig. 6.2 reveals a problem.

Apart from the three targets circled in Fig. 6.2, the next most dominant features are the blue bands that extend with respect to azimuth, range, elevation. These bands are not the result of reflections from the ground. The grazing angle to the ground is shallow enough that backscatter is not reflected back to the radar system. These bands, like the hallos of color that surround the larger targets, are indicative of an important problem in ultra-high-resolution, volume images from the perspective of imaging the stratigraphy of a snowpack. If a fraction of the return from one region is added to the return of surrounding regions, the true value for the return from the two regions becomes ambiguous.

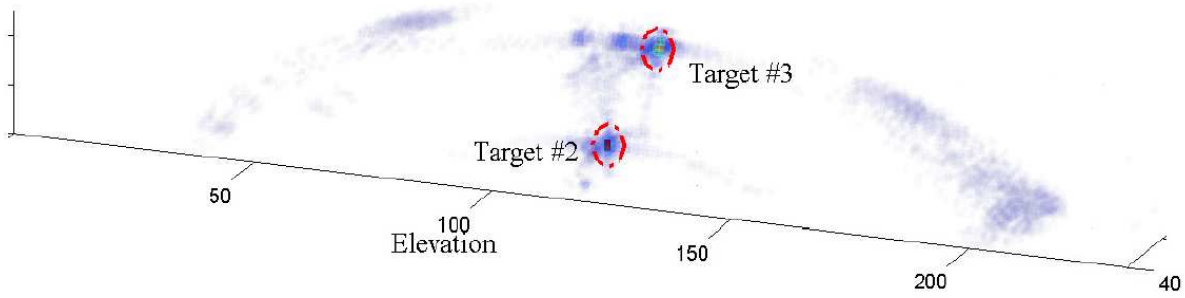

Figure 6.3: A three-dimensional rendering of the same data set used to generate Fig. 6.2 to evaluate bleeding and to check for aliasing with respect to elevation. The image encompasses a volume from 8 m to 18 m down range, from -4 m to 4 m across azimuth, and from -25 m to 25 m across elevation. Target #2 and Target #3 are labeled; Target #1 is visible as the light-blue node in front of Target #2. The 50 m span with respect to elevation should reveal any aliasing, which does not appear to be a problem.

In an effort to avoid this ambiguity, Taylor windows are applied to the three dimensions of the data. Taylor windows weight data according to a distribution similar to a Gaussian bump. A Taylor window is applied to the chirped frequencies in each pulse; another is applied to each column in the synthetic aperture; and, yet another is applied to each row in the aperture. The rendering in Fig. 6.2 includes the application of these Taylor windows. However, they provide little improvement over the rendering where they are not applied. The most noticeable difference, which is difficult to detect, is a slight suppression of the bleeding with respect to range due to the Taylor window over the chirped frequencies.

Additionally, 50 m spans are imaged for each dimension to determine with respect to which axis the problem is worse and to determine if aliasing, the phenomenon whereby the signal from one location appears in another, contributes to the problem. A rendering of a 50 m span across the elevation and azimuth axes is provided below in Fig. 6.3 and Fig. 6.4, respectively. The image of the 50 m span with respect to range is not included.

Comparison of the 50 m spans with respect to elevation and azimuth in Fig. 6.3 and Fig. 6.4, respectively, suggests that some of the bleeding is due to aliasing in azimuth. Although the presence of blue arches in Fig. 6.3 is undeniable, they are much less pronounced than those in Fig. 6.4. The darkest manifestations appear in the uppermost arch, which is unrelated to the targets and corresponds to fixtures on the edge of the roof that are more

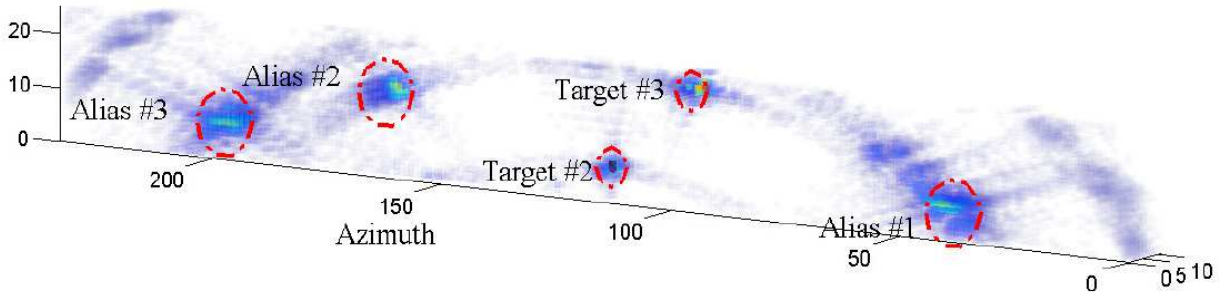

Figure 6.4: A three-dimensional rendering of the same data set used to generate Fig. 6.2 to evaluate bleeding and to check for aliasing with respect to azimuth. The image encompasses a volume from 8 m to 18 m down range, from -25 m to 25 m across azimuth, and from -4 m to 4 m across elevation. Target #2 and Target #3 are labeled; Target #1 is not visible. The 50 m span with respect to azimuth reveals a problem with aliasing.

visible in the 50 m range span (not shown). Along the trajectory of the bands corresponding to the two bright targets in the elevation span, there are no secondary bright spots which would indicate aliasing.

The darker arches visible in Fig. 6.4, corresponding to the azimuth axis, can be explained by the presence of aliasing. Three major examples of aliasing, each labeled, manifest themselves in Fig. 6.4. The math of $30° - 60° - 90°$ triangles reveals that anything outside the central 10.5 m (1/5 of the 50 m span) at the bottom of Figs. 6.3 and 6.4 and outside the central 24.5 m (1/2 of the 50 m span) at the top of the figures is outside the 30° main beam corresponding to any of the antenna positions. Therefore, the bright spots labeled as examples of aliasing, which are all outside the regions accessible by the main beams, must be due to aliasing as opposed to physical scatterers.

Alias #1 and Alias #3 derive from a scatter at the roof's edge that is clearly visible in the 50 m range span (not shown). Alias #2, however, which is in the arch associated with Target #3, derives from Target #3. As with the bright spot corresponding to the actual target location, the aliased version has dark bands extending on either side that end up contributing to the dark bands from the original target.

These bands from the aliased bright spots can provide an explanation for why the bands are darker with respect to azimuth. The spatial sampling frequency of 2.5 cm with

respect to elevation is greater than the spatial sampling frequency of 3.33 cm with respect to azimuth. The spatial sampling frequencies reflect the dimensions of the horn antennas with respect to azimuth and elevation, as required by Eq. 4.62. However, the effective aperture appears to be the same for both dimensions, since the beam width is 30° for both dimensions. Applying a 30° beam width to the beam width equation reveals that the effective aperture is actually 4.6 cm for each dimension, which would explain the aliasing with respect to azimuth and suggest even finer spatial sampling with respect to elevation.

Although improved spatial resolution can prevent some of the bleeding in Fig. 6.2, it does not entirely solve the problem. However, the bleeding seems to behave in predictable ways, describing arches with contours that depend on the position of the scatterer from which they originate and falling off in intensity at predictable rates. A processing algorithm needs to be developed to remove the bleeding to ensure that fractions of the backscatter associated with the scatterers from one region are not added to the backscatter from adjacent regions.

6.2 Demonstration of Non-nadir, Volume Imaging of a Snowpack

Two field deployments are arranged to demonstrate the repeatability of non-nadir, volume imaging of a snowpacks with the preliminary system. The demonstration of non-nadir, volume imaging of a snowpack is not a trivial matter. Although wavelengths transmitted at nadir have been shown to interact with snow packs across several bandwidths to produce backscatter at electromagnetic boundaries within the snowpack [1]–[10], a non-nadir image of snowpack volume relies on the different phenomenon of volume scattering to produce backscatter. Although theory and other types of measurements suggest volume-scattering-based images are possible, such images have yet to be demonstrated. Questions also arise as to whether backscatter from the ground will drown out the signal from the snow. These questions are addressed by the non-nadir, volume images of the snowpack provided by the preliminary scanner.

6.2.1 First Field Deployment

Special thanks are in order to Snowbird Ski Resort for its cooperation with this research project. The preliminary system is first deployed on February 9, 2010 in an overflow parking lot at the Resort. A second field deployment is made at this same site on February 23,

2010. The deployment site is selected because of the opportunity it affords for uninterrupted views of an alpine snowpack reposing on a gentle slope of sufficient size to entirely occupy a volume defined by the range-dependent resolution limits of the preliminary system. The snow from the parking lot is plowed away from and not pushed into the slope in a way that avoids a mass of dense ice that would distort the signal. A picture of the location is provided in Fig. 6.5.

Field Deployment Set-up

The scanning platform and the microASAR of the preliminary system require supporting infrastructure when they are deployed. This infrastructure, with its components and connections, is depicted in Fig. 6.6.

The grid used to create the synthetic aperture for the deployment on the first day spans 140 cm x 140 cm, with nodes separated by 2.5 cm with respect to elevation and 3.33 cm with respect to azimuth. (Unfortunately, the scan discussed in Section 6.1, demonstrating three-dimensional imaging, was not processed until after the first field deployment and the knowledge about the need to increase spatial sampling frequency is not applied, as is apparent in the aliased images of the snowpack that can be rendered from the data.) Again mechanical problems with the scanning platform and time constraints prevent a synthetic aperture of larger dimensions from being created. To ensure a metal lip at the tailgate end of the truck bed does not interfere with the scan, the grid is set to begin from the very top of the scanning platform at the tailgate end of the truck. Therefore, the origin from which all locations are measured in any images rendered from the data is in the upper corner of the scanning platform nearest the snow.

Due to an exceptionally poor snow year, the depth of the snowpack during the first deployment is measured to be only 4 ft 2 inches (127 cm). The range resolution of the preliminary system is so poor (0.8 m) as to almost encompass this depth. Therefore, to image the snowpack, the superior, range-dependent resolution with respect to azimuth and elevation are relied upon. To harness the resolutions along these axes, the scanning platform is oriented so that the range direction cuts through the snowpack almost parallel to layers within the snowpack at its base. The orthogonal azimuth and elevation directions cut across

Figure 6.5: Site of field deployments on the day of the first deployment, with the one-and-half ton diesel truck, on which the scanning platform is deployed, in the positions from which the truck and the platform are located during the scan. When the truck and scan were initially positioned, the parking lot was essentially free of cars for more than 100 m downrange of the truck. During the course of the scan however, vehicles parked as close as 30 m in a region to the front of the truck cab, but were removed by the end of the scan.

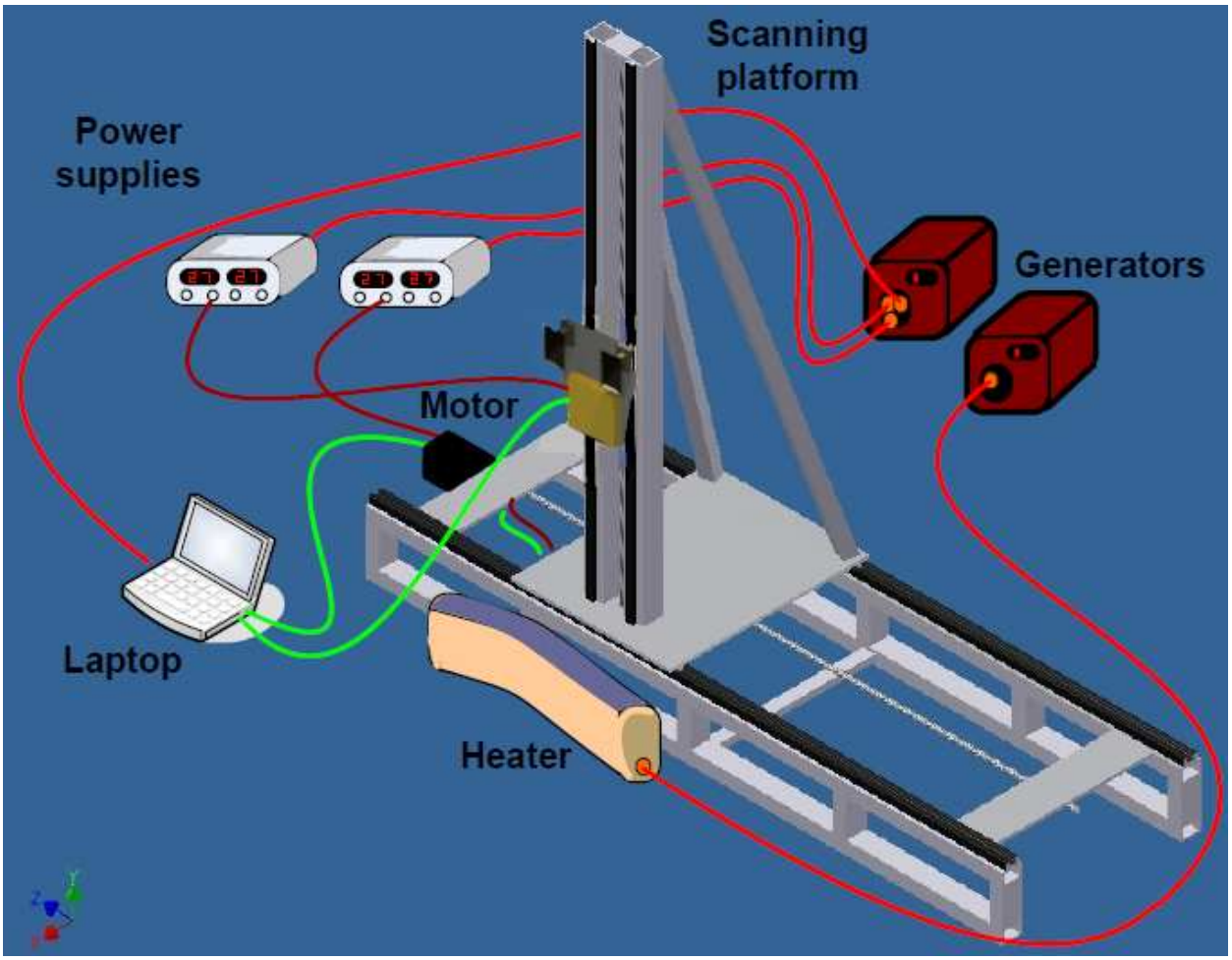

Figure 6.6: Components and connections necessary to deploy the preliminary system in the field. The infrastructure includes two generators, each providing just over 1500 Watts of AC power and two DC power supplies, providing 2.7 Amps at 27 Volts to the radar and a similar current at 35 volts to the motors on the scanning platform via the dark red cords. The motors, one visible at the far end of the scanning platform and the other (not visible) located under the base plate, are connected serially, both in terms of their power supply and in terms of their communication links. Also included is a laptop used to set up the scanning grid, control the motors, retrieve position information from the motors, and relay that information to the microASAR module, via communication cables depicted in bright green. A 1500 Watt space heater warms the plastic tent in which the scanning platform is deployed to keep the platform warm and to prevent binding. Fortunately, the truck bed is large enough to hold this tent.

Figure 6.7: View along the snowpack into the scanning platform, providing orientation for the axes along which the three-dimensional images are rendered and picturing characteristics of the snowpack that can be demonstrated in those images.

the layers so that they can be imaged. The more shallow the slope, the more the elevation direction becomes perpendicular to the layers of the snowpack. A picture, as provided in Fig. 6.7—looking along the snowpack into the scanning platform—aids in an understanding of this orientation.

A vector normal to the surface of the plastic tent, extending forward along the range direction from bellow the tent cuts through the snowpack at its base for a great distance before traversing layer boundaries and a greater distance before exiting the snowpack. The same is not true for a vector along the elevation axis, which quickly traverses layers and strikes the ground after traversing a distance just over that of the snow's depth.

First Demonstration of Non-nadir, Volume Imaging of a Snowpack

Figure 6.7 pictures important characteristics of the snowpack that manifest themselves in the data. First, the slope of the snowpack is shallow, 20° at most. Second, the slope is non-linear, having a concave shape. Third, the headwall of the snowpack slowly advances across azimuth as range increases. Fourth, as range increases, the height of the headwall relative to the synthetic aperture decreases due to a slight downward slope in the bed on which the snowpack rests. Fifth, the distance, along the range axis, from the bottom corner of the synthetic aperture closest to the snow is 6.5 meters (as determined by approximate measurement).

Additional characteristics about the snowpack become visible when it is viewed from the opposite direction. This view, from behind the scanning platform, is provided in Fig. 6.8. The view from behind the scanning platform has the added advantage of providing the view that the synthetic aperture sees. As shown in Fig. 6.8, sixth, the snowpack has a shelf of about two meters at its base where the slope is very gentle. Seventh, the headwall and the bed of the slope bend inward. All seven of these characteristics, including an eighth, the depth of 4 ft 2 inches, can be demonstrated in the images generated from the data captured by the scan.

Table 6.4: Important Snowpack Characteristics

	Characteristic
1	Shallow slope (20° at most)
2	Concave shape to slope
3	Snowpack headwall advances across azimuth with increasing range
4	Slight downward tilt with increasing range
5	6.5 m to snowpack along range from closest corner of synthetic aprerture
6	2 m shelf at the base of the snowpack
7	Headwall and slope bend inward
8	Depth of 4 ft 2 inch

Table 6.7 reviews the eight characteristics of the snowpack as demonstrated in three-dimensional images rendered from the scan. Different rotations of a three-dimensional image

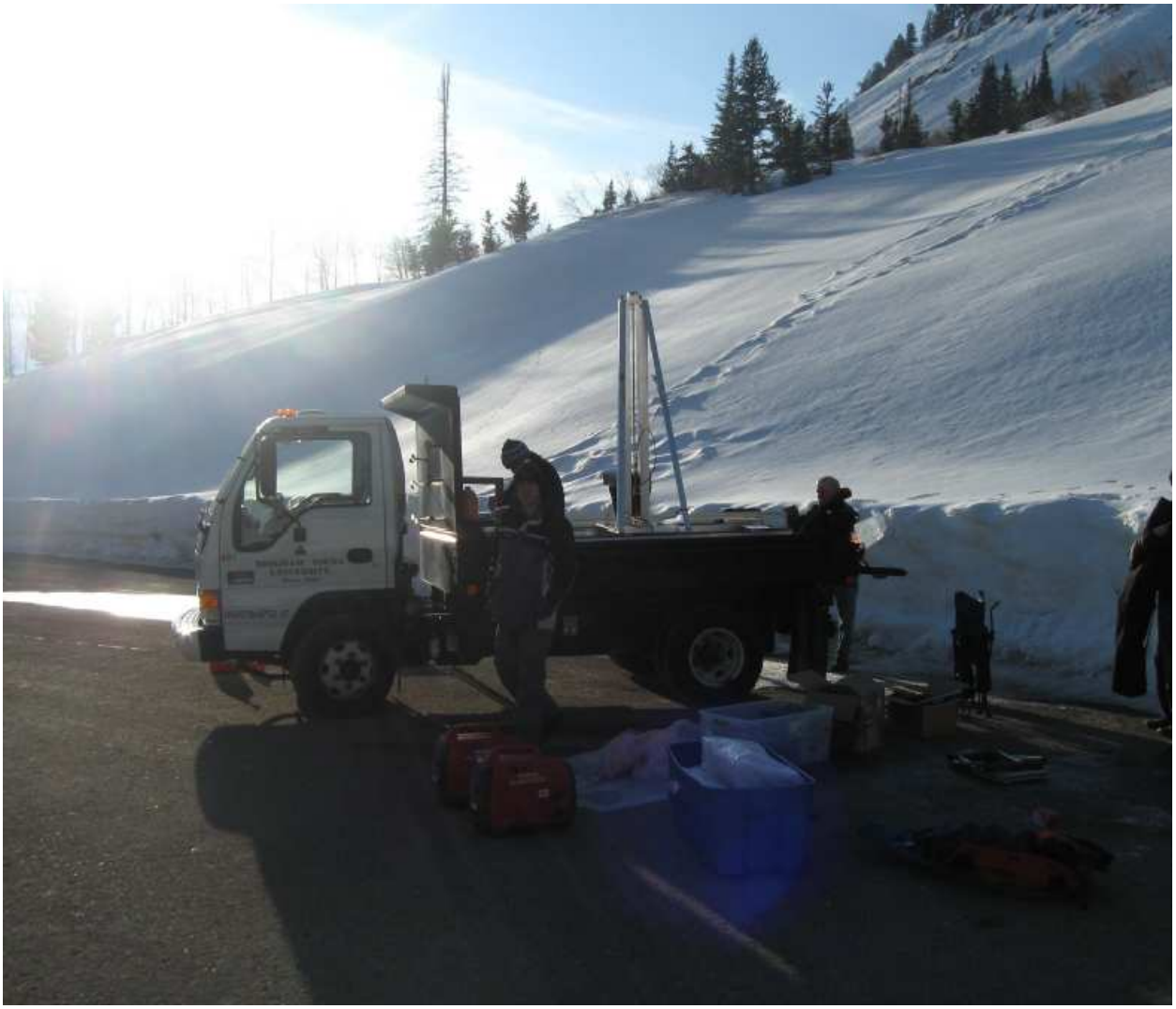

Figure 6.8: View from behind the scanning platform, picturing additional snowpack characteristics that can be demonstrated in images of the snowpack.

are rendered in Figs. 6.9 through 6.12 over a volume covering a large portion of the snowpack pictured in Figs. 6.7 and 6.8.

Along azimuth and range, the image spans from -5 m to 7 m and from 6 m to 18 m respectively (a 12 m span, approximately 40 ft, along these axes). Along elevation, the image covers a span from -5 m to 1 m. With respect to azimuth and elevation an interpolation factor from just over 2 to just under 1 is applied across these axes. With respect to range, an interpolation factor of 5.335 is employed. Along all three axes, each voxel represents 15 cm. The data is windowed to only report returns greater than 1.2×10^9 to clarify the image.

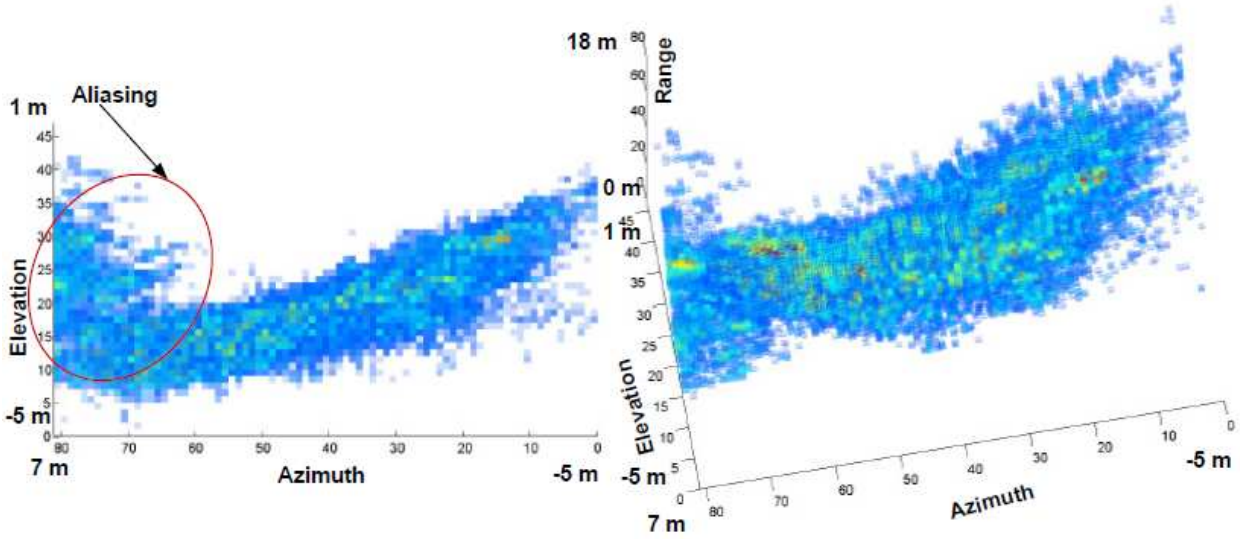

Figure 6.9: First set of rotations of a three-dimensional image of the snowpack from the first deployment. The image covers an area of 40 ft x 40 ft; a span from -7 m to 5 m with respect to azimuth, a span from 6 m to 18 m with respect to range, and a span from -5 m to 1 m with respect to elevation.

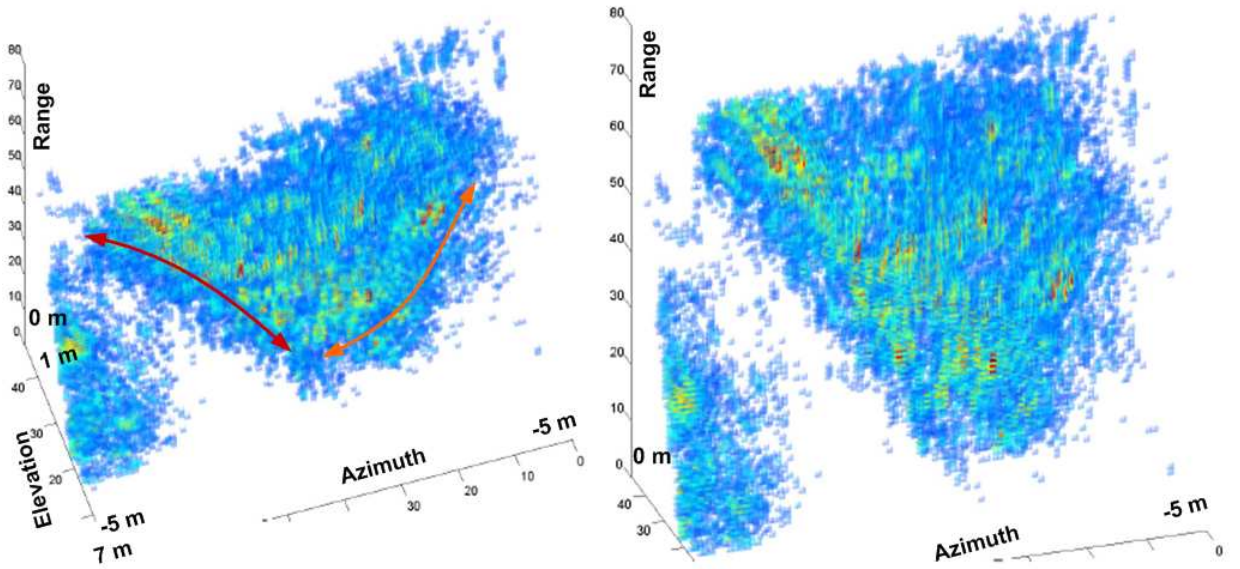

Figure 6.10: Second set of rotations of the three-dimensional image of the snowpack from the first deployment. The image covers an area of 40 ft x 40 ft; a span from -7 m to 5 m with respect to azimuth, a span from 6 m to 18 m with respect to range, and a span from -5 m to 1 m with respect to elevation. See text for a discussion of the red and orange arrows.

The first two characteristics of (1) slopes less than 20° and (2) concave slopes are illustrated in the first set of rotations in Fig. 6.9, especially in the first rotation on the left. In the left-hand corner of the first two rotations, a shape appears, circled in red on the left, that can be shown to be an aliased portion of the snowpack. The shape should be ignored in all of the rotations that follow. The rotation on the left also demonstrates (6) the shelf at the base of the snowpack and (8) 4 ft 2 inch snow depths.

The characteristic that (3) the headwall advances across azimuth as range increases is clearly demonstrated in the second set of rotations in Fig. 6.10. In the rotation on the left, the headwall is outlined in red, and the slope is outlined in orange. The (7) bend in the headwall is also visible in the rotation on the left. Although better confirmations of (4) the downward tilt as range increases can be seen in rotations not shown, the downward tilt can still be seen in the rotation on the left.

In the rotation on the right, the (3) progression of the headwall is even more clearly visible. In the second set of rotations, the overall contour of the snowpack over the large area of 40 ft x 40 ft maintains its integrity. Also, (5) the 6.5 m distance between the scanning platform and the snowpack can be seen in the way that the snowpack appears to begin just over 6 m from the synthetic aperture to the left of center in the various.

The images provided in Figs. 6.9 and 6.10, the images to be discussed in Figs. 6.11 through 6.14, and all the images that the data are capable of generating, demonstrate the characteristics of the snowpack in the right locations relative to the corner origin of the synthetic aperture. The preliminary scanner, therefore, achieves, in part, the second goal behind its design, by demonstrating non-nadir, volume images of a snowpack. Additional analysis of the images provide suggestions about how better images can be acquired in the future, furthering the aims of the second goal.

Avoidance of Ground Signals at Shallow Grazing Angles

Since the largest constituent of snow by volume is air, a fear exists that the signal from the potentially moist ground and angular rock surfaces under a snowpack might drown out the signal from the snow, or might be very difficult, if not impossible, to decouple from the snow signal. However, the snowpack appears to float in the air for all of the rotations of

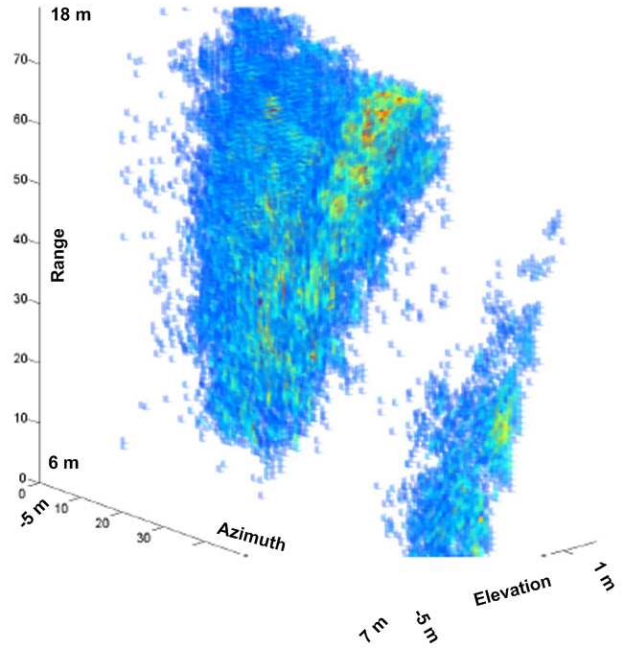

Figure 6.11: Rotation of a three-dimensional image showing the underside of the snowpack from the first deployment.

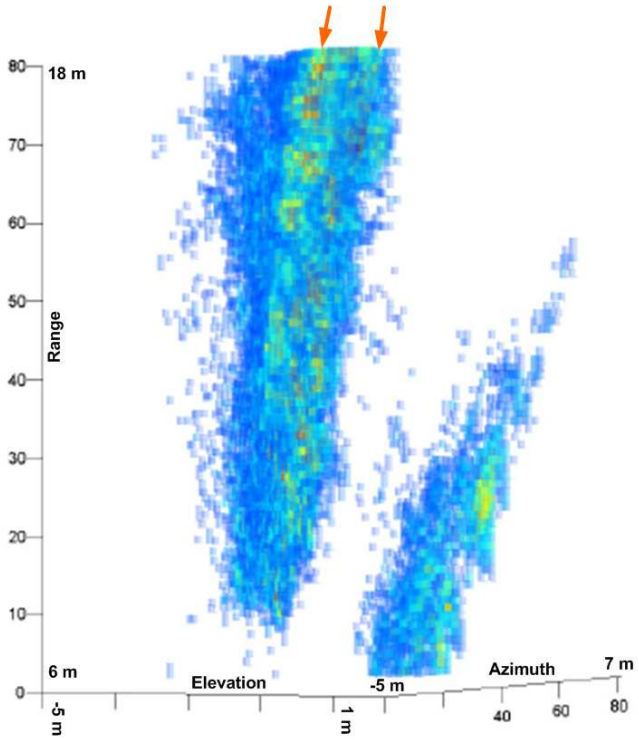

Figure 6.12: Rotation of the three-dimensional image showing a layered structure for at least 40 ft along the headwall of the snowpack at its base (from first deployment). The orange arrows indicate location and orientation of layers visible in the image.

its image, with no apparent indication of presence of the ground. Perhaps this observation becomes most apparent when reviewing Fig. 6.11, depicting the underside of the snowpack, with the portion closest to the the radar system at the bottom of the figure.

It would seem that the shallow grazing angles with respect to the ground, as determined by the orientation of the scanning platform, generate specular reflections that transmit energy away from the radar system. As a result, the ground, like the gravel on the roof pictured in Fig. 6.1, does not stand out.

That the ground does not appear in short range images, bodes well for the development of longer range systems. An inability to decouple returns from the snowpack and the ground could have ruled out the concept of a radar-based avalanche-prediction system. Since the grazing angles should be shallow for remote, large-area radar-imaging systems, the ground signal is likely not to present problems in images produced by longer-rang, larger-area systems.

Analysis of Layered Structure and Other Issues

With a demonstration of non-nadir, volume images of a snowpack, interest turns to the question of the ability of the images to reveal layers and what this bodes for future systems at much higher frequencies and sensitivities to snowpack strata. As seen in Fig. 6.8, a relatively flat shelf extends along the base of the snowpack. Since the range dimension runs parallel to the snowpack in this region, the shelf at the base of the snowpack is the most likely region where layering would be visible in images of the snowpack.

In the steeper regions of the snowpack, the snowpack becomes rotated so that the coarse azimuth resolution cuts into the snowpack, commingling backscatter from adjacent layers in the returns. Since the shelf along the bottom of the snowpack extends around 2 m into the snowpack, the 80 cm range resolution remains parallel to the snowpack for multiple resolution cells, reducing the likelihood of commingled returns. Therefore, layers are most likely to appear in the base region.

A good view of the base region is achieved by rotating the underside-snowpack view in Fig. 6.11. In Fig. 6.11 the base region along the headwall extends diagonally, upward and to the right along the snowpack image, just above the aliased shape. Fig. 6.12 makes the

headwall even more visible by further rotating the snowpack image so that the full height of the headwall can be see all along the distance it traverses. At the base of the snowpack, all along the headwall in Fig. 6.12, a layered structure is clearly visible. The layered structure comprises a band of cool returns sandwiched between two bands of bright returns (see orange arrows). This layered structure extends at least 40 ft in the region where a layered structure would most likely be present.

The layered structure at the base of the snowpack becomes more clear when it is, in effect, low-pass filtered in an image rendered from only the last 23.33 cm of the scan with respect to azimuth (creating a synthetic aperture of 23 cm x 140 cm). Figure. 6.13 provides an imaged slice from such an aperture. Incidently, Fig. 6.13 demonstrates (8) the 4 ft 2 inch depth of the snowpack, (6) the shelf at the base of the snowpack, (1) slopes in the neighborhood of 20°, and the (6) concave contour.

Three main features stand out from the filtered image of the snowpack provided in Fig. 6.13. First, two bands along the shelf of the snowpack, indicated by red arrows, appear to differentiate layers within the snowpack. Second, a bright spot appears in the middle of the image. Third, to the right of the bright spot, the top and bottom layers appear to be replaced by a single layer of strong return in the middle of the snowpack.

The left- and right-hand sides of Fig. 6.13 suggest conflicting things about the structure of the snowpack. On the left, three distinct layers are suggested, namely, top, bottom, and middle, with the top and bottom layers being the brightest. On the right, a top, bottom, and middle layer are also suggested, but the middle layer is brightest and the top and bottom are faint.

One possible explanation for the discrepancy is that on the left-hand side, the shelf of the snowpack is imaged, whereas on the right-hand side, the steeper upper portion of the slope is imaged. For the shallow shelf portion, the range direction runs parallel to the snowpack. However, as shown in Fig. 6.8, the steeper upper slope wraps in front of the synthetic aperture so that the range direction starts to cut through the snowpack toward the ground. As this happens, more of the snowpack is imaged along the range direction as opposed to the elevation directions. The poor resolution with respect to range makes

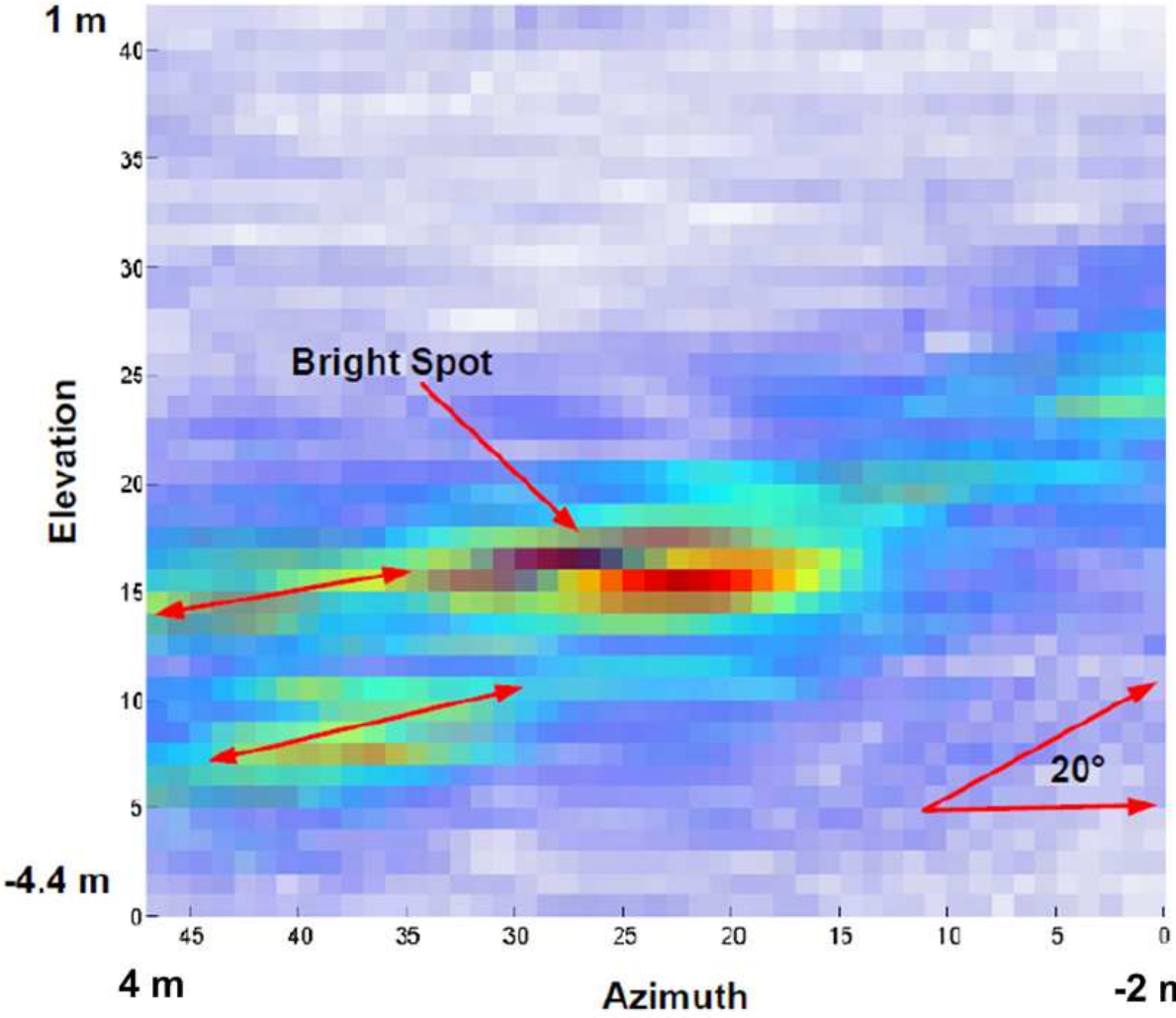

Figure 6.13: A three-dimensional rendering of the snowpack in Fig. 6.8, generated from only the final 23.33 cm of the scan positions with respect to azimuth (creating a synthetic aperture of 23 cm x 140 cm). The image brings out the more prominent structures of the snowpack and looks downrange from from behind the scanning platform at a slice 11.5 m to 14.4 m out. The dimensions of the slice along azimuth and elevation are as displayed. Voxels with respect to azimuth and elevation cover distance of 13 cm along each axis. See the text for a discussion of the red arrows.

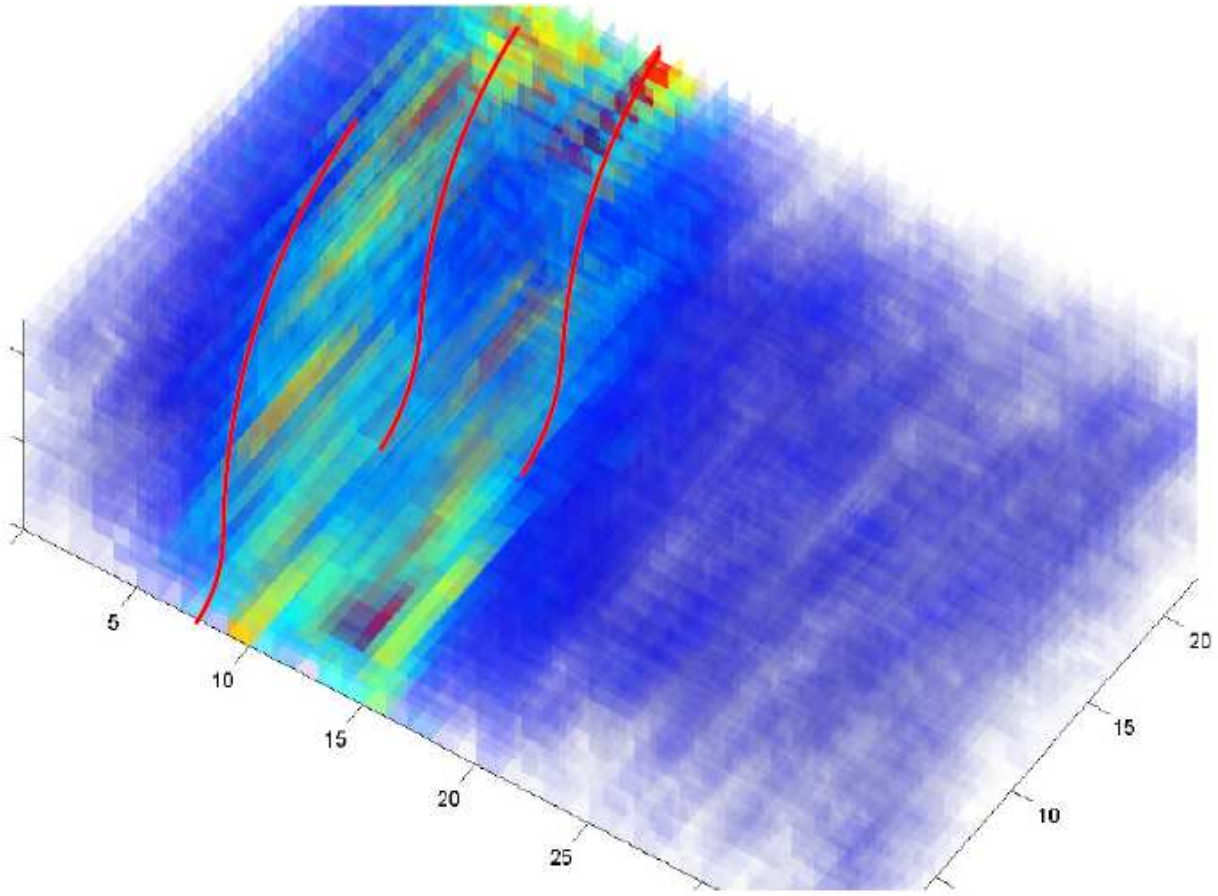

Figure 6.14: A three-dimensional rendering of the bottom shelf of the snowpack from the last 23.33 cm with respect to azimuth of the scan, to better bring out layered structure. The rendering is rotated at an angle that best displays the top and bottom layers within the snowpack and encompasses a span from 1.5 m to 4 m from the origin with respect to azimuth and 11.5 m to 14 m with respect to range. Red lines indicate suggested layers—see text.

the layers difficult to distinguish as the signals from the layers that are near to one another commingle in cells of range resolution.

The distances over which the layered structure on the left-hand side maintains integrity suggest that the layered pattern arises from something real in the snowpack. Figure 6.15 depicts an area of 3.5 m with respect to azimuth and 2.5 m with respect to range (8.2 ft x 11.5 ft). The filtered image is rotated to best demonstrate the integrity of the structure. The region depicted in Fig. 6.15 is not the only region where the layered structure manifests. Images of the layered structure can be generated along the entire bottom shelf of the snowpack, as demonstrated by Fig. 6.12.

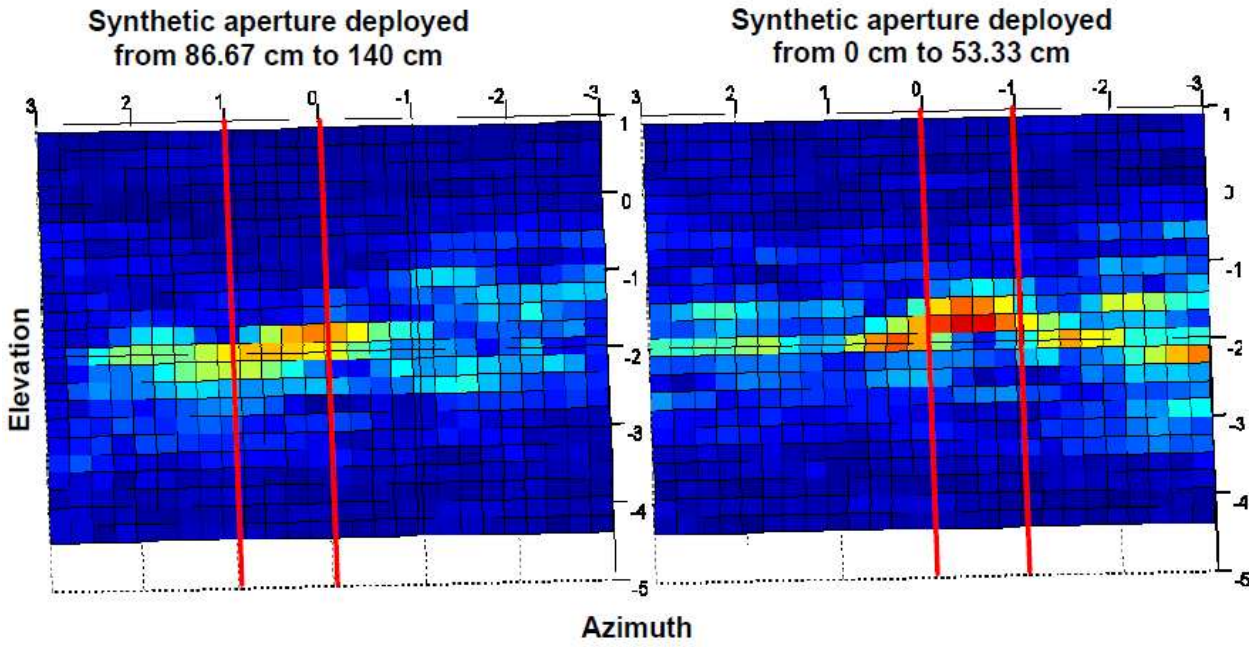

Figure 6.15: Comparison of two slice plots of an image of the bottom shelf of the snowpack at a range of 10 m. Azimuth and elevation with respect to the imaging origin are as depicted on the plots. The plots correspond to two different synthetic apertures with azimuth spans from 0 cm to 53.33 cm and from 86.67 cm to 140 cm. As expected the bright spot shifts by about 1 m. The resolution with respect to azimuth is 52 cm due to the short azimuth dimensions. The red lines delineate different spans of a meter in length on either side of the original origin of the synthetic aperture.

Returning to the features identified in Fig. 6.13, the bright spot appears to be an artifact from the antenna gain pattern of the small antennas. The antenna gain pattern ensures that the strongest returns come from scatterers closest to a point directly in front of the center of the synthetic aperture, as occurs with the bright spot in Fig. 6.13. This theory is supported by changing the center of the synthetic aperture. The center of the synthetic aperture can be changed by only processing the data from positions pertaining to two different spans of the overall grid of positions collected with respect to azimuth. The results of such processing are depicted in Fig. 6.15.

Figure 6.15 compares the position of the bright spot on the shelf of the snowpack at a distance of 10 m when the first 53.33 cm of the synthetic aperture is processed and when the last 53.33 cm is processed. The centers of the synthetic apertures corresponding to the

two images are separated by 86.67 cm. Therefore, a bright-spot shift of a little less than a meter is expected. As expected, the bright spot shifts about a meter, with the bright spot shifting from a region between the -1 m and 0 m marks to a region between the 0 m and 1 m marks. The course resolution in Fig. 6.15 arises because of the short azimuth spans of the two synthetic apertures. Future systems need to address the issue of bright spots. As is clear from Fig. 6.13, a bright spot drowns out sensitive information about snowpack structure.

Attribution of Possible Physical Properties to the Layered Image Structure from the First Deployment

That the preliminary system suggests an ability to detect different physical layers is important to the overall goal of assisting in avalanche detection. However, it is important to determine to what physical properties the radar system might be responding. The most likely answer to this question is that the radar is responding to water content. Although water content is not the property most highly correlated with avalanche activity, it is still a property of the snowpack that could create a layer at the top and bottom of the snowpack.

Due to problems with the communication link between the laptop and the radar, the scan for the first deployment is performed in 5 blocks. Each block includes all of the vertical spans corresponding to runs of about 30 cm down azimuth. As a result of the time required to download these blocks, verify their integrity, the need to repeat sections of the scan, and certain mechanical problems, the overall scan takes from 12:00 p.m to 5:00 p.m. to complete. During this 5 hour period, the snowpack is subject to the full heat of a day on which the average temperature is 33° F, but rises as high as 42° F.

A layer of snow subjected to the sun and to these temperatures increases in water content, which causes more backscatter. In the middle regions of the snowpack, however, the insulating properties of the overburdening snow protects the mid portion of the snowpack from high temperatures. The snowpack remains frozen and dry in this region. As explained in Section 2.2.1, the only other region of the snowpack that is subject to warm temperatures is at the bottom of the snowpack. The bottom of the snowpack is warmed from the earth and can also become moist. This temperature profile, very common in alpine snowpacks, with high temperatures at the top and bottom of the snowpack and low temperatures in

between, is depicted in Fig. 2.7. A similar profile describes water content. Therefore, the increased water content at the top and bottom of the snowpack can explain the top and bottom layers in snowpack images.

A more interesting, but less likely explanation arises from two layers in the snowpack that are intimately related with avalanche formation. These are layers of faceted snow, and they are pictured in the infrared image provided in Fig. 6.16. Infrared images are useful because the intensity in an infrared image is correlated with the specific surface area of the snow crystals from which they reflect. As explained in Section 2.2.1, faceted crystals have low specific surface areas. Research has been done to determine the specific surface area of snow crystals from infrared images of snow [22]. The darker the reflection in an infrared image of the snowpack, the less specific surface area reflecting the infrared wavelengths and the more faceted the snow.

Theoretically the layers of faceted snow depicted in Fig. 6.16 could act as a waveguide. This waveguide conducts electromagnetic away from the radar system. As a result, the signal from the middle of the snowpack is relatively weak.

Lessons Learned from First Deployment

Several things can be learned from the volume images of snow produced by the preliminary scanner during the first deployment. First, a volume of snow provides a good medium for producing backscatter at non-nadir angles. As discussed, previous studies rely on nadir, normal angles of incidence and electromagnetic boundaries to generate boundary reflections [1]–[10]. However, when imaging large areas of a snow pack from a remote location, non-nadir, non-normal grazing angles, many of which are very shallow, are the norm. Specular reflections occurring at boundary layers bounce electromagnetic energy away from the radar for such scans. The preliminary system demonstrates that volume scattering can be relied upon to produce the backscatter necessary to generate the three-dimensional, non-nadir, volume images that can make a remote, large-area, radar-imaging system possible.

Second, return from the ground does not drown out the signal from the snowpack. The shallow grazing angles with respect to the ground, common for remote, large-area scans, generate specular reflections that transmit energy away from the radar. As a result, the

Figure 6.16: Infrared image (wavelengths around 930 nm) of the lower two-thirds of the snowpack during the first deployment. Two layers of dangerous faceted snow appear as dark, 4 cm bands across the snowpack.

ground does not appear to present a problem at shallow grazing angles. This finding bodes well for the development of longer range systems, removing the specter of a potentially thorny problem.

Third, wavelengths at C-band can penetrate large distances through a snowpack, suggesting that shorter wavelengths can be employed to good effect on future systems. Since the range axis is oriented almost parallel to the shelf of the snowpack, waves must travel a great distance through the snow to create the resultant images. The images generated from the data show strong reflections even after the waves responsible for those reflections have traveled several meters through the snow. Although shorter wavelengths, which would

provide much more information about snow properties and improved resolution, do not have the same penetration capabilities, the penetration capabilities of wavelengths in C-band bode well for the ability of much shorter wavelengths to penetrate the depth of an alpine snowpack.

Fourth, volume images of snow are possible at a distance. Although resolution along azimuth and elevation start to break down quickly with range for the data set provided from the first deployment, decent volume images of the snowpack can still be generated at a range of 30 m (100 ft) (not shown). Unfortunately, for the data set from the first deployment, at this distance, the resolution is reduced to 2 ft, and very little information is provided about the snow, except its presence and general shape.

Fifth, the synthetic aperture of the preliminary system creates bright spots. The bright spots favor the return from certain regions over the return from other regions, probably because of the contour of the main beam of the small antenna used to generate the synthetic aperture. These bright spots cause serious distortions in images. Appropriate windowing to flatten the contour of the main beam may help this problem.

Sixth, the images produced from the scan data are consistent with the ability of the system to differentiate between layers within the snowpack with different physical properties. The property responsible for the layered structure in the images cannot be determined with certainty. However, the possibility remains good that properties relevant to avalanche formation may be detectable, especially at the shorter wavelengths more suited to detect these properties.

6.2.2 Second Field Deployment

To further demonstrate the repeatability of images snowpack volumes and to further explore the possibility of imaging layers, the preliminary system is redeployed on February 23, 2010. To capitalize on lessons learned from the roof-scan performed on February 17th (discussed in Section 6.2.1) and to avoid aliasing with respect to azimuth, the spatial frequency is increased with respect to azimuth. For the second deployment, the nodes of the grid scanned are spaced at a distance of 2.5 cm with respect to both the azimuth and the elevation axes.

Table 6.5: Distance with Respect to Range for the Three Corner Reflectors.

Measurement	Distance
1	7.92 m
2	13.34 m
3	13.41 m

The dimensions of the scan are 150 cm with respect to elevation and 90 cm with respect to azimuth. Due to mechanical difficulties, the span of the azimuth dimension is cut short. However, the total time of the scan, taken staring at 12:00 p.m., is reduced to under two hours for most of the relevant measurements (excepting the measurements from the final 30 cm of the scan with respect to azimuth, which were also taken during a relatively cool time of the day), meaning that the snowpack undergoes less warming and is likely to have a lower water content.

Unfortunately, during the scan many more cars make use of the parking lot, with cars occupying a portion of the range as close as 50 ft to 60 ft from the scanner. These cars come and go during the scan and make a mess of the data for target distances greater than about 50 ft from the scanner.

Repeatability of Non-nadir, Volume Imaging of a Snowpack

The primary purpose of the second deployment is to verify the ability of the preliminary system to capture data from which volume images of a snowpack can be rendered. For this reason, the scanning platform is deployed at the same site as the first deployment, in relatively the same location. The depth of the snowpack increases between deployments to 5 ft 1 inch. Additionally, corner reflectors are placed on the snowpack for a final, vertical scan to verify that the masses appearing in the images are, in fact, the snowpack. Figure 6.17 pictures, from the side, the snowpack on the day of the second deployment, the relative orientation of the scanner, and the corner reflectors used in the last, vertical scan.

The picture in Fig. 6.17 can be used to discuss some important differences between the scans made during the first and second deployments, apart from the depth of the snow increasing by a foot. In an effort to image regions of the snowpack closer to the radar, thereby

Figure 6.17: Side view of the second deployment, picturing the snowpack and the relative orientation of the scanning platform during the second deployment. Three corner reflectors used to verify the location of snowpack are circled in red, with the ranges to those corner reflectors provided in Table 6.5. The man just behind the truck is taking pictures of a snow pit from which measurements of snowpack layers are made in an effort to correlate physical measurements with radar data. A snow pit adjacent to the one in the picture was dug for the first deployment.

improving resolution, the scanning platform is tilted more abruptly toward the snowpack. The tilt can be traced in Fig. 6.17 by the line described by the top of the plastic tent covering the scanning platform. Due to this tilt, the second scan captures data that allows for images much closer to the scanner.

In theory, as discussed below, the closer regions of the snowpack can be imaged—due to the more abrupt tilt—with improved resolution with respect to azimuth and elevation. The images of most value from the second deployment come from a region before the closest

Table 6.6: Measurements for the Scanning Platform Relative to the Snowpack During the Second Deployment.

Measurement	Distance/Anlge
Bottom right corner to snow	5.26 m
Top right corner to snow	13.5 m
Bottom left corner to snow	8.08 m
Top left corner to snow	16.00 m
Sideways distance to snow	1.98 m
Angle between scanner and headwall-normal	25°

corner reflector circled in red in Fig. 6.17. The images of most value from the first deployment come from a region well after the first corner reflector up until the second and third corner reflectors in Fig. 6.17.

Additionally, because of the abrupt tilt toward the snowpack, a vector along the range direction no longer runs parallel to the layers of the snowpack within the bottom shelf of the snowpack for as great a distance as it did in the first deployment. The increased snow depth has also filled in some of the shelf. Finally, the headwall may have come to more resemble an incoming wave with snow at its top overhanging snow at its bottom.

To verify that the images generated from the data correspond to the snowpack, more extensive measurements of the relative orientation of the scanning platform to the snowpack are taken during the second deployment. The distance along a vector normal to the synthetic aperture from each corner of the platform is measured. The measurements are taken with the aid of a laser pointer reflected onto the snowpack. When the distance to the point from the laser can be accessed, a measuring tape is used. Otherwise, a laser range finder is used. Additionally, the shortest distance from the nearest corner of the scanning platform to the headwall of the snowpack is measured and the angle between the azimuth track of the scanning platform and a vector normal to the headwall at the point closest to that track is measured. The results of the measurements are provided in Table 6.6. In Table 6.6, the right corners of the scanning platform are the corners closest to the snowpack.

The measurements provide a good guide to the general locations of where snowpack characteristics should appear, but cannot be relied upon for pinpoint accuracy. The absence

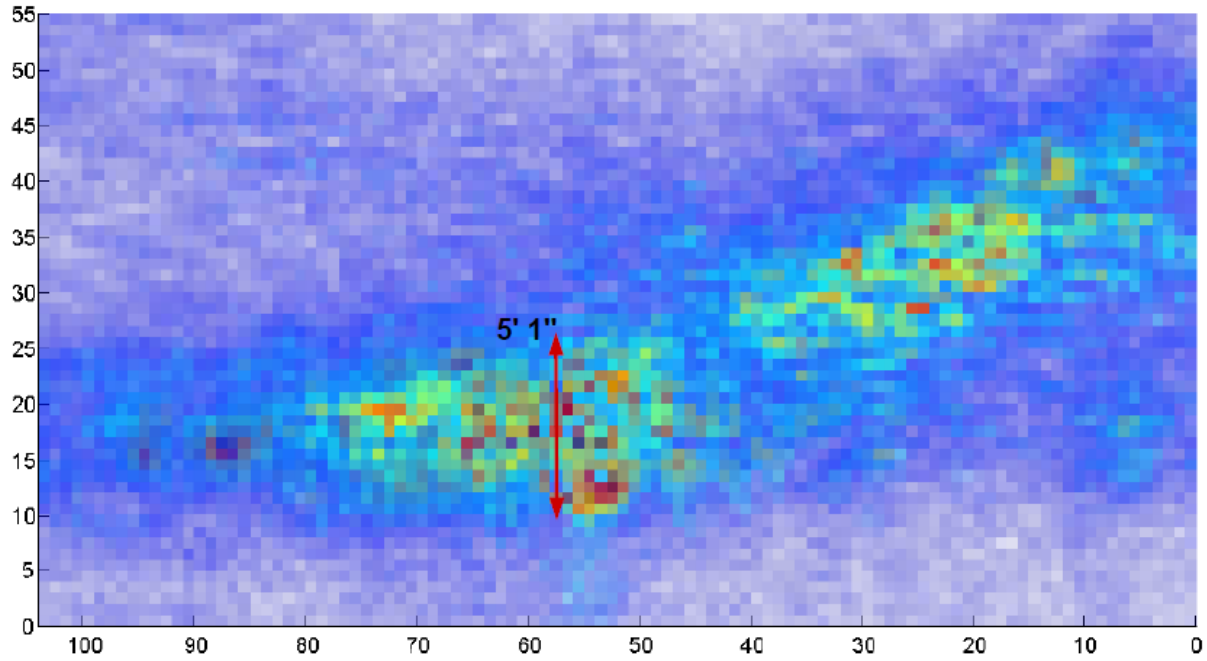

Figure 6.18: A three-dimensional rendering of the snowpack in Fig. 6.17, looking downrange from from the scanning platform at a slice 6 m to 10 m out. The dimensions of the slice along azimuth are -2 m to 7.5 m and along elevation are -3.75 m to 1.25 m, both with respect to the origin. Each voxel represents 9.2 cm with respect to both azimuth and elevation. The data is windowed to suppress the strong returns from the bright spot directly in front of the synthetic aperture.

of individual targets in the images, the possibility of a misaligned laser pointer, inaccuracies from the range finder, and all of the shallow angles involved, make accurate measurements extremely difficult despite the pains taken to obtain them. Nevertheless, the evidence is very strong that images from the first two deployments are images of the snowpacks that they purport to image. When images from the second deployment, similar to the one provided in Fig. 6.18, are compared with measurements in Table 6.6, a general agreement obtains. In interpreting Fig. 6.18, as with Fig. 6.13, it is helpful to review Fig. 6.8, which pictures the snowpack for the first deployment from a vantage point similar to that from which the images for both deployments are rendered. However, the differences between the two deployments should be kept in mind.

Similar to the way in which Fig. 6.13 demonstrates the characteristics of its corresponding snowpack, Fig. 6.18 demonstrates the same characteristics, as they are modified for the second deployment. Figure 6.18 demonstrates (8) the 5 ft 1 inch depth of the snowpack, (6) the shortened shelf at the base of the snowpack, and (1) slopes in the neighborhood of 20 degrees. The slope in the figure also describes (2) a concave contour. Characteristics (3) and (4) can be demonstrated by rotating the three-dimensional rendering. The analog to characteristic (5) can be demonstrated with an image encompassing the distance between the scanning platform and the snowpack. Again, the snowpack seems to float in the air, indicating that even at the more abrupt tilt angle of 25° returns from the ground do not present a problem.

Further comparisons between the images generated from the scans of the two deployments reveal that a bright spot also appears in Fig. 6.18. However, the bright spot appears to be about a meter from the origin in Fig. 6.18. The reason for this discrepancy is not readily apparent. In both figures, a shelf appears at the bottom of the snowpack. However, the shelf in Fig. 6.18 appears compressed relative to the shelf in Fig. 6.13. The compressed extent of the shelf in Fig. 6.18 can be explained by the more abrupt tilt with which the scanning platform faces the snowpack in the second deployment.

Ideally, the layers along the shelf as imaged in Fig. 6.13 for the first deployment could be confirmed in the images from the second deployment. Although they cannot be confirmed in Fig. 6.18, where the brightest returns from the bright spot in front of the scanning platform are suppressed, a layered structure does appear to manifest along the base shelf where the the bright spot is not suppressed, as shown in Fig. 6.19. A very clear band of almost transparent returns is sandwiched between to red bands in the region of the base, spanning a distance of about a meter with respect to azimuth. The compressed nature of the shelf due to the abrupt tilt angle of the scanning platform may explain why the pattern does not extend a greater distance with respect to azimuth. Additional layering appears in the green, transparent, green spot pattern that follows the contour of the snowpack up slope. Since the returns are so strung in the region of the bright spot, the rest of the snowpack is very muted, but still visible.

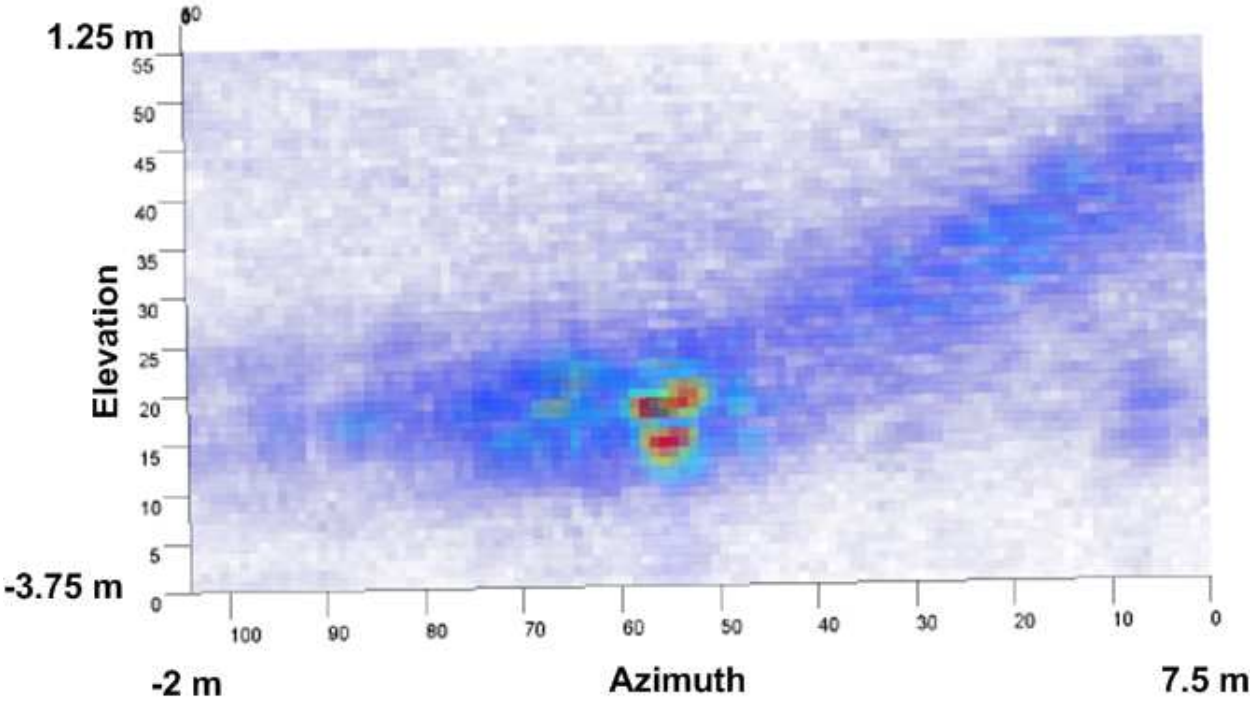

Figure 6.19: A three-dimensional rendering of the snowpack in Fig. 6.17 showing layers in the base shelf. The dimensions of the slice along azimuth are -2 m to 7.5 m and along elevation are -3.75 m to 1.25 m, both with respect to the origin. Each voxel represents 9.2 cm with respect to both azimuth and elevation. The data is no longer windowed to suppress the strong returns from the bright spot, allowing returns as high as 7 x 10^9.

Two additional similarities between the images from the two deployments exist. First, for a reason that is not readily apparent, the signal from the regions between the shelf and the upper slope is muted in the images from the two deployments. This may be due to specular reflections from layers in the snowpack oriented to conduct energy away from the radar at the transition region to the steeper, upper slopes. Second, the higher and steeper portions of the snowpack are thinner as compared to the portion of the snowpack corresponding to the bottom shelf. This may be because more of the snowpack is imaged by the range dimension, with its coarser resolution on the steeper slopes.

The images from the second deployment appear to provide ample corroborating evidence of the ability of the scanning system to produce a non-nadir, volume images of a snowpack. Additionally, although time was insufficient to run a complete scan with the corner reflectors pictured in Fig. 6.17, images from the single vertical scan (not shown) indicate

return from the snowpack concentrated between the elevations of the corner reflectors for the relevant ranges. The preliminary scanner, therefore, demonstrates the ability to image a the volume of a snowpack with repeatable verifiability. Furthermore, the image in Fig. 6.19 corroborates the layered structure at the snowpack base as seen in images from the first deployment. As before, this layered structure may be attributable to the moisture content corresponding to the daytime temperature profile of alpine snowpacks.

Attribution of Possible Physical Properties to a New Layered Image Structure from the Second Deployment

A search for layers in the snowpack is extended to the thinner upper slope for the second deployment. Happily, the closer ranges provided by the advanced tilt angle may offer improved resolutions with respect to azimuth and elevation with which to explore the image of the upper slope for layers. This improved resolution may make up for the abrupt tilt into the snowpack, avoiding the problems that made it difficult to distinguish layers in the image of the upper slope, Fig. 6.13, from the first deployment.

Careful analysis of the upper slope in the image provided in Fig. 6.18 reveals a relatively thin, bright band along the snowpack surface. Underneath this bright band is a relatively cool, thin band followed by a thick, bright band. The return under this broad band is relatively cool.

To better illustrate this pattern, thin slices are imaged, of thicknesses equal to the 80 cm range-resolution, taken from a range of 3.7 m to a range of 7.7 m. The five imaged slices are depicted below in Fig. 6.20. Light orange and blue arrows are included to suggest the proposed pattern of a thin, bright return layer, followed by a thin, cool return layer, followed by a thick, bright return layer.

The proposed bright bands are not uninterrupted. However, bright spots do line up along the proposed bands, which follow the contour of the snowpack, in the locations where they would be expected to appear in all five images. Furthermore, the pattern seems to be consistent over all five images, which cover a distance of 13 ft down range, suggesting the patterns to be more real than imagined.

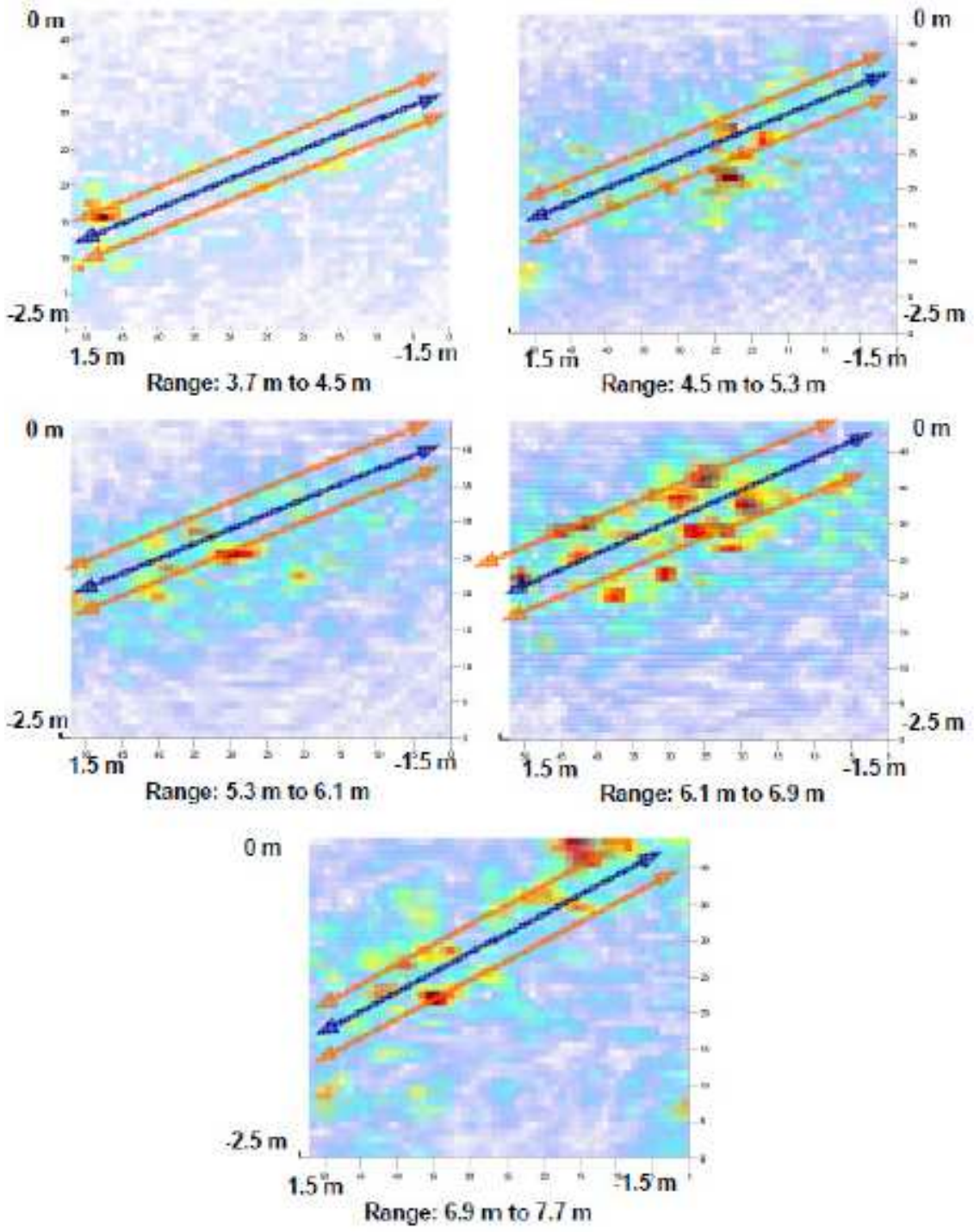

Figure 6.20: Three-dimensional renderings of slices of the snowpack in Fig. 6.17. The slices correspond in thickness equal to the range resolution of 80 cm. The endpoints, relative to the origin, for the spans covered with respect to azimuth and elevation are provided. Each voxel has dimensions of 5.8 cm with respect to azimuth and elevation. Actual resolutions vary from 6.8 cm with respect to elevation at 3.7 m to 23.6 cm with respect to azimuth at 7.7 m.

Importantly, the proposed bands migrate upward between images. This migration is consistent with characteristic (4), namely that the snowpack is disposed on a downward tilt with respect to range. Unfortunately, the downward tilt of the snowpack and the abrupt tilt of the radar line-of-sight into the snowpack mean that resolution with respect to azimuth and elevation are compromised. Of the two tilts, the tilt into the snowpack at 25° is the more pronounced.

Over 80 cm, a tilt into the snowpack of 25° causes the range direction to vary 37 cm. Therefore, layers separated by as much as 37 cm within the snowpack can contribute to the return in a single resolution cell, no matter how small the resolutions with respect to azimuth and elevation. The ambiguity as to where, within a snowpack, contributions are coming from to generate the voxels in a snowpack image could explain some of the irregularities in Fig. 6.20, but it also adds ambiguity to interpretations of those figures in terms of physical snow properties.

Launching waves into a snowpack at close range so that the range direction is parallel to the layers in the snowpack presents a challenge. With improved resolution, the orientation of the range direction with respect to the layers in the snowpack would not matter nearly as much. Therefore, to achieve high resolutions with respect to azimuth and elevation that relate to the snowpack in an uncompressed way, range resolution should be improved by increased bandwidth (see Eq. 4.6).

Despite the ambiguities introduced by the disproportionately coarse range resolution, the patterns demonstrated in Fig. 6.20 merit attention. As the angles between the range direction and the snowpack are relatively constant, the ambiguity introduced applies equally to all imaging voxels. Patterns in the snowpack should appear, albeit somewhat disturbed, in images of the snowpack. An effort to correlate the patterns to properties in the snowpack is warranted.

The top bright bands in Fig. 6.20 may be explained by increased water content due to worming in the snowpack. The presence of warming, melting, and increased water content is supported with evidence from a snow pit (dug in the location indicated in Fig. 6.17) that suggests that melting occurred from the top of the snowpack down to between 12 cm to 20 cm below the surface. Upon a drop in temperature, the melt region in question refreezes into

a loosely formed, but very thick shell, or crust, on top of the snowpack. This melt region is pictured in Fig. 6.22.

Water content, however, cannot explain the thick, bright band below the cool band. According to expectations, the regions below the top bright band, the band warmed by the sun, should grow increasingly cool, due to the insulating properties of snow, until a possible band of brightness occurs at the bottom of the snowpack, due to warming from the ground. The bright band from the ground does not appear. And, contrary to expectation, the middle section is characterized by a broad, bright band.

Snow densities recorded from the snow pit, together with other features in the snowpack can be combined to provide a possible explanation. Figure 6.21 records the density of the snowpack from the second deployment as a function of snowpack height. Also recorded from the snow pit in Fig. 6.21, are measurements of snow hardness (hand scale), crystal type, and crystal size, all as functions of snowpack height.

Denser snow provides stronger returns. As indicated by Fig. 6.21, the snow is most dense in the middle of the snowpack. The large crystal sizes in this region correspond to high density snow. The the larger 3.5 mm grains in the lower middle of the snowpack shown in Fig. 6.21 may also produce more Rayleigh scattering. This region of dense snow can account for the broad, bright band below the thin, cool band in the images.

At the top of the snowpack, the snow is relatively new, having undergone less of the abrasive interactions that break down snow crystals over time, allowing them to be packed more tightly together. In the top of the snowpack, therefore, the lightest snow is found. An infrared picture of this light, low density snow is provided in Fig. 6.22. The light, low density snow toward the top of the snowpack, as recorded in Fig. 6.21 and pictured in Fig. 6.22, can account for the thin, cool band.

Toward the bottom of the snowpack, the density is not as high as it is in the middle of the snowpack, but the snow is still dense. However, the bottom of the snowpack is dominated by faceted crystal forms. These faceted forms have lower specific surface areas

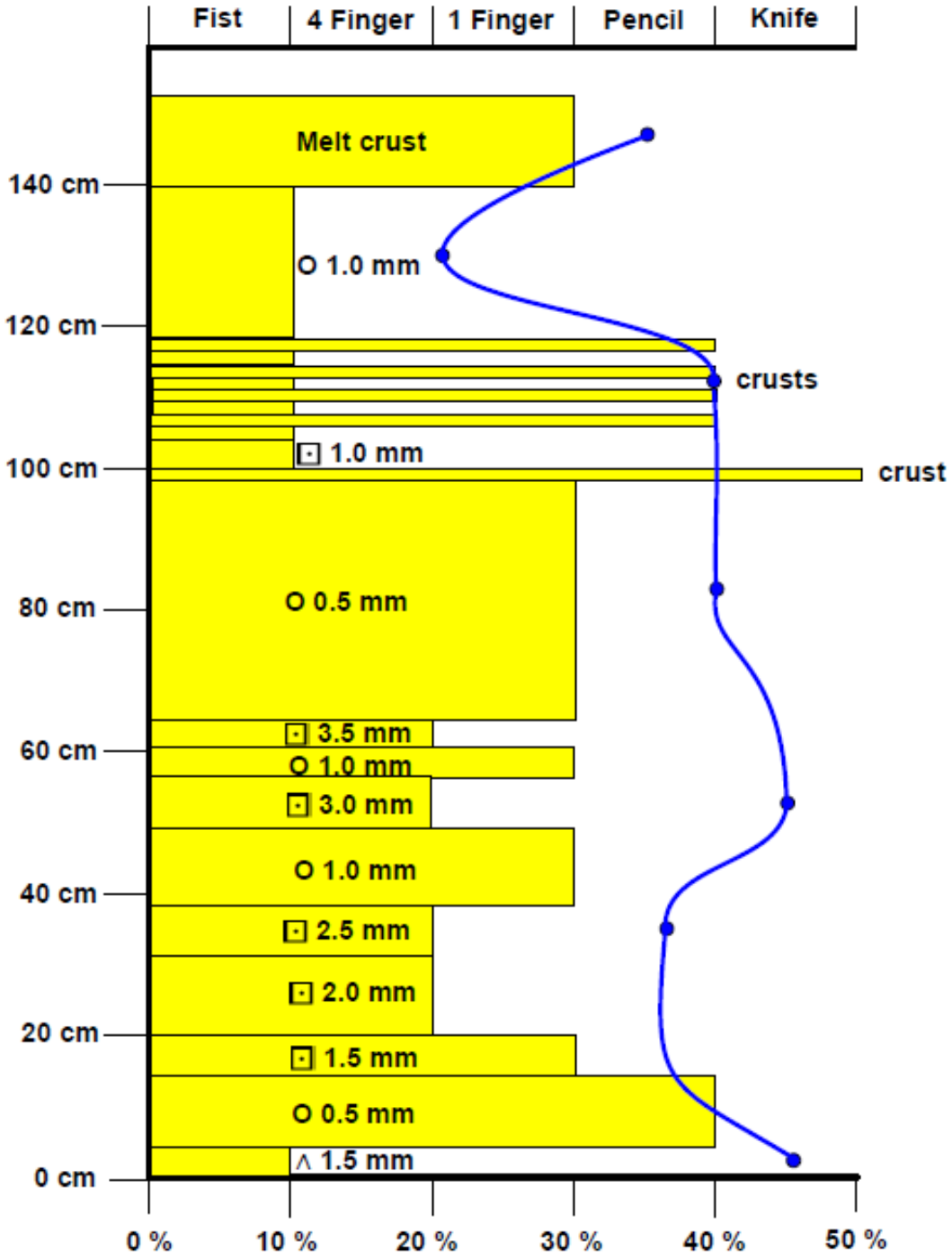

Figure 6.21: A record, for the second deployment snowpack, of measurements of snow density, snow hardness (yellow bands measured on the hand scale), crystal type, and crystal size as a function of snowpack height. The carrot denotes depth hoar, squares denote faceted crystals, and circles denote rounds. Hardness is measured by the hand scale [11]. The blue line, indicative of percent density, is interpolated from seven samples of snow taken at the locations indicated by the blue dots. Zero height is at ground level.

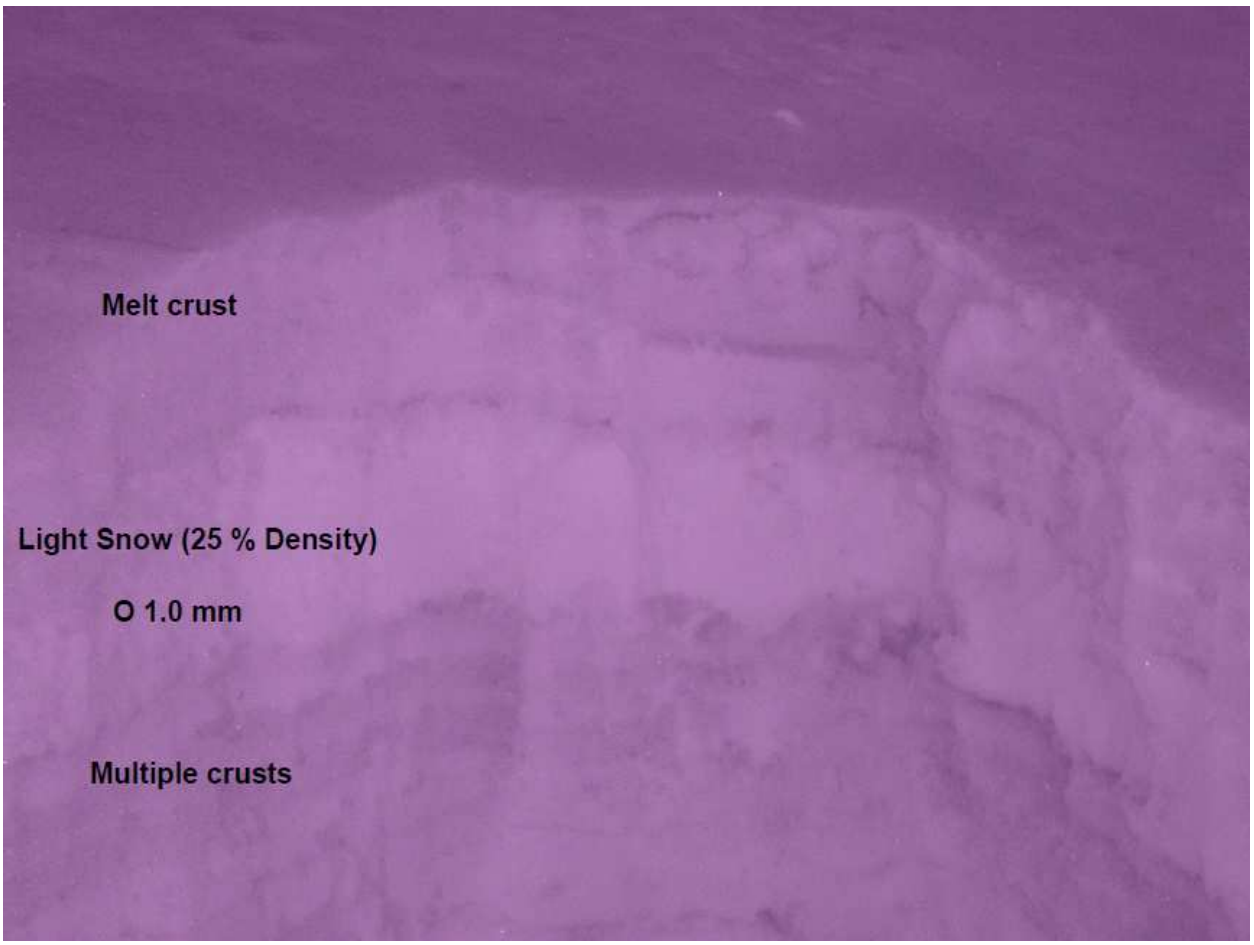

Figure 6.22: An infrared picture of the upper third of the snowpack, during the second deployment. The location of the snow pit from which the picture is taken, is indicated in Fig. 6.17. The infrared picture shows a region of melt-refreeze at the top of the snowpack, a region of light, low density snow underneath, and, at the bottom, a region characterized by several layers of distinct crusts separated by bands of snow. The crusts are visible as the striations in the region marked multiple crusts.

and, therefore, may produce weaker returns, as demonstrated in Fig. 5.6. Faceting at the base of the snowpack can explain the relatively week reflections in this region.

The multiple layers of crusts pictured at the bottom of the infrared image in Fig. 6.22, and recorded in Fig. 6.21, might provide an alternative explanation for the cool, thin band in the images provided in Fig. 6.20. These layers may act as specular surfaces. Owing to the swallow grazing angle, specular surfaces would redirect electromagnetic energy away from the radar system, thereby, explaining the cool response in the images for the relevant regions.

Lessons Learned from Second Deployment

The second deployment provides its own lessons. First, non-nadir, volume-scattering-based images of a snowpack are repeatable with the preliminary scanner. Additional measurements ensure that the snowpack in the images corresponds to the physical snowpack. Therefore, snow volumes, not just electromagnetic boundaries, can serve as a source of imaging backscatter. Second, the important finding that the ground does not interfere with the signal from the snowpack is confirmed. The abrupt tilt angle of 25° employed for the second deployment suggests that grazing angles can rise as high as 25° and returns from the ground will not be a problem. These two points are important to remote, large-area, imaging radar systems directed at snowpacks.

Third, the next step to improving resolution is increasing bandwidth. When it comes to efforts to image the stratigraphy of a snowpack, resolution with respect to azimuth and elevation are at the mercy of range resolution. Coarse range resolution introduces ambiguities into voxels with respect to azimuth and elevation where the range axis cannot be made exactly parallel to the snowpack—this is almost always the case in the undulating terrain where snowpacks are found. These ambiguities complicate the ability of voxels to accurately depict snowpack stratigraphy.

Fourth, in both deployments, patterns consistent with snowpack layers exhibit themselves in the images. Not only is the layered structure seen at the base of the snowpack in the images from the first deployment corroborated, but new patterns seem to manifest themselves. The new patterns follow the contours of the snowpack, as expected and maintain integrity over large areas. The ability to distinguish physical properties within a snowpack, therefore, seems likely at high frequencies.

Fifth, bright bands on the top of the snowpack suggest the ability of the preliminary system to detect changes in water content due to warming during the day. Sixth, more accurate results for avalanche relevant properties, without the effects of heating on the snowpack might require faster scan times, and scans performed in the evening and morning hours.

Seventh, explanations consistent with the physical properties of the snowpacks can be made. These properties may include water content, density, and specific surface area.

However, any attribution of physical properties of a snowpack to proposed image layers remains speculative.

6.3 Conclusions

In accordance with the first goal of the preliminary system, the system demonstrates the ability to generate three-dimensional images at ultra-high resolutions, resolutions measured in inches. In accordance with the second goal, the preliminary system also demonstrates the ability to image snow by means of volume scattering at non-nadir angles. The preliminary system also demonstrates the repeatability of three-dimensional volume images of a snowpack. The coarser resolution images from the preliminary system for longer ranges suggest that higher resolution images would be possible over great distances for an improved system.

Also in accordance with the second goal, the preliminary system uncovers assets and problems for future systems. In terms of assets, the resultant images indicate that at the shallow grazing angles (angles up to at least 25°) that should obtain for long-range, large-area, radar imaging, ground signals should be muted, leaving only the signal of interest from the snowpack. The images from the preliminary system also contain layered structures consistent with layers within the snowpacks that they image. Although accounts of these patterns can be made that are consistent with the physical properties of snowpacks imaged, attribution of patterns to actual physical properties remains speculative. The results from the preliminary system also raise some problems that need to be addressed. Images of corner reflectors show bleeding around scatters, especially with respect to the orthogonal range, azimuth, and elevation axes, that can compromise images by commingling returns. This problem needs to be addressed.

Chapter 7

Conclusion

The ability of radar to capture data remotely, quickly, and over large areas, makes radar a prime candidate for providing the information necessary for improved avalanche prediction, which presently is not based on data from large areas as it should be. To acquire data over large areas practically, a radar must be able to generate and map backscatter from a snowpack for spatially-variant, shallow grazing angles. The radar systems from previous snowpack studies do not have this capability, precluding them from capitalizing on the principal advantages of radar.

At shallow grazing angles, backscatter is primarily generated from volume scattering. Various mechanisms, such as Rayleigh and Mie scattering, hold the promise for generating backscatter with information about the physical properties of snowpack strata, such as density, grain size and shape, water content and distribution. To provide a radar system capable of generating and mapping this backscatter, this thesis designs a three-dimensional, volume-imaging SAR with ultra-high resolution. The ability of a preliminary system to meet these specifications and the implications of the images from the preliminary system for future systems are discussed.

Previously un-demonstrated non-nadir, volume images of snowpacks, as required for remote, large area scans, are demonstrated on more than one occasion by the preliminary system. As another hopeful harbinger of the potential for future systems, the preliminary system demonstrates that the shallow incident angles of a remote scan diminish returns from the ground, avoiding the potentially very difficult problem of decoupling signals from the ground and snow—for angles at least as large as 25°. Furthermore, despite the low-frequency- and low-bandwidth-limitations of the preliminary system, the resultant images from the system demonstrate structures and patterns consistent with the layers of a snowpack. Physical

properties consistent with these patterns, but not conclusively attributable, include density and with water content. The possibility of detecting and assessing avalanche-relevant properties at higher frequencies that are more likely to be responsive to these properties remains good. Also, the results from the preliminary system provide insights that inform the development of future systems that should more closely resembling the full SAR system designed in this thesis.

7.1 Future Work

The ability of the preliminary system to produce volume images of snowpacks warrants development of additional generations of radar systems. These systems should address the problems mentioned in the preceding chapters. The mechanical problems with the scanner need to be resolved. Additionally, greater facility in capturing, downloading, and processing backscatter and position data needs to be achieved.

Greater facility in data capture can be achieved by changing the processing algorithm from one that requires pauses and dwell times at the various nodes in a scan grid to one that can process data from continuous scans. Continuous scans could be performed much more quickly. An ethernet link from the radar to a laptop could allow for backscatter and position data to be downloaded instantaneously, allowing for verification of data before entire scans, or large portions thereof have been run. Adjustments to the processing algorithm could then be applied to see images of the snowpack develop as it is scanned. These improvements are all necessary to allow more interaction with the snowpack in terms of more scans, at more angles, subject to less sun, and with more frequency to capture temporally-evolving snowpacks. The measures are necessary to better determine which physical properties in a snowpack can be attributed to patterns in images from the scans.

Improvements need to be made in terms of the signal-conditioning module. The signal-conditioning module needs to have a higher bandwidth. For reasons discussed, range resolution is the weak link that compromises the ability of azimuth and elevation resolution to differentiate the stratigraphy of a snowpack. Where the range axis is not perfectly parallel with the strata of the snowpack, the resolution cells along range pick up returns from adjacent strata. A bandwidth of 1.5 GHz (10 cm resolution) is desired, but a bandwidth of 500 MHz

(30 cm resolution) would mitigate the ambiguities that range resolution currently imposes upon image voxels with respect to azimuth and elevation.

The second deployment demonstrates the ability of the scanning platform to launch waves close enough to the snowpack to achieve resolutions along azimuth and elevation that are in the sub 10 cm range. Sufficiently fine range resolution is needed to allow azimuth and elevation resolutions to accurately reflect changes in the snowpack stratigraphy with respect to azimuth and elevation. With sufficient range resolution, properties like water content and density represent low-hanging fruit for confirmed attribution, and should be reflected in C-band images, as the first two deployments suggest. Additional work with processing algorithms to reduce bleeding should increase the likelihood of success.

Ultimately, a signal-conditioning module with higher transmit frequencies is desired. As discussed in Chapter 3, higher frequencies mean smaller wavelengths that are much more likely to be responsive to physical properties in the snowpack. According to the theory of Rayleigh scattering, a move up to X-band would make backscatter much more responsive to particle size. According to the theory of Mie scattering, a move up to the K-bands, especially Ka-band, would tap into resonance profiles bearing size and shape information. Even the ability to detect very general differences in shape, such as the difference between sharp, angular facets and rounded grains, would allow for the detection and assessment of some of the most dangers layers in the snowpack. Additional backscatter mechanisms, such as those linked to surface roughness demonstrated by by surface hoar, are also likely to make backscatter more responsive to important physical properties in a snowpack with decreasing wavelengths and increasing frequencies. Increased frequencies can also offer higher resolution. At higher frequencies, high resolution can start to be maintained at distances for which it can start to become possible to determine the feasibility of larger scanning platforms to create long-range, large-area images of snowpack stratigraphy.

Although significant obstacles would need to be overcome, a network analyzer, because of the large range of frequencies it can produce, might be reconfigured to serve as a signal conditioning module. Such a modified signal-conditioning module would be particularly valuable where the network analyzer spanned frequencies up to 50 GHz. A system with such a module would allow for all manner of wavelengths to be applied to different types of

ice grains, clusters, and water contents and distributions in a snowpack to better understand the corresponding backscatter signatures for layers important to avalanche formation.

In the event that such efforts would allow densities to be attributed to image patterns, as suggested from the results of the preliminary system, preliminary efforts in actually aiding in the prediction of avalanches could be undertaken. Such efforts could begin by looking for exceptionally dense snow on top of the snowpack, where low density snow traditionally belongs. The high density snow sought after is wind-deposited snow, the heavy trigger of many avalanches. Wind-deposited snow is infamous for being undetected in its rapid accumulations during inclement weather. The ability of radar to scan large areas quickly provides an ideal solution for detecting and assessing this hazard.

Also, to better understand the physical layers to which structures in images from future systems may correspond, better backscatter models need to be generated for these layers. As discussed in Chapter 3, current models do not take into account the shapes and water distributions most likely to to be correlated with avalanche relevant layers. Empirically results suggest that these oversights have detectible implications for volume scattering coefficients [42], [44]. The requisit models necessary to overcome these oversites could be generated from electromagnetic modeling software employed on volume maps of the microstructure of samples of the relevant types of snow as produced by X-ray diffraction. Examples of such microstructure maps are provided in [19], [20], and [21].

7.2 Impressions on Likelihood of Success

The results from the preliminary system bode well for the possibility of using radar in a way that can assist in avalanche prediction. The system has demonstrated the ability of volumes of snow to provide sufficient backscatter to image snowpacks at the shallow angles that obtain over long-range, large-area scans. The system has demonstrated that returns from the ground should not be a problem at these shallow angles—at least for angles as large as 25°. The promise remains open, and is foreshadowed in some of these layered structures in the resultant images, of imaging property-specific, snowpack stratigraphy.

However, in addressing the probability of success, a distinction should be made between avalanche prediction in a strong sense and in a weak sense. In the strong sense, a

radar-based system could provide stratigraphy reproducing images of the physical properties relevant to avalanche potential so that predictions can be made without a-priori knowledge of the snowpack. Achieving capabilities in the strong sense is preferable, but such capabilities are not necessary.

In the weak sense, success means that radar systems are a useful part of a broader approach to avalanche prediction, tracking properties correlated with known layers of concern. The ability to track secondary properties, such as density, associated with known layers of interest, such as wind-deposited snow, may provide sufficient assistance to avalanche professionals to warrant radar-based systems. Radar systems would be employed by avalanche professionals with a good deal of familiarity about the snowpack they would seek to image. After the results from the preliminary system, success in the weak sense seems feasible; success in the strong sense seems more uncertain. Whether radar-based systems obtain success in the weak sense, or the strong sense, the largest obstacle seems to be the construction of large scanning platforms, with dimensions measured in tens of meters to create the requisite apertures.

Bibliography

[1] H. P. Marshall, M. Schneebeli, G. Koh, M. Matzl, and C. Pielmeier, "Snow stratigraphy measurements with high-frequency FMCW radar: Comparison with snow micropenetrometer," *Cold Regions Science and Technology*, vol. 47, pp. 108–117, 2007. 1, 2, 37, 40, 41, 42, 151, 161, 177

[2] D. A. Ellerbruch, W. E. Little, H. S. Boyne, and D. D. Bachmann, "Microwave characteristics of snow," in *Proceedings of the* 45^{th} *Annual Western Snow Conference*, Albuquerque, NM, Apr. 1977, pp. 630–77. 2

[3] H. S. Boyne and D. A. Ellerbruch, "Microwave measurements of snow stratigraphy and water equivalence," in *Proceedings of the* 47^{th} *Annual Western Snow Conference*, Sparks, NV, Apr. 1979, pp. 651–79. 2

[4] D. A. Ellerbruch and H. S. Boyne, "Snow stratigraphy and water equivalence measured with an active microwave system," *Journal of Glaciology*, vol. 26, no. 94, pp. 225–33, 1980. 2

[5] H. Gubler and P. Weilenmann, "Seasonal snow cover monitoring using FMCW radar," in *Proceedings of the International Snow Science Workshop*, Lake Tahoe, CA, Oct. 1986, pp. 87–97. 2

[6] K. Fuijino and G. Wakahama, "Snow stratigraphy measured by an active microwave system," *Annals of Glaciology*, vol. 6, pp. 207–10, 1985. 2

[7] H. Marshall, G. Koh, and R. Forster, "CLPX-ground: Ground-based frequency modulated continuous wave (FMCW) radar," National Snow and Ice Data Center, Boulder, CO, 2004, digital media available at $http : //nsidc.org/data/docs/daac/nsidc0164_clpx_fmcw/$. 2, 147, 148

[8] H. P. Marshall and G. Koh, "FMCW radars for snow research," *Cold Regions Science and Technology*, vol. 52, pp. 118–131, 2008. 2, 53

[9] M. N. Demuth, H. P. Marshall, and E. M. Morris, "High resolution near-surface snow stratigraphy inferred from ground-based 8-18 GHz FMCW radar measurements: Devon Ice Cap, Nunavut, Canada 2005-06, cryosat validation experiment," in *Proceedings of the* 64^{th} *Eastern Snow Conference*, St. Johns, Newfoundland, Canada, May–Jun. 2007, pp. 9–14. 2

[10] H. P. Marshall, K. Birkeland, K. Elder, and T. Meiners, "Helicopter-based microwave radar measurements in alpine terrain," in *Proceedings of the International Snow Science*

Workshop, Whistler, British Columbia, Canada, Sept. 2008, pp. 20–26. 2, 3, 37, 40, 41, 151, 161, 177

[11] D. McClung and P. Schaerer, *The Avalanche Handbook*. Norwood, MA: Artech House, 2006. 9, 10, 11, 15, 18, 20, 22, 23, 27, 29, 31, 32, 35, 190

[12] B. Tremper, *Staying Alive in Avalanche Terrain*. Seattle, WA: The Mountaineers Books, 2001. 10, 23, 27, 28, 29

[13] J. Jamieson, "Avalanche prediction for persistant snow slabs," Ph.D. dissertation, University of Calgary, Calgary, Canada, 1995. 10, 11

[14] H. Bader and B. Salem, "On the mechanics of snow slab release," *Cold Regions Science and Technology*, vol. 17, pp. 287–300, 1990. 10

[15] S. Colbeck, "The layered character of cnow covers," *Review of Geophysics*, vol. 29, pp. 81–96, 1991. 10, 31

[16] M. de Quervain, "On the metamorphism and hardening of snow under constant temperature gradient," *Int. Assoc. Sci. Hydrol.*, pp. 46 225–46 239, 1958. 13

[17] S. C. Colbeck, "Theory of metamorphism of dry snow," *Journal of Geophysical Research*, pp. 5475–5482, 1983. 13

[18] ——, "An overview of seasonal snow metamorphism," *Reviews of Geophysics and Space Physics*, vol. 20, pp. 45–61, 1982. 13

[19] F. Flin, J. B. Brzoska, B. Lesaffre, C. Colou, and R. A. Pieritz, "Full three-dimensional modelling of curvature-dependent snow metamorphism: first results and comparison with experimental tomographic data," *J. Phys. D. Appl. Phys.*, vol. 36, pp. A49–A54, 2003. 13, 198

[20] F. Flin and J. B. Brzoska, "The temperature-gradient metamorphism of snow: vapour diffusion model and application to tomographic images," *Annals of Glaciology*, vol. 49, pp. 17–21, 2008. 13, 198

[21] F. Flin, J. B. Brzoska, R. Pieritz, B. Lesaffre, C. Coleou, and Y. Furukawa, "A tentative model for the temperature gradient snow metamorphism and its first validations on x-ray microtomographic data," in *Furukawa1Proc. 8th Int. Conf. X-ray Microscopy IPAP Conf.*, 2007, pp. 306–308. 13, 198

[22] M. Matzl, "Quantifying the stratigraphy of snow profiles," Ph.D. dissertation, Swiss Federal Institute of Technology, Zurich, 2006. 15, 177

[23] S. C. Colbeck, "Sintering in a dry snow cover," *Journal of Applied Physics*, vol. 84, pp. 4585–4589, 1998. 16

[24] ——, "Sintering of unequal grains," *Journal of Applied Physics*, vol. 89, pp. 4612–4618, 2001. 16

[25] K. W. Birkeland, R. F. Johnson, and D. S. Schmidt, "Near-surface faceted crystals formed by diurnal recrystallization: A case study of weak layer formation in the mountain snowpack and its contribution to snow avalanches," *Artic and Alpine Research*, vol. 30, pp. 200–204, 1998. 23

[26] K. W. Birkeland, "Terminology and predominant processes associated with the formation of weak layers of near-surface faceted crystals in the mountain snowpack," *Artic and Alpine Research*, vol. 30, pp. 193–199, 1998. 23

[27] S. R. Brevfogle, "Growth characteristics of hoar frost with respect to avalanche occurrence," in *International Snow Science Workshop Proceedings*, 1986. 25

[28] J. C. Giddings and E. Lachapelle, "The formation rate of depth hoar," *Journal of Geophysical Research*, vol. 67, pp. 2377–2383, 1961. 28

[29] E. Akitave, "Studies of depth hoar," in *Contributions from the Institute of LowTemperature Science, Series A, No.26*, 1974, pp. 1–67. 28

[30] C. Fierz, "Field observation and modelling of weak-layer evolution," *Annals of Glaciology*, vol. 26, pp. 7–13, 1998. 31

[31] S. C. Colbeck and J. Jamieson, "The formation of faceted layers above crusts," *Cold Regions Science and Technology*, vol. 33, pp. 247–252, 2001. 31

[32] G. Koh, "Complex dielectric constant of ice at 1.8 GHz," *Cold Regions Science and Technology*, vol. 25, pp. 119–121, 1997. 39

[33] ——, "Dielectric constant of ice at 26.5-40 GHz," *Journal of Applied Physics*, vol. 71, pp. 5119–5122, 1992. 39

[34] A. Denoth, "Wet snow pendular regime: the amount of water in ring-shaped configurations," *Cold Regions Science and Technology*, vol. 30, pp. 13–18, 1999. 40

[35] ——, "Structural phase changes of the liquid water component in alpine snow," *Cold Regions Science and Technology*, vol. 37, pp. 227–232, 2003. 40

[36] S. M. Wentworth, *Applied Electromagnetics: Early Transmission Lines Approach.* Hoboken, NJ: John Wiley & Sons, Inc., 2007, pp. 353–368. 42

[37] G. Mie, "Beitrage zur optik truber medien," *Annalen der Physik*, vol. 25, p. 377, 1908. 45

[38] F. T. Ulaby, R. K. Moore, and A. K. Fung, *Microwave Remote Sensing.* Norwood, MA: Artech House, 1981, vol. 1. 45, 46, 68, 71, 72, 92, 94, 97, 107, 109

[39] D. Deirmendjian, *Electromagnetic Scattering on Spherical Polydispersions.* New York, NY: American Elsevier Publishing Co., Inc., 1969. 46, 49

[40] D. Kerr, *Propagation of Short Radio Waves.* New York, NY: Dover Publications, Inc., 1951. 48

[41] A. D. Papatsoris and P. A. Wilson, "A rigorous explanation of the resonances observed in the scattering from spherical ice particles," *IEEE Transactions on Antennas and Propatation*, vol. 42, pp. 1350–1354, 1994. 48, 49

[42] S. Colbeck, "The geometry and permittivity of snow at high frequencies," *Journal of Applied Physics*, vol. 53, pp. 4495–4500, 1982. 51, 52, 198

[43] D. Polder and J. V. Santen, "The effective permeability of mixtures of solids," *Physica*, vol. 12, pp. 257–271, 1946. 52

[44] M. T. Hallikainen, F. T. Ulaby, and M. Abdelrazik, "Dielectric properties of snow in the 3 to 37 GHz range," *IEEE Transactions on Antennas and Propatation*, vol. AP-34, pp. 1329–1340, 1986. 52, 53, 198

[45] V. Lytle and K. Jezek, "Dielectric permittivity and scattering measurements of Greenland firn at 26.5-40 GHz," *IEEE Transactions on Geoscience and Remote Sensing*, vol. 32, pp. 290–295, 1994. 53

[46] J. L. Prince and J. M. Links, *Medical Imaging Signals and Systems*. Upper Saddle River, NJ: Pearson Prentice Hall Bioengineering, 2006, pp. 4, 16. 62

[47] H. R. Raemer, *Radar System Principles*. Boca Raton, FL: CRC Press, 1997, pp. 5–7. 66

[48] R. O. Harger, *Synthetic Aperture Radar Systems: Theory and Design*. New York, NY: Academic Press, 1970, pp. 43–49. 66

[49] P. Z. Peebles, *Radar Principles*. New York, NY: John Wiley & Sons, Inc., 1998. 68

[50] D. G. C. Luck, *Frequency Modulated Radar*. New York, NY: McGraw-Hill, 1949, pp. 3–38. 74

[51] M. Duersch, "BYU micro-SAR: A very small, low-power LFM-CW synthetic aperture radar," Master's thesis, Brigham Young University, 2004. 74, 135

[52] D. R. Wehner, *High-Resolution Radar*, 2nd ed. Boston, MA: Artech House, 1995, pp. 3–5. 74

[53] A. V. Oppenheim, A. S. Willsky, and S. H. Nawab, *Signals & Systems*, 2nd ed. Upper Saddle River, NJ: Prentice Hall, 1997, ch. 4. 74, 75

[54] G. A. Showman, "An overview of radar imaging," October 2009, chapter on Radar Imaging from unpublished manuscript. 78, 113, 116

[55] A. V. Oppenheim, A. S. Willsky, and S. H. Nawab, *Signals & Systems*, 2nd ed. Upper Saddle River, NJ: Prentice Hall, 1997, ch. 1. 82

[56] D. H. Staelin, A. W. Morgenthaler, and J. A. Kong, *Electromagnetic Waves*. Upper Saddle River, NJ: Prentice Hall, 1998, ch. 2. 83

[57] M. N. O. Sadiku, *Numerical Techniques in Electromagnetics*, 2nd ed. Boca Raton, FL: CRC Press, 2001, ch. 5.3. 83

[58] A. Reigber, A. Moreira, and K. Papathananassiou, "First demonstration of airborne SAR tomography using multibaseline L-band data," *IEEE Trans. On Geosci. and Remote Sensing*, vol. 38, pp. 2142–2152, Sep. 2000. 105

[59] ——, "Adaptive spectral estimation for multibaseline SAR tomography with airborne L-band data," in *Proceedings of IEEE 2003 International Geoscience and Remote Sensing Symposium*, Toulouse, France, July 2003. 105

[60] S. Guillaso and A. Reigber, "Polarimetric SAR tomography," available at: http://earth.esa.int/workshops/polinsar2005/participants/58/paper_article_guillaso.pdf. 105

[61] A. Reigber, K. Papathanassiou, S. Cloude, and A. Moreira, "SAR tomography and interferometry for the remote sensing of forested terrain," German Aerospace Center (DLR), Institute of Radio Frequency Technology, P.O. Box 1162, D-82230 Oberpfaffenhofen, Germany. 105

[62] O. Frey, F. Morsdorf, and E. Meier, "Tomographic processing of multi-baseline P-band SAR data for imaging of a forested area," in *IGARSS 2007, International Geoscience and Remote Sensing Symposium*, 2007. 105

[63] J. P. Fitch, *Synthetic Aperture Radar*. New York, NY: Springer Verlag, 1988, pp. 139–144. 130

[64] W. G. Carrara, R. S. Goodman, and R. M. Majewski, *Spotlight Synthetic Aperture Radar Signal Processing Algorithms*. Boston, MA: Artech House, 1995, ch. 5, particular attention should be paid to Section 5.3.1). 134

[65] N. C. Currie and C. E. Brown, *Principles and Applications of Millimeter-Wave Radar*. Norwood, MA: Artech House, 1987, ch. Part III. 134

[66] J. D. Taylor, *Ultra-Wideband Radar Technology*. Boca Raton, FL: CRC Press LLC, 2001. 134

[67] E. Zaugg and D. Long, "Coherent multi-frequency-band resolution enhancement for synthetic aperture radar," in *Proceedings of the International Geoscience and Remote Sensing Symposium*, Cape Town, South Africa, 2009. 135

[68] V. Liepa, K. Sarabandi, and M. A. Tassoudji, "A pulsed network analyzer based scatterometer," in *Proceedings of IGARSS 1989 and Canadian Symposium on Remote Sensing*, 1989. 135

[69] F. Ulaby, T. Haddock, J. East, and V. Liepa, "Millimeter-wave network analyzer-based scatterometer," in *Proceedings of IGARSS 1986 Symposium*, Zurich, Switzerland, 1986. 135

[70] "vol3d," Matlab tool distributed online at MATLAB CENTRAL: An open exchange for the MATLAB and Simulink user community, available at *http* : *//www.mathworks.com/matlabcentral/fileexchange/*4927−*vol*3*d*−*m*−*vol*3*dtool*−*m*. 154